Alma Mater Studiourm - Università di Bologna

DOTTORATO DI RICERCA IN
ASTROFISICA

Ciclo 34

Settore Concorsuale: 02/C1 - ASTRONOMIA, ASTROFISICA,
FISICA DELLA TERRA E DEI PIANETI

Settore Scientifico Disciplinare: FIS/05 - ASTRONOMIA E ASTROFISICA

TOWARDS A FULL COSMOLOGICAL EXPLOITATION OF COSMIC VOIDS

Presentata da: Sofia Contarini

Coordinatore di Dottorato
Andrea Miglio

Supervisore
Federico Marulli

Co-supervisore
Lauro Moscardini

Esame finale anno 2022

Contents

Abstract **6**

Introduction **9**

1 Cosmological framework **13**
1.1 Fundamentals of General Relativity . . . 13
1.1.1 The cosmological constant . . . 15
1.2 The Friedmann-Leimaître-Robertson-Walker metric . . . 16
1.3 The Hubble-Leimaître's law and the definition of redshift . . . 17
1.3.1 Other distance definitions . . . 19
1.4 Friedmann Equations . . . 21
1.4.1 The Einstein-de Sitter model . . . 23
1.5 The Standard Cosmological model . . . 26

2 Structure formation **28**
2.1 Linear theory . . . 28
2.1.1 Jeans instability in an expanding universe . . . 30
2.1.2 Statistical properties of the Universe . . . 32
2.1.3 Evolution of the power spectrum . . . 34
2.1.4 The bias parameter . . . 36
2.1.5 Clustering estimators . . . 36
2.2 Nonlinear theory . . . 37
2.2.1 Spherical evolution . . . 38
2.2.2 The Zel'dovich approximation . . . 42
2.3 Numerical simulations . . . 43
2.3.1 Halo finding algorithms . . . 45
2.3.2 Building a mock catalogue . . . 47

3 Tensions in the standard cosmological model **50**
3.1 Alternatives to the standard ΛCDM model . . . 52
3.1.1 Dynamical DE models . . . 52
3.1.2 Modified gravity models . . . 54
3.1.3 Massive neutrinos . . . 58

4 Statistical properties of cosmic voids **60**
4.1 Void definition . . . 62
4.2 Excursion-set formalism . . . 62
4.3 Size function . . . 63
4.4 Void density profiles . . . 66
4.5 Void-galaxy cross-correlation function . . . 69
4.6 Observational tests . . . 71
4.6.1 Geometric distortions . . . 72
4.6.2 Dynamic distortions . . . 73
4.7 Voids as cosmological probes . . . 75

5 Numerical tools to build cosmic void catalogues **77**
5.1 `CosmoBolognaLib` . . . 77
5.2 Void finders . . . 77
5.3 Cleaning algorithm . . . 81

6 Voids in biased tracers **84**
6.1 CoDECS simulations . . . 84
6.2 Data preparation . . . 85
6.3 A new extension of the Vdn model . . . 87
6.4 Bias of tracers in overdensity and underdensity regions . . . 89
6.5 Results: calibration on the data . . . 93
6.6 Results: size function of voids in biased tracers . . . 97

7 Voids in modified gravity scenarios with massive neutrinos **102**
7.1 DUSTGRAIN-*pathfinder* simulations . . . 103
7.2 Data preparation for the unbiased and biased cases . . . 106
7.3 Results: void profiles . . . 108
7.4 Results: void size function in the DM field . . . 114
7.5 Results: void size function in the biased tracer field . . . 118

8 Void size function forecasts for the *Euclid* mission **129**
8.1 Flagship simulation . . . 130
8.2 Void catalogues . . . 131
8.3 Calibration methodology . . . 134
8.4 Bayesian statistical analysis . . . 135
8.5 Cosmological forecast models . . . 137
8.6 Results: calibration and comparison with mock data . . . 138
8.7 Results: forecasts on the void size function constraining power . . . 142
8.8 Results: study on the complementarity of the forecasted cosmological constraints . . . 147

9 Further studies with voids as cosmological probes **155**
9.1 Further *Euclid* forecasts with voids . . . 155
9.1.1 Void-galaxy cross-correlation cosmology . . . 156
9.1.2 Void-lensing cross-correlation cosmology . . . 161
9.2 Probe combination: void and cluster number counts . . . 167

10 Conclusions and future perspectives **175**

Appendices **180**

A Measuring the linear bias **181**

B Testing systematic uncertainties deriving from the calibrated bias relation **184**

C The void-lensing Fisher matrix **187**

Bibliography **189**

Abstract

Observing the Universe at large scales, a stately fraction of its volume is dominated by almost empty space. Alongside the luminous filamentary structures of the Universe, characterised by energetic astrophysical phenomena, there are vast and smooth regions that have remained outside Cosmology spotlight during the past decades: cosmic voids. Although essentially devoid of matter, voids enclose fundamental information about the cosmological framework. Thanks to their large sizes and low-density interiors, voids constitute unique laboratories to study dark energy and modified gravity theories, as well as models including massive neutrinos, primordial non-Gaussianity and physics beyond the Standard Model.

The number density of voids as a function of their radius, as known as void size function, has been modelled from first principles by Sheth & van de Weygaert (2004) with the subsequent contribution of Jennings, Li & Hu (2013). The resulting theoretical model is commonly named Vdn and its high accuracy in the prediction of the abundance of voids identified in the total matter distribution has been largely demonstrated, provided that the observed sample of voids is analysed following the same assumptions adopted by the model. Specifically, this means that the voids are defined as spherical, non-overlapping regions with internal densities below a given threshold.

To this purpose, we improved an already existing algorithm for void cleaning, aimed at removing spurious underdensities and shaping voids following the prescriptions given by the theory. Moreover, we extended the applicability of the Vdn model to voids identified in the distribution of biased tracers, such as dark matter haloes, galaxies and galaxy clusters. In particular, we parametrised the model as a function of the large scale bias, building an efficient methodology to predict the abundance of voids traced by different types of mass tracers.

Afterwards, we applied the methodology previously developed to study cosmic voids in alternative cosmological scenarios, characterised by modified gravity and the inclusion of massive neutrinos. So we analysed a set of simulations specifically designed for these studies with the aim of investigating the degeneracies between cosmological models that simultaneously feature a modification of General Relativity – in the form of $f(R)$ gravity (Hu & Sawicki, 2007) – and the presence of massive neutrinos. We studied the cosmic void density profiles and abundances in the distribution of both dark matter particles and dark matter haloes, investigating the requirements to be addressed in order to maximise the discriminating power of cosmic voids. We found a clear evidence of the enhancement of gravity in the void density profiles measured in $f(R)$ cosmologies, especially at $z \sim 1$. However, any peculiar trend in the shape of void profiles has revealed to be almost completely overridden by the presence of massive neutrinos because of their thermal free-

streaming. On the other hand, we found that the void size function, measured at high redshifts and for large void radii, will possibly represent an effective probe to disentangle these degenerate cosmological scenarios, which is key in the perspective of the upcoming wide-field redshift surveys.

Furthermore, we investigated the constraining power of different void statistics expected for the upcoming medium-class ESA mission, *Euclid* (Laureijs et al., 2011; Amendola et al., 2018; Euclid Collaboration: Blanchard et al., 2020). We mainly focused on the exploitation of the void size function, studying the abundance of voids in the official *Euclid* mock galaxy light-cone, prepared to match the features of the upcoming spectroscopic survey. We found an excellent agreement between the predictions of the Vdn model and the measured mock void abundances, providing reliable void number estimates to serve as a basis for further cosmological applications using voids. Then we computed the forecasts on the cosmological constraints achievable on different dynamical dark energy models, including in the analysis the modelling of both geometrical and redshift-space distortions. In particular, we considered the wCDM and w_0w_aCDM scenarios. The first implements a constant dark energy equation of state parameter, w, and the second parametrises dynamical dark energy models with the popular Chevallier-Polarski-Linder (Chevallier & Polarski, 2001; Linder, 2003) equation of state. We showcased the impressive constraining power of the void size function on the main cosmological parameters, estimating the expected dark energy figure of merit and comparing the obtained confidence contours with those coming from different void statistics and different cosmological probes. Moreover we highlighted how the confidence contours derived from the void size function are in some cases almost independent of and orthogonal to those obtained with standard probes (e.g. weak lensing and galaxy clustering), demonstrating the potential of the combination of these cosmological constraints.

Further studies on voids finalised at providing forecasts for the *Euclid* mission are reported in Hamaus et al. (2022) and Bonici et al. (2022, in preparation). In the first work we derived the constraining power from the modelling of the observed void-galaxy cross-correlation function for the *Euclid* spectroscopic survey, while in the second we analysed the combination of angular void clustering, galaxy weak lensing and their cross-correlation, in the perspective of the *Euclid* photometric survey. In both works we derived cosmological forecasts extremely competitive with those of the *Euclid* main probes and we proved the strong contribution of voids in constraining several cosmological parameters.

As a first exploration of the synergy of the void size function with primary probes, we studied the combination between void and galaxy cluster number counts. The results, which will be presented in Pelliciari et al. (2022, in preparation), highlighted the exceptional orthogonality of the two probes and the significant enhancement provided by cosmic voids thanks to combination techniques.

As future development of this work, we will apply our void size function modelling pipeline to real galaxy surveys, starting in particular with the final SDSS-III Baryon Oscillation Spectroscopic Survey (BOSS) Data Release 12 (Dawson et al., 2013) dataset and other state-of-the art catalogues.

Introduction

The Universe has recently entered a phase of accelerated expansion. This revolutionary discovery goes back to more than two decades ago and was originally achieved thanks to distant type Ia supernovae (Riess et al., 1998; Perlmutter et al., 1999; Schmidt et al., 1998). The following observations of the cosmic microwave background anisotropies and the large scale structure (e.g. Eisenstein et al., 2005a; Komatsu et al., 2011; Bennett et al., 2013; Planck Collaboration et al., 2020a), have then supported this scenario, which is now widely accepted among the scientific community. The standard paradigm of modern cosmology, the Λ-cold dark matter (ΛCDM) model, interprets the accelerating expansion of the Universe as due to the existence of an extra component called *cosmological constant*, Λ. Thanks to its simplicity and its concordance with the majority of current cosmological observations, the ΛCDM is nowadays the most popular and widespread cosmological model (Shafieloo & Clarkson, 2010; Heavens et al., 2017).

However, this scenario has been often questioned, since it clashes with both some theoretical and observational issues. The first concerns for instance the coincidence and the fine-tuning problems (Weinberg, 1989; Carroll, 2001; Martin, 2012, but see Bianchi & Rovelli (2010) for an alternative perspective), while the latter is raised in particular by the recent discordant measurements of the Hubble constant, H_0, together with other well-known anomalies and tensions (see e.g. Bernal, Verde & Riess, 2016; Moresco & Marulli, 2017; Verde, Treu & Riess, 2019, and references therein). Hence, new ideas and different theoretical approaches have been proposed to solve or alleviate these possible fundamental inconsistencies.

Among the presented solutions, there are models that interpret the dark energy component as a dynamical variable slowly varying with the cosmic time, or as exotic new forms of energy that would cause the observed late time accelerated expansion of the Universe (see e.g. Frieman, Turner & Huterer, 2008; Wen, Wang & Luo, 2018, and references therein). There are also alternative explanations which involve a modification of General Relativity in a manner that leads to accelerating solutions. The overall picture is made even more uncertain by the observational degeneracies arising when including in these models the effects caused by massive neutrinos (Howlett et al., 2012; He, 2013; Motohashi, Starobinsky & Yokoyama, 2013; Baldi et al., 2014; Wright, Winther & Koyama, 2017; Giocoli, Baldi & Moscardini, 2018)

Therefore, the efforts of the scientific community are now focused on testing these alternative cosmological scenarios through precision observations. In this challenge, a number of different cosmological probes come to our aid, among which we highlight: the modelling of the cosmic microwave background (CMB) temperature anistropies (see e.g. Fixsen et al., 1996; Komatsu et al., 2011; Planck Collaboration et al., 2020b), the study of galaxy clustering, particularly effective thanks to the baryonic acoustic oscillations (BAO) imprints (see e.g. Crocce & Scoccimarro, 2008; Percival et al., 2010; Beutler et al., 2011; Anderson et al., 2014) and the observation of the weak lensing effect by large scale structures (see e.g. Hildebrandt et al., 2017; Abbott et al., 2018a, and Bartelmann & Schneider, 2001 for a review). Despite the effectiveness of these probes in constraining the cosmological model, some of its aspects remain still poorly determined and many issues still unsolved.

To shed light on the fundamental laws and components of the Universe, acting behind the scenes of the cosmological scenario, we must move the Cosmology spotlight to novel and orthogonal probes. Their complementarity with the standard probes allows us indeed to break the degeneracies afflicting different cosmological parameters, and to achieve more precision in discerning the cosmological model that is most in agreement with the observations.

Among these additional probes, we want to focus our attention on the Universe darkest regions, that is on those vast areas where the luminous matter is almost absent and only emerges along the edges. These objects, called *cosmic voids* for they intrinsic underdense nature, are characterised by sizes up to hundreds of megaparsec (Gregory & Thompson, 1978; Tikhonov & Karachentsev, 2006; Thompson & Gregory, 2011; Szapudi et al., 2015) and dominate the large-scale structure (LSS) of the Universe in terms of volume (Platen, van de Weygaert & Jones, 2007), playing a fundamental role in the formation of its filamentary pattern (de Lapparent, Geller & Huchra, 1986; Zeldovich, Einasto & Shandarin, 1982; Sheth & van de Weygaert, 2004; van de Weygaert & Schaap, 2009), the so-called *cosmic web*. Voids constitute a unique cosmological probe: their interiors, spanning a large range of scales and featuring low matter density, make them particularly suited to study dark energy and modified gravity (Lee & Park, 2009; Biswas, Alizadeh & Wandelt, 2010; Li & Efstathiou, 2012; Clampitt, Cai & Li, 2013a; Spolyar, Sahlén & Silk, 2013a; Cai, Padilla & Li, 2015; Pisani et al., 2015; Zivick et al., 2015; Achitouv, 2016; Pollina et al., 2016; Sahlén, Zubeldía & Silk, 2016; Falck et al., 2018; Sahlén & Silk, 2018; Paillas et al., 2019; Perico et al., 2019; Verza et al., 2019), as well as massive neutrinos (Massara et al., 2015; Banerjee & Dalal, 2016; Kreisch et al., 2019a; Sahlén, 2019; Schuster et al., 2019; Kreisch et al., 2021), primordial non-Gaussianity (Chan, Hamaus & Biagetti, 2019), and physics beyond the standard model (Peebles, 2001; Reed et al., 2015; Yang et al., 2015; Baldi & Villaescusa-Navarro, 2016).

Nevertheless, studying voids requires sky surveys of very large volume, deep enough to measure an extremely high number of redshifts also for low-mass galaxies, and to map in detail significant contiguous fractions of the observable Universe. This is why, only in recent years, thanks to the advent of wide-field redshift surveys, cosmic voids have started to gain popularity as cosmological probes. However, the way will be probably downhill for voids in the next future, since we expect a huge amount of data to come from the upcoming sky surveys such as the ESA *Euclid* mission[1] (Laureijs et al., 2011; Amendola et al., 2018), the NASA Nancy Grace Roman Space Telescope[2] (NGRST, formerly called WFIRST) Green et al., 2012) and the Vera C. Rubin Observatory[3] (LSST, LSST Dark Energy Science Collaboration, 2012).

[1] http://www.euclid-ec.org
[2] https://roman.gsfc.nasa.gov/
[3] Legacy Survey of Space and Time; http://www.lsst.org

With this Thesis work we accompany the reader on a journey into these deep and obscure regions of the Universe, to mainly study their abundance (i.e. the void size function), but also their internal density (i.e. the void-galaxy cross-correlation function) and their clustering (i.e. the void auto-correlation), with the ultimate goal of fully exploiting voids as cosmological probes. However, before venturing in this exploration, we need to equip us with all the necessary tools (i.e. the theoretical background and the computational instruments) to understand the cosmological framework we are going to explore. Let us review the main stages of our trip:

- In Chapter 1 we provide the fundamentals for the mathematical description of the modern cosmological models. We supply the main elements of the General Theory of Relativity, passing through the derivation of the Friedmann Equations, and we eventually illustrate the main features of the currently adopted standard model of Cosmology.
- In Chapter 2 we review the Jeans theory, which provides the modelling of structure formation, and we present the theoretical description of the linear and nonlinear statistics of the Universe. Lastly, we introduce the reader to the cosmological simulations, fundamental to test the predictions of the proposed cosmological models and produce different realisations of our Universe.
- In Chapter 3 we expose the issues and the tensions of the ΛCDM model and we review some of the popular alternatives to this scenario, focusing in particular on models implementing dynamical dark energy, modified gravity and massive neutrinos.
- In Chapter 4 we finally take the path to cosmic voids. We start learning about their statistics, their observable features, and their potential as cosmological probes. Here we provide the theory of the size function, density profiles and clustering of cosmic voids.
- In Chapter 5 we introduce the numerical tools necessary to perform void analysis, i.e. the void finding and void cleaning algorithms, strictly necessary to build the catalogue of voids we will analyse.
- In Chapter 6 we start presenting our analyses, studying the number counts of voids identified in simulated catalogues of biased mass tracers. To model this statistic, we propose an extension of the void size function models already present in the literature and we prove its effectiveness in modelling cosmic void counts.
- In Chapter 7 we test the methodology introduced in the previous chapters with alternative cosmological scenarios, i.e. analysing voids identified in simulations implementing both modified gravity and massive neutrinos. We focus in particular on the cosmic degeneracies between these scenarios and the standard ΛCDM model, assessing the disentangling power of void density profiles and number counts.
- In Chapter 8 we study the void size function in the perspective of the *Euclid* spectroscopic survey. We model the observed void number counts by means of galaxy mock catalogues and we forecast the expected constraining power from this statistic, with a preliminary exploration of its combination with different cosmological probes.

- In Chapter 9 we present three additional studies, complementary to the main ones on the void abundance. We compute forecasts from the observed void-galaxy cross-correlation function, and from a combination of void clustering and weak lensing, for the spectroscopic and photometric *Euclid* surveys respectively. Then, we present a first approach to the probe combination technique, focusing on the constraints deriving from the cluster mass function and the void size function.
- In the end, in Chapter 10, we sum up the presented results, preparing the path for future works, in which will apply all the acquired knowledge and methodologies to exploit voids with real data catalogues.

Now that everything is settled, we are ready to embark on this journey.

Chapter 1

Cosmological framework

The study of the physical properties of our Universe is a very wide subject of research, going from planets in our Solar System, to the birth and death of stars in the Milky Way, to the orbits of galaxies grouped in clusters. Cosmology in particular focuses on the largest scales of our Universe, considering the latter as a whole.

In this chapter we provide a summary of the cosmological framework on which this Thesis work is built, focusing on the mathematical structure of the modern cosmological models based on the General Theory of Relativity (GR). In particular, we define the Friedmann-Robertson–Walker metric, which models the curvature of the space-time in homogeneous and isotropic universes. Then we introduce the Hubble-Leimaître's law together with the definition of redshift, and we derive the Friedmann Equations as solutions to the Einstein's Field Equation. Moreover we illustrate the main features of the currently adopted Standard Cosmological model.

1.1 Fundamentals of General Relativity

On very large scales the predominant interaction between massive bodies such as galaxies and clusters of galaxies is the force of gravity. The cosmological models, aiming at describing the Universe as a whole, are therefore mainly based on the description of the action of this force. Nowadays the most powerful and widespread theory of gravity is the GR, introduced by Einstein (1915) in order to combine his former theory of Special Relativity with the gravitational interaction. This model is based on the notion that space-time can be warped by mass and energy. As a consequence, gravity is defined not as a force per se but as the direct result of a non-Euclidean space-time geometry.

In this context, the space-time is a four-dimensional differentiable manifold, in which every point on it is called *event* and has four coordinates, i.e. three space-like and one time-like. The properties of the space-time geometry are described by the *metric tensor* $g_{\mu\nu}$, which accounts for the intrinsic curvature of the manifold and characterises the distance relations between events. We can express the distance $\mathrm{d}s^2$ between two infinitesimally close events as:

$$\mathrm{d}s^2 = g_{\mu\nu}\mathrm{d}x^\mu\mathrm{d}x^\nu \quad (\mu, \nu = 0, 1, 2, 3) \ , \tag{1.1}$$

where $x^\mu = (ct, x, y, z)$ and $x^\nu = x^\mu + \mathrm{d}x^\mu = [c(t + \mathrm{d}t), x + \mathrm{d}x, y + \mathrm{d}y, z + \mathrm{d}z]$; x^μ represents the spatial coordinates, with $\mu = 1, 2, 3$, then c the speed of light and t the proper time. This displacement can be explicitly separated as:

$$\mathrm{d}s^2 = g_{00}\mathrm{d}t^2 + 2g_{0\nu}\mathrm{d}x^\nu \mathrm{d}t + g_{\mu\nu}\mathrm{d}x^\mu \mathrm{d}x^\nu \ , \tag{1.2}$$

where $g_{00}\mathrm{d}t^2$ is the time component, $g_{\mu\nu}\mathrm{d}x^\mu\mathrm{d}x^\nu$ the spatial components and $2g_{0\nu}\mathrm{d}x^\nu\mathrm{d}t$ the mixed components. The shortest path between any two events is called *geodesic*, and extends the concept of straight lines, characteristic of flat Minkowski space, to curved spaces. We can derive it simply by minimising $\mathrm{d}s^2$:

$$\delta \int \mathrm{d}s = 0 \ . \tag{1.3}$$

Any free particle moves along these geodesics. These paths can be obtained by solving the so-called geodesic equation:

$$\frac{\mathrm{d}^2 x^\mu}{\mathrm{d}\lambda^2} + \Gamma^\mu_{\alpha\beta}\frac{\mathrm{d}x^\alpha}{\mathrm{d}\lambda}\frac{\mathrm{d}x^\beta}{\mathrm{d}\lambda} = 0 \ , \tag{1.4}$$

where λ is a generic scalar parameter of motion (e.g. the proper time) which monotonically increases along the particle's path, Γ are the Christoffel's symbols which contain the metric tensor

$$\Gamma^\mu_{\alpha\beta} = \frac{1}{2}g^{\mu\nu}\left[\frac{\partial g_{\alpha\nu}}{\partial x^\beta} + \frac{\partial g_{\beta\nu}}{\partial x^\alpha} - \frac{\partial g_{\alpha\beta}}{\partial x^\nu}\right] \ , \tag{1.5}$$

and

$$g^{\mu\nu}g_{\alpha\nu} = \delta^\mu_\alpha \tag{1.6}$$

is the Kronecker delta, which is equal to the unity if $\mu = \alpha$, and 0 otherwise. According to GR, the metric tensor itself is influenced by the distribution and by the motion of the matter.

We can now introduce the energy-momentum tensor $T_{\mu\nu}$, which describes the density, the flux energy and the momentum of matter. For a perfect-fluid with pressure p and density ρ, the energy-momentum tensor can be expressed as:

$$T_{\mu\nu} = (p + \rho c^2)U_\mu U_\nu - p g_{\mu\nu} \ , \tag{1.7}$$

where $U_\mu = g_{\mu\nu}U^\nu = g_{\mu\nu}\frac{\mathrm{d}x^\nu(\lambda)}{\mathrm{d}\lambda}$ is the 4-velocity of the fluid and $x^\nu(\lambda)$ is the world line of a fluid element. In differential geometry, the energy conservation law can be found by imposing the covariant derivative to be null:

$$T^\nu_\mu;\nu = 0 \ , \tag{1.8}$$

where, conventionally, the semicolon indicates the covariant derivative. Einstein demonstrated that from Eq. (1.8) it is possible to derive the Poisson's equation in the classical limit:

$$\nabla^2\phi = 4\pi G\rho \ , \tag{1.9}$$

which relates the gravitational potential, ϕ, to the density of the source of the gravitational field, ρ. This implies that the metric tensor is connected to the energy-momentum tensor with an equation which contains only the first two derivatives of $g_{\mu\nu}$, and has zero covariant derivative. From the expression of the Riemann–Christoffel tensor:

$$R^\mu_{\alpha\beta\nu} = \frac{\partial\Gamma^\mu_{\alpha\nu}}{\partial x^\beta} + \frac{\partial\Gamma^\mu_{\alpha\beta}}{\partial x^\nu} + \Gamma^\mu_{\gamma\beta}\Gamma^\gamma_{\alpha\nu} - \Gamma^\mu_{\gamma\nu}\Gamma^\gamma_{\alpha\beta} \ , \tag{1.10}$$

we can assess the curvature of the space-time manifold by defining the so-called Ricci tensor, $R_{\mu\nu}$, and Ricci scalar, R:

$$R_{\mu\nu} = R^{\alpha}_{\mu\alpha\nu} \text{ and } R = g^{\mu\nu} R_{\mu\nu} \ , \tag{1.11}$$

where the scalar curvature comes from the contraction of the Ricci tensor with the metric $g_{\mu\nu}$. From these Einstein defined his own tensor:

$$G_{\mu\nu} \equiv R_{\mu\nu} - \frac{1}{2} g_{\mu\nu} R \ , \tag{1.12}$$

and built his equation of gravity, fundamental pillar of modern Cosmology:

$$G_{\mu\nu} = \frac{8\pi G}{c^4} T_{\mu\nu} \ , \tag{1.13}$$

where G is the Newtonian gravitational constant. The quantity $8\pi G/c^4$ ensures to obtain the Poisson's equation in the weak gravitational field limit (i.e. Newtonian gravity).

1.1.1 The cosmological constant

In order to recover static-Universe solutions from his field equation, Einstein introduced in 1917 a constant Λ, called the *cosmological constant*, to balance gravity's attractive action on matter and match the general consensus of the time. In fact, as we will demonstrate in Sect. 1.4, the Einstein's field equation only admits collapsing- or expanding-Universe solutions, while it was commonly believed at that time that the Universe was static (i.e. neither contracting nor expanding) and both spatially and temporally infinite. With a suitable choice of Λ, which has to be small enough to ensure the recovery of Newtonian theory in the weak field approximation, we can indeed obtain a static model for our Universe:

$$R_{\mu\nu} - \frac{1}{2} g_{\mu\nu} R - \Lambda g_{\mu\nu} = \frac{8\pi G}{c^4} T_{\mu\nu} \ . \tag{1.14}$$

Historically, the addition of the Λ term is marked as "Einstein's greatest blunder" not only because he inserted the cosmological constant to recover, erroneously, a static universe, but also because (i) the value of Λ required to his purpose should have been extremely fine-tuned and (ii) the solutions of Eq. (1.14) would have led to an *unstable* equilibrium (Bianchi & Rovelli, 2010).

Nowadays we know from the observations of the flux of distant type Ia supernovae (SNIa) (Riess et al., 1998; Perlmutter et al., 1999) that our Universe is not only expanding, but that it is currently in an accelerated expansion. Therefore, even if the historical reason for the introduction of the cosmological constant was different, it has now been re-included in Einstein's field equation thanks to its repulsive effect. In particular, Λ takes different meanings depending on its position in the Einstein's field equation:

- left-hand side: interpretation of Λ as a geometrical modification of gravity, as described by GR;
- right-hand side: interpretation of Λ as an additional energy component called *dark energy* (DE).

It was then Alexander Friedmann the first who studied the dynamical solutions of the Einstein's field equation modified with the addition of the cosmological constant, describing the expansion or contraction of an isotropic homogeneous Universe as a function of time (Friedmann, 1922). We will present the main results of his theoretical studies in Sect. 1.4.

1.2 The Friedmann-Leimaître-Robertson-Walker metric

Most of the models developed in modern Cosmology are based on the so-called *cosmological principle* (CP), which is the assumption of isotropy and homogeneity of the Universe on sufficiently large scales (i.e. hundreds of Mpc nowadays, where 1 Mpc $= 10^6$pc $\simeq 3.09 \cdot 10^{13}$ km). Homogeneity is the property of looking identical everywhere, and isotropy in every direction. These assumptions are observationally confirmed today on sufficient large scale, i.e. over hundreds of Megaparsecs (see e.g. Yadav, Bagla & Khandai, 2010; Scrimgeour et al., 2012; Nadathur, 2013; Kim et al., 2021, for a different estimations of this scale). Once assumed the validity of this hypothesis, the goal is to build a model of the Universe satisfying the CP. We can define a universal time such that the spatial metric is the same at each position in space. Thanks to the assumption of isotropy, the mixed components g_{0i} of the equation (1.2) have to be null. Thus we can obtain the general form of the metric:

$$\mathrm{d}s^2 = c^2\mathrm{d}t^2 - g_{ij}\mathrm{d}x^i\mathrm{d}x^j = (c\mathrm{d}t)^2 - \mathrm{d}l^2 \ . \tag{1.15}$$

Any point of the Universe can be described with a set of three spatial coordinates x_i ($i = 1, 2, 3$), called *comoving coordinates*, and one temporal coordinate, t, called *proper* or *cosmic time*, which are defined in a reference system at rest with the Universe expansion. To determine g_{ij} we have to find a spatial 3D metric which follows the requirements of homogeneity and isotropy.

As shown in Sect. 1.1, the geometrical properties of the space-time are described by the metric. Thanks to the assumption of the CP, the tensor R_{ijkl} does not depend on the derivatives of the metric g_{ij}. For the symmetry properties of the deriving form of the Riemann tensor, we can introduce the most general form of Eq. (1.15), in the *Friedmann-Leimaître-Robertson-Walker* (FLRW) metric:

$$\mathrm{d}s^2 = c^2\mathrm{d}t^2 - a^2(t)\left[\frac{\mathrm{d}r^2}{1-\kappa r^2} + r^2(\sin^2\theta\ \mathrm{d}\phi^2 + \mathrm{d}\theta^2)\right] \ , \tag{1.16}$$

where $a(t)$ is the cosmic scale factor (or the expansion parameter), having the dimensions of a length, and κ is the curvature parameter. Equation (1.16) expresses the metric in spherical polar coordinates (ρ, ϕ, θ), related to the Cartesian ones by the transformation:

$$\begin{cases} x_1 = \rho\sin\theta\cos\phi \\ x_2 = \rho\sin\theta\sin\phi \\ x_3 = \rho\cos\theta \end{cases} , \tag{1.17}$$

where the ranges of these values are $0 \leq \rho < \infty$, $0 \leq \theta < \pi$ and $0 \leq \phi < 2\pi$ and ρ is considered dimensionless.

Given an energy-momentum tensor, the value of κ and the function $a(t)$ can be derived by the Einstein's Field Equations. In particular, the curvature of the space-time can be positive, zero or negative. This is determined by the value of the parameter κ, which has only three possible solutions and shapes the geometry of the Universe:

- $\kappa = 1 \;\rightarrow$ hyper-spherical geometry: space is closed but with no boundaries, in analogy to the surface of a sphere in two dimensions;
- $\kappa = 1 \;\rightarrow$ flat geometry: space is Euclidean and infinite;
- $\kappa = -1 \;\rightarrow$ hyperbolic geometry: space is open and infinite, in analogy to the surface of a saddle in two dimensions.

1.3 The Hubble-Leimaître's law and the definition of redshift

The *proper distance*, $D_{\rm pr}$, is defined as the physical distance between a point P_0, which can be located at the origin of the coordinate system (r, θ, ϕ), and another point P. This quantity depends on time through the scale parameter $a(t)$ and can be expressed as:

$$D_{\rm pr} = a(t) \int_0^r \frac{\mathrm{d}r'}{\sqrt{1 - \kappa r'^2}} = a(t) F(r, \kappa) \ . \tag{1.18}$$

At time t, the proper distance is related to the present one ($t = t_0$) by the following relation:

$$D_{\rm C} \equiv D_{\rm pr}(t_0) = a_0 F(r) \ , \tag{1.19}$$

where $a_0 \equiv a(t = t_0)$. Hereafter if a variable has the subscript "0", it will indicate that it is calculated at the present time, $t = t_0$. The quantity $D_{\rm C}$, already introduced in Sect. 1.2, is the so-called the *comoving distance* and by definition it remains constant with the expansion of the Universe. The direct connection between the two definitions is given by the equation:

$$D_{\rm pr} = \frac{a(t)}{a_0} D_{\rm C} \ . \tag{1.20}$$

The expansion of the Universe causes a continuous drifting apart between any two points in the space. We can compute the *radial velocity* between these points as the derivative of $D_{\rm pr}$ with respect to t:

$$v_r = \frac{\mathrm{d}}{\mathrm{d}t} D_{\rm pr} = \frac{\mathrm{d}}{\mathrm{d}t}[a(t)F(r)] = \dot{a}(t)F(r) + a(t)\dot{F}(r) \ . \tag{1.21}$$

Given the time-independence of the term $F(r)$, the previous relation yields:

$$v_r = \dot{a}(t)F(r) = \frac{\dot{a}(t)}{a(t)} D_{\rm pr} = H(t) D_{\rm pr} \ , \tag{1.22}$$

which is the well-known *Hubble-Leimaître's law*, where the *Hubble parameter* is defined as $H(t) \equiv \dot{a}/a$. $H(t)$ is a function of time and has the same value across the Universe at a given cosmic time. Its value at the present time $H(t_0) = H_0$, called the *Hubble constant*, describes the isotropic expansion rate of the Universe and is constant for all space for a fixed cosmic time. Moreover, it is conventional to introduce a dimensionless parameter, h, redefining the Hubble parameter as:

$$H_0 \equiv 100h \text{ km s}^{-1} \text{ Mpc}^{-1} \ . \tag{1.23}$$

The value of the Hubble constant is still not known with extremely great precision. Some the latest estimates give values of around 70 km s^{-1} Mpc^{-1}, for example: $H_0 = 69.13 \pm 2.34$ km s^{-1} Mpc^{-1}, obtained by modelling the BAO measurements from galaxy surveys (Wang, Xu & Zhao, 2017), $H_0 = 74.03 \pm 1.42$ km s^{-1} Mpc^{-1}, by using distance ladders as Cepheids or SNIa (Riess et al., 2019), $H_0 = 67.4 \pm 0.5$ km s^{-1} Mpc^{-1}, from the CMB angular spectrum (Planck Collaboration et al., 2020a), $H_0 = 67.7^{+4.3}_{-.42}$ km s^{-1} Mpc^{-1}, from the analysis of gravitational waves (Mukherjee et al., 2020) and $H_0 = 73.9 \pm 3.0$ km s^{-1} Mpc^{-1}, from geometric distance measurements to Megamaser-hosting galaxies (Pesce et al., 2020).

Being H_0 expressed in units of s^{-1}, the inverse of the Hubble parameter may provide a rough estimate of the age of the Universe, by taking the simplified assumption that for all its history the Universe has expanded with the same rate. We call the global motion of objects in the Universe with respect to each other the *Hubble Flow*. One of its consequences is that the observed spectrum of very distant objects is reddened, i.e. shifted towards longer wavelengths. This phenomenon, similar to the *Doppler effect* of sound waves, is called the *redshift* of the electromagnetic spectrum. Let us consider an electromagnetic source that emits light at a specific monochromatic wavelength $\lambda_{\rm em}$, in the reference system of the source. Let us indicate the shifted wavelength of the radiation which arrives to the observer as $\lambda_{\rm obs}$. The relative difference from the two electromagnetic radiations

$$z \equiv \frac{\lambda_{\rm obs} - \lambda_{\rm em}}{\lambda(t)} = \frac{\Delta\lambda}{\overline{\lambda}} \ , \tag{1.24}$$

can in principle be less than zero (*blueshift*), when the source is approaching the observer, or greater than zero (*redshift*), when the source is receding.

Let us now consider an observer located at a distance d from an emitting source. By definition photons move along null geodesics ($ds^2 = 0$ for massless particles) during the expansion of the Universe. Taking once again the FLRW metric in polar coordinates expressed in Eq. (1.16), and considering $\mathrm{d}\phi = \mathrm{d}\theta = 0$ for simplicity, we have:

$$c^2 \mathrm{d}t^2 - a^2(t) \frac{\mathrm{d}r^2}{1 - \kappa r^2} = 0 \ . \tag{1.25}$$

Integrating the metric along the path, the previous equation becomes:

$$\int_{t_{\rm em}}^{t_{\rm obs}} \frac{c \ \mathrm{d}t}{a(t)} = \int_0^r \frac{\mathrm{d}r'^2}{\sqrt{1 - \kappa r'^2}} = F(r) \ . \tag{1.26}$$

We suppose now that a second photon is emitted from the source at $t'_{\rm em} = t_{\rm em} + \delta t_{\rm em}$ and reaches the observer at $t'_{\rm obs} = t_{\rm obs} + \delta t_{\rm obs}$. $F(r)$ is independent of the Universe's expansion because of the assumption of comoving coordinates, so the difference between the two photon paths is given only in terms of time:

$$\int_{t'_{\rm em}}^{t'_{\rm obs}} \frac{c \ \mathrm{d}t}{a(t)} = F(r) \ . \tag{1.27}$$

If the time intervals $\delta t_{\rm em}$ and $\delta t_{\rm obs}$ are small, $a(t)$ can be considered almost constant, so the equivalence between Eqs. (1.26) and (1.27) implies:

$$\frac{\delta t_{\rm obs}}{a(t_{\rm obs})} = \frac{\delta t_{\rm em}}{a(t_{\rm em})} \ . \tag{1.28}$$

Now, since $\delta t = 1/\nu$ and $\lambda = c/\nu$, for an observer located at present time and an emitting source at a generic instant t, we have:

$$1 + z = \frac{a_0}{a(t)} \ . \tag{1.29}$$

Thanks to this relation, the measure of the redshift can be used to infer the distance of extragalactic sources, and is nowadays commonly exploited thanks to the development of spectroscopy and photometry techniques. However, it is important to remind that the light's frequency (and the redshift) is also affected by gravitational fields and other relativistic effects, therefore it is not strictly correct to consider the frequency shifts from very distant sources due to the Doppler effect alone (Weinberg, 1972).

1.3.1 Other distance definitions

We have shown how the comoving coordinates are connected to the concept of proper distance, $D_{\rm pr}$. The latter represents the distance between events happening at the same proper time, so it is easily understandable that this kind of measure is physically impossible to take. It is therefore useful to define other kinds of distances that are, at least in principle, directly measurable from astronomical objects, exploiting their observational properties as in the case of the redshift.

One option is to use the *standard candle* method, assigning to the observed object a *luminosity distance*, $D_{\rm L}$. A standard candle object is an object with known luminosity L. An example of this kind of objects are SNIa, whose light curves are characterised by a fairly consistent peak in luminosity given by the fixed critical mass of their progenitors. In principle, assuming to have an object with the same intrinsic luminosity throughout the space-time, we can compute its luminosity distance by measuring its flux, f, i.e. their luminosity per unit of area:

$$D_{\rm L} = \left(\frac{L}{4\pi f}\right)^{1/2} . \tag{1.30}$$

The flux of the source, measured by the observer placed at P_0 at time t_0, can be expressed as:

$$f = \frac{L_{\rm obs}}{4\pi D_{\rm C}^2} \ . \tag{1.31}$$

The denominator is the surface area of a sphere centred in P_0. However, this sphere is inflated by the Universe expansion, so we have to take into account both the scale factor on the measured distance, $4\pi D_{\rm C}^2 = 4\pi a_0^2 r^2$, and the Doppler effect on the received emission light. The emitted luminosity is defined as the rate of change of the energy of the source:

$$L \equiv \frac{{\rm d}E}{{\rm d}t} \ . \tag{1.32}$$

From Eq. (1.28) we can see that photons emitted by the source in a small interval δt arrive to the observer in an interval $\delta t_{\rm obs} = \delta t \; a_0/a(t)$, where $t = t_{\rm em}$, i.e. the time of photon emission. Considering these two effects we can re-write Eq. (1.32) as:

$$L = L_{\rm obs}\left[\frac{a_0}{a(t)}\right]^2 , \tag{1.33}$$

so that the flux f becomes:

$$f = \frac{L_{\rm obs}}{4\pi a_0^2 r^2} = \frac{L}{4\pi a_0^2 r^2}\left[\frac{a(t)}{a_0}\right]^2 . \tag{1.34}$$

Since the luminosity distance is defined by conserving the flux, preserving the inverse square law of decrease in luminosity from a point source we obtain:

$$D_{\rm L} \equiv \frac{a_0^2 r}{a(t)} = a_0 r(1+z) . \tag{1.35}$$

Another method to measure the distances of cosmological objects from their properties is the *standard ruler* method. It is based on the observation of objects with a known intrinsic dimension. An example of standard rulers are the BAO, i.e. the fluctuations visible in the distribution of baryonic matter on large scales: their characteristic length is given by the path travelled by acoustic waves in the primordial plasma before the Universe cooled down, stopping the expansion of the plasma density waves. Let us consider a standard ruler of size ℓ, with a proper distance from the observer r, and subtending an angle $\Delta\theta$, as shown in Fig. 1.1. So, assuming the small-angle approximation, we can compute the so-called *comoving angular diameter distance*, $D_{\rm M}$, as:

$$D_{\rm M} \equiv \frac{\ell}{\Delta\theta} = a(t) r \tag{1.36}$$

in which t is the time corresponding to the emission of the radiation from the source. By comparing the luminosity distance with the angular diameter distance, we obtain the Etherington's reciprocity theorem (Etherington, 1933):

$$\frac{D_{\rm L}}{D_{\rm M}} = (1+z)^2 , \tag{1.37}$$

from which we can derive that having objects representing both a standard ruler and a standard candle, their angular-diameter distance will be always smaller than their luminosity distance. Eq. (1.37) provides a powerful probe to test the validity of the FLRW metric, in particular the assumptions of homogeneity and isotropy (e.g. Li, Wu & Yu, 2011), and consequently plays an important role in the validation of current cosmological models.

As a final note we point out that, by definition, all the cosmological distance definitions are coincident for $r \to 0$ and $t \to t_0$

$$D_{\rm pr} \simeq D_{\rm C} \simeq D_{\rm L} \simeq D_{\rm M} , \tag{1.38}$$

recovering the Euclidean behavior at the small distances.

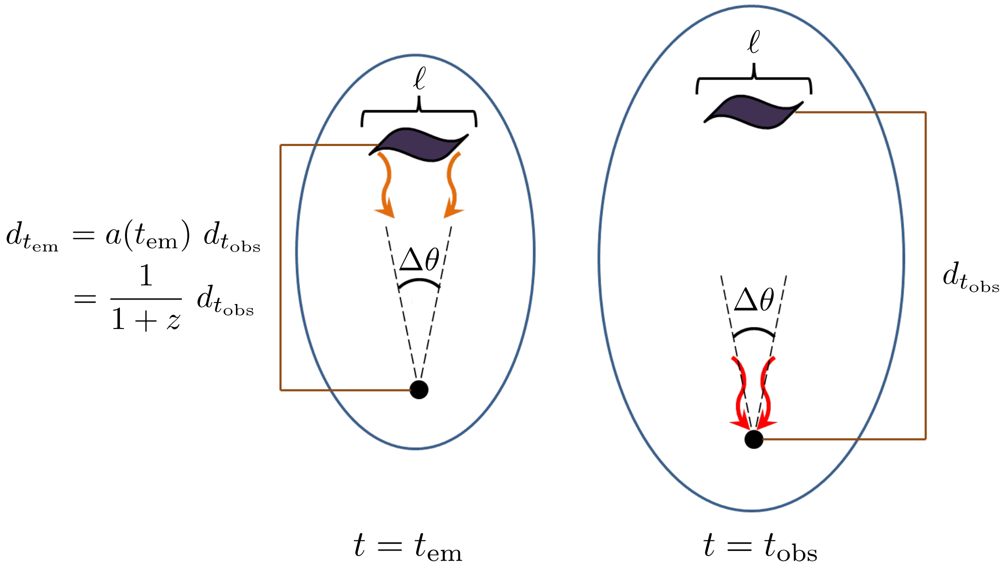

Figure 1.1: An object (standard ruler), aligned perpendicularly to the line of sight, emits photons at time $t = t_{\rm em}$ at distance z. At the time of observation $t = t_{\rm obs}$, the body appears to subtend an angle $\Delta\theta$, though the space in-between the observer and the standard ruler has expanded during the photons' travel by a factor of $(1+z)$. Credits to: http://www.astro.wisc.edu/~waligorski/index.html.

1.4 Friedmann Equations

Assuming the validity of the CP and considering the energy-momentum tensor to be that of a perfect-fluid, we can apply the FLRW metric to solve the Einstein's field equation. The resulting system of equations, proposed by Friedmann in 1922, provides the time evolution of $a(t)$ and describes the dynamic evolution of the Universe. These equations are called the *first* and the *second Friedmann Equations* and can be expressed as follows:

$$\ddot{a} = -\frac{4\pi}{3} G \left(\rho + \frac{3p}{c^2}\right) a \ , \tag{1.39}$$

$$\dot{a}^2 + \kappa c^2 = \frac{8\pi}{3} G \rho a^2 \ . \tag{1.40}$$

Each of these two equations can be recovered from the other one by applying the adiabatic condition:

$$\mathrm{d}\mathcal{U} = -p\mathrm{d}V \ , \tag{1.41}$$

where $\mathcal{U}$ and V represent the internal energy and the volume of the Universe, respectively. The validity of Eq. (1.41) persists as long as the Universe is considered as a closed system, which expands and evolves without energy losses. This equation can be also expressed as:

$$\mathrm{d}\left(\rho c^2 a^3\right) = -p\mathrm{d}a^3 \ , \tag{1.42}$$

from which it follows:

$$\dot{\rho} + 3\left(\rho + \frac{p}{c^2}\right)\frac{\dot{a}}{a} = 0 \ . \tag{1.43}$$

The density, ρ, and the pressure, p, in these equations have to be considered as the sum of all the densities and all the pressures of the Universe's components, respectively.

A general approach to develop Friedmann Equations is to introduce a generic equation of state (EoS) for the fluid composing the Universe. Adopting once again the perfect-fluid approximation, the equation of state of such fluid can be expressed in the form:

$$p = w\rho c^2 \ , \tag{1.44}$$

where w is defined so that the sound speed is:

$$c_\mathrm{s} \equiv \left(\frac{\partial p}{\partial \rho}\right)^{1/2}_\mathrm{s} = c\sqrt{w} \ . \tag{1.45}$$

To have physically meaningful w, this parameter must belong to the so-called *Zel'dovich interval*:

$$0 \leq w < 1 \ . \tag{1.46}$$

These limits ensure to have a positive (or null) value for the sound speed, which at the same time is smaller than the speed of light.

The value of w depends on the type of component of the Universe. In particular, the "ordinary" components can be divided into two big main families: relativistic and non-relativistic. The first case is represented by dust, characterised by $w \simeq 0$, i.e. with negligible pressure, while a non-degenerate and ultra-relativistic fluid is described by an EoS with $w = 1/3$. This is the case for a radiative fluid or, more generally, for photons and relativistic particles like neutrinos. The cosmological constant Λ is instead defined to behave as a perfect-fluid with $w = -1$ and it follows the Eq. (1.14), in analogy to the other components.

With these definitions it is now possible to express the energy-momentum tensor as the sum of all the components i:

$$T_{\mu\nu} \equiv \sum_i T^{(i)}_{\mu\nu} \ . \tag{1.47}$$

Moreover, from the combination of Eqs. (1.42) and (1.44), we can derive the relations describing the variation of Universe's different components with the cosmic time:

$$\rho_w \propto a^{-3(1+w)} \propto (1+z)^{3(1+w)} \ . \tag{1.48}$$

As a direct consequence of the previous relations, we can assert that different components have dominated through the succession of the cosmic epochs, prevailing one over the others.

We can re-write Eq. (1.40) to derive the curvature of the Universe previously inserted in the FLRW metric:

$$\frac{\kappa}{a^2} = \frac{1}{c^2}\left(\frac{\dot{a}}{a}\right)^2\left(\frac{\rho}{\rho_c} - 1\right) \ , \tag{1.49}$$

where we introduced the *critical density* parameter:

$$\rho_\mathrm{crit}(t) \equiv \frac{3}{8\pi G}\left(\frac{\dot{a}}{a}\right)^2 = \frac{3H^2(t)}{8\pi G} \ , \tag{1.50}$$

which by definition represents the density requested to obtain a universe with flat geometry ($\kappa = 0$). The cases in which $\rho < \rho_{\rm crit}$ correspond to the scenarios in which the Universe is subject to an eternal expansion, while the case $\rho > \rho_{\rm crit}$ implies an slowdown of the expansion followed by a contraction. The value of the critical density calculated today ($t = t_0$) depends on the Hubble constant H_0. The value for $\rho_{\rm crit,0} \equiv \rho_{\rm crit}(t_0)$ is:

$$\rho_{\rm c,0} \simeq 1.9 \times 10^{-26} \; h^2 \; {\rm kg \; m^{-3}} \; . \tag{1.51}$$

From the critical density we can define the dimensionless *density parameter*:

$$\Omega(t) \equiv \frac{\rho(t)}{\rho_{\rm c}(t)} \; , \tag{1.52}$$

which can be expressed for each component, Ω_{w_i}. By definition the *total density parameter* is the sum of all of them:

$$\Omega_{\rm tot} \equiv \sum_i \Omega_{w_i} \; , \tag{1.53}$$

In a flat universe we have $\Omega_{\rm tot} = 1$, while in open or closed universes $\Omega_{\rm tot} < 1$ and $\Omega_{\rm tot} > 1$, respectively.

Using the definition of Ω, the second Friedmann equation can be rewritten as:

$$1 - \Omega(t) = -\frac{\kappa c^2}{a^2(t) H(t)^2} \; . \tag{1.54}$$

Note that the right hand side of this equation cannot change its sign during the expansion of the Universe, so neither can the left hand side. From this fundamental relation follows that a universe governed by the Friedmann equations cannot change its geometry during its evolution.

Now it is useful to express Eq. (1.40) in terms of Ω, H and z, which are more representative parameters of the observable Universe. To do this we use the definitions of the density parameter (Eq. 1.52), of redshift (Eq. 1.29) and the Hubble's law (Eq. 1.22), obtaining:

$$H^2(z) = H_0^2 (1+z)^2 \left[\Omega_{0,\kappa} + \sum_i \Omega_{0,w_i} (1+z)^{1+3w_i} \right] \equiv H_0^2 E^2(z) \; , \tag{1.55}$$

in which $\Omega_{0,\kappa} \equiv 1 - \sum_i \Omega_{0,w_i}$ is the so-called *curvature density parameter.*

1.4.1 The Einstein-de Sitter model

Let us now develop Eq. (1.40) by applying Eq. (1.14) for a universe with a single component. The resulting relation is:

$$\ddot{a} = -\frac{4\pi}{3} G \rho (1 + 3w) a \; . \tag{1.56}$$

From the latter it results clear that, if w belongs to the Zel'dovich interval (Eq. 1.46), i.e. for ordinary cosmological components like matter ($w = 0$) and radiation ($w = 1/3$), then the corresponding mono-component universe is characterised by a decelerated expansion ($\ddot{a} < 0$). From the Hubble's law we can conclude that $a(t)$ grows monotonically, given the positive sign of $H(t)$. This implies that, going back in time, there must be an instant at which $a(t)$ is equal to zero, at some finite time in the past. This event is called *Big Bang* and implies that the Universe's initial state was as an infinitely small, hot and dense singularity. All possible cosmological models assuming a single-fluid component with $-1/3 < w < 1$, have necessarily an instant at which $a(t)$ vanishes, while the density and the expansion speed diverge:

$$\lim_{t\to 0} \rho(t) = \lim_{t\to 0} \left(\frac{a_0}{a}\right)^{-3(1+w)} \to \infty \ . \tag{1.57}$$

A generic model that includes the hypothesis of mono-component fluid and that assumes a flat geometry ($\kappa = 0$) is called *Einstein-de Sitter Model* (EdS). In this model Eq. (1.55) reduces to:

$$H(z) = H_0(1+z)^{\frac{3(1+w)}{2}} \ . \tag{1.58}$$

Since we have already demonstrated that different components of the Universe (matter, radiation and Λ) can become dominant at different cosmic epochs, we can assume that our Universe is entirely composed by only one type of fluid, at any time. So we can divide the history of the Universe into epochs based on which component was the dominant in that time interval, as shown in Fig. 1.2. It is easy to derive the time dependence of each component's density by developing the adiabatic condition expressed in Eq. (1.43) with Eq. (1.44). From this it is possible to conclude that the matter and radiation densities change during the Universe's expansion with different rates. In particular, at early times the radiation results the dominant component (*radiation-dominated era*) while at late times the matter component becomes the most relevant (*matter-dominated era*). Moreover, interpreting the DE component as fluid with $w = -1$, we can demonstrate that its density is independent of the time and starts to be dominant only at very recent epochs (*DE-dominated era*). We point out that the single-component approximation is accurate only in periods far from the moments of equivalences, i.e the transitions in which one component starts to prevail on the others. In Table 1.1 we report a list of useful relations derived assuming the EdS model and expressing the behaviour of the main quantities characterising this type of universe. These dependencies are expressed for a generic fluid with parameter w, and then computed for both the matter-dominated epoch ($w = 0$) and the radiation-dominated epoch ($w = 1/3$). From these relations we can derive for the matter component ($w = 0$):

$$\rho_{\rm m} = \rho_{0,\rm m}(1+z)^3 \,, \tag{1.59}$$

while for the radiation component ($w = 1/3$):

$$\rho_{\rm r} = \rho_{0,\rm r}(1+z)^4 \,. \tag{1.60}$$

By equalising these relations we can find the redshift at which the matter and radiation components have the same density. Considering the measured density values, we can calculate the time in which this event, called *matter-radiation equivalence*, took place:

$$z_{\rm eq} = \frac{\rho_{0,\rm m}}{\rho_{0,\rm r}} - 1 \simeq 3 \cdot 10^4 \ . \tag{1.61}$$

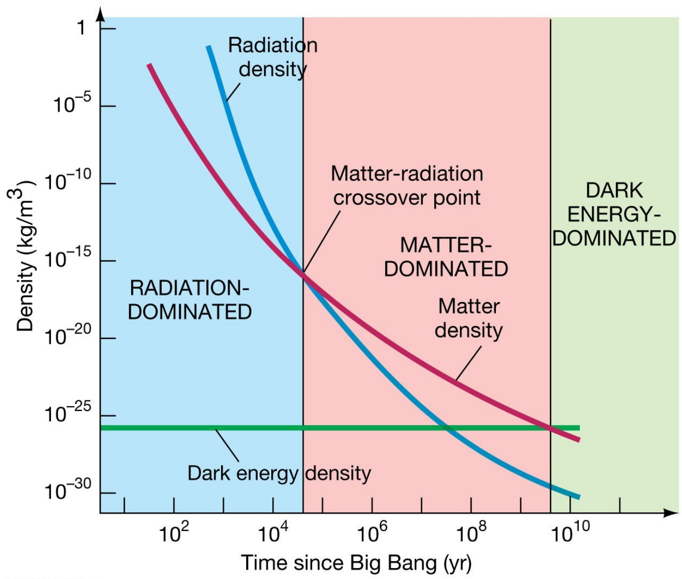

Figure 1.2: Trends with time of the three main Universe's components: radiation, matter, DE. With the time evolution different components start to predominate on the others because of the relative change in density. Credits to: https://pages.uoregon.edu/jimbrau/astr123/Notes/Chapter27.html.

Generic w	$w = 0$	$w = 1/3$
$a(t) = a_0 \left(\frac{t}{t_0}\right)^{\frac{2}{3(1+w)}}$	$a(t) \propto t^{2/3}$	$a(t) \propto t^{1/2}$
$t = t_0(1+z)^{\frac{-3(1+w)}{2}}$	$t \propto (1+z)^{-3/2}$	$t \propto (1+z)^{-2}$
$H(t) = \frac{2}{3(1+w)} t^{-1}$	$H(t) = \frac{2}{3t}$	$H(t) = \frac{1}{2t}$
$t_0 = \frac{2}{3(1+w)} \frac{1}{H_0}$	$t_0 = \frac{2}{3H_0}$	$t_0 = \frac{1}{2H_0}$
$\rho = \frac{1}{6\pi G(1+w)^2} \frac{1}{t^2}$	$\rho = \frac{1}{6\pi G} \frac{1}{t^2}$	$\rho = \frac{3}{32\pi G} \frac{1}{t^2}$

Table 1.1: Dependencies obtained for the EdS Universe in three different cases: for a generic fluid component (*first column*), for a matter-dominated universe, (*second column*) and for a radiation dominated universe (*third column*).

1.5 The Standard Cosmological model

From the beginning of the 21$^{\text{st}}$ century, the most commonly accepted model describing our Universe is the so-called ΛCDM model. This model is supported by a large set of observational data and provides us with a reasonable framework for structure formation. It describes an almost flat Universe, which is characterised by the CP and whose evolution is governed by the Friedmann Equations and therefore also by the GR.

According to the ΛCDM model, our Universe experienced a thermal history, i.e. its evolution is tightly related to its temperature, which initially was much higher than today. At the present time the temperature of the photons permeating the Universe is $T = 2.7255 \pm 0.0006$ K (Fixsen et al., 1996; Planck Collaboration et al., 2020a). This is the value of the CMB temperature, the relic radiation from the surface of last scattering happened only about $3.8 \cdot 10^6$ years after the Big Bang ($z \simeq 1100$). Before the last scattering, the Universe was filled by a hot plasma composed by protons and electrons fully ionised. In this context, electromagnetic radiation was continuously scattered by baryonic matter, so that the Universe was completely opaque and in thermal equilibrium. Because of its continuous expansion, the Universe cooled down until electrons recombined with protons, at $z \simeq 1500$, allowing the photons to freely propagate. Thanks to the succeeding prevalence of the matter component, gravitationally bound objects started to form, giving rise to the formation of the currently observed large-scale structures.

The ΛCDM model provides for a present-day universe made up of DE (or vacuum energy, with a density energy $\Omega_{0,\Lambda} \simeq 0.7$), associated with a cosmological constant, a non-ordinary matter component (that we will present later as cold dark matter, with $\Omega_{0,\mathrm{cdm}} \simeq 0.25$) and ordinary, observable matter component (i.e. formed by baryons, $\Omega_{0,\mathrm{b}} \simeq 0.05$) and radiation component ($\Omega_{0,\mathrm{r}} \simeq 10^{-5}$). These components' energy density values are in agreement with the condition of flatness: $\Omega_{0,\mathrm{tot}} = \Omega_{0,\Lambda} + \Omega_{0,\mathrm{cdm}} + \Omega_{0,\mathrm{b}} + \Omega_{0,\mathrm{r}} \simeq \Omega_{0,\Lambda} + \Omega_{0,\mathrm{m}} \simeq 1$. By using the first Friedman equation (Eq. 1.39) it is easy to demonstrate that a multi-component universe composed by the cosmological constant and matter leads to:

$$\ddot{a} = -aH(t)^2 \frac{\Omega_\mathrm{m}}{2} + aH(t)^2 \Omega_\Lambda \text{ , with } \Omega_\Lambda \equiv \frac{\Lambda c^2}{3H(t)^2} \ . \tag{1.62}$$

In order to obtain an accelerated expansion, we have therefore to impose the condition $\Omega_\Lambda > \Omega_\mathrm{m}/2$, which is indeed satisfied by the present-day density values.

In Sect. 1.4.1 we stated that the early Universe is well described by an EdS model characterised by $\ddot{a} < 0$. However, having now established that in recent cosmic times the Universe is experiencing an accelerated expansion, so with $\ddot{a} > 0$, we must include a flex in the function $a(t)$. It can be easily demonstrated that, given the present-day values of the densities, this inversion in the expansion rate occurs at $z_\mathrm{f} \simeq 0.7$. With additional mathematical derivations, we can find the moment corresponding to the equivalence between matter and cosmological constant, i.e. $\Omega_\mathrm{m}(z_{\mathrm{eq},\Lambda}) = \Omega_\Lambda(z_{\mathrm{eq},\Lambda})$. This event takes place at $z_{\mathrm{eq},\Lambda} \simeq 0.33$, an epoch very close (from the cosmological point of view) to the present time. This result implies that DE and matter are currently of the same order of magnitude and that the contribution of Λ became relevant only at recent times.

A robust characterisation of ΛCDM scenario involves the definition of six fundamental parameters:

- Ω_m: total matter density parameter,

- $\Omega_{\rm b}$: baryonic matter density parameter,
- H_0: Hubble constant,
- $A_{\rm s}$: primordial power spectrum amplitude,
- $n_{\rm s}$: spectral index of the primordial power spectrum,
- τ : reionisation optical depth,

where $\Omega_{\rm m}$ and $\Omega_{\rm b}$ are usually expressed with their present-day values, respectively, so we take for granted from now on the subscript "0". The strongest constraints on this set of parameters derives from the analysis of the CMB power spectrum in combination with lensing measurements. The values for these fundamental parameters, as reported in Planck Collaboration et al. (2020a), are $\Omega_{\rm m}h^2 = 0.143 \pm 0.001$, $\Omega_{\rm b}h^2 = 0.0224 \pm 0.0001$, $\ln\left(10^{10}A_{\rm s}\right) = 3.04 \pm 0.01$, $H_0 = 67.4 \pm 0.5$ km s^{-1} Mpc^{-1}, $n_{\rm s} = 0.965 \pm 0.004$ and $\tau = 0.054 \pm 0.007$.

The ΛCDM model is currently broadly accepted, but despite the refinements and the remarkable successes it achieved, some of its theoretical roots remain poorly understood. For example, we do not have yet a physical description of the major component of the matter, called for its obscure[1] nature *dark matter* (DM), and the very existence of DE is even more mysterious. As we presented in Sect. 1.1.1, the latter was theorised to account for the accelerated expansion of the Universe, but it cannot be associated with any known form of energy. Moreover, its density is extremely low compared to the other components of our Universe, around $\rho_{0,\Lambda} \simeq 7 \cdot 10^{-27}$ kg m^{-3}.

Similarly, the DM was introduced by Zwicky (1937) to make sense of observed gravitational effects that could not be explained by the known theories of gravitation without an excess of non-visible mass. DM can be interpreted as particles or small objects interacting only with matter (this includes also the self-interaction) through gravity and possibly the weak force. The existence of the DM is nowadays confirmed by several evidences, and some of the most valid probes to quantify its effects are the gravitational lensing by galaxy clusters, the redshift-space distortions on the large-scale mass distribution and the fluctuations of the density spectrum due to BAO. The DM can be classified into two main types:

- *hot dark matter* (HDM) made of low mass relativistic particles, for which the best candidates are massive neutrinos;
- *cold dark matter* (CDM) made of massive non-relativistic particles, for which the best candidates are currently the weakly interacting massive particles (WIMPS).

In the last decades, several particle candidates have been proposed and tested. As we will see in Chapter 2, the structure formation and evolution models imply that the great majority of the DM component must be cold.

[1]Here the adjective has not the meaning of *unknown* only. According to the standard ΛCDM model indeed, DM does not interact with the electromagnetic field, i.e. it does not absorb, reflect or emit light, therefore is only detectable thanks to its gravitational effects on visible matter.

Chapter 2

Structure formation

Looking at the Universe at the Mpc scales, its matter distribution appears to be quite inhomogeneous, showing the characteristics of a highly nonlinear evolution. On scales of collapsed objects, density contrast fluctuations are indeed of the order of hundreds. However, from the temperature fluctuations in the CMB maps it is possible to derive the amplitude of the density perturbations in the cosmic fluid at the time of recombination. In particular:

$$\frac{\delta T}{\overline{T}} \approx 10^{-5} \ ,$$

where $\overline{T}$ is the mean black body temperature of the CMB. We expect the same order of magnitude for the density contrast at that epoch, assuming the perturbations to be adiabatic. Therefore we can conclude that the Universe was almost homogeneous at this epoch since the amplitude of the density fluctuations was very small. Nevertheless, the effect of gravity must have been such as to make the already existing perturbations grow with a sufficient rate. Already in 1902, Jeans had developed a theory that would later be applied to provide an analytical description of this phenomenon. As we will see in Sect. 2.1.1, Jeans theory predicts that the small inhomogeneities present in the primordial fluid are amplified during the Universe evolution, giving rise to the currently observed collapsed structures. However, the description provided by this model results accurate as long as the structures analysed remain in the linear regime. The latter breaks down for gravitational bound objects, in which the DM reaches the nonlinear stage and the baryonic component become dynamically important. The analytical description of the matter evolution in the nonlinear regime is achievable only for few and extremely simple models, e.g. the spherical evolution model and the Zel'dovich approximation, which we will introduce in Sect. 2.2.1 and Sect. 2.2.2. Nowadays the treatment of structure evolution in the nonlinear regime is mostly done with numerical N-body simulations, which we will present in Sect. 2.3.

2.1 Linear theory

The aim of the Jeans theory is to describe how fast initial density perturbations have to grow to reproduce the inhomogeneities observed today. This model can be applied to non-relativistic matter and on scales not exceeding the cosmological horizon, which represents the sphere that comprehends all the volume of the Universe that is in causal connection with the observer. The cosmological horizon is defined as:

$$R_{\rm h} \equiv a(t) \int_{t_{\rm BB}}^{t} \frac{c\, {\rm d}t'}{a(t')} \ , \tag{2.1}$$

where time $t_{\rm BB} = 0$ identifies the instant of the Big Bang, i.e. the beginning of the Universe expansion. The cosmological horizon separates the Universe in two different regions:

- the scales $r > R_{\rm h}$, where gravity is the only force in action and the growth of the perturbations has to be treated with the relativistic theory. On these scales the density fluctuations can always grow, giving birth to collapsed structures;

- the scales $r < R_{\rm h}$, where the microphysical processes become important and different components behave in different manners. On these scales the Jeans theory provides a reliable description of these phenomena in linear theory.

On scales $r > R_{\rm h}$ the gravitational interaction is the only force acting on the density perturbations. In absence of radiative processes these perturbations can grow indefinitely. To derive the rate of their growth, density fluctuations can be treated as small closed universes evolving in a background EdS universe. From the second Friedmann equation we obtain the following relations:

$$H_{\rm B}^2 = \frac{8\pi}{3} G\rho_{\rm B}, \qquad H_{\rm P}^2 = \frac{8\pi}{3} G\rho_{\rm P} - \frac{c^2}{a^2} \ , \tag{2.2}$$

where the subscripts B and P refer to the background and the perturbed universe, respectively. Being the perturbation universe totally enclosed in the background one, their corresponding scale factors are initially the same and we can impose the equivalence of their Hubble parameters, which yields:

$$\delta = \frac{\rho_{\rm P} - \rho_{\rm B}}{\rho_{\rm B}} = \frac{3c^2}{8\pi G} \frac{1}{\rho_{\rm B} a^2} \propto \rho_{\rm B}^{-1} a^{-2} \ . \tag{2.3}$$

From Sect. 1.4.1 we know the evolution of the background perturbation follows the one of the component resulting dominant at a given epoch. Therefore we can use the relations reported in Table 1.1 and divide the behaviour of the density perturbation in two regimes, according to the matter-radiation equivalence time (see Eq. 1.61):

$$\begin{aligned} &\rho_{\rm B} \propto a^{-4} \ \rightarrow \ \delta = \delta_{\rm r} \propto a^2 \propto t, &&\text{for } z > z_{\rm eq} \\ &\rho_{\rm B} \propto a^{-3} \ \rightarrow \ \delta = \delta_{\rm m} \propto a \propto t^{2/3}, &&\text{for } z < z_{\rm eq} \ . \end{aligned} \tag{2.4}$$

As anticipated, the density perturbations on scales larger than the cosmological horizon are destined to always grow.

The analysis of the perturbations on scales $r < R_{\rm h}$ will instead be treated in details in the next section. In particular, in the following we will study their dynamic and evolution by applying the Jeans theory to a collisional and self-gravitating fluid embedded in an expanding background.

2.1.1 Jeans instability in an expanding universe

Let us assume a homogeneous and isotropic background, composed by a fluid having a constant matter density $\rho(\mathbf{x}, t)$ and enclosed in an expanding universe. The equations of motion of such a fluid, in the Newtonian approximation, are:

$$\frac{\partial \rho}{\partial t} + \nabla \cdot (\rho \mathbf{v}) = 0 \qquad \text{continuity equation} \tag{2.5a}$$

$$\frac{\partial \mathbf{v}}{\partial t} + (\mathbf{v} \cdot \nabla)\mathbf{v} = -\frac{1}{\rho}\nabla p - \nabla \Phi \qquad \text{Euler equation} \tag{2.5b}$$

$$\nabla^2 \Phi = 4\pi G \rho \qquad \text{Poisson Equation} \tag{2.5c}$$

$$\frac{\mathrm{d}S}{\mathrm{d}t} = 0 \qquad \text{adiabatic condition} \tag{2.5d}$$

$$p = p(\rho, S) = p(\rho) \qquad \text{equation of state} \tag{2.5e}$$

where $\mathbf{v}$ is the velocity vector of a fluid element, Φ is the gravitational potential, S the entropy and p the pressure. The last equation has been introduced to neglect any dissipative terms, i.e. viscosity or thermal conduction.

These equations are satisfied by a background (subscript "B") solution in which the continuity equation gives us the relation:

$$\dot{\rho_{\mathrm{B}}} + 3H(t)\rho_{\mathrm{B}} = 0 \ . \tag{2.6}$$

The velocity is formed by the sum of two components, namely the Hubble flow and the peculiar velocity $\mathbf{v}_{\mathrm{p}}$ of the fluid:

$$\mathbf{V} \equiv \dot{\mathbf{x}} = H(t)\mathbf{x} + \mathbf{v}_{\mathrm{p}} \ , \tag{2.7}$$

where $\mathbf{x}$ indicates the fluid position vector.

Using the definition of the dimensionless density perturbation, the so-called *density contrast*:

$$\delta(\mathbf{x}, t) \equiv \frac{\delta\rho(\mathbf{x}, t)}{\rho_{\mathrm{B}}} \ , \tag{2.8}$$

we can introduce a small perturbation ($\delta \ll 1$) in each variable of the set of equations (2.5) and obtain a hydrodinamic system for a fluctuation in the density field that can be linearised.

The solving relation for the density contrast is a differential equation, which in Fourier space has the form:

$$\ddot{\delta_{\mathbf{k}}} + 2H(t)\dot{\delta_{\mathbf{k}}} + (k^2 c_s^2 - 4\pi G \rho_{\mathrm{B}})\delta_{\mathbf{k}} = 0 \ , \tag{2.9}$$

where $k = |\mathbf{k}|$ is the absolute value of the wavenumber, $\delta_{\mathbf{k}} = \delta_k(t)$ is the amplitude of the Fourier transform of $\delta(\mathbf{x}, t)$ and $c_{\mathrm{s}} = \sqrt{\partial p / \partial \rho}$ the sound speed. The last equation is the so-called *dispersion relation*, where the term $2H(t)\dot{\delta_k}$ is related to the Hubble friction and the term $k^2 c^2 \delta_{\mathbf{k}}$ accounts for the characteristic velocity field of the fluid. Both these terms tend to dissipate the fluctuations, hampering their growth. Equation (2.9) is a second-order differential equation for δ_k and its solutions can be separated depending on the value of the wavelength $\lambda = 2\pi/k$, in relation to the characteristic scale called *Jeans length*:

$$\lambda_{\rm J} \propto c_s \left(\frac{\pi}{G\rho_{\rm B}}\right)^{1/2} , \tag{2.10}$$

which is expressed in physical units.

For $\lambda < \lambda_{\rm J}$ the perturbation propagates as a sound wave with constant amplitude and with a phase velocity $c_{ph} = \omega/k$, where $\omega(k) = \sqrt{k^2 c_s^2 - 4\pi G\rho_{\rm B}}$. This velocity tends to become equal to $c_{\rm s}$ for $\lambda \ll \lambda_{\rm J}$.

On the other hand, for $\lambda > \lambda_{\rm J}$ the dispersion relation has growing and decaying mode solutions:

$$\delta(\mathbf{x}, t) = A(\mathbf{x})\delta_+(t) + B(\mathbf{x})\delta_-(t) , \tag{2.11}$$

where A and B are two functions depending on the comoving coordinates, and δ_+ and δ_- represent the time-dependent growing and decaying modes, respectively. Applying now the dependencies for an EdS universe with $\Omega_{\rm m} = 1$ (see Table 1.1) we obtain the following trends:

$$\delta_+(t) \propto t^{2/3} \propto a(t) \tag{2.12}$$

and

$$\delta_-(t) \propto t^{-1} \propto a^{-3/2} . \tag{2.13}$$

Since the decaying solution does not give rise to gravitational instability (i.e. collapsed structures), we are interested only in the growing one. For a generic universe, the growing solution has an integral form given by the following equation:

$$\delta_+(z) = H(z) \int_z^\infty \frac{{\rm d}z'(1+z')}{H^3(z')} , \tag{2.14}$$

which has no analytical solution. However, we can provide a parametric solution to approximate its trend:

$$f \equiv \frac{{\rm d}\log \delta_+}{{\rm d}\log a} \simeq \Omega_{\rm m}^\gamma + \frac{\Omega_\Lambda}{70}\left(1 + \frac{1}{2}\Omega_{\rm m}\right) . \tag{2.15}$$

This is called the *linear growth rate* and its exponent γ is predicted to have a value approximately of 0.545 according to GR (Coles & Lucchin, 2002). This relation implies that, while the matter energy density plays a crucial role for the growth of the fluctuations, the cosmological constant Λ has a more negligible impact on it. The estimate of the linear growth rate through observations represents a powerful method to search for deviations from GR on cosmological scales. We show an example of this technique in Fig. 2.1. Here we report the analysis of Moresco & Marulli (2017), who have tested alternative models to the standard ΛCDM scenario by comparing their corresponding theoretical values of $f\sigma_8(z)$ with different measurements on growth rate of cosmic structures. In particular, the model predictions are computed by allowing the variation of one single cosmological parameter at a time: besides the reference flat ΛCDM model, computed with the cosmological parameters of Planck Collaboration et al. (2016a), $f\sigma_8(z)$ is evaluated for cosmological models with a different value of $\Omega_{\rm m}$, $w_{\rm de}$ (see also Sect. 3.1.1 in the next chapter), $\sum m_\nu$ (see also Sect. 3.1.3 in the next chapter) or γ.

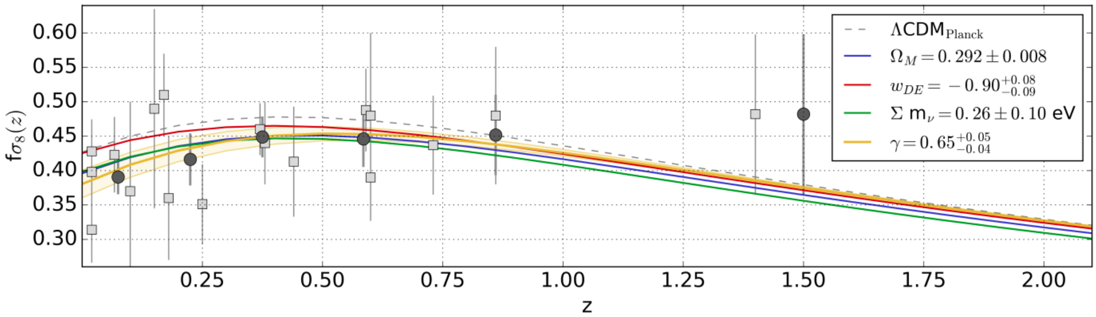

Figure 2.1: Measurements of growth rate of cosmic structures at different redshifts compared with the $f\sigma_8(z)$ predictions, computed for the cosmological models listed in the plot legend. Constraints on $f\sigma_8(z)$, especially when combined to those of $H(z)$, are key to testing gravity models and discriminate between alternative cosmological frameworks. Credits to Moresco & Marulli (2017).

2.1.2 Statistical properties of the Universe

In Sect. 2.1.1 we analysed the linear evolution of a single perturbation of the density field, whose growth is defined by $\delta(\mathbf{x}, t) = \delta_+(t)\delta(\mathbf{x})$. However, in more realistic cases we expect the density fluctuations to exist on a variety of mass and spatial scales, so the final collapsed structures will depend on the growth of different perturbations covering different scales. For a realistic description of the growth of the structures we have therefore to represent the density perturbation as a superposition of plane waves, which evolve independently of each other.

Let us introduce the spatial Fourier transform of $\delta(\mathbf{x})$:

$$\delta(\mathbf{k}) = \frac{1}{(2\pi)^3} \int \mathrm{d}^3\mathbf{x}^{-i\mathbf{k}\cdot\mathbf{x}} \delta\mathbf{x} \ . \tag{2.16}$$

We can now define the *power spectrum* of the density field as the variance of the amplitudes at a given value of the wavenumber $\mathbf{k}$:

$$\langle \delta(\mathbf{k})\delta^*(\mathbf{k}') \rangle = (2\pi)^3 P(k) \delta_D^{(3)}(\mathbf{k} - \mathbf{k}') \ , \tag{2.17}$$

where $\delta_D^{(3)}$ represents the 3-dimensional Dirac delta function. We also have $\delta^*(\mathbf{k}) = \delta(\text{-}\mathbf{k})$ because of the reality of δ, where the "*" indicates the complex conjugate operation. We obtain the analogous quantity of the power spectrum in real space, i.e. the *two-point correlation function* (2PCF), $\xi(r)$, by Fourier-transforming Eq. (2.17):

$$\xi(r) = \frac{1}{(2\pi)^3} \int \mathrm{d}^3\mathbf{k} P(k) e^{i\mathbf{k}\cdot\mathbf{x}} \ . \tag{2.18}$$

The 2PCF quantifies the spatial clustering of cosmic matter and it can be also defined with a statistical approach:

$$\langle \delta(\mathbf{x})\delta(\mathbf{x}') \rangle = \xi(|\mathbf{x} - \mathbf{x}'|) = \xi(\mathbf{r}) = \xi(r) \ , \tag{2.19}$$

where r is the comoving distance between $\mathbf{x}$ and $\mathbf{x}'$, and $\xi(\mathbf{r}) = \xi(r)$ is due to the CP. Using a discretised representation of the density field, we can interpret $\xi(r)$ also as the probability excess $\mathrm{d}P_{12}$ of finding a pair of objects separated by a comoving distance $\mathbf{r}$, in two independent volume elements $\mathrm{d}V_1$ and $\mathrm{d}V_2$, with respect to a random uniform distribution of objects:

$$\mathrm{d}P_{12} = n^2[1 + \xi(r)]\mathrm{d}V_1\mathrm{d}V_2 \ . \tag{2.20}$$

According to the inflation[1] theory, the primordial density perturbations are generated by stochastic quantum fluctuations in a scalar field (i.e *inflaton*) (Guth & Pi, 1982), therefore their amplitudes are accurately described by a Gaussian distribution. With this assumption, the power spectrum describes completely the distribution of fluctuations. Given the absence of any preferred scale during the creation of the perturbations, the initial spectrum follows a power law given by:

$$P(k) = Ak^n \ , \tag{2.21}$$

where the spectral index, n, is generally assumed to be close to unity (Zeldovich, 1972). While the shape of the power spectrum can be considered fixed, its amplitude A has to be constrained with observations. In particular, the most reliable and precise measure of A is obtained from the analysis of the temperature fluctuations in the CMB (Planck Collaboration et al., 2020a).

Since the amplitudes of the fluctuations have a Gaussian distribution in real space, their mean value is statistically null by definition. Instead, the fluctuation amplitude variance σ^2 is defined by:

$$\sigma^2 = \langle|\delta(\mathbf{x})^2)|\rangle = \sum_{\mathbf{k}}\langle|\delta_{\mathbf{k}}|^2\rangle = \frac{1}{V_u}\sum_k \delta_k^2 \ , \tag{2.22}$$

where the average is taken over an ensemble of the Universe realisations of volume V_u. By assuming the validity of the CP and considering the limit $V_\mathrm{u} \to \infty$, it yields:

$$\sigma^2 \to \frac{1}{2\pi^2}\int_0^\infty P(k)k^2\mathrm{d}k \ . \tag{2.23}$$

According to Eq. (2.22), to compute σ^2 we would need to evaluate the density for each point of the space, and this would require the reconstruction of the entire density field, which is obviously not possible in practice. A convenient method is to represent the fluctuation field by "filtering" on some resolution scale R, instead of using a punctual variance. With this approach we can recover the density fluctuation from a discrete distribution of tracers as:

$$\delta_M = \frac{M - \langle M\rangle}{\langle M\rangle} \ , \tag{2.24}$$

where $\langle M\rangle$ is the mean mass present inside a spherical volume of radius R. Using this definition in combination with equation Eq. (2.22), we obtain the *mass variance*:

$$\sigma_M^2 = \langle\delta_M^2\rangle = \frac{\langle(M - \langle M\rangle)^2\rangle}{\langle M\rangle^2} \ , \tag{2.25}$$

[1]The inflation is defined as a phase of exponential expansion of the Universe, set in the early stages after the Big Bang. See Guth (1981) for a detailed description.

which represents the variance of the convolution of the punctual density with a *window function* W of radius R:

$$\delta_M(\mathbf{x}) = \delta(\mathbf{x}) \otimes W(\mathbf{x}, R) \ . \tag{2.26}$$

From the last two equations, using the convolution theorem and in the limit $V_\mathrm{u} \to \infty$, we have:

$$\sigma_M^2 = \frac{1}{(2\pi)^3} \int P(k) \hat{W}^2(\mathbf{k}, R) \mathrm{d}^3\mathbf{k} \ , \tag{2.27}$$

where $\hat{W}$ is the Fourier-transform of the window function and is a function of R (and therefore of M). Though the normalisation of the power spectrum is not predicted by inflation theory, an equally valid approach is to fix the value of the mass variance computed with a filtering of $R = 8\ h^{-1}$ Mpc at the present time:

$$\sigma_8^2 = \frac{1}{2\pi^2} \int P(k) k^2 W^2(R = 8\ h^{-1}\ \mathrm{Mpc}) \mathrm{d}k \ . \tag{2.28}$$

The square root of this quantity, i.e. σ_8, besides representing the mass fluctuation in spheres with radius 8 h^{-1} Mpc, is a free parameter representing the normalization of the power spectrum and is key in predicting the phenomenology of the low-redshift Universe.

2.1.3 Evolution of the power spectrum

The density perturbations entering the cosmological horizon in an epoch before the radiation-matter equivalence, $t_\mathrm{h} < t < t_\mathrm{eq}$, are damped by an effect called *stagnation*, or *Mészáros effect* (Mészáros, 1974). This effect is a manifestation of the fact that the Hubble drag term during the radiation dominated era is larger than during the matter dominated era. Indeed, comparing the free-fall time ($\tau_\mathrm{ff} \propto 1/\sqrt{G\rho_\mathrm{m}}$), i.e. the characteristic time that would take a perturbation to collapse under its own gravitational force, and the Hubble time (see Table 1.1), i.e. the characteristic time for the expansion of the Universe, we find:

$$\frac{\tau_H}{\tau_\mathrm{ff}} \propto (\rho_\mathrm{m}/\rho_\mathrm{rad})^{1/2} \gg 1 \quad \text{for} \quad t < t_\mathrm{eq} \ , \tag{2.29}$$

otherwise

$$\frac{\tau_H}{\tau_\mathrm{ff}} \sim 1 \quad \text{for} \quad t > t_\mathrm{eq} \ . \tag{2.30}$$

Being in Eq. (2.29) the free-fall time larger than the expansion time the density perturbations cannot grow and this effect affects the primordial shape of the perturbations power spectrum.

Now, since the cosmological horizon expands with time (see definition in Eq. 2.1), we can conclude that larger perturbations will enter the cosmological horizon at later times, hence they will undergo less stagnation (or zero stagnation, if they do not enter the horizon before t_eq). On the other hand, the perturbations on scales bigger than the horizon, so having $\lambda > \lambda_\mathrm{h}$ (where $\lambda_\mathrm{h} \equiv R_\mathrm{h}$), continue to grow at the same rate independently of the scale or wavenumber, following the trends we saw in Eq. (2.4). As a consequence, the power spectrum at the moment of the equivalence has a peak in correspondence of $k_\mathrm{h,eq}$, i.e. the wavenumber associated with the cosmological horizon at the equivalence time. This value mostly depends on $\Omega_\mathrm{m} h^2$ and $\Omega_\mathrm{r} h^2$, so on the matter and radiation densities and the Hubble parameter.

The shape of the observed power spectrum $P(k)$ depends on the amount and on the nature of the matter in the Universe, providing powerful constraints for Cosmology. We can indeed define two types of DM particles according to their nature at the time of their decoupling from radiation: hot dark matter, i.e. particles still relativistic at the decoupling, and CDM, i.e. particles non relativistic before the decoupling. As simple consequence of their nature, CDM particles are supposed to be more massive than HDM particles. As shown in Fig. 2.2, for a matter component consisting entirely of HDM particles the matter power spectrum falls off sharply to zero to the right of the peak. Modern observations based on CMB, galaxy clusters, lensing and Lyα forest confirm with great accuracy a scenario in which the Universe matter component is mainly cold (see Tegmark et al., 2004, and references therein).

The shape of the power spectrum $P(k)$ at the equivalence time can be reproduced defining a *transfer function*, $T(k)$. This function gives us the fraction of the primordial power spectrum that is not affected by the microphysical effects inside the horizon. Considering a generic cosmological time represented by t_i, the transfer function is defined as follows:

$$P(k, t_{eq}) = P(k, t_i)T^2(k) \ . \tag{2.31}$$

For the CDM scenario, we have:

$$T(k) = \begin{cases} 1 & \text{for} \quad k < k_{H,\mathrm{eq}}, \\ \propto k^{-2} & \text{for} \quad k > k_{H,\mathrm{eq}} \ . \end{cases} \tag{2.32}$$

This function therefore acts as a filter that smooths larger wavenumbers.

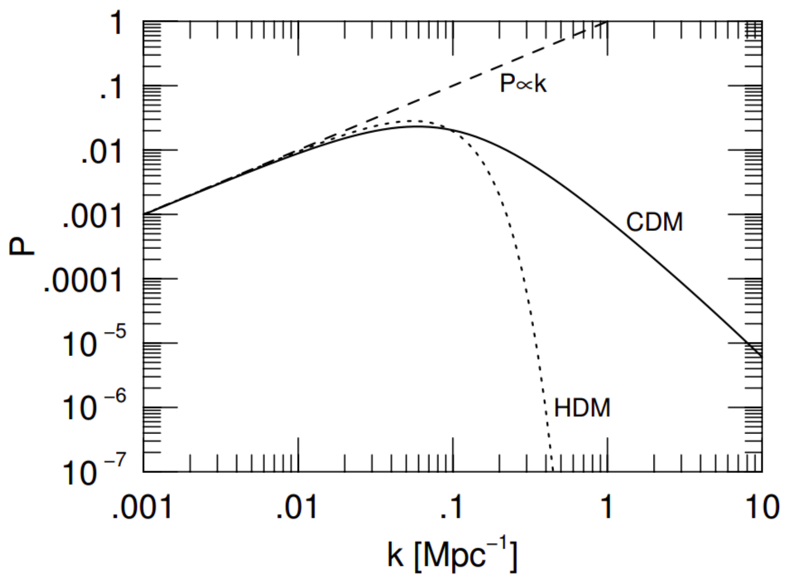

Figure 2.2: The power spectrum at the equivalence time for a matter component entirely formed by CDM (solid line) or HDM (dotted line). The dashed line represents the primordial Zel'dovich power spectrum, having a spectral index $n = 1$. Credits to Ryden (2016).

2.1.4 The bias parameter

A fundamental problem in Cosmology is to understand how the spatial distribution of tracers (i.e. luminous objects) is related to that of the total underlying distribution of mass. Let us consider the number counts of whatever mass tracer (subscript "tr") in a volume V, defining an overdensity field as:

$$\delta_{\rm tr} \equiv \frac{N_{\rm tr}(V) - \bar{N}_{\rm tr}(V)}{\bar{N}_{\rm tr}(V)} \ , \tag{2.33}$$

where $N_{\rm tr}$ and $\bar{N}_{\rm tr}$ are the number of tracers and the mean number of tracers, respectively. Some of the commonly used mass tracers in Cosmology are galaxies, galaxy clusters and DM haloes. However, we cannot expect the distribution of galaxies or cluster of galaxies to reflect the distribution of the total matter in the Universe (subscript "m"). The simplest approach to parametrise the relation between $\delta_{\rm tr}$ and $\delta_{\rm m}$ is the linear, local, non-stochastic bias model:

$$\delta_{\rm m} = b\delta_{\rm tr} \ , \tag{2.34}$$

where b is the linear bias factor, which depends on the cosmological scenario and epoch, and on tracer properties such as luminosity, colour and redshift. Equation (2.34) was proposed by Kaiser (1984) to describe objects in the linear regime and does not hold for small scales, where the relation becomes very complex due to the nonlinear evolution related to hydrodynamic phenomena.

An analytical parametrisation of the bias was proposed by Mo & White (1996a) for the DM halo bias, which was found applying the so-called *excursion-set* formalism (that we will introduce in Sect. 4.2):

$$b(M,z) = 1 + \frac{1}{\delta_{\rm c}}\left(\frac{\delta_{\rm c}^2}{\sigma_M^2\delta_+^2(z)} - 1\right) \ , \tag{2.35}$$

where δ_+ is the growing mode of the density perturbation. Equation (2.35) implies that for DM haloes the bias factor is positive and grows with the redshift and mass, as also confirmed by simulations (e.g. Hu & Kravtsov, 2003).

Another convenient definition of bias is based on the 2PCF: it can be measured by computing the square root of the ratio of the tracer 2PCF and that of the total matter component:

$$b = \sqrt{\frac{\xi_{\rm tr}}{\xi_{\rm m}}} \ . \tag{2.36}$$

While $\xi_{\rm tr}$ has to be inferred from the distribution of tracers, $\xi_{\rm m}$ can be derived analytically from the theory.

2.1.5 Clustering estimators

The estimation of the 2PCF (Eq. 2.18) of a data sample is usually performed by comparing the number of pairs of objects in the considered sample to those taken in a random distribution, generated with the same geometry and number density trend of the selected data sample. Let us assume a catalogue of $N_{\rm D}$ objects and its the associated random of $N_{\rm R}$ objects.

We define the number of data pairs as a function of the separation between the pairs, $\mathrm{dd}(r)$, normalised by the total number of pairs, as:

$$\mathrm{DD}(r) = \frac{\mathrm{dd}(r)}{N_\mathrm{D}} \ , \tag{2.37}$$

and the corresponding quantity for the random catalogue:

$$\mathrm{RR}(r) = \frac{\mathrm{rr}(r)}{N_\mathrm{R}} \ , \tag{2.38}$$

with $\mathrm{rr}(r)$ being the number of random pairs at distance r. Then we can count the pairs data-random cross-correlating the two catalogues. Using an analogous notation, we have:

$$\mathrm{DR}(r) = \frac{\mathrm{dr}(r)}{N_\mathrm{D} N_\mathrm{R}} \ , \tag{2.39}$$

Now, the 2PCF in one of its simplest form can be written as:

$$\hat{\xi}_\mathrm{N}(r) = \frac{\mathrm{DD}(r)}{\mathrm{RR}(r)} - 1 \ . \tag{2.40}$$

This is the so-called Peebles-Hauser, or natural, estimator (Peebles & Hauser, 1974). This estimator is affected by low accuracy at large scales, due to the discreteness of the sample. Thus, more accurate estimators are generally adopted, which consider also the cross terms between the data and random catalogue. One widely-used estimator of this type is the following:

$$\hat{\xi}_\mathrm{LS}(r) = \frac{\mathrm{DD}(r) - 2\mathrm{DR}(r) + \mathrm{RR}(r)}{\mathrm{RR}(r)} \ . \tag{2.41}$$

This is called the Landy-Szalay estimator (Landy & Szalay, 1993) and it is characterised by a nearly Poissonian variance. It provides an unbiased estimate of the 2PCF in the limit $N_R \to \infty$, with minimum variance. The Landy-Szalay estimator is one of the most commonly used for astrophysical and cosmological applications, and is also the one that will be used in this Thesis work.

2.2 Nonlinear theory

The cosmic structures that we observe in today Universe, such as galaxies, clusters and DM haloes, are the result of gravitational instabilities occurred throughout the cosmological history. To describe the formation of these objects characterised by a strongly nonlinear regime ($\delta \gg 1$), the small-perturbations approximation can not be applied anymore. After the linear regime breaks down, therefore when δ becomes comparable to unity, the weakly-nonlinear regime sets in. Already in the weakly nonlinear stage, the fluctuation distribution function starts to deviate from the Gaussian shape. Moreover, we have to take into account that the evolution of the baryonic component is different from the DM one. Baryons are indeed subject to hydrodynamical effects, like star formation, SNe explosion, and the feedback of active galactic nuclei (AGN). All of these phenomena make even more difficult the description of the whole scenario with a full and solid theory. Even if some approximated analytical models have been proposed to describe what happens during this phase, we generally rely on N-body simulations to reproduce accurately the weakly-nonlinear and NL perturbation growth.

2.2.1 Spherical evolution

Though numerical simulations are needed to study in details the nonlinear growth of cosmic structures, we can study the evolution of perturbations in the nonlinear regime by making use of some assumptions. In particular, the analytical model that we present here, the so-called *spherical evolution model* (Gunn & Gott, 1972), is sufficiently accurate to describe the *isolated* formation of *spherical* collapsed overdensities (i.e. DM haloes) and underdensities (i.e. cosmic voids). Considering an initially spherical perturbation, which can be positive or negative, we can represent it as a closed or open universe, respectively, that evolves in an EdS background. We consider an initial time $t_i > t_{\rm eq}$, where $t_{\rm eq}$ is the matter-radiation equivalence time, thus we study the evolution of perturbations in the matter-dominated cosmic epoch, but at redshifts high enough for assuming an EdS model for the background. Assuming again the validity of the CP, we can suppose that each perturbation can be treated as an independent Friedmann universe until it evolves adiabatically. The only interaction we have to take into account is therefore only the gravitational one. In this model we consider a spherical top-hat perturbation and model it as a set of concentric shells. As stated in Sheth & van de Weygaert (2004), the evolution of the considered perturbation only depends on the total energy embedded in the shell, on its peculiar velocity, and not on the radial distribution of the density field inside it.

Overdensities

Let us consider the evolution of an initially overdense shell in an EdS Universe. We know from Sect. 2.1.1 that for a matter perturbation in an expanding universe the growing and decaying mode of perturbation scale as $\delta_+ \propto t^{2/3}$ and $\delta_- \propto t^{-1}$, respectively. Therefore the density contrast can be expressed as the combination of these two modes:

$$\delta_i = \delta_+(t_i)\left(\frac{t}{t_i}\right)^{2/3} + \delta_-(t_i)\left(\frac{t}{t_i}\right)^{-1} . \tag{2.42}$$

Assuming a null initial velocity for the perturbations, we can compute the derivative of the latter relation with respect to the time considering $t = t_i$, finding:

$$\frac{2}{3}\delta_+(t_i) - \delta_-(t_i) = 0 \Longrightarrow \delta_-(t_i) = \frac{2}{3}\delta_+(t_i) . \tag{2.43}$$

Therefore, Eq. (2.42) can be written, for $t = t_i$, as:

$$\delta_i = \frac{5}{3}\delta_+(t_i) . \tag{2.44}$$

Hence 3/5 of the initial perturbation is represented by the growing mode, while the remaining 2/5 decays with time, tending to become negligible.

Now, let us consider the density parameter of the perturbation universe, $\Omega_{\rm P}$. This perturbation can be described in terms of a closed universe, which we know from Sect. 1.4.1 that will undergo to a collapse. Consequently, we can impose the relation $\Omega_{\rm P} > 1$:

$$\Omega_{\rm P}(t_i) \equiv \frac{\rho_{\rm P}(t_i)}{\rho_{\rm c}(t_i)} = \frac{\rho_{\rm B}(t_i)(1+\delta_i)}{\rho_{\rm c}(t_i)} = \Omega(t_i)(1+\delta_i) > 1 , \tag{2.45}$$

where Ω is the initial density parameter of the background universe, and $\rho_{\rm c}$ is the critical density. So we find that for a closed Universe, it is necessary that $(1+\delta_i) > \Omega(t_i)^{-1}$. By considering a mono-component Universe with $w = 0$, we can use Eq. (1.54) to find the threshold for $\delta(t_i)$ that will lead to the collapse:

$$\delta(t_i) = \frac{3}{5}\delta_i > \frac{1-\Omega_{0,\mathrm{B}}}{(1+z)\Omega_{0,\mathrm{B}}} \ . \tag{2.46}$$

From this equation we can see that for closed or flat background universes (i.e. for $\Omega_{0,\mathrm{B}} \geq 1$) the collapse is achieved for any positive value of the initial density contrast, while for open universes (i.e. for $\Omega_{0,\mathrm{B}} < 1$) the expansion inhibits the collapse if δ_i is not sufficiently large.

What we expect for an overdense perturbation growing in our Universe is therefore an initial expansion, slower than the Hubble flow, followed by a gradual halting until the reaching of a maximum radius r_{max}. After this moment, called *turn around*, the perturbation reverses its motion and decouples from the Hubble flow towards its final collapse. It is possible to show that the density of the perturbation at the turn around (i.e. for $t = t_{\mathrm{max}}$) is:

$$\rho_{\mathrm{P}}(t_{\mathrm{max}}) = \frac{3\pi}{32Gt_{\mathrm{max}}^2} \ . \tag{2.47}$$

We can calculate the density contrast of the perturbation at the turn around by computing the background density at t_{max} from the equations in Table 1.1. This yields:

$$\delta(t_{\mathrm{max}}) \simeq \frac{\rho_{\mathrm{P}}(t_{\mathrm{max}})}{\rho_{\mathrm{B}}(t_{\mathrm{max}})} - 1 = \left(\frac{3\pi}{4}\right)^2 - 1 \simeq 4.6 \ . \tag{2.48}$$

The last relation suggests that, at the moment of the turn around, the collapsing region is already in the nonlinear regime and is nearly 5 times denser than the background universe. The same quantity obtained using the linear theory, would be instead:

$$\delta(t_{\mathrm{max}}) = \delta(t_i)\left(\frac{t_{\mathrm{max}}}{t_i}\right)^{2/3} \simeq 1.06 \ . \tag{2.49}$$

After the turn around, the physical scale of the perturbation decreases until $t = 2t_{\mathrm{max}}$, time at which the full collapse would be reached, forming a singularity. Nevertheless, even though a strictly gravitational description implies that the comoving radius of the overdensity shrinks to zero, in reality the matter in the collapsing region will eventually virialise. The hydrodynamical interactions (for the baryonic matter) or the increase of the dispersion velocity of the particles (for the DM) within the shell will lead towards a dynamical equilibrium. Therefore, it is usual to assume that the final size of a collapsed spherical object corresponds to its virial radius. From numerical simulations we know that the virialisation is reached at a time $t_{\mathrm{vir}} = 3t_{\mathrm{max}}$, at which the size of the perturbation becomes stable, at the virialisation radius R_{vir}.

Let us assume that the perturbation system has kinetic energy $\mathcal{T}$ (or internal thermal energy, associated with motions of particles) and gravitational potential energy $\mathcal{V}$. The final result is a system which satisfies the *virial theorem*, which states that:

$$2\mathcal{T} + \mathcal{V} = 0 \ . \tag{2.50}$$

Considering the potential energy of a self-gravitating sphere of mass M

$$\mathcal{V} = -\frac{3}{5}\frac{GM^2}{R}, \tag{2.51}$$

the total energy of the system becomes:

$$E = \mathcal{T} + \mathcal{V} = \frac{1}{2}\mathcal{V} = -\frac{3}{10}\frac{GM^2}{R} \ . \tag{2.52}$$

Let us also assume the absence of any mass or energy loss since the turn around, $E(t_{\rm vir}) = E(t_{\rm max})$, which leads to $2R_{\rm vir} = R_{\rm max}$. From the fact that $\rho_{\rm p}(t_{\rm vir}) \propto R_{\rm vir}^{-3}$, it follows that

$$\rho_{\rm P}(t_{\rm vir}) = 8\rho_{\rm P}(t_{\rm max}). \tag{2.53}$$

Therefore we can now compute the density contrast at $t_{\rm coll} = 2t_{\rm max}$ and $t_{\rm vir} = 3t_{\rm max}$:

$$\begin{aligned} \delta(t_{\rm coll}) &= \frac{8\rho_{\rm P}(t_{\rm max})}{\rho_b(t_{\rm max})}\left(\frac{t_{\rm coll}}{t_{\rm max}}\right)^2 \simeq 180\,, \\ \delta(t_{\rm vir}) &= \frac{8\rho_{\rm P}(t_{\rm max})}{\rho_b(t_{\rm max})}\left(\frac{t_{\rm vir}}{t_{\rm max}}\right)^2 \simeq 400\,. \end{aligned} \tag{2.54}$$

While the same quantities extrapolated from the linear theory are:

$$\begin{aligned} \delta(t_{\rm coll}) &= 1.06\left(\frac{t_{\rm coll}}{t_{\rm max}}\right)^{2/3} \simeq 1.69\,, \\ \delta(t_{\rm vir}) &= 1.06\left(\frac{t_{\rm vir}}{t_{\rm max}}\right)^{2/3} \simeq 2.2\ . \end{aligned} \tag{2.55}$$

The quantities in Eq. (2.54) depend strongly on the cosmological model assumed for the background universe, hence on its curvature. On the other hand, the dependence of their linearly extrapolated counterpart is much weaker (Jenkins et al., 2001; Kitayama & Suto, 1996).

Underdensities

The evolution of an underdense spherical region is different from that of its overdense counterpart. We can generally define these regions as *voids*. In this case, the net radial acceleration is directed outward with respect to the centre of the sphere and it is directly proportional to the mean density contrast $\Delta(r, t)$ of the void. Since the inner shells are more underdense, they are affected by a stronger outward acceleration than the outer shells.

Let us consider an inverse top-hat spherically symmetric underdense perturbation as a set of concentric shells with respective radii r_i. The mass M contained within the perturbation radius r determines the acceleration experienced by each shell, which in the Newtonian regime (i.e. $\dot{r} \ll c$ and $r \ll c/H$) is:

$$\frac{{\rm d}^2 r}{{\rm d}t^2} = -\frac{GM}{r} = -\frac{4\pi G}{3}\rho_{\rm B}(1+\Delta)r\ , \tag{2.56}$$

where $\rho_{\rm B}$ represents the density of the background universe. At the initial time we have:

$$\begin{aligned} M &= \frac{4\pi}{3}\rho_{\rm B} r_i^3(1+\Delta_i)\,, \\ \Delta_i &= \frac{3}{r_i^3}\int_0^{r_i}\delta_i(r)r^2{\rm d}r\ , \end{aligned} \tag{2.57}$$

where Δ_i is the average value of δ_i within r_i. Equation (2.56) can be solved analytically giving, in the case of an EdS model for the background Universe, the following parametric form for the evolution of the density deficit:

$$1 + \Delta(r,t) = \frac{\rho(r,t)}{\rho_{\rm B}(r,t)} = \frac{9}{2}\frac{(\sinh\theta - \theta)^2}{(\cosh\theta - 1)^3} \; , \tag{2.58}$$

in which we introduced the *dimensionless conformal time*:

$$\mathrm{d}\theta = \frac{r_i}{r}\sqrt{\left|\frac{5}{3}\Delta_i(t)\right|} H_i(t)\mathrm{d}t \; . \tag{2.59}$$

From these equations it is possible to derive the linear initial density deficit:

$$\Delta_i^{\rm L}(\theta) = -\left(\frac{3}{4}\right)^{2/3} \frac{3}{5}(\sinh\theta - \theta)^{2/3} \; . \tag{2.60}$$

We make explicit the superscripts L to underline that the density contrast is computed in linear theory. We will indicate with the NL the nonlinear counterpart and, in absence of any superscript, we take for granted the reference to the nonlinear theory unless indicated otherwise. As matter streams out of the voids, the value of density decreases asymptotically to $\delta = -1$. Since the density gradually decreases going towards the centre of a void, the matter near the centre moves outward faster than matter in proximity of the external boundaries. Shells that were initially close to the centre will ultimately catch up the shells further outside, until they eventually pass them. This phenomenon is called *shell-crossing*[2], and brings to the tendency of astrophysical objects to accumulate around voids, leading to the formation of sheets and filaments. Fig. 2.3 shows the evolution of an underdensity profile up to the shell-crossing event, which leads to the formation of a high-density ridge. From the shell-crossing on, the evolution of the void can be described by a self-similar outward moving shell (Suto, Sato & Sato, 1984). The solutions in Eq. (2.58) represent a family of trajectories labeled by r_i and parametrised by θ. We can find out when and where shell-crossing phenomenon first occurs by differentiating the parametrised solutions with respect to r and θ, and requiring that $\mathrm{d}r$ and $\mathrm{d}t$ vanish. From these solutions we can show that, at the shell-crossing event, the void has a precisely determined excess Hubble expansion rate (Sheth & van de Weygaert, 2004):

$$H_{\rm sc} = \frac{4}{3}H(t_{\rm sc}) \; , \tag{2.61}$$

where $H(t_{\rm sc})$ is the Hubble parameter of the background Universe. Therefore the low-density environment expands faster than the Hubble flow, thus more rapidly with respect to the background Universe.

Now, substituting $\theta_{\rm sc}$ in Eq. (2.60) we find that at the shell-crossing event, the void interior has a relative density

$$1 + \delta_{\rm v}^{\rm NL} \simeq 0.205 \; , \tag{2.62}$$

[2] In principle, the shell-crossing phenomenon can be associated to the formation of an ideal void (spherical, isolated and without substructures) and marks the transition from a quasi-linear towards a mildly-nonlinear stage.

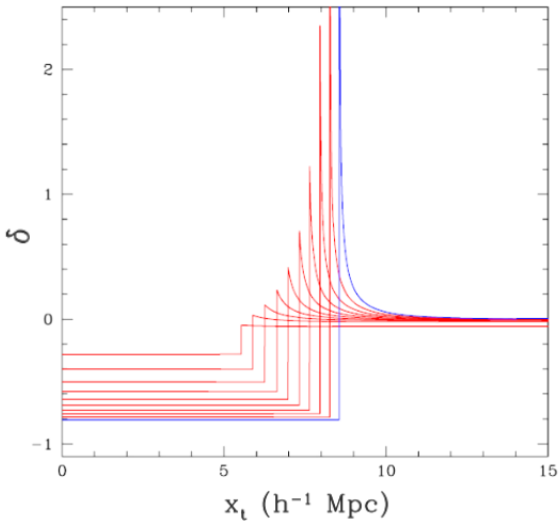

Figure 2.3: Spherical model for voids represented by a top-hat profile evolving up to the epoch of shell-crossing, marked by a blue line. Credits to van de Weygaert & Platen (2011).

which implies that the void has expanded by a factor of $(1+\delta_v^{\rm NL})^{-1/3} = 1.697$ in comoving radius. Note that these numbers do not depend on the size of the void. Moreover, from the latter relation we see that voids are only nearly nonlinear objects, since $|\Delta_{sc}| \simeq 0.795 < 1$. The linear extrapolated quantity of Eq. (2.62) is:

$$\delta_{\rm v}^{\rm L} \simeq -2.71 \ . \tag{2.63}$$

This is the underdense counterpart of the critical density contrast $\delta(t_{\rm coll})$ found in Eq. (2.55).

We can conclude that in the evolution of spherical voids, an expansion occurs, in contrast with the collapse for the overdensities. During this evolution, void borders become denser and the central parts reach lower density contrasts. Icke (1984a) demonstrated that voids are likely to assume a spherical form, differently from collapsing objects, which tendentially evolve into filamentary or sheet-like structures. Moreover, since the expansion of a void can be considered as the time reversal of the collapse of an overdensity, for the underdensities any eventual initial asphericity tends to be cancelled.

2.2.2 The Zel'dovich approximation

The transition between linear and nonlinear regimes can be described analitically for the density contrast by means the Zel'dovich approximation (Zel'Dovich, 1970) (see Shandarin & Zeldovich, 1989 for an exhaustive review). The Zel'dovich approximation is particularly suitable in comoving coordinates $\vec{r} = \vec{x}/a(t)$, where $a(t)$ is the scale factor and $\vec{x}$ are physical coordinates. It relates $\vec{r}$ to the initial Lagrangian coordinates $\vec{q}$ at $t \to 0$ with an explicit relation:

$$\vec{r}(\vec{q}, t) = \vec{q} + \delta_+(t)\vec{s}(\vec{q}) \ , \tag{2.64}$$

where the vector field $\vec{s}(\vec{q})$ is called the *initial displacement field* and it is determined by the initial density perturbations, while $\delta_+(t)$ (often indicated with the notation $D(z)$) is the amplitude of the growing mode, dependent only on the cosmological parameters. The Zel'dovich approximation assumes that $\vec{s}(\vec{q})$ is a potential vector field:

$$\vec{s}(\vec{q}) = -\nabla_q \Psi(\vec{q}) \ . \tag{2.65}$$

The main limit of this approach is that it considers only the displacement caused by initial forces. Therefore particles are not subject to additional interactions at later times. This implies that two particles can cross each other without causing any deviation in their motion. This is called *shell-crossing problem* and affects mainly the modelling of the small scales, where nonlinearity develops first.

An additionally important aspect of the Zel'dovich approximation, is the deformation of mass elements. This deformation is described by the following tensor:

$$d_{ij} = -\frac{\partial^2 \Psi}{\partial q_i \partial q_j} \ . \tag{2.66}$$

From Eq. (2.64) we can infer an explicit expression for the density as a function of Lagrangian coordinates and time. Considering the conservation of mass in differential form we obtain:

$$\rho(\vec{r}, t)\mathrm{d}^3\vec{r} = \bar{\rho}(t)\mathrm{d}^3\vec{q} \ , \tag{2.67}$$

and consequently the density evolution becomes:

$$\begin{aligned} \rho(\vec{x}, t) &= \bar{\rho}\Big[\delta_{ij} + \delta_+(t) d_{ij}\Big] \\ &= \bar{\rho}[1 - \delta_+(t)\lambda_1]^{-1}[1 - \delta_+(t)\lambda_2]^{-1}[1 - \delta_+(t)\lambda_3]^{-1} \ , \end{aligned} \tag{2.68}$$

where λ_i $(i = 1, 2, 3)$ are the eigenvalues of the symmetric deformation tensor d_{ij}, defined with the relation $\lambda_1 > \lambda_2 > \lambda_3$. On the basis of the second equation of Eq. (2.68), we can immediately infer two key features about the structure formation described by the Zel'dovich approximation. The first is that the density becomes infinite when $\delta_+(t)\lambda_i = 1$. The second is that the collapse is anisotropic unless the eigenvalues are exactly $\lambda_1 = \lambda_2 = \lambda_3$. Therefore, the structure generally collapses along a preferential axis, i.e. the one associated to the largest λ_i. On the other hand, if the eigenvalues are negative, the brackets in the second equation of Eq. (2.68) can not be null at any time, so a dilatation takes place instead of a collapse. Different combinations of positive and negative eigenvalues will lead therefore to different evolutionary outcomes.

2.3 Numerical simulations

The formation of cosmic structures can be approximated as the dynamical evolution of a system of particles, tracers of the total mass distribution. Given the large number of particles required to mimic the Universe with sufficient accuracy, the treatment of this system is generally too complicated to be studied analytically. For this reason, numerical simulations are employed by cosmologists to analyse the LSS of the Universe also in the nonlinear regime, without the necessary simplifications adopted to reach analytical solutions. Once the cosmological scenario has been fixed by selecting an underlying theory and a set of cosmological parameters, the simulation is run to make the initial system evolve. Consequently, the final outcome can be compared with observations.

The most important effect to consider to mimic the evolution of density perturbations is the gravitational interaction, which is dominant on large scales and influences the majority of the matter component of the Universe (i.e. DM). Simulations in which only the gravitational force is considered are called *N-body simulations*. To obtain a more realistic description of the LSS, the hydrodynamic effects resulting from the presence of the baryonic matter have also to be taken into account. Simulations in which also the baryonic component is evolved are called *hydrodynamic simulations*.

The first studies in which numerical simulations were employed are Aarseth (1963), Peebles (1970) and Press & Schechter (1974), treating simple N-body problems with few hundred particles. Thanks to the advancement both of the technology and the computational techniques, nowadays we can make reliable predictions about a very large range of phenomena, using simulations having billions of particles. Despite the incredible successes of this branch of research, some strong limits in the creation of cosmological simulations are still present. Once that the number of particles has been fixed by the computational capability, the spatial resolution of the simulation is fully determined by the covered volume. Small volumes allow us to study galaxy formation models that resolve the physical processes, given the high resolution of the analysed portion of the universe. Big volumes allow us to study in more detail the LSS, treating statistically the properties of the universe. Simulations characterised by both high resolution and large volume are currently still difficult to achieve.

Let us now briefly introduce the theory on which all the numerical simulations are based. The simplest kind of N-body simulations, which considers only gravitational effects, solves the following differential equation system:

$$\begin{cases} \mathbf{F}_i = GM_i \sum_{i\neq j} \frac{M_j}{r_{ij}^2}\hat{\mathbf{r}}_{ij}^2 \\ \ddot{\mathbf{x}}_i = \frac{\mathrm{d}\mathbf{v}_i}{\mathrm{d}t} = \frac{\mathbf{F}_i}{\mathrm{M}_i} \\ \dot{\mathbf{x}}_i = \frac{\mathrm{d}\mathbf{x}_i}{\mathrm{d}t} = \mathbf{v}_i \end{cases} . \tag{2.69}$$

In this equation, for each i-th particle, we have that $\mathbf{F}_i$ is the gravitational force, M_i is the mass, $\mathbf{x}_i$ is the comoving coordinates, $\mathbf{v}_i$ the velocity components. Then r_{ij} is the comoving distance between the i-th and j-th particles, and $\hat{r}_{ij}$ is the related versor. Given the system of equations (2.69), the Euler equation of motion reported in the system (2.5) can be re-written as:

$$\frac{\mathrm{d}\mathbf{x}_i}{\mathrm{d}t} + 2\frac{\dot{a}}{a}\mathbf{v}_i = -\frac{1}{a^2}\nabla\Phi = -\frac{G}{a^3}\sum_{i,j\neq i} m_j \frac{\mathbf{x}_i - \mathbf{x}_j}{|\mathbf{x}_i - \mathbf{x}_j|^3} = \frac{\mathbf{F}_i}{a^3} , \tag{2.70}$$

where a is the scale factor. Applying the Second Friedman Equation reported in Eq. (1.40), the Poisson Equation of the system (2.5) it becomes:

$$\nabla^2\Phi = 4\pi G\bar{\rho}(t)a^2\delta = \frac{3}{2}H_0^2\Omega_0\frac{\delta}{a} , \tag{2.71}$$

where $\bar{\rho}(t)$ is the average non-relativistic matter density, δ the local density contrast, H_0 is the Hubble parameter and Ω_0 the non-relativistic matter density parameter.

A N-body simulation consists in the integration of the dynamical equations over discretised time steps, δt. At every time interval, the total gravitational force of the system, $\mathbf{F}_i$, is calculated. The simplest method to calculate the gravitational force acting on the i-th particle is the *particle-particle method*, which is the most accurate but also the most expensive in terms of computational time: for each time step it requires the computation of the $N(N-1)/2$ distances between the particles, so the number of operations scales as $\mathcal{O}(N^2)$. More efficient methods to compute the gravitational interaction are the so-called *hierarchical tree* and *particle-mesh*, see Barnes & Hut (1986) and Hockney & Eastwood (1981) for the details.

Then, the motion equation is evaluated by numerical integration and the new positions, $\mathbf{x}_i(t \pm \delta t)$, and velocities, $\mathbf{v}_i(t \pm \delta t)$, are obtained. So the time is updated, $t = t + \delta t$ and the process repeated. The value of δt can be chosen following different criteria, which can be suitable for different approaches. They can be divided into three main categories: (i) total energy conservation, (ii) convergence of final positions and velocities and (iii) reproducibility of the initial conditions (Bagla & Padmanabhan, 1997).

2.3.1 Halo finding algorithms

The final output of a N-body simulation is a set of snapshots, which provides the configuration of the system of particles for a sequence of instants, reproducing the evolution the total matter density field. A possible approach to link these particle distributions to the biased mass tracer field is to employ halo finding algorithms, which aim at grouping DM particles into DM haloes and and sub-haloes. Two standard techniques for halo identification are the *spherical overdensity* (SO, Press & Schechter, 1974) and the *Friends-of-Friend* (FoF, Davis et al., 1985), which have provided the basics for the development of subsequent and more refined finding algorithms.

The SO method is based on the definition of a spherical overdensity regions around density peaks, which are found by sorting particles by local density. Given a density peak, a DM halo is identified by growing a sphere around it, stopping when the mean density within this sphere, Δ, reaches the condition $\Delta(z) = \Delta_\mathrm{c} \cdot \rho_\mathrm{crit}(z)$, where Δ_c is the selected overdensity threshold and $\rho_\mathrm{crit}(z)$ the critical density of the Universe at a given redshift (see Eq. 1.50). This yields to:

$$\frac{4}{3}\pi R_c^3\, \Delta_\mathrm{c}\, \rho_\mathrm{crit} = M_\mathrm{c}\,, \tag{2.72}$$

providing the definition for the halo virial radius, R_c, and viral mass, M_c.

The FoF algorithm defines instead as haloes those groups of DM particles separated by distances lower than a given linking length, $\ell = b\,\overline{d}$, where $\overline{d}$ is the mean inter-particle separation of the DM particle catalogue, and b is a free parameter of the code. This algorithm will be employed to build the halo catalogues used in Chapter 6.

Closely related to the presented halo finding techniques is the `SUBFIND` algorithm (Springel et al., 2001; Dolag et al., 2009), which will be used in the context of Sect. 9.2. This algorithm identifies gravitationally bound structures by associating a spherical overdensity virial mass to locally overdense regions, usually pre-identified by FoF group finder. Other popular examples of more refined halo finding algorithms are `Denhf` (Tormen, Moscardini & Yoshida, 2004; Giocoli, Tormen & van den Bosch, 2008) and Robust Overdensity Calculation using K-Space Topologically Adaptive Refinement (`ROCKSTAR`) (Behroozi, Wechsler & Wu, 2013), which will be used for the preparation on the data analysed in Chapter 7

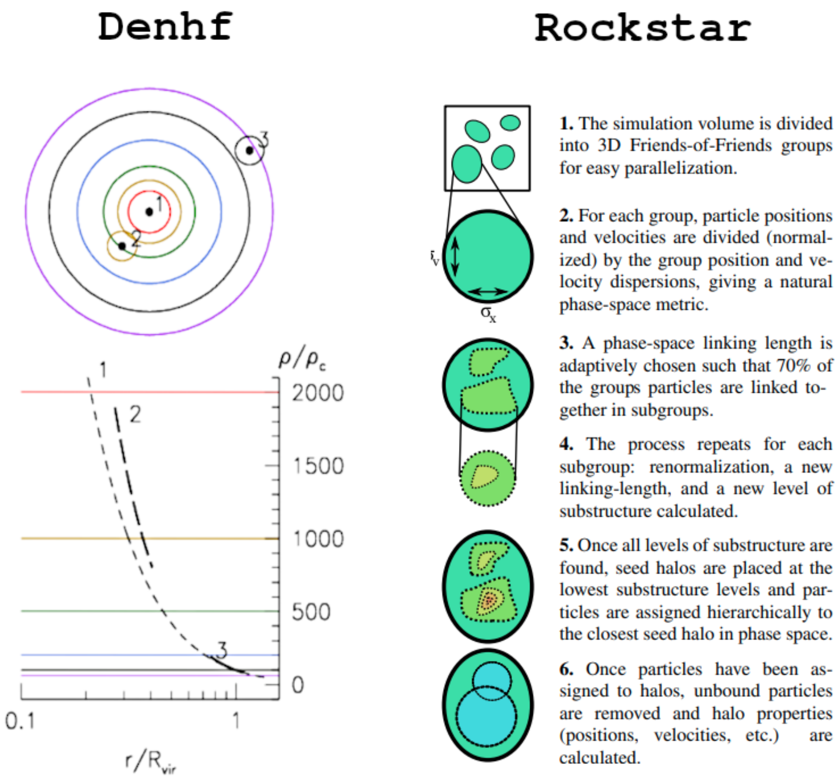

Figure 2.4: *Left*: scheme of the procedure performed in the `Denhf` algorithm to identify halos as spherical overdensities with internal density equal to a given value $\Delta_c = \rho/\rho_{\mathrm{crit}}$. Credits to Despali et al. (2016). *Right*: main steps followed by the `ROCKSTAR` algorithm to build a hierarchy of haloes and sub-haloes. Credits to Behroozi, Wechsler & Wu (2013).

and Chapter 8, respectively. As we will describe in the following, these finders use different approaches to assign the mass and other structural properties to the identified haloes: while `Denhf` aims for a definition of the halo mass more linked to observational data sets, `ROCKSTAR` focuses on an accurate reconstruction of halo merging histories and physical properties.

As `SUBFIND`, `Denhf` is based on the SO methodology. For each particle in the snapshot, the algorithm estimates the local DM density, ρ_i, by using the distance of the 10-th nearest neighbour, $d_{i,10}$. Then the particles are sorted according to the local density: the first halo is located at the position of the densest particle. Now a sphere is grown around this centre until the embedded mean density surpasses a desired critical value. In particular, the halo virial radius and viral mass are defined according to Eq. (2.72), choosing a specific value for the density contrast Δ_c, as 200, 500 or 1000. At this point all the DM particles within the sphere are assigned to the newly identified halo, and the procedure is repeated for the remaining densest particles that do not belong to an already identified halo. A visual representation of this procedure is reported on the left side of Fig. 2.4.

ROCKSTAR is a phase-space halo finder (i.e. it operates in 6 dimensions, given by the 3D values of positions and velocities) based on adaptive hierarchical refinement of FoF groups, which allows a robust identification of haloes and sub-haloes. In particular, this algorithm first identifies particle groups with a FoF variant with a linking length larger than the usual[3]. Then, for each FoF group, ROCKSTAR builds a hierarchy of subgroups in phase space by progressively and adaptively reducing the value of the linking length: the 70% of the particles (fraction that can also be tuned by the user) of the main FoF group are gathered in sub-groups. The procedure is repeated to form a hierarchy of FoF sub-groups. Finally all the particles in the base FoF group are assigned hierarchically in phase space, starting from the lowest substructure levels. At the end of this procedure all the bounded particles will constitute a single halo, for which the main properties are then computed. A schematic visualisation and description of this process is reported on the right side of Fig. 2.4. Thanks to the accuracy checks performed across multiple time-steps, the ROCKSTAR algorithm allows an accurate tracking of histories and properties of haloes, recovering e.g. their expected mass accretion, merger events and shapes.

Many other halo finding algorithms have been proposed during the years and can be exploited according to characteristics required for a given analysis, e.g. computational performances, halo identification accuracy and predicted halo observational proprieties. We refer the reader to Knebe et al. (2011) for a detailed comparison between different halo finders.

2.3.2 Building a mock catalogue

Once we identified the DM haloes in the distribution of DM particles, we need to simulate the luminous astrophysical objects (i.e. galaxies and cluster of galaxies) in order to reproduce real survey data. A possible strategy is to follow the evolution of the baryonic matter, beside that of the DM. This requires to simulate, in addition to the effects of the gravitational force, all the known physical processes involved during galaxy formation and evolution, like radiative cooling, re-heating, turbulence, shocks, ecc. The modelling of these processes is a very complex task for a twofold reason: firstly because of our lack of knowledge about the micro-physics involved, and secondly because of the expensive computational resources required to handle the calculus of all forces acting on DM and baryonic particles. However, it is important to underline that baryonic interactions become relevant only on relatively small scales, therefore LSS on sufficiently large scales (larger than few Mpc) can be considered unaffected by these processes. Simulations in which the baryonic physics is taken into account to reproduce the feedbacks from stellar radiative processes, supermassive black holes and active galactic nuclei are called *hydrodynamic*. An example of hydrodynamic simulations is given by the Magneticum[4] (Dolag et al., in preparation), which will be analysed in Sect. 9.2.

Other approaches aimed at reproducing the clusters and the galaxies embedded in the DM haloes exploit instead semi-analytic methodologies, making use of both numerical and analytic techniques to approximate the physics involved in baryonic processes, with a degree of approximation that depends on the complexity of the physical phenomena

[3]Common values for building halo catalogues range from $b = 0.15$ to $b = 0.2$ (More et al., 2011), but in this case the algorithm uses $b = 0.28$ to have more bounded particles and consequently model properly also the most ellipsoidal haloes.

[4]http://www.magneticum.org/

modelled. Moreover, different type of algorithms have been proposed to have an higher accuracy in reproducing galaxy observable properties but a lower understanding of the physical processes involved in galaxy formation and evolution. Among these, we first introduce the halo-occupation distribution (HOD) method. In one of its simplest forms, this algorithm associates a number of galaxies (divided in central and satellites) to each halo of the catalogue according its total mass, and assigns observable properties (e.g. stellar mass or luminosity) to the galaxies, relying on some statistical conditional functions. Then we have the halo-abundance matching (HAM) and the sub-halo-abundance matching (SHAM): with this approach we assign the generated galaxies to an hosting structure (halo or sub-halo) assuming a monotonic relation between the galaxy properties and the host halo or sub-halo mass, respectively for the HAM and the SHAM method. The HOD and the SHAM algorithms will be involved in the preparation of the galaxy catalogue employed in Chapter 8. An honorable mention goes to the sub-halo clustering and abundance matching (SCAM) technique, which aims at applying both the HOD and SHAM approaches in sequence, providing a parametrised model to fit both the abundance and the clustering properties of a target population (see e.g. Ronconi et al., 2020).

As final remark, we underline that objects in a snapshot, whether we consider DM haloes or galaxies, are all characterised by the same cosmological age. However, to have a direct comparison with observations, we need to mimic the time evolution characterising astrophysical objects distant from the observer. This is obviously a direct consequence of the finite value of the light speed. The catalogues characterised by this feature are called *light-cones* and are generally build by stacking sequentially different slices of cosmological snapshots relative to different cosmic epochs. See Fig. 2.5 for a visual representation.

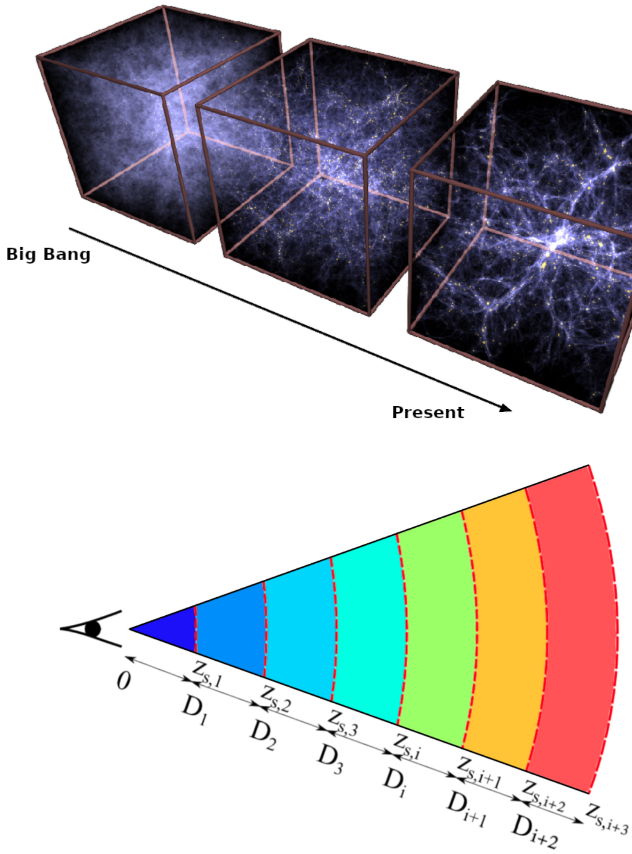

Figure 2.5: *Upper*: set of cosmological snapshots taken at different times: from billions of years after the Big Bang to current structures. Looking at each box separately it is possible to appreciate the evolution in the formation of the LSS. Credit: CXC/MPE/V.Springel. *Lower*: schematic representation of the light-cone construction from the simulation. The slices in colour show the portion of the matter extracted from each simulation snapshot with comoving distance between D_i and D_{i+1}, within the aperture of the field of view. Credit: Giocoli et al. (2016).

Chapter 3

Tensions in the standard cosmological model

In the last decades the ΛCDM model (see Sect. 1.5) has filled up a rather impressive trophy case thanks to its remarkable successes in explaining a wide range of cosmological observations. Among these, the present-day accelerated expansion of the Universe (Riess et al., 1998; Perlmutter et al., 1999), the observed abundances of different types of light nuclei (i.e. hydrogen, deuterium, helium, and lithium, see e.g. Schramm & Turner, 1998; Steigman, 2007; Iocco et al., 2009; Cyburt et al., 2016), the angular power spectrum and statistical properties of the CMB anisotropies (Planck Collaboration et al., 2020b), and statistical properties of the LSS of the Universe (Bernardeau et al., 2002; Bull et al., 2016). However, despite its widespread popularity, this scenario is currently under intense investigation, since it clashes with both some theoretical and observational issues.

For what concerns the theoretical issues, we first underline that the ΛCDM model does not provide a physical description for the CDM nature[1] (see also Sect. 1.5). Moreover, cosmological models based on Einstein's classical theory result unreconciled to quantum theory and imply a cosmological singularity in the Universe past life. Then, the two (historical) arguments against the validity of the cosmological constant are the so-called *coincidence* and *fine-tuning* problems (Weinberg, 1989; Martin, 2012; Burgess, 2013; Solà, 2013; Velten, vom Marttens & Zimdahl, 2014, but see also Bianchi & Rovelli, 2010 for an alternative perspective). The first problem is related to the *coincidence* of living in the precise era of transition between the matter domination and the late time acceleration one, i.e. when $\Omega_\Lambda \approx \Omega_{\rm m}$ (see Sect. 1.5), which can be considered statistically unlikely given the dramatically different evolution histories of these components (Sect. 1.4.1). The second problem is associated with the large discrepancy between theoretical expectations and the observations on the value of the cosmological constant Λ. Indeed, on one hand, we expect from the quantum field theory that particles in the Standard Model contribute to the value of the cosmological constant in a non negligible amount (Weinberg, 1989):

$$|\Lambda_{\rm th}| \lesssim 10^{-26}\ {\rm kg\ m^{-3}} \simeq 10^{-47}{\rm GeV}^4\ . \tag{3.1}$$

On the other hand, the value of the cosmological constant inferred from observation

[1] In the case of models that assume further degrees of freedom other than the cosmological constant also the very nature of the DE remains unexplained.

(Planck Collaboration et al., 2016a) is:

$$\Lambda_{\rm obs} \simeq 10^{95} \text{ kg m}^{-3} \simeq 10^{-74} \text{GeV}^4 , \tag{3.2}$$

which is roughly 120 order of magnitude larger than the observed value. Another formulation of this problem also inquiries the profound explanation of the extremely low, but non null, value of the cosmological constant.

For what concerns the observational issues, the increasing precision of modern cosmological and astrophysical measures, as well as the more accurate theoretical modelling of the data, has brought to statistically relevant tensions on the cosmological parameter values derived with different probes. These discrepancies arise in particular when considering probes covering different ranges of redshift: those related to local measurement (*late* or *low-redshift* probes) and those related to the measure of CMB anisotropies (*early* or *high-redshift* probes). Among the today most puzzling tensions we find (see Di Valentino et al., 2021a,b,c, for a review):

- the Hubble parameter tension (see also Sect. 1.3), i.e. local direct measurements of H_0, exploiting the distance ladder approach (see e.g. Freedman et al., 2001; Riess et al., 2011, 2016; Freedman et al., 2019), are in about 4.4σ tension with CMB indirect measurements, inferring the value of the Hubble constant assuming the ΛCDM model (Planck Collaboration et al., 2020a);

- the growth of structures tension, i.e. direct measurements of the growth rate of cosmological perturbations from weak lensing and clustering (Heymans et al., 2012; Erben et al., 2013; Joudaki et al., 2017, 2018; Abbott et al., 2018b; Troxel et al., 2018; Hildebrandt et al., 2020) indicate a lower growth rate than that indicated by the *Planck* data at a level of about $2-3\sigma$. This tension is often quantified using the parameter $S_8 \equiv \sigma_8\sqrt{\Omega_{\rm m}/0.3}$ (along the main degeneracy direction of weak lensing measurements) and can also be related to $f\sigma_8(z=0)$ (measured by galaxies' redshift-space distortions), where f is defined in Eq. (2.15);

- the curvature tension, i.e. the *Planck* data lead to a preference at 3.4σ for a closed Universe (Planck Collaboration et al., 2020a; Di Valentino, Melchiorri & Silk, 2020; Handley, 2021), in disagreement with the concordance flat ΛCDM scenario, which implies a flat space geometry. This tension with the flat ΛCDM model predictions is connected with the oddly higher lensing contribution in the CMB power spectra, characterised by the A_L parameter (Calabrese et al., 2008; Planck Collaboration et al., 2020a), which is strongly degenerate with Ω_κ;

- the Universe age tension, i.e. the age of the Universe obtained from local measurements using very old-dated objects (e.g. the first stars in the Milky Way or populations of stars in globular clusters, see Bond et al., 2013; Schlaufman, Thompson & Casey, 2018; Jimenez et al., 2019; Valcin et al., 2020) appears to be marginally larger than the corresponding age obtained using the CMB *Planck* data, in the context of the ΛCDM cosmology (Planck Collaboration et al., 2020a).

These tensions and the other significant issues of the ΛCDM model may reflect a breakdown of the assumed standard scenario and may hint towards undiscovered physics.

3.1 Alternatives to the standard ΛCDM model

Among the alternatives to the standard ΛCDM model proposed to face the issues exposed above, we will provide a brief introduction on the two categories of models in which the physical scenarios of accelerating cosmologies are usually separated: DE and modified gravity (MG) models (see e.g. Yoo & Watanabe, 2012; Amendola et al., 2013; Joyce, Lombriser & Schmidt, 2016, for a review). Essentially, DE models modify the right-hand side of the Einstein's field equation (Eq. 1.14), i.e. the stress-energy content of the Universe, adding a component with an equation of state parameter $w \simeq -1$, which may also be time-dependent. Instead, the MG category considers the left-hand side of the Einstein equation, modifying the Einstein–Hilbert action, i.e. GR itself. However, we underline that not all the models in the literature belong unambiguously to one category or the other, in fact while the modifications of the Einstein's field equation (i.e. the physical interpretations) may look different, the overall effect on the cosmological scenario can coincide.

Additionally, we will present the degeneracies between the effects of some of these models and those including massive neutrinos. Neutrinos are indeed another elusive component of the ΛCDM cosmology, and although the Standard Model of particle physics assumes they are massless, the evidence of solar neutrino oscillations proved they in fact possess a mass (Becker-Szendy et al., 1992; Fukuda et al., 1998; Ahmed et al., 2004). Many works have have pointed out that the presence of massive neutrinos causes imprints on the observable Universe LSS strongly degenerate with DE and MG theories (He, 2013; Motohashi, Starobinsky & Yokoyama, 2013; Upadhye et al., 2014; Baldi et al., 2014; Lorenz, Calabrese & Alonso, 2017; Giocoli, Baldi & Moscardini, 2018) and can also help reducing the tensions related to the standard ΛCDM cosmology (Lesgourgues & Pastor, 2006; Costanzi et al., 2014; Poulin et al., 2018; Sakstein & Trodden, 2020; Lambiase et al., 2019).

3.1.1 Dynamical DE models

The first category of theories we describe follows the approach of parametrising the Universe background quantities only, deriving consequently the associated Hubble rate (Eq. 1.55). We can follow the strategy to choose minimally-coupled scalar field models (Wetterich, 1988; Ratra & Peebles, 1988), also known as *quintessence*, which corresponds to consider a rest-frame sound speed[2], c_s, and a cosmic fluid with a null anisotropic stress[3], σ. The name "quintessence" refers to a *fifth element*, other than baryons, DM, radiation and neutrinos, which is identified as the missing cosmic energy density component with negative pressure, responsible for the accelerated expansion of the Universe. The basic idea of quintessence models is that DE is in the form of a time-varying scalar field, ϕ, that is slowly rolling down toward its potential minimum. In these theories the evolution of

[2] In practise, we impose the sound speed to be equal to the speed of light ($c_s = 1$ in natural units, i.e. $c = \hbar = 1$), causing the smoothing of DE perturbations on sub-horizon scales. An example of popular models beyond the simple quintessence are the so-called *k-essence* models, which are defined by an arbitrary sound speed in addition to a free equation of state parameter w.

[3] The anisotropic stress quantifies how much the pressure of the fluid varies with the direction and the study of its perturbation is crucial to understand the evolution of inhomogeneities in the early, radiation-dominated Universe (Hu, 1998; Koivisto & Mota, 2006).

the scalar field, assumed to be spatially homogeneous, is governed by:

$$\ddot{\phi} + 3H\dot{\phi} + V'(\phi) = 0 \ , \tag{3.3}$$

where $V(\phi)$ is the potential energy and the overdots denote the derivative with respect to the time while the prime with respect to the scalar field ϕ, respectively. Then, from the the energy density and the pressure of the scalar field we can derive the equation of state:

$$w \equiv \frac{p}{\rho} = \frac{\frac{1}{2}\dot{\phi}^2 - V(\phi)}{\frac{1}{2}\dot{\phi}^2 + V(\phi)} \ , \tag{3.4}$$

where $\frac{1}{2}\dot{\phi}^2$ is the kinetic energy. The parameter w can vary in the range $[-1, 1]$, but since we want to recover accelerating Universe solutions we must impose $w < -1/3$. If the scalar field evolves very slowly with time then the kinetic energy term will be much smaller than the potential energy term and w will tend to -1. In this case the scalar field behaves like the cosmological constant.

We will now introduce some DE models, which assume a generic quintessence-like component with an equation of state w (Eq. 3.4) expressed by means of simple parametrisations:

- the wCDM cosmology, which implements a constant (i.e. time independent) DE equation of state;
- the Chevallier-Polarski-Linder (CPL) (Chevallier & Polarski, 2001; Linder, 2003) parametrisation, in which the equation of state follows the equation

$$w_{\mathrm{CPL}}(z) = w_0 + w_a \frac{z}{z+1} \ ; \tag{3.5}$$

- the Jassal-Bagla-Padmanabhan (Jassal, Bagla & Padmanabhan, 2005) (JBP) parametrisation, in which w takes the form

$$w_{\mathrm{JBP}}(z) = w_0 + w_a \frac{z}{(z+1)^2} \ ; \tag{3.6}$$

- the logarithmic (LN) parametrisation introduced by Efstathiou (1999)

$$w_{\mathrm{LN}}(z) = w_0 + w_a \ln\left(\frac{1}{z+1}\right) . \tag{3.7}$$

Finally, among the most popular DE models used in the literature, we report also a more complex alternative, which is an unified DM and DE model that avoids the potential energy fine-tuning of the quintessence. This scenario implements an exotic background fluid, i.e. a generalised Chaplygin gas (GCG) (Kamenshchik, Moschella & Pasquier, 2001; Dvali & Turner, 2003), described by the following equation of state:

$$p = -\frac{A}{\rho^\alpha} \ , \tag{3.8}$$

where A is a positive constant and $0 < \alpha \leq 1$. Inserting this equation of state into the energy conservation equation (Eq. 1.43) yields:

$$\rho(t) = \left[A + \frac{B}{a^{3(1+\alpha)}}\right]^{\frac{1}{1+\alpha}} , \tag{3.9}$$

where B is an integration constant. From this relation we can see that, in early epochs ($a \ll 1$) the Chaplygin gas energy density follows the trend $\rho \propto a^{-3}$, while in late epochs ($a \gg 1$) its trend is $\rho \approx A^{\frac{1}{1+\alpha}} = const$. Thus this single fluid behaves as DM or DE according to the cosmic time (see Sect. 1.4.1). Introducing now $A_s = A/\rho_0^{1+\alpha}$, with ρ_0 representing the today's value of the energy density of the GCG, we can derive the DE equation of state:

$$w_{\mathrm{GCG}} = -\frac{A_s}{A_s + (1 - A_s)(1+z)^{3(1+\alpha)}} . \tag{3.10}$$

Since at low redshift the speed of sound for the Chaplygin gas model becomes approximately proportional to α, we generally impose the upper bound $|\alpha| \leq 10^{-5}$ to avoid the growth of inhomogeneities at late epochs (Sandvik et al., 2004).

In Chapter 8 we will focus on the analysis of two of the presented DE equation of state parametrisations: the constant w parametrisation and the CPL parametrisation. The first is the simplest case for a dynamical DE and it is in fact considered only for its simplicity (only one additional degree of freedom with respect to the ΛCDM model). The second model is one of the most employed in the literature thanks to its statistical agreement with most of the observational data (see e.g. Zhao et al., 2007; Shi, Huang & Lu, 2012; Planck Collaboration et al., 2016b; Ebrahimi, Monemzadeh & Moshafi, 2018; Tamayo & Vázquez, 2019). The direct motivation of proposing such a parametrisation form is to overcome the issue of the divergence at high redshifts of the linear form $w(z) = w_0 + w_a z$. Other advantages have been pointed out by Linder (2003), such as a simple physical interpretation (the parameters w_0 and w_a represent indeed the equation of state's present value and its overall time evolution, respectively), a manageable 2D-phase space, a well behaved and bounded behavior for high redshifts (but see Ma & Zhang, 2011 for the problems related to the description of the future evolution, i.e. approaching to $z = -1$) and high accuracy in reconstructing many scalar field equations of state.

3.1.2 Modified gravity models

MG models affect in general both the background and the perturbation equations, thus, besides leading to a cosmic acceleration, these models also introduce new physics on small scales. Having new degrees of freedom in the gravitational sector, MG theories must employ some *screening mechanism* in order to evade the very constraining local tests of gravity (Le Verrier, 1859; Bertotti, Iess & Tortora, 2003; Will, 2005).

As already mentioned, one of the simplest ways to modify the GR equations is to modify the left-hand side of the Einstein's field equation (Eq. 1.14). We can write the Einstein-Hilbert action, S, as the following:

$$S = \int \mathrm{d}^4x\sqrt{-g}\left(\frac{M_{\mathrm{P}}^2 R}{2} - \frac{1}{2}\dot{\phi}^2 - V(\phi)\right) + S_m[A^2(\phi)g_{\mu\nu}, \psi] , \tag{3.11}$$

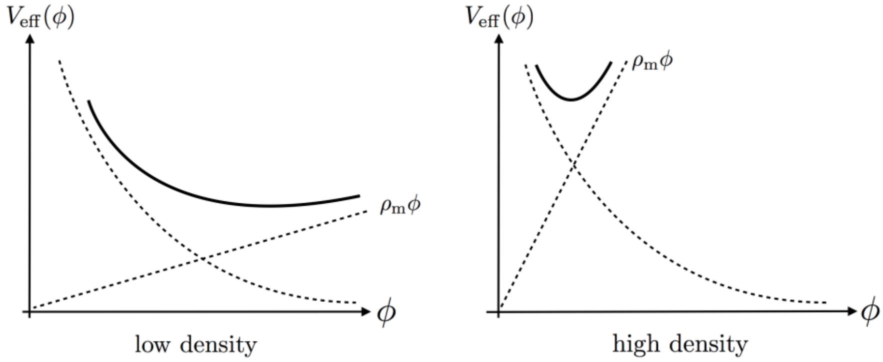

Figure 3.1: Chameleon effective potential in regions of low and high density. *Left*: the curvature of the potential is shallow in large regions at low density, consequently the scalar field becomes light and mediates a long range fifth force. *Right*: the scalar field acquires a large mass on small scales featuring high density, therefore leads to the suppression of the additional fifth force around matter overdensities. Credits to Elder et al. (2016).

where $M_{\rm P}^2 = \frac{1}{8\pi G}$ is the reduced Planck mass and S_m is the action of the matter field ψ. According to this formulation, the gravitational interaction is mediated by the scalar field as well as the tensor field of GR. These are the bases of the so called scalar-tensor theories, of which one of the most common representative is the Brans–Dicke theory (Brans & Dicke, 1961). In this specific case the potential and the coupling of the scalar field in Eq. (3.11) become $V(\phi) = 0$ and $A^2(\phi) = \exp\left[-\phi/(M_{\rm P}\sqrt{3/2+\omega})\right]$, respectively, with ω being a constant parameter. Thanks to Solar System tests we can place a constraining limit to the latter, i.e. $\omega \gtrsim 4 \times 10^4$ (Clifton et al., 2012; Will, 2014), which implies a very weak coupling of the field to the matter, making the Brans–Dicke theory essentially equivalent to a DE model.

In more general scalar-tensor theories it is possible to choose $V(\phi)$ and $A(\phi)$ suitably to evade Solar System constraints and having at the same time an interesting phenomenology for the scalar field. The trick is in the exploitation of the scalar field's response to the *effective* potential, which depends on the external matter sources. This allows us to build scenarios where the field behaves differently according the matter density of the environment. A well-known example of this scenario is the so-called *Chameleon field* (Khoury & Weltman, 2004b,a), in which the effective mass of the scalar field:

$$m_{\rm eff}^2(\phi) = \frac{{\rm d}^2 V_{\rm eff}}{{\rm d}\phi^2} = \frac{{\rm d}^2 V}{{\rm d}\phi^2} + \frac{{\rm d}^2 A}{{\rm d}\phi^2}\bar{\rho} \tag{3.12}$$

is shaped to acquire a high value in proximity of high-density regions and a smaller one in low-density regions, as represented in Fig. 3.1. One potential that satisfies this requirement is Ratra–Peebles (Ratra & Peebles, 1988) inverse power-law potential:

$$V(\phi) = \frac{M^{4+n}}{\phi^n} \ , \tag{3.13}$$

where n is a positive constant. See e.g. Khoury & Weltman (2004b,a); Hinterbichler

& Khoury (2010) for other popular examples of potentials and couplings implementing screening mechanisms like the one just described.

We will now provide some details on one of the most-studied scalar-tensor theories in order to provide the theoretical background required for Chapter 7. This class of models, called $f(R)$ gravity, consists of higher-curvature corrections to the Einstein–Hilbert action:

$$S = \frac{M_{\mathrm{P}}^2}{2} \int \mathrm{d}^4x \sqrt{-g}\big(R + f(R)\big) + S_m[g_{\mu\nu}, \psi] \; , \tag{3.14}$$

where $f(R)$ is a function only of the Ricci scalar, chosen to become significant in the low-curvature regime, i.e. $R \to 0$. In this class of MG theories, GR is recovered by imposing f to be proportional to the cosmological constant $f = -2\Lambda^{\mathrm{GR}}$ and more general cosmic acceleration solutions can be obtained by following Capozziello & Fang (2002); Capozziello, Carloni & Troisi (2003); Carroll et al. (2004). However, the original formulation of the proposed models leads to predictions in disagreement with precision tests of gravity, as demonstrated by Erickcek, Smith & Kamionkowski (2006). This is due to the fact that $f(R)$ models are actually scalar-tensor theories in disguise (Barrow & Cotsakis, 1988; Chiba, 2003). A possible strategy to demonstrate it was given e.g. by Joyce et al. (2015), who performed the following field redefinition and conformal transformation:

$$V(\phi) = \frac{M_{\mathrm{P}}^2}{2} \frac{\left(\phi \frac{\mathrm{d}f}{\mathrm{d}\phi} - f\right)}{\left(1 + \frac{\mathrm{d}f}{\mathrm{d}\phi}\right)^2} \quad , \quad A^2(\phi) = e^{\sqrt{\frac{2}{3}}\frac{\phi}{M_{\mathrm{P}}}} \tag{3.15}$$

which is equivalent to the Brans–Dicke with $\omega = 0$ and a non-null potential.

A well-studied $f(R)$ model, compatible with both local tests of gravity and the observed expansion of the Universe on large scale, is the one introduced by Hu & Sawicki (2007):

$$f(R) = -m^2 \frac{c_1 \left(\frac{R}{m^2}\right)^n}{c_2 \left(\frac{R}{m^2}\right)^n + 1} \, , \tag{3.16}$$

where $m^2 \equiv H_0^2 \Omega_{\mathrm{m}}$ defines the mass scale m, while c_1, c_2 and n are non-negative free parameters of the model. In particular we want to focus on the case in which $c_1/c_2 = 6\Omega_\Lambda/\Omega_{\mathrm{m}}$, where Ω_Λ and Ω_{m} represent the present vacuum density and matter density parameters, respectively. Indeed, under this specific condition, the background expansion history is consistent with the one predicted by the ΛCDM model. Moreover, imposing $c_2(R/m^2)^n \gg 1$ the scalar field $f_R \equiv \mathrm{d}f(R)/\mathrm{d}R$ can be approximated by:

$$f_R \approx -n \frac{c_1}{c_2^2} \left(\frac{m^2}{R}\right)^{n+1} . \tag{3.17}$$

In Chapter 7 we will restrict our analysis to the case $n = 1$. With this choice the scalar field can in fact be expressed by means of the parameter c_2 only and the model at the present epoch can be represented by the parameter f_{R0}:

$$f_{R0} \equiv -\frac{1}{c_2} \frac{6\Omega_\Lambda}{\Omega_{\mathrm{m}}} \left(\frac{m^2}{R_0}\right)^2 , \tag{3.18}$$

where R_0 indicates the background value of the Ricci scalar at the present time. Now we can derive the modified Einstein equations by varying the action defined in Eq. (3.11) with respect to the metric $g_{\mu\nu}$:

$$f_R R_{\mu\nu} - \frac{1}{2} f g_{\mu\nu} - \nabla_\mu \nabla_\nu f_R + g_{\mu\nu} \Box f_R = 8\pi G T_{\mu\nu} \,, \tag{3.19}$$

where ∇ is the covariant derivative and $\Box$ is the D'Alembert operator defined as $\Box \equiv g^{\mu\nu}\nabla_\mu\nabla_\nu$. Here f_R turns out to be the responsible for the modification of the GR theory and plays the role of a new dynamical scalar degree of freedom. From the trace of Eq. (3.19) we can obtain the equation of motion for this scalar field:

$$\nabla^2 \delta f_R = \frac{a^2}{3} \left[\delta R(f_R) - 8\pi G \delta\rho_m\right] \,, \tag{3.20}$$

where a is the scale factor of the metric. To obtain the equivalent of the Poisson equation for the scalar metric perturbation $2\psi = \delta g_{00}/g_{00}$, we extract the time-time component from Eq. (3.19):

$$\nabla^2 \psi = \frac{16\pi G}{3} a^2 \rho_m - \frac{a^2}{6} \delta R(f_R) \,, \tag{3.21}$$

assuming small perturbations on a homogeneous background[4] and a slow variation for f_R (quasi-static field).

From Eqs. (3.20) and (3.21) it is possible to derive the exact solution for the extreme cases $|f_{R0}| \gg |\psi|$ and $|f_{R0}| \ll |\psi|$. It can be demonstrated that, when the field is large, thus in the former case, the Compton wavelength of the scalar field $\mu^{-1} = (3 \, \mathrm{d}f_R/\mathrm{d}R)^{1/2}$ determines the interaction range of an additional fifth force, which can enhance the gravity field up to a factor of $4/3$ for $k \gg \mu$. Standard gravity is instead restored for scales $k \ll \mu$. In the latter case, instead, the value of f_{R0} is small and Eq. (3.21) can be approximated by the standard Poisson equation, leading to the recovery of GR in regions of high space-time curvature thanks to the effect of the Chameleon-screening mechanism. By solving Eq. (3.20) under the assumption of small perturbations in the homogeneous background, $\delta f_R \leq \bar{f}_R$, we can obtain the screening condition for an ideal spherical source of mass M causing the fluctuation of the scalar field:

$$|f_R| \leq \frac{2}{3} \psi_N(r) \,, \tag{3.22}$$

where $\psi_N = GM/r$ is the Newtonian potential of the overdensity. In this approximation, the enhancement of gravity is carried out only by the distribution of mass outside the radius for which $\psi_N(r) = 3/2 \; |f_R|$, that constitutes the transition point between the screened and un-screened regimes.

We can now assess valid estimations for the free parameter f_{R0}. The case in which $f_{R0} \ll \psi_N$ has no relevant cosmological interest since the fifth force is always screened, hence the resulting scenario is indistinguishable from GR even on large scales. On the other hand, for $f_{R0} \gg \psi_N$, we would face the implausible situation in which gravity is always enhanced. Therefore the parameter f_{R0} should be settled around the same order of magnitude of the Newtonian potential ψ_N, that in turn typically shows values in the range $10^{-5} \leq \psi_N \leq 10^{-6}$.

[4] $\delta f_R \equiv f_R - \bar{f}_R$, $\delta R \equiv R - \bar{R}$ and $\delta\rho_m \equiv \rho_m - \bar{\rho}_m$, where the barred values represent the background quantities.

3.1.3 Massive neutrinos

Neutrinos are massive particles contributing to the total matter content of the Universe and to the growth of cosmic structures. Given their small masses, neutrinos decouple from high relativistic particles at the early stages of the Universe, when their thermal energy drops below their mass. Precision cosmology allows nowadays to put strong constraints on their physics and especially on the sum of their mass eigenstates $M_\nu \equiv \sum m_\nu$. The total neutrino mass is indeed constrained by several astronomical observations to be $M_\nu \lesssim 0.1 - 0.3$ eV (see e.g. Seljak, Slosar & McDonald, 2006; Riemer-Sørensen et al., 2013; Lu et al., 2015, 2016; Cuesta, Niro & Verde, 2016; Kumar & Nunes, 2016; Yèche et al., 2017; Poulin et al., 2018), and their contribution to the total amount of energy in the Universe at late cosmological epochs can be computed as (Mangano et al., 2005):

$$\Omega_\nu \approx \frac{M_\nu}{93.14\ h^2\ \mathrm{eV}}\,. \tag{3.23}$$

Given their weak interaction cross-section, neutrinos can be considered as a DM component. However, contrary to CDM particles, neutrinos can free-stream from high density perturbations of matter thanks to their high thermal velocity. Indeed we can derive the typical scales travelled by neutrino perturbations, described by the free-streaming length:

$$\lambda_{\mathrm{FS}}(z, M_\nu) = a(z)\frac{2\pi}{k_{\mathrm{FS}}} = 7.7(1+z)\frac{H_0}{H(z)}\left(\frac{1\mathrm{eV}}{M_\nu}\right)\ h^{-1}\ \mathrm{Mpc}\,, \tag{3.24}$$

where k_{FS} is the associated free-streaming wavenumber, which during the neutrino non-relativistic transition, z_{nr}, reaches the minimum value (Lesgourgues et al., 2013):

$$k_{\mathrm{FS}}(z_{\mathrm{nr}}) \simeq 0.0178\left(\Omega_{\mathrm{m}}\frac{M_\nu}{1\mathrm{eV}}\right)^{1/2}\ h^{-1}\ \mathrm{Mpc}\,. \tag{3.25}$$

Therefore modes with $k < k_{\mathrm{FS}}$ evolve as CDM perturbations since neutrino velocities can be neglected, while on small scales ($k \gg k_{\mathrm{FS}}$) free-streaming leads to the slowdown of the neutrino perturbation growth. Besides suppressing the clustering below their thermal free-streaming scale, neutrinos also affect the shape of the matter auto-power spectrum (Brandbyge et al., 2008; Saito, Takada & Taruya, 2008, 2009; Brandbyge & Hannestad, 2009, 2010; Agarwal & Feldman, 2011; Wagner, Verde & Jimenez, 2012), the halo mass function (Brandbyge et al., 2010; Marulli et al., 2011; Villaescusa-Navarro et al., 2013), the scale-dependent bias (Chiang, LoVerde & Villaescusa-Navarro, 2019), the clustering properties of CDM haloes and redshift-space distortions (Viel, Haehnelt & Springel, 2010; Marulli et al., 2011; Villaescusa-Navarro et al., 2014; Castorina et al., 2014, 2015; Zennaro et al., 2018; García-Farieta et al., 2019).

Moreover, it has been demonstrated that the observable footprints predicted by MG theories are strongly degenerate with the signatures induced by the presence of massive neutrinos. Indeed, the typical range of the fifth force for $f(R)$ models, determined by the Compton wavelength μ^{-1}, can reach a few tens of Mpc (see e.g. Cataneo et al., 2015) depending on the value of the parameter f_{R0}, and it is comparable with the free-streaming scale of neutrinos, which can be estimated with Eq. (3.24). The neutrinos free-streaming can have thus a counteractive effect on the enhanced growth of the cosmic structures, causing a compensation on the cosmological statistical variations given by MG theories. This poses a notable challenge for cosmology, since robust methods and different cosmological probes are required to achieve tight constraints on both massive neutrinos and MG, and especially to disentangle their combined effects.

In Chapter 7 we will evaluate the contribution of cosmic voids – which we will formally introduce in Chapter 4 – in this context. Indeed, thanks to their peculiar underdense nature and exceptional spatial extension, comparable to the ranges covered by the fifth force of $f(R)$ models and by the neutrino free-streaming, voids are particularly sensitive to both these components. We will demonstrate how their statistics may play the role of key probes in the disentangling of the presented degenerate scenarios.

Chapter 4

Statistical properties of cosmic voids

We can describe cosmic voids as those large and underdense regions that emerge between the filaments and the walls of the cosmic web, filling most of the volume of the Universe. What we learnt from Sect. 2.2.1 is that voids originate from the evolution of underdensities in the primordial matter density field, growing in size with an expansion rate that is inversely proportional to the density they enclose. As they expand, the density within these objects decreases mainly as consequence of the redistribution of mass over the expanding volume and secondarily due to the mass lost to the surrounding overdensities. Since matter from the inner parts accumulates near the boundary, a ridge develops around the void, as shown in Fig. 4.1.

Analogously to galaxy clusters, their positive counterparts in the density field, voids number counts and density profiles provide powerful cosmological probes. However, the identification of cosmic voids is not trivial, since their shape and position have to be reconstructed starting from the distribution of luminous tracers arranged mostly on their boundaries. Despite these major problems, cosmic voids gained increasingly popularity in the last decades thanks to some really intriguing features: voids are for their nature only mildly nonlinear (nonlinear effects occur only near the edges) and tend to become more spherical as they evolve, which suggests that their evolution should be easier to reconstruct than that of positive perturbations. These characteristics allow us to predict the void statistical distribution as a function of their size. This property is particularly important to constrain cosmological parameters and makes voids fundamental probes that can be exploited to improve upon current constraints on DE and to discriminate between the competing cosmological models introduced in Chapter 3 (more details will be provided in Sect. 4.7).

In this section, we will discuss the specific void definition adopted in this Thesis work. Then we propose a brief review of the excursion-set formalism that, in combination with the spherical collapse model, provides insights into many aspects of halo formation and can be used to predict the DM halo abundances and clustering. The analogous spherical expansion model can likewise be used to make excursion-set predictions for voids (Sheth & van de Weygaert, 2004), leading to the statistical distribution of voids as a function of their size. Finally, we overview the main features associated to the density profiles of cosmic voids.

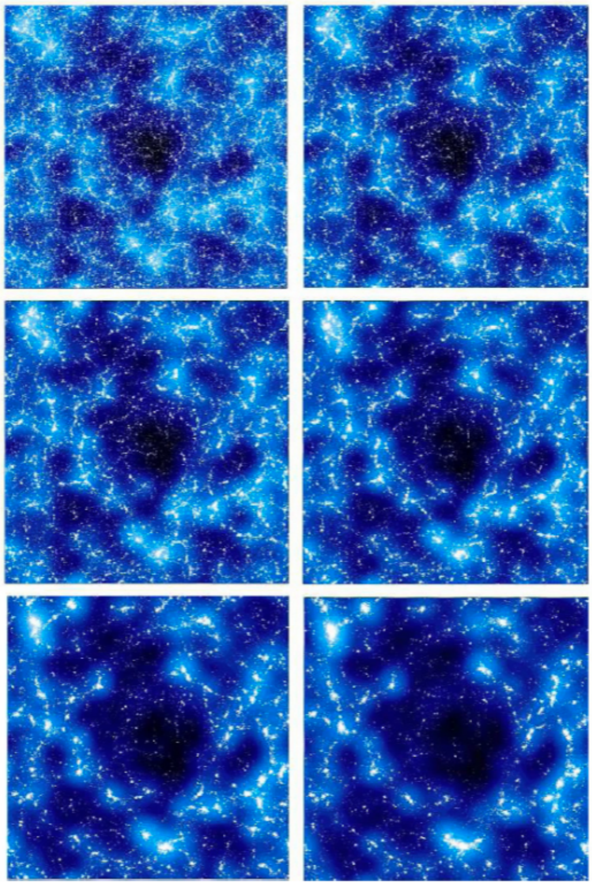

Figure 4.1: Simulation of an evolving void in a ΛCDM scenario, shown at six different epochs: $a = 0.05$, 0.15, 0.35, 0.55, 0.75 and 1.0. The simulation slice shown in these images is 50 h^{-1} Mpc wide and is 10 h^{-1} Mpc thick. Credits: van de Weygaert & Platen (2011).

4.1 Void definition

Despite the increasing usage of cosmic void statistics in the recent literature, a widespread and unique definition of cosmic voids has not yet been provided, and this fact represents one of the main issues in their cosmological usage. For instance, there is not a common set of values (or, at least, range of values) to classify voids according to their internal density, size and shape. Given the focus of this Thesis work on the void size function, we will define voids in agreement with the theoretical size function prescriptions, which we will introduce in Sect. 4.3. Thus, we consider voids as ideal, non-overlapping spheres, embedding a fixed negative density contrast $\delta_{\rm v}^{\rm NL}$. We will see in the next chapters which values of internal density contrast are more appropriate for cosmological analyses.

Beyond the void definition adopted in this work, other methods to define and detect cosmic voids have been proposed by the scientific community. In particular, voids can be simply identified as regions empty of mass tracers, or at least with densities lower than a given fraction of the mean cosmic density (Elyiv et al., 2013; Micheletti et al., 2014). Alternatively, voids can be defined based on their geometry, such as as underdense geometrical structures, composed by polyedra, spheres or tessellations (Platen, van de Weygaert & Jones, 2007; Neyrinck, 2008; Sutter et al., 2015). Otherwise, we can rely on dynamical criteria in which mass tracers are used to reconstruct the velocity density field (Forero-Romero et al., 2009; Lavaux & Wandelt, 2010; Elyiv et al., 2015). In the latter case, the void centres are defined as the points from which particles escape with the maximal velocity. These different definitions have all been employed in the development of void finder algorithms during the last decades. An analysis of the different classes of void finders will be presented in Sect. 5.2.

4.2 Excursion-set formalism

The excursion-set formalism is an analytical framework to study the LSS of the Universe. This approach allows us to predict the number density of structures by relating the cosmological linear perturbation theory to its nonlinear counterpart at late time. In this section we will introduce the general concepts needed to formulate the theoretical model describing the abundance of voids as a function of their sizes.

In real space, the linear density fluctuation field smoothed on a scale R is given by:

$$\delta(\mathbf{x}, R) = \frac{1}{(2\pi)^3} \int \delta(\mathbf{k}) W(\mathbf{k}, R) e^{-i\mathbf{k}\cdot\mathbf{x}} \mathrm{d}^3 k \ , \tag{4.1}$$

where $\delta(\mathbf{k})$ is the Fourier transform of the density perturbation $\delta(\mathbf{x}) \equiv [\rho(\mathbf{x}) - \rho_{\rm m}]/\rho_{\rm m}$, $\rho(\mathbf{x})$ is the local density at the comoving position $\mathbf{x}$, $\rho_{\rm m}$ is the background matter density and $W(\mathbf{k}, R)$ is a window function in Fourier space. It is common to relate the smoothing scale R to the corresponding variance of the linear density field, computed in terms of the size of the considered region:

$$\sigma^2(R) \equiv S(R) = \frac{1}{2\pi} \int k^2 P(k) |W(k, R)|^2 \mathrm{d}k \,, \tag{4.2}$$

where $P(k)$ is the matter power spectrum in linear perturbation theory that we introduced in Sect. 2.1.2. We can refer to a trajectory $\delta(x, S)$ as a sequence of overdensities given by subsequent increases in the smoothing scale by increments ΔS. When a top-hat filter in k-space is used then $\delta(x, S)$ executes a random walk. Given an underlying Gaussian distribution for the linear density field, the excursion-set formalism allows us to associate probabilities to random walks that satisfy a given set of criteria for the smoothing scale at which they cross various density thresholds. For the collapse of perturbations, the spherical evolution model in combination with the excursion-set provides a good description of the statistics of DM haloes. As discussed in Sect. 2.2.1, a collapse occurs when the linear density fluctuation reaches a critical value or barrier $\delta_{\rm c}^{\rm L}$, whose value is computed in linear theory. We can then use the excursion-set formalism to determine the fraction of trajectories that cross this barrier for the first time (i.e. solving the so-called *one-barrier problem*), accounting also for the *cloud-in-cloud* process. The cloud-in-cloud problem consists in counting as haloes only those objects which are not embedded in larger ones, i.e. when a trajectory pierces the $\delta_{\rm c}^{\rm L}$ barrier more than once only the crossing with the smallest value of $\sigma(M)$ has to be considered.

To extend the model to underdense regions we must first specify a threshold related to void formation. One possibility is to select the value of the shell-crossing phenomenon, $\delta_{\rm sc}^{\rm L}$, (see Sect. 2.2.1), but in this case we prefer to choose a generic negative density contrast value, $\delta_{\rm v}^{\rm L}$, to keep the treatment more general. Contrary to the overdense case, the hierarchical clustering of voids implies more complex phenomena and then it is not sufficient to replace the quantity $\delta_{\rm c}^{\rm L}$ with $\delta_{\rm v}^{\rm L}$ to obtain a description of the void distribution. We need in this case to consider a *two-barrier problem*. In addition to avoiding the double counting associated with the *void-in-void* process, associated to the merger of voids and analogous to the cloud-in-cloud process, we need to take into account the possibility for a small-scale void to be embedded in a sufficiently large-scale overdensity: the collapse of the larger surrounding region will eventually squeeze and vanish the underdense region it surrounds. This is called *void-in-cloud* problem and leads to avoid the counts of voids located inside collapsing regions. Finally, the opposite situation in which a large-underdense region embeds a small-overdense one is irrelevant for the formation of high-density collapsed structures, since DM haloes within voids are not likely to be torn apart as the void expands around them. The asymmetry between the void-in-cloud and cloud-in-void processes leads to a symmetry breaking between the emerging halo and void populations: although they evolve out of the same symmetric Gaussian initial conditions, over- and underdensities are expected to evolve towards a distribution with different characteristics.

We show in Fig. 4.2 a summary of the four processes of halo and void formation described by the excursion-set formalism. This approach provides the basics to the modelling of the theoretical void size function, which we describe in the next section.

4.3 Size function

The comoving number density of cosmic voids as a function of their size, i.e. the void size function, has been modelled for the first time by Sheth & van de Weygaert (2004) (hereafter SvdW model), with the same excursion-set approach used for the mass function of DM haloes (Peacock & Heavens, 1990; Cole, 1991; Bond et al., 1991; Mo & White, 1996b). As we saw in the previous section, the distribution of fluctuations that become voids, i.e. the multiplicity function, is obtained as the conditional first crossing distribution of the matter density contrast filtered at decreasing Lagrangian radius in a double barrier

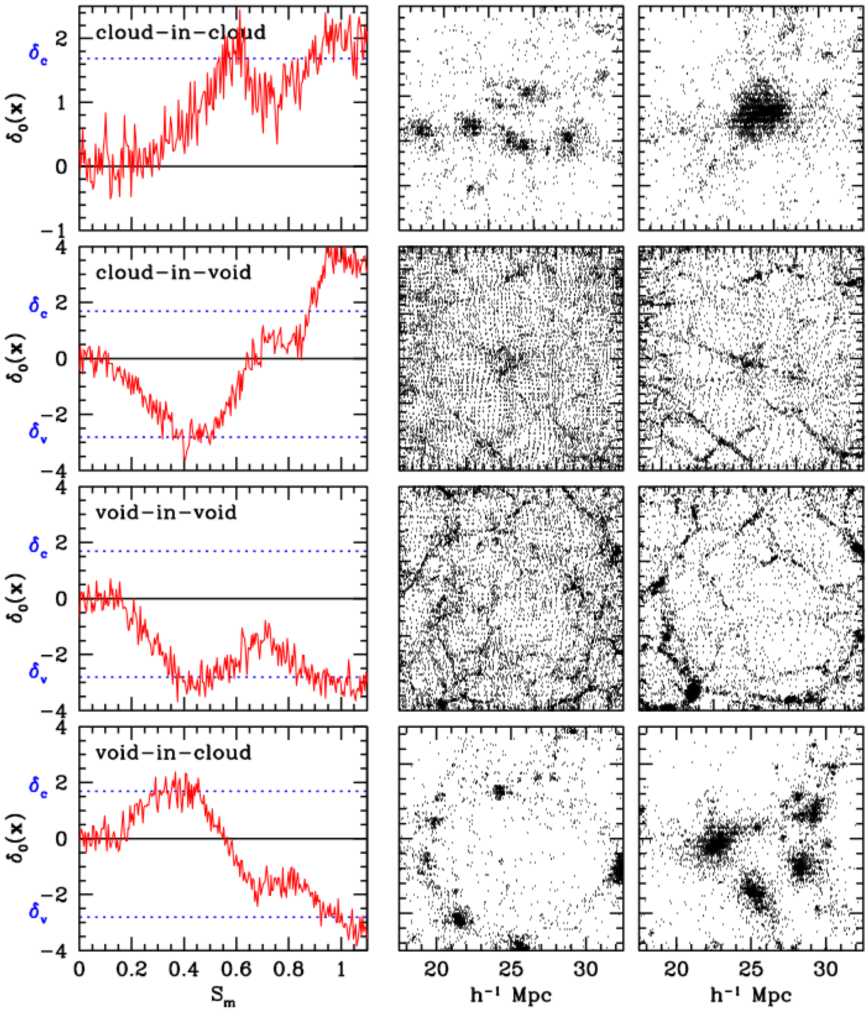

Figure 4.2: Four modes of the excursion-set formalism. Each row illustrates one of the four basic processes of hierarchical clustering: the cloud-in-cloud, cloud-in-void, void-in-void and void-in-cloud (from top to bottom). Each mode is illustrated using three frames. The leftmost panels show the trajectory associated to a local density perturbation $\delta_0(x)$ as a function of the mass resolution scale $S_{\rm m}$. For the sake of clarity, we point out that increasing values of $S_{\rm m}$ corresponds to decreasing cosmological scales. In each leftmost sub-plots the dashed horizontal lines indicate the collapse barrier $\delta_{\rm c}^{\rm L}$ and the void-formation barrier $\delta_{\rm v}^{\rm L}$. The boxes in the two columns on the right show how the corresponding particle distribution evolves when each barrier is pierced: on small scales first (second column, central panels) and on large scales later in time (third column, rightmost panels). Credits: Sheth & van de Weygaert (2004).

problem: a fluctuation becomes a void at a radius $R_{\rm v}$ if the filtered density contrast first crosses the void formation threshold $\delta_{\rm v}^{\rm L}$ at $R_{\rm v}$, without having crossed the threshold for collapse $\delta_{\rm c}^{\rm L}$ at any larger scale. Let us stress the fact that the multiplicity function of Sheth & van de Weygaert (2004) is derived for spherical fluctuations in Lagrangian space, i.e. the initial density field linearly evolved to the epoch of interest, while the observed voids live in the fully nonlinear evolved density field in comoving coordinates, i.e. the Eulerian space. Nevertheless, the spherical approximation allows us to easily go back and forth from Lagrangian to Eulerian space in all the computations. The void size function probes the inner region of cosmic voids and in contrast to the collapsing case, i.e. halo formation (Monaco, 1995; Sheth & Tormen, 2002), the spherical approximation is accurate enough for this purpose, at least for voids of scales detectable by modern redshift surveys (Icke, 1984b; Verza et al., 2019).

The excursion-set theory applied to underdensities (Sheth & van de Weygaert, 2004) predicts that the fraction of the Universe occupied by cosmic voids is given by:

$$f_{\ln\sigma} = 2\sum_{j=1}^{\infty} j\pi x^2 \sin(j\pi\mathcal{D}) \exp\left[-\frac{(j\pi x)^2}{2}\right], \tag{4.3}$$

where

$$x \equiv \frac{\mathcal{D}}{|\delta_{\rm v}^{\rm L}|}\,\sigma\,, \tag{4.4}$$

and

$$\mathcal{D} \equiv \frac{|\delta_{\rm v}^{\rm L}|}{\delta_{\rm c}^{\rm L} + |\delta_{\rm v}^{\rm L}|}\,. \tag{4.5}$$

In the previous equations σ is the square root of the mass variance and $\delta_{\rm c}^{\rm L}$ represents the critical value for the collapse of an overdense shell in an EdS universe. The latter is expected to vary within $1.06 \leq \delta_{\rm c}^{\rm L} \leq 1.686$, since both the turn-around or the collapse density contrast value can be considered acceptable assumptions (see Sect. 2.2.1).

Equation (4.3) can be simplified by applying the approximation (used in the `CosmoBolognaLib` libraries, see Sect. 5.1) proposed by Jennings, Li & Hu (2013), which is accurate at the 0.2% level or better everywhere:

$$f_{\ln\sigma}(\sigma) = \begin{cases} \sqrt{\frac{2}{\pi}}\frac{|\delta_{\rm v}^{\rm L}|}{\sigma}\exp\left(-\frac{\delta_{\rm v}^{\rm L\,2}}{2\sigma^2}\right), & x \leq 0.276 \\ 2\sum_{j=1}^{4} j\pi x^2 \sin(j\pi\mathcal{D}) \exp\left[-\frac{(j\pi x)^2}{2}\right] & x > 0.276\,. \end{cases} \tag{4.6}$$

With the kernel probability distribution given in Eq. (4.3), it is straightforward to obtain the number density distribution of voids as a function of their size in linear theory by applying:

$$\frac{{\rm d}n^{\rm L}}{{\rm d}\ln r^{\rm L}} = \frac{f_{\ln\sigma}(\sigma)}{V(r^{\rm L})}\frac{{\rm d}\ln\sigma^{-1}}{{\rm d}\ln r^{\rm L}}\,, \tag{4.7}$$

where $V(r^{\rm L}) = 4\pi(r^{\rm L})^3/3$ is the volume of the spherical fluctuation of radius $r^{\rm L}$. We recall that the superscript L indicates a value derived in linear theory. In order to derive the void size function in the nonlinear regime, a conservation criterion has to be applied. The model of the void size function developed by SvdW relies on the assumption that, when going from linear to nonlinear, the total number of voids is conserved. While reaching shell-crossing, underdensities are expected to have expanded by a factor $a \propto (\delta_{\rm v}^{\rm L})^{-3}$, thus a correction in radius by this factor is required:

$$\left.\frac{\mathrm{d}\, n}{\mathrm{d}\, \ln r}\right|_{\rm SvdW} = \frac{\mathrm{d}\, n}{\mathrm{d}\, \ln(a\, r^{\rm L})}\ , \tag{4.8}$$

for which we can explicit the relation:

$$\frac{r}{r^{\rm L}} = \left(\frac{\overline{\rho}}{\rho_{\rm v}}\right)^{1/3}\ , \tag{4.9}$$

where $\overline{\rho}$ is the mean density of the Universe and $\rho_{\rm v}$ is the average density within the void. The SvdW size function takes into account the void-in-cloud process, affecting mostly voids on small scales. This is considered by defining $\mathcal{D}$ in Eq. (4.3) as a function of both the overdensity and the underdensity threshold. On the other side, the void-in-void side effect is not considered in the SvdW model. Jennings, Li & Hu (2013) argued that, since multiple countings of voids in the same region leads to a volume fraction occupied by underdensities which is larger than the total volume of the Universe, the SvdW was unphysical. So they introduce a *volume conserving* model (hereafter Vdn model) which embeds a prescription to account for this: it is assumed that the total volume occupied by cosmic voids is conserved in the transition from the regime of linearity to that of nonlinearity. Its final expression is:

$$\left.\frac{\mathrm{d}\, n}{\mathrm{d}\, \ln r}\right|_{\rm Vdn} = \frac{\mathrm{d}\, n}{\mathrm{d}\, \ln r^{\rm L}}\frac{V(r^{\rm L})}{V(r)}\frac{\mathrm{d}\, \ln r^{\rm L}}{\mathrm{d}\, \ln r}\ . \tag{4.10}$$

A comparison between the theoretical void size functions computed with the models described above is reported in Fig. 4.3.

The SvdW model has been tested on both simulated DM particle and halo catalogues, finding that it systematically overpredicts the comoving number density of cosmic voids, as we can see in Fig. 4.4. To overcome this mismatch the underdensity threshold $\delta_{\rm v}^{\rm L}$ was commonly left as a free parameter, tuned on simulations. This severely affects the possibility of using the void size function as a cosmological probe. Jennings, Li & Hu (2013) have shown that the Vdn model does not require such a fine-tuning of the size function parameters, as long as the void catalogue is appropriately cleaned from spurious voids. However their results are limited to the case of cosmic voids detected on simulated DM (i.e. unbiased) distributions. In Chapter 6 we will extend their study to the case of samples of biased tracers, such as simulated DM halo catalogues, which are more representative of the realistic case of galaxy surveys.

4.4 Void density profiles

Another fundamental quantity to describe the structure of cosmic voids in a statistical sense is their density contrast profile. To simplify the notation, let us assume in this section and in the following that the considered voids are traced by galaxies. We define the void density profile as the spherically averaged relative deviation of mass density

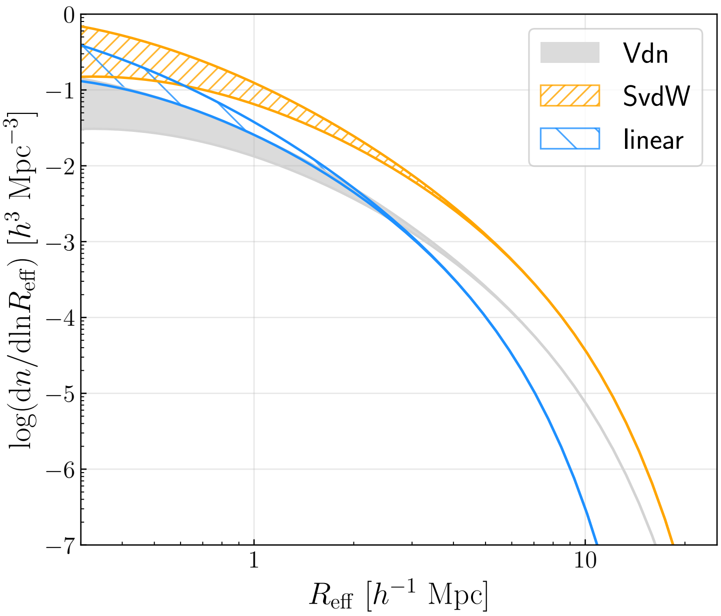

Figure 4.3: Comparison between different void size function models. The Vdn model is represented in grey, the linear model in blue, and the SvdW model in orange. The shaded or hatched regions are obtained by varying $\delta_{\rm c}$ in the range $1.06 \leq \delta_{\rm c}^{\rm L} \leq 1.686$. We can note that this variation changes the abundances significantly only at $R_{\rm eff} \lesssim 1\ h^{-1}$ Mpc. These results are obtained by exploiting the `CosmoBolognaLib` (that we will introduce in Sect 5.1) assuming a ΛCDM model characterised by $\Omega_{\rm m} = 0.26$, $h = 0.715$, $\sigma_8 = 0.8$, $\Omega_{\rm b} = 0.044$ and $n_s = 0.96$.

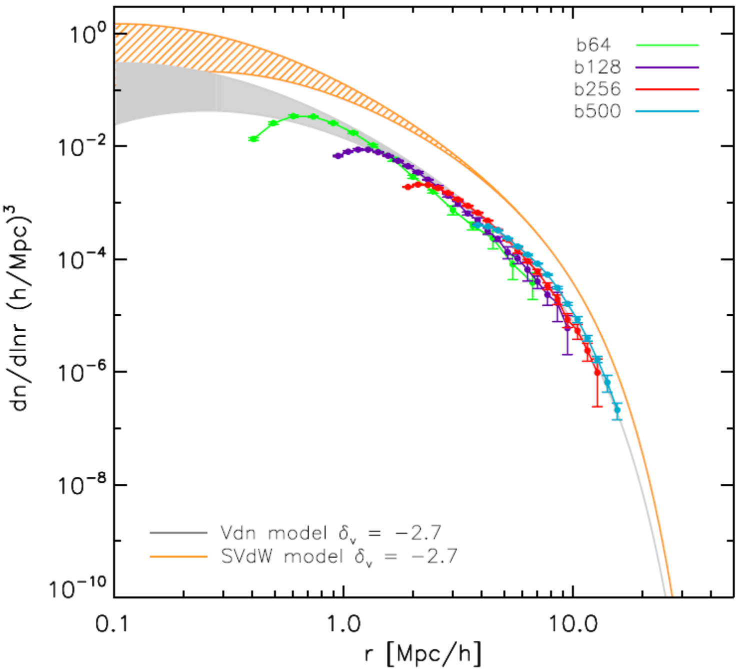

Figure 4.4: Comparison of the void abundance in simulations with respect to predictions. The results refer to the DM distribution in simulations for the ΛCDM model with different box sizes: 64 h^{-1} Mpc (green), 128 h^{-1} Mpc (purple), 256 h^{-1} Mpc (red) and 500 h^{-1} Mpc (cyan). The error bars represent the scatter on the mean from 8 different realisations of the cosmology reported in Fig. 4.3, for each box size. The range in predictions covers the parameter interval $\delta_c^L = [1.06, 1.686]$ with $\delta_v^L = -2.7$ and are consistent with simulations for the Vdn model (grey shaded), but not for the SvdW model (orange hatched). Credits: Jennings, Li & Hu (2013).

computed around a void centre from the mean value of galaxies in the universe:

$$u_{\rm v}(r) \equiv \frac{n_{\rm vg}(r)}{\langle n_{\rm g} \rangle} - 1 = \frac{\rho_{\rm v}(r)}{\overline{\rho}} - 1 \,, \tag{4.11}$$

where $n_{\rm vg}(r)$ is the galaxy number density in a sphere of radius r centred on a void and $\langle n_{\rm g} \rangle$ the overall mean number density of galaxies; $\rho_{\rm v}$ and $\overline{\rho}$ are their corresponding mass density quantities, respectively. Void density profiles have been studied in detail in the recent literature (see Hamaus et al., 2020, and references therein). Void profiles typically exhibit a few very characteristic features: a deep underdense core with central density increasing with void size, and an over-dense ridge (*compensation wall*) that exceeds the mean density of the Universe and then stabilises around $\delta \simeq 0$. The height of the compensation wall decreases with void size, causing internal slope to become smaller and the wall to flatten along the profile.

Different functional forms have been proposed for the void density profile in the literature. These can be divided into two main categories: phenomenological models aiming at finding a suitable form to fit the void density profile (Paz et al., 2013; Nadathur et al., 2015), and theoretically motivated models (see e.g. Finelli et al., 2016). Let us present the most popular example of void profile equation belonging to the first category, i.e. the functional form proposed by Hamaus, Sutter & Wandelt (2014):

$$u_{\rm v}(r) = \delta_{\rm c}^{\rm L} \frac{1 - (r/r_s)^{\alpha}}{1 + (r/r_{\rm v}^{\rm L})^{\beta}} \,, \tag{4.12}$$

where $\delta_{\rm c}^{\rm L}$ is the central density contrast (i.e. at $r = 0$), r_s is a scale radius at which the density equals the galaxy mean density $\langle n_{\rm t} \rangle$, and α, β describe the inner and outer slopes of the profile, respectively. We show in Fig. 4.5 the accuracy of Eq. (4.12) in fitting the void stacked density profiles. This functional form reproduces indeed very well the profile shapes for voids with different mean effective radii, especially when avoiding the most central regions of the underdensities.

4.5 Void-galaxy cross-correlation function

Let us now introduce a quantity closely related to the void density profile: the void-galaxy cross-correlation function, $\xi_{\rm vg}(r)$. The latter is associated to the probability of finding a galaxy at a comoving distance r from a void centre. It can be expressed in terms of the integrated void density contrast profile, computed in a void-centred sphere of radius r and volume V:

$$\xi_{\rm vg}(r) = \frac{1}{3r^2} \frac{\rm d}{{\rm d}r} [r^3 \, \Delta(r)] \,, \tag{4.13}$$

where

$$\Delta(r) = \frac{3}{r^3} \int^r u_{\rm v}(r') \, r'^2 {\rm d}r' \,, \tag{4.14}$$

and $u_{\rm v}(r)$ is the quantity defined in Eq. (4.11). At the first order, we can relate the void-galaxy cross-correlation function to the galaxy auto-correlation function (or 2PCF, see Sect. 2.1.2), $\xi_{\rm gg}(r)$, as:

$$\xi_{\rm vg}(r) = b_{\rm v} b_{\rm g} \; \xi_{\rm gg}(r) \,, \tag{4.15}$$

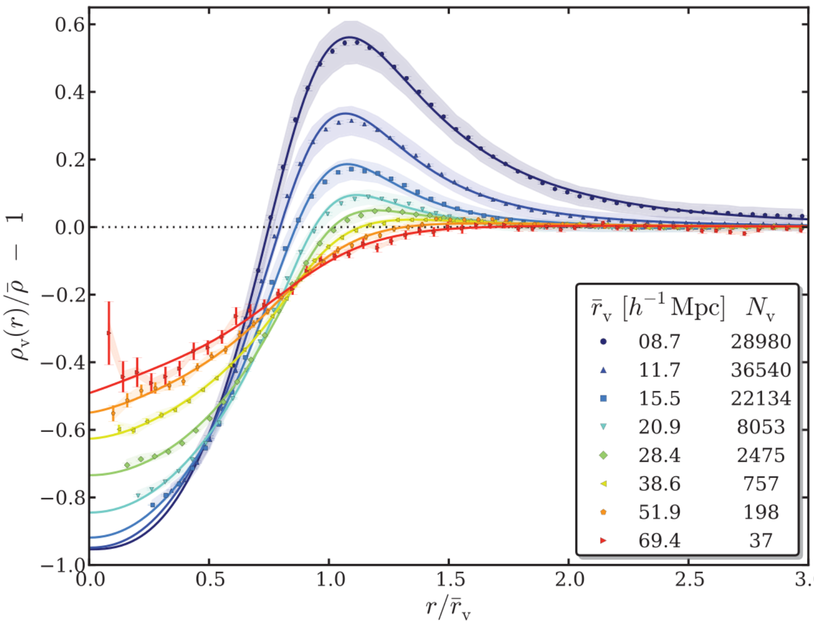

Figure 4.5: Stacked real-space density profiles of voids traced by mock galaxies at $z = 0$. The mean effective radii and void counts, $N_{\rm v}$, are indicated in the inset. The shaded regions represent the standard deviation σ within each of the stacks (scaled down by 20 for visibility), while the error bars show standard errors on the mean profile $\sigma/\sqrt{N_{\rm v}}$. The solid lines represent the individual best-fit solutions of the form reported in Eq. (4.12). Credits: Hamaus, Sutter & Wandelt (2014).

where b_g and b_v are the galaxy and void biases, respectively. Analogously to b_g, we can compute b_v as in Eq. (2.36), using the auto-correlation function of voids, $\xi_{vv}(r)$, in the numerator. The latter can be estimated with the same methods adopted for $\xi_{gg}(r)$, described in Sect. 2.1.5, using the positions of void centres as input data catalogue.

A different way to compute b_v is by using the *peak background split* (PBS) formalism (Sheth & van de Weygaert, 2004; Chan, Hamaus & Biagetti, 2019). We first define:

$$b_{\rm v}(r_{\rm v}) = 1 + \frac{\nu^2 - 1}{\delta_{\rm v}^{\rm L}} + \frac{\delta_{\rm v}^{\rm L}\,\mathcal{D}}{4\,\delta_{\rm c}^{\rm L\,2}\,\nu^2}\ , \tag{4.16}$$

where $\nu \equiv |\delta_{\rm v}^{\rm L}|/\sigma_{\rm v}$. Now we can obtain the (effective) void bias by weighting Eq. (4.16) with the void size function defined in Sect. 4.3:

$$b_{\rm v,eff} = \frac{\displaystyle\int \frac{{\rm d}n}{{\rm d}r_{\rm v}} b_{\rm v}(r_{\rm v})\,{\rm d}r_{\rm v}}{\displaystyle\int \frac{{\rm d}n}{{\rm d}r_{\rm v}}\,{\rm d}r_{\rm v}}\ , \tag{4.17}$$

where the integration is performed over the radii covered by the measured void size function. We will make use of these theoretical prescription in Chapter 9 in order to model the void power spectrum $P_{vv}(k)$, i.e. the Fourier transform of $\xi_{vv}(r)$.

4.6 Observational tests

A relatively novel approach aimed at extracting cosmological constraints from voids is the study of these objects as *standard spheres*. In analogy to what described for standard rulers (see Sect. 1.3.1), we can assume the average shape of voids to obey spherical symmetry. Let us stress the fact that, even if single void shape may appear elongated along a preferential axis or show strong irregularities near the edges, the average of a sufficiently high number of cosmic voids suppresses any individual asphericity. Therefore, we can consider stacked voids as standard spheres with which to probe the expansion history of the Universe: only if we assume the correct fiducial cosmological model in converting observed coordinates into comoving, then the stacked voids will appear spherically symmetric. This technique is commonly known as the Alcock-Paczyński (AP) test (Alcock & Paczynski, 1979). As we will see in Sect. 4.6.1, deviations of the mean shape from the spherical geometry can be physically modelled and are cosmology dependent, so their study constitutes a powerful method to test the cosmological model.

Nevertheless, dealing with real data, the peculiar motions of mass tracers (e.g. galaxies) lead to the breaking of the spatial symmetry along the line of sight of the observer. In particular, since the measured tracer redshifts deviate from the true ones, the derived shape of voids results modified by the so-called redshift-space distortions (RSD hereafter). Therefore, in order to successfully apply the AP test to voids, we need to accurately model the RSD affecting underdensity regions. Despite the complexity of this phenomenon on intermediate and small scales, i.e. where the nonlinear clustering is stronger, its modelling inside voids is in principle straightforward. Indeed, it has been shown that voids interiors are characterised by a laminar, single-stream outflow of mass tracers that is well described by linear theory (Hamaus, Sutter & Wandelt, 2014; Hamaus et al., 2014, 2015; Pisani, Sutter & Wandelt, 2015; Hamaus et al., 2016; Paz et al., 2013). We will provide in Sect. 4.6.2 the bases for the theoretical modelling of the RSD inside voids.

4.6.1 Geometric distortions

Let us consider a cosmic void formed by a number of mass tracers, neglecting for the moment their peculiar velocities. We can express the comoving separation, s, between the void centre and a mass tracer by decomposing it in parallel and transverse components:

$$s_{||} = \frac{c}{H(z)}\delta z \quad \text{and} \quad s_{\perp} = D_{\rm M}(z)\delta\theta \ , \tag{4.18}$$

where δz and $\delta\theta$ represent the redshift and the angular separations, respectively, while $D_{\rm M}$ is the angular-diameter distance we introduced in Eq. (1.36). Let us notice that when assuming space flatness (i.e. $\Omega_{0,\kappa} = 0$), the angular-diameter distance coincides with the comoving distance $D_{\rm C}$ at $z = 0$ (see Eq. 1.19). Now the main point is that these quantities depend on $H(z)$, so we need to assume a fiducial cosmological model to compute their values. Following the approach of e.g. Sánchez et al. (2017a), we can introduce two parameters that inherit the dependence on cosmology:

$$q_{||} \equiv \frac{s_{||}}{s^*_{||}} = \frac{H^*(z)}{H(z)} \quad \text{and} \quad q_{\perp} \equiv \frac{s_{\perp}}{s^*_{\perp}} = \frac{D_{\rm M}(z)}{D^*_{\rm M}(z)} \ , \tag{4.19}$$

where the starred quantities are those evaluated with the assumed fiducial cosmology. In the case where the latter coincides with the true cosmology, $q_{||}$ and $q_{\perp}$ are trivially both equal to unity. From the quantities in Eq. (4.19) we can derive the void-tracer separation:

$$s = \sqrt{q^2_{||} s^{*2}_{||} + q^2_{\perp} s^{*2}_{\perp}} \ . \tag{4.20}$$

In order to exploit the AP effect through the symmetry of stacked voids it is convenient to introduce the parameter:

$$\varepsilon \equiv \frac{q_{\perp}}{q_{||}} = \frac{D_{\rm M}(z)H(z)}{D^*_{\rm M}(z)H^*(z)} \ . \tag{4.21}$$

Indeed, in absence of an absolute scale (such as the BAO one) to compare with s, the parameters $q_{||}$ and $q_{\perp}$ remain degenerate while their ratio can be determined. However, void-centric distances are commonly expressed in units of the effective void radius, defined as the radius of a sphere having the same volume of the void. Since the observed void volume is proportional to $s^*_{||} s^{*2}_{\perp}$, the true value of void radius can be related to the fiducial one through the relation (Ballinger, Peacock & Heavens, 1996; Eisenstein et al., 2005b; Xu et al., 2013; Sánchez et al., 2017a; Hamaus et al., 2020; Correa et al., 2020):

$$R = q^{1/3}_{||} q^{2/3}_{\perp} R^* \ . \tag{4.22}$$

We will make use of these fundamental relations to correct the values of the void radii as a function of the assumed cosmology and thus extract unbiased cosmological constraints from the void size function (in Chapter 8) and from the void-galaxy cross-correlation function (in Sect. 9.1.1).

4.6.2 Dynamic distortions

As we introduced in Sect. 1.3, the main contribution on the observed redshift is given by the cosmological Hubble expansion, z_h. However, this quantity is affected also by the Doppler effect, which is caused by the peculiar motions of the cosmic tracers along the line of sight, $z_d = v_{||}/c$. Therefore we can express the total observed redshift, z, as:

$$1 + z = (1 + z_h)(1 + z_d) \ . \tag{4.23}$$

Then, since for cosmological distances z_d is much smaller than z_h, we can re-write the angular-diameter distance as in the following:

$$D_{\mathrm{M}}(z) \equiv \int_0^z \frac{c}{H(z')}\mathrm{d}z' \simeq D_{\mathrm{M}}(z_h) + cz_d\frac{1+z_h}{H(z_h)} \ . \tag{4.24}$$

Now, assuming the observer to be located at the origin of the coordinate system (z, θ, ϕ), we can transform $D_{\mathrm{M}}(z)$ into the comoving space vector $\mathbf{x}$ using:

$$\mathbf{x}(z,\theta,\phi) = D_{\mathrm{M}}(z)\begin{pmatrix} \cos\theta\cos\phi \\ \sin\theta\cos\phi \\ \sin\phi \end{pmatrix} \ . \tag{4.25}$$

Then, using $z_d = v_{||}/c$, Eq. (4.24) yields:

$$\mathbf{x}(z) \simeq \mathbf{x}(z_h) + \mathbf{v}_{||}\frac{1+z_h}{H(z_h)} \ , \tag{4.26}$$

where $\mathbf{v}_{||}$ is the projection of the velocity vector $\mathbf{v}$ along the line-of-sight, as represented in Fig. 4.6. Following the notation adopted in this figure, we indicate with lower-case letters the quantities related to the mass tracers and with upper-case letters those related to void centres. Therefore we denote with $\mathbf{X}$ and Z the void centre position and redshift, while with $\mathbf{x}$ and z the tracer position and redshift, respectively. To simplify the system we also assume the void centre to be along the observer line-of-sight and we use the distant-observer approximation to assume $\mathbf{X}$ and $\mathbf{x}$ to be parallel.

First, we consider the system in real space, i.e. the left-side part of Fig. 4.6. By definition, the peculiar motion of the mass tracers does not contribute to the value of observed positions, so $\mathbf{x}(z) = \mathbf{x}(z_h)$. We call $\mathbf{r}$ the vector connecting the void centre and the mass tracer positions, $\mathbf{r} \equiv \mathbf{x} - \mathbf{X}$, and analogously the relative velocity $\mathbf{u}$ between the two objects, $\mathbf{u} \equiv \mathbf{v} - \mathbf{V}$. Now, we analyse the system in redshift space, i.e. the right-side part of Fig. 4.6. In this case the Doppler effect is not neglected, so $z_d \neq 0$, and we can derive the observed spatial separation $\mathbf{s}$ between the void centre and the tracer by using Eq. (4.26):

$$\mathbf{s} \equiv \mathbf{x}(z) - \mathbf{X}(Z) \simeq \mathbf{x}(z_h) - \mathbf{X}(Z_h) + \frac{1+z_h}{H(z_h)}(\mathbf{v}_{||} - \mathbf{V}_{||}) = \mathbf{r} + \frac{1+z_h}{H(z_h)}\mathbf{u}_{||} \ . \tag{4.27}$$

Here we have adopted the approximation $(z_h) \simeq (Z_h)$, which is accurate to the $\mathcal{O}(10^{-3})$ on scales of $|\mathbf{r}| \sim \mathcal{O}(10)\ h^{-1}$Mpc and velocities of $|\mathbf{u}_{||}| \sim \mathcal{O}(10^2)$ km s^{-1} Mpc^{-1} (Hamaus et al., 2020). This approximation becomes exact when we perform a void-stacking procedure, averaging on different voids. Indeed, assuming the cosmological principle, we expect

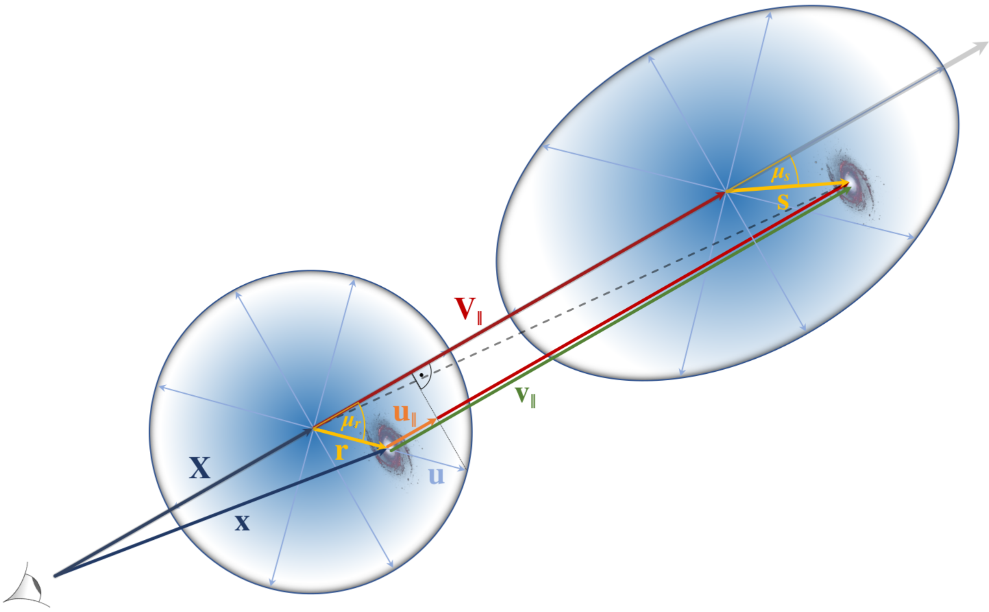

Figure 4.6: Void translation and deformation from real (left side) to redshift (right side) space. The comoving separation in real space, $\mathbf{r}$, between the void centre and the mass tracer can be converted in redshift space, $\mathbf{s}$, by considering the different velocity components of the system. Being the velocity displacements represented in units of $(1 + z_h)/H(z_h)$, the resulting relation between real- and redshift-space separations can be approximated as $\mathbf{s} = \mathbf{r} + \mathbf{u}_{||}$. Credits: Hamaus et al. (2020).

statistical homogeneity and isotropy such that $\langle \mathbf{u} \rangle = \langle \mathbf{u}_{||} \rangle = 0$ (see Ruiz et al., 2015; Lambas et al., 2016; Ceccarelli et al., 2016; Wojtak, Powell & Abel, 2016, for detailed studies on void inner and bulk dynamics).

Similarly to what happens for galaxy clusters, voids can be considered coherent extended objects moving with the background Hubble flow together with the mass tracers defining these systems. As represented in Fig. 4.6, this results in a translation of the observed centre of the system. However, the relative separation $\mathbf{s}$ between the mass tracers belonging to the void is not affected by their individual motion, but only by their relative velocity $\mathbf{u}_{||}$. Then, given the tendency of mass tracers to flow towards the outskirts of voids, their relative velocities with respect to the void centre lead to an observed stacked shape that results elongated along the line-of-sight.

In Chapter 8 we will introduce a semi-analytical methodology to account for the apparent elongation of voids in redshift space by rescaling consistently the void size function expected for the *Euclid* mission. Another approach is to follow the prescriptions of Hamaus et al. (2020) to model theoretically the RSD: we impose local mass conservation and consequently express the mass tracer velocity field with respect to the void centre as given by Peebles (1980):

$$\mathbf{u}(\mathbf{r}) = -\frac{f(z_h)}{3}\frac{H(z_h)}{1+z_h}\Delta(r)\,\mathbf{r}\ , \tag{4.28}$$

where $f(z)$ is the linear growth rate defined in Eq. (2.15) and $\Delta(r)$ is the average density contrast inside a spherical region defined in Eq. (4.14). We will adopt this methodology in Sect. 9.1.1 to relate the observed void-galaxy correlation function to its value in real space and extract cosmological forecasts for the *Euclid* mission.

4.7 Voids as cosmological probes

Redshift surveys (past, present and upcoming) have been designed to optimize the analyses of statistics related to overdensity regions, but leave on the other side cosmic depressions still under-explored. This is due to the demanding resources necessary to carry out a survey favorable to void science. Analogously to numerical simulations (see Sect. 2.3), the building of a redshift survey is a compromise between sky coverage and depth, which translates into large volumes and high tracer density. Voids exploitation would in principle require both these features: big volumes contribute in reaching a good statistic also for large voids, while high tracer density allows us to achieve an accurate reconstruction of void interiors together with the precise identification of the smallest underdensities. Having a deep survey would also imply the mapping of high-redshift regions, but for the study of cosmic voids this attribute is in fact less important since voids result shallower and harder to identify at high redshifts.

Despite the scarcity of large and complete void catalogues, in the last decades voids have started to become effective and competitive probes of Cosmology. Indeed, thanks to their formidable spatial extension and extremely low-density interiors, voids represent unique laboratories to perform astrophysical and cosmological tests. In particular, void inner parts are by definition almost devoid of matter, so the DE results dominant in these objects and regulates their expansion throughout the cosmic history. Therefore void sizes (Bos et al., 2012; Pisani et al., 2015; Pollina et al., 2016; Sahlén, Zubeldía & Silk, 2016; Verza et al., 2019, and see also Chapter 8 and Section 9.1.2) and observed shapes (Lee

& Park, 2009; Biswas, Alizadeh & Wandelt, 2010; Lavaux & Wandelt, 2012, and see also Sect. 9.1.1) represent high-sensitive statistics to the DE equation of state (see Sect. 3.1.1).

Moreover, voids constitute the perfect environment for investigating the implications of MG theories (see Sect. 3.1.2). Indeed, screening mechanisms operate weakly within cosmic voids, making them potentially more affected by the possible deviations from GR (Clampitt, Cai & Li, 2013a; Barreira et al., 2015; Voivodic et al., 2017; Falck et al., 2018; Sahlén & Silk, 2018; Sahlén, 2019; Perico et al., 2019, see also Chapter 7). These deviations are expected to modify void matter density profiles with respect to GR and can be revealed by measuring the lensing signal around voids (Spolyar, Sahlén & Silk, 2013b; Melchior et al., 2014; Cai, Padilla & Li, 2015; Barreira et al., 2015; Clampitt & Jain, 2015; Sánchez et al., 2017b; Baker et al., 2018; Davies et al., 2021). MG also enhances void expansion, which results in stronger RSD around voids (see e.g Achitouv et al., 2017). Finally, MG imprints are captured in environmental differences that can emerge in the comparison of the properties of galaxies belonging to over- and underdense regions (see e.g Hui, Nicolis & Stubbs, 2009; Zhao et al., 2010; Jain & VanderPlas, 2011; Jain, 2011; Cabré et al., 2012).

Voids are also particularly sensitive to neutrinos (see Sect. 3.1.3): the density fraction of neutrinos is more prominent in underdense regions compared to the high-density ones and the typical void size spans the range of neutrino free-streaming scale, which in turn depends on the neutrino mass (see Eq. 3.25). Indeed, both the void density profiles and void abundances have been shown to possess a great potential in constraining the neutrinos species total mass (see e.g. Massara et al., 2015; Sahlén, 2019; Kreisch et al., 2019b, 2021, and also Chapter 7).

Another strong point of cosmic voids is their complementarity to standard probes (Nadathur et al., 2020; Kreisch et al., 2021; Paillas et al., 2021). Voids represent indeed the negative density counterpart of galaxy clusters and feature those regions of the Universe that remain unexplored by other probes. This entails two important aspects: void statistics are almost independent of those of standard probes and lead to constraints that show high degrees of orthogonality with respect to other cosmological contours. These aspects are fundamental in the perspective of a joint analysis between voids and other probes, which represents a fundamental tool to disentangle the degeneracies between the estimated cosmological parameters. We will provide some insights on the potential of the synergy between voids and other cosmological probes in Chapter 8 and Sect. 9.2.

Chapter 5

Numerical tools to build cosmic void catalogues

In this chapter, we introduce the numerical tools employed for the preparation of the data analysed in this Thesis work. In particular, we will present the set of libraries used for all the cosmological calculations and the statistical treatment of the data. Finally, we will describe the numerical algorithms used to build and clean the samples of cosmic voids.

5.1 `CosmoBolognaLib`

The `CosmoBolognaLib`[1] is a large set of *free software* C++/Python libraries, that provide an efficient numerical environment for cosmological investigations of the LSS of the Universe (Marulli, Veropalumbo & Moresco, 2016). This software is particularly suited to handle with catalogues of astronomical objects, both real and simulated. Thanks to the large amount of functions implemented, the `CosmoBolognaLib` offers the necessary tools to analyse large data sets and to perform statistical analyses with optimised performances. In particular, in this Thesis work we make use of these libraries to manage catalogues in different formats, to measure and model the cosmic tracer bias and the void size function, as well as to perform Bayesian statistical analyses.

5.2 Void finders

Since there is not general concordance on the definition of voids yet, many different void finders have been proposed and exploited in the last decades (see Colberg et al. (2008) for a cross-comparison of the different techniques). Following the strategy of Lavaux & Wandelt (2010) we can classify void finding algorithms in three main classes, on the basis of the type of criterion applied:

- *Density criterion.* These algorithms define voids as regions empty of tracers or with local density below a fixed value (Elyiv et al., 2013; Micheletti et al., 2014). In this case tracers are divided in *wall tracers* and *field tracers* depending on the density

[1] `https://gitlab.com/federicomarulli/CosmoBolognaLib`

of the region in which they are located ("strongly overdense" regions and "mildly underdense" regions, respectively).

- *Geometrical criterion.* This class includes void finders that identify voids as geometrical underdense structures like spherical cells or polyhedra (Sutter et al., 2015; Platen, van de Weygaert & Jones, 2007; Neyrinck, 2008). In particular, these algorithms reconstruct a continuous 3D density field and search for the local density minima to obtain the void distribution.

- *Dynamical criterion.* These void finders are based on dynamical criteria in which tracers are not exploited to reconstruct underlying mass distribution but are used as test particles of the cosmic velocity field. Therefore, in these algorithms, a void is defined as a region from which the matter is evacuated (Forero-Romero et al., 2009; Lavaux & Wandelt, 2010; Elyiv et al., 2015).

Other algorithms are instead classified as "2D void finders" (Sánchez et al., 2017b; Cautun et al., 2018) since they operate on the distribution of mass tracers projected along the line of sight of the observer. They can be based on the three aforementioned methodologies and particularly suited for the study of weak lensing around void (see Davies et al., 2021, for a comparison between void finders applied to weak lensing analyses).

For the main analyses of this Thesis work we will make use of the Void IDentification and Examination toolkit (`VIDE`) (Sutter et al., 2015) to construct our void catalogues. `VIDE` belongs to the class of algorithms based on geometrical criteria and it implements an enhanced version of the ZOnes Bordering On Voidness (ZOBOV) algorithm (Neyrinck, 2008). ZOBOV is a popular publicly available code that finds density depressions in a 3D set of points, without any free parameter or assumption about the void shape. The void finding procedure consists of three main steps:

1. As a first step, the finder reads the tracer positions and associates to each tracer a cell of volume that is closer to it than to any other tracer. This technique is referred to as *Voronoi tessellation*, and the resulting cells are denoted *Voronoi* cells. Then the algorithm associates a density to each Voronoi cell that is, assuming equal weights for all particles, the inverse of the Voronoi cell volume. In this way we obtain a continuous and well-defined density field.

2. As a second step, local density minima are found and their surrounding basins identified. Density minima are defined as the cells whose density is lower than the density of every other adjacent cell (i.e. *natural neighbours*). A representation of this procedure is reported in Fig. 5.1. Then, starting from these density minima, the surrounding Voronoi cells are merged consecutively if their individual density is above the one of the previously merged cell. The process of merging is stopped once a cell of lower density is encountered. The result of this procedure is the creation of local density basins, called *zones*.

3. Finally, zones are merged to become voids making use of the so-called *watershed algorithm* (e.g. Platen, van de Weygaert & Jones, 2007). This method, illustrated in Fig. 5.2, consists of rising a density threshold starting from each zone local density minimum. During the raising, all the surrounding regions, that have a value of density lower than the threshold, are added to the basin of a starting minimum. As

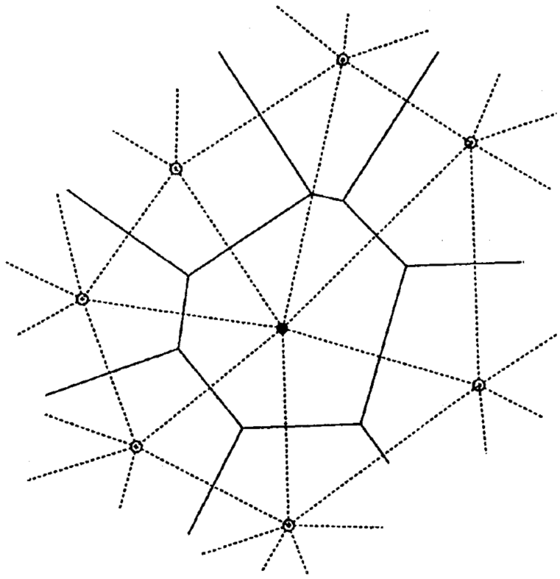

Figure 5.1: Natural neighbours of a local density minimum. The black dot represents the centre of a local density basin, while the open circles its natural neighbours, associated with higher density regions. The solid edges mark the Voronoi cell surrounding the central point, along with the connecting Voronoi edges. The dashed lines delineate instead the corresponding *Delaunay triangles*, whose centres are by definition the vertices of the Voronoi diagram. Credits: Platen, van de Weygaert & Jones (2007).

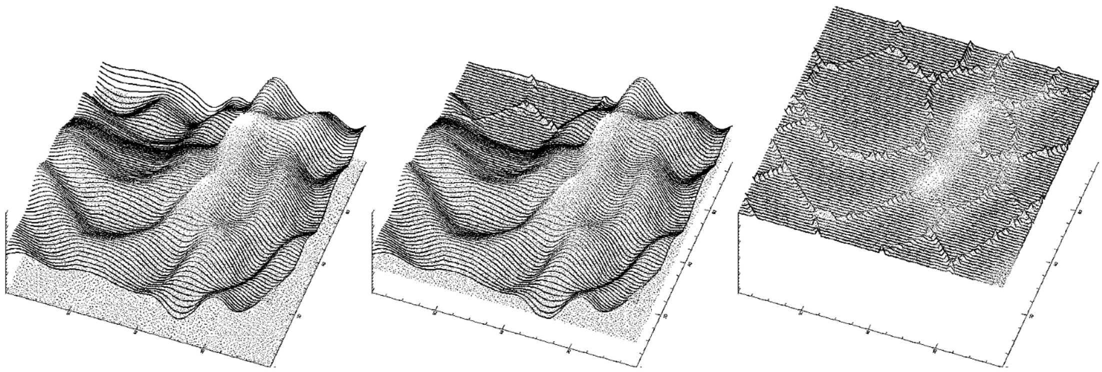

Figure 5.2: Principle of the watershed technique represented in three panels. The *left panel* shows the shape of the density field. Starting from the local minima, the surrounding basins of the surface start to flood as the water level continues to rise (dotted plane initially below the surface). Where two basins meet up near a ridge of the density surface, a "dam" is erected (*central frame*). Ultimately, in the *right frame* the entire surface is flooded, leaving a network of dams which defines a segmented volume and delineates the corresponding cosmic web. Credits: Platen, van de Weygaert & Jones (2007).

long as shallower zones are added to the original zone, the final void consists of all such merged zones, which are still recorded as its sub-voids. When a deeper zone is encountered, the process is stopped.

Therefore, the set of voids created with this technique is naturally organised with a hierarchical structure of nested voids. Each of the voids found with `VIDE` has its centre defined as volume-weighted barycentre, $\overline{X}$, of the N Voronoi cells that define the void,

$$\overline{X} = \frac{\sum_{i=1}^{N} \overline{x}_i V_i}{\sum_{i=1}^{N} V_i} \ ,$$

where $\overline{x}_i$ are the coordinates of the i-th tracer of that void, and V_i the volume of its associated Voronoi cell. The void radius, r_v, is calculated from the total volume of the void, V_v. The latter is defined as the radius of a sphere having the same volume of the void:

$$V_\mathrm{v} \equiv \sum_{i=1}^{N} V_i = \frac{4\pi}{3} r_\mathrm{v}^3 \ .$$

We underline that this centre does not necessarily coincide with the position of a tracer.

We briefly describe also the void finder based on dynamical criteria that will be presented in Sartori et al. (2022, in preparation), which is based on that presented in Elyiv et al. (2015) and is already implemented in the `CosmoBolognaLib`. We report in the following the main steps of the code.

1. The aim of the first step is to reconstruct dynamically the displacement field of cosmic tracers. This is performed exploiting the *Zel'dovich Approximation* (see Sect. 2.2.2), to reconstruct the initial tracers Lagrangian positions by randomising the Eulerian coordinates. In fact, the tracers positions are paired to the random ones such as the total action of the system is minimised. We obtain in this way the displacement field, which approximates the velocity field of cosmic structures.

2. The second step consists in converting the displacement field in a continuous divergence field by smoothing it with a Gaussian filter. Then the code finds the local minima in the divergence field, corresponding to density minima and also to the sources of maximum displacement. Therefore, cosmic voids are considered as *sinks* in the reverse streamlines of tracers.

3. Finally, once all the minima in the density field are identified, the algorithm provides a void catalogue, reporting their centres and radii.

In this algorithm the void centre is identified as the absolute minimum value of the divergence field within a void:

$$\mathbf{r}_\mathrm{v} = \min(\boldsymbol{\nabla} \cdot \mathbf{v})_\mathrm{v} \tag{5.1}$$

This type of procedure has the advantage of employing Lagrangian coordinates, which considerably reduces the *shot noise* problem, caused by the discrete mass tracers. Indeed, this algorithm does not need to perform the reconstruction of the density field. In Fig. 5.3 we show an application of this void finder. The code is applied on a box of DM particles at $z = 0$, from which the displacement is reconstructed. As expected, the tracer position is aligned with the maxima of the divergence field and the particle displacement is directed from the overdensities towards the underdensities.

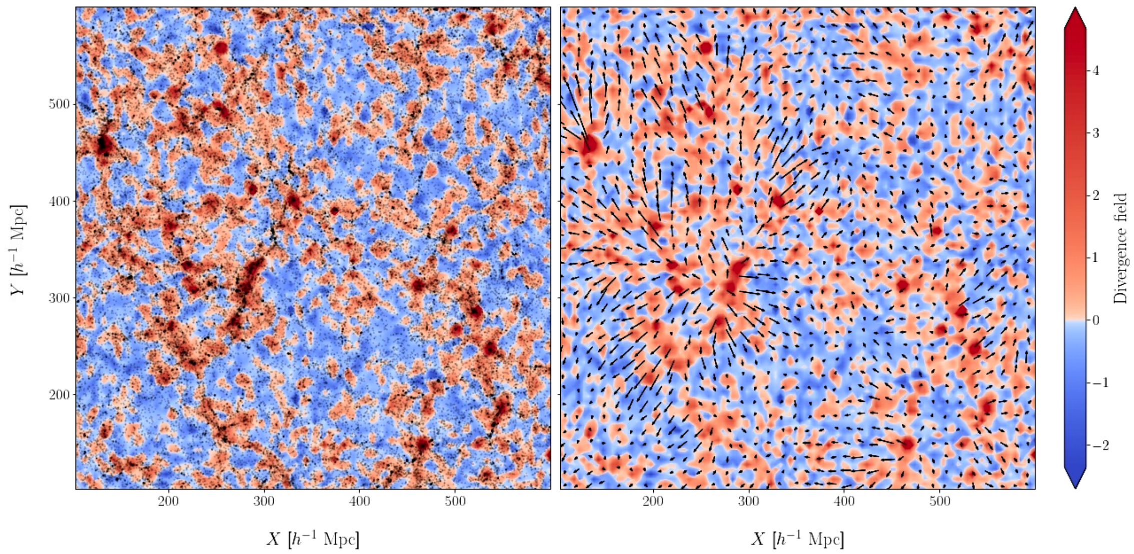

Figure 5.3: Example of reconstruction of the divergence field performed with the algorithm that will be presented in Sartori et al. (2022, in preparation). *Left*: superimposition with the tracer position. *Right*: superimposition with the reconstructed displacement field.

5.3 Cleaning algorithm

As already said, many different definitions of cosmic voids have been proposed during the years. It is thus particularly important to adopt the same definition when detecting voids and modelling their statistics or, alternatively, to clean properly the void catalogues detected with standard methods. This latter approach is the one that we choose to follow. As widely described in Ronconi & Marulli (2017), a new algorithm has been recently implemented in the `CosmoBolognaLib` environment to clean void catalogues and make them directly comparable to model predictions. It is important to highlight that the cleaning procedure is almost independent of the void finder adopted to build the catalogue, since only the positions of void centres are required. The cleaning algorithm can be divided in three main steps:

- The *spurious* voids are removed from the catalogue, with the following criteria: *(i)* voids whose effective radius does not belong to a selected range $[R_{\rm min}, R_{\rm max}]$ and *(ii)* voids whose central density is higher than $(1+\delta_{\rm v}^{\rm NL})\overline{\rho}$, where $\delta_{\rm v}^{\rm NL}$ is a given non-linear underdensity threshold, and $\overline{\rho}$ is the mean density of the sample. The last criterion is necessary to take into account the cloud-in-void phenomenon.

- The radius of voids is re-scaled: the algorithm considers the density profile of each void and, treating the void as a sphere located at its centre, the value of the radius is increased or decreased until the sphere reaches the selected density contrast $\delta_{\rm v}^{\rm NL}$.

- Check for overlaps: when two voids do overlap, i.e. when the sum of their radii is greater than the distance between their centres, the one of them with higher density contrast is rejected, avoiding double countings. This step is necessary also to account for void-in-void phenomenon.

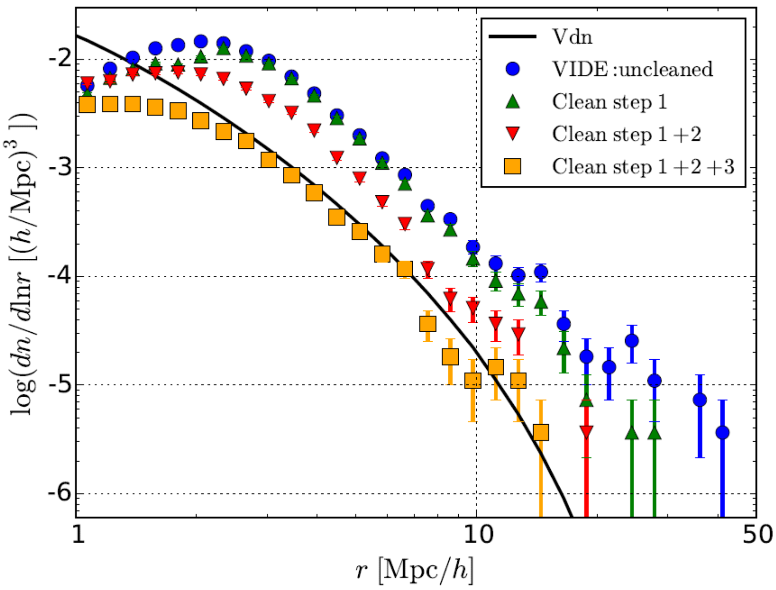

Figure 5.4: The effect of the different steps of the cleaning algorithm on the void size function. The blue dots show the size distribution of voids detected by VIDE from a ΛCDM N-body simulation. The green triangles, the red upside-down triangles and the orange squares are the size distribution of voids after the application of the first, second and third steps of the cleaning procedure, respectively. The theoretical void size function is reported as a black solid line and represents the Vdn model predictions for the considered cosmological model. Credits: Ronconi & Marulli (2017).

The effect of these steps on a void catalogue built with VIDE is reported in Fig. 5.4. The sample of voids is extracted from a ΛCDM N-body simulation with 256^3 DM particles and box side of length 128 h^{-1} Mpc. This procedure provides a set of spherical voids that enclose the shell-crossing density contrast, $\delta_v^{NL} = -0.795$ (see Sect. 2.2.1). The same value, in its linear expression, is used also to compute the theoretical predictions of the Vdn model (see Sec 4.3). This is crucial in order to standardize the outcome of void finders of different types, aligning the definition of voids to the one employed to derive the theoretical size function.

This cleaning procedure has been tested systematically by Ronconi et al. (2019), applying it on a set of N-body simulation snapshots at different redshifts. The DM simulations analysed have different resolution and boxside length. The results of these tests are shown in Fig. 5.5. The coloured symbols mark the void size distribution measured in the simulation snapshots, while the grey shaded region represents the model predictions for different values of the overdensity threshold δ_c[2]. We can see that the size distribution of voids is in agreement with the theoretical predictions.

[2]As we mentioned in Sect. 4.3, this value may in principle assume both the value of the turn-around or the collapse density contrast for overdensitities, so here is left to vary in the range $1.06 \leq \delta_c^L \leq 1.686$. From Fig. 5.5 we can appreciate that this threshold plays a major role only on very small scales, where the phenomenon of the cloud-in-void becomes important.

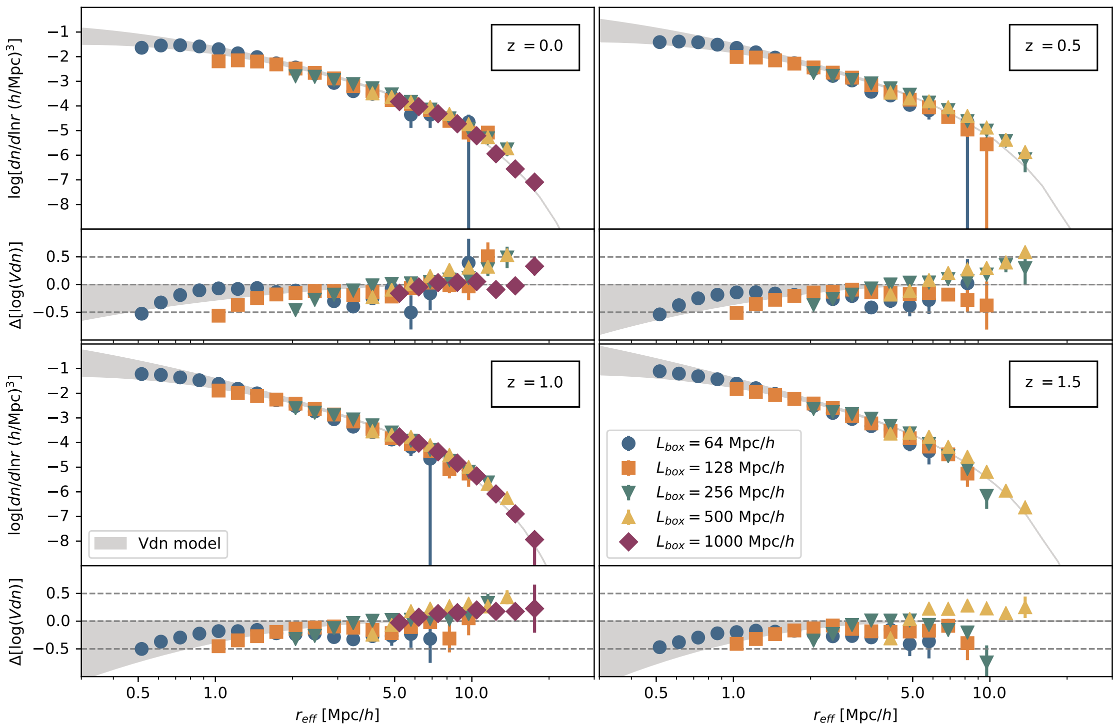

Figure 5.5: *Upper part of each panel*: Void size function prediction (grey shaded region) at four different redshifts (different panels) compared to the distribution of cosmic voids after applying the cleaning method described in Sect. 5.3 (different markers correspond to different simulations with box side L_{box}). *Lower part of each panel*: Logarithmic differences between the measured distribution and the Vdn model prediction. For the largest simulation ($L_{\text{box}} = 1000\ h^{-1}$ Mpc) only $z = 0$ and $z = 1$ are available, thus the corresponding abundances are missing from the $z = 0.5$ and $z = 1.5$ panels.

Chapter 6

Voids in biased tracers

To exploit cosmic voids as cosmological probes, their statistical properties have first to be modelled reliably (Nadathur & Hotchkiss, 2015a). In this chapter and in the following (Chapter 7 and Chapter 8) we will focus mainly on void abundances, i.e. on the void size function (see Sect. 4.3). As we have seen in Chapter 5, the theoretical model proposed by Sheth & van de Weygaert (2004) and lately modified by Jennings, Li & Hu (2013) allow us to accurately reproduce the number function of voids identified in unbiased simulated tracer catalogues as long as the void sample is properly prepared (see Sect. 5.3). However, when dealing with biased tracers of the density field, e.g. galaxies, galaxy clusters or DM haloes, this pipeline does not work anymore (see e.g. Jennings, Li & Hu, 2013). Indeed, it has been shown that the tracer bias plays a crucial role in determining the void profiles and size distributions (Sutter et al., 2014b; Nadathur & Hotchkiss, 2015a,b; Pollina et al., 2016, 2017, 2019). Having a solid model to account for the effect of the tracer bias is thus mandatory to extract robust cosmological constraints from void statistics.

In this chapter, we present the work we published in Contarini et al. (2019). Firstly, we propose and test an extension of the popular Vdn model (Eq. 4.10) to the case of voids identified in the distribution of biased tracers, providing a new parametrisation of the underdensity threshold of the Vdn model as a function of the large-scale linear bias of the tracers. This represents a crucial ingredient to extract cosmological constraints from the statistical distribution of voids detected from real galaxy or cluster catalogues, when no direct information on the DM field is available. Secondly, we investigate the cosmological constraints that can be inferred from the void size function at different redshifts and for different mass tracer selections.

6.1 CoDECS simulations

In this chapter we make use of simulated halo catalogues extracted from a set of the COupled Dark Energy Cosmological Simulations (CoDECS, Baldi, 2012). The selected snapshots derive from high resolution N-body simulations of the standard ΛCDM cosmology, performed with the `C-GADGET` module (Baldi et al., 2010). In particular, these simulations are built assuming a model consistent with seven-year Wilkinson Microwave Anisotropy Probe (WMAP7) constraints (Komatsu et al., 2011), with $\Omega_\Lambda = 0.7289$, $\Omega_\mathrm{m} = 0.2711$, $\Omega_\mathrm{b} = 0.0451$, $h = 0.703$, $n_s = 0.96$ and $A_\mathrm{s} = 2.194 \times 10^{-9}$, corresponding to $\sigma_8 = 0.809$. The CoDECS followed the dynamical evolution of $2 \cdot 1024^3$ particles: half of them are DM particles, while the other half is composed by non-collisional gas particles. Specifically, the catalogue covers a volume of 1 $(h^{-1}\ \mathrm{Gpc})^3$, with a mass resolution of $\sim 6 \times 10^{10}\ h^{-1}\ M_\odot$ for the DM particles.

To test the procedure described in Sect. 6.3, we built a set of DM halo catalogues using a FoF algorithm[1] (see Sect. 2.3.1), applying five different mass selection cuts: $2 \times 10^{12}, 2.5 \times 10^{12}, 5 \times 10^{12}, 7.5 \times 10^{12}, 10^{13}\ h^{-1}\ M_\odot$, at three different redshifts $z = 0,\ 0.55,\ 1$. These mass cuts[2] are applied to the FoF mass in order to inspect a sufficiently wide range of values for tracers' bias. The redshifts are chosen instead to span a significant fraction of cosmic time over which FoF haloes with masses greater than $10^{12}\ h^{-1}\ M_\odot$ are resolved. This range allows us to test the method on haloes corresponding to common density peaks (low redshifts, low masses) and on newly forming haloes corresponding to rare density peaks. The results obtained for the halo catalogues with $M_{\rm min} = 2.5$ and $7.5 \times 10^{12}\ h^{-1}\ M_\odot$ are consistent with the ones of the other catalogues, and do not add any relevant information to the overall outcome of the chapter. Thus, we will not show them in the figures of this chapter, with the only exception of Fig. 6.6.

6.2 Data preparation

We build the void catalogue by means of the void finder `VIDE`, described in Sect. 5.2. Then we apply the pipeline introduced in Ronconi & Marulli (2017) (Sect. 5.3) to the candidate list of underdensities identified by `VIDE` to make them directly comparable to the Vdn model predictions. In particular, the effect of the cleaning procedure is to reshape the selected voids as spherical non-overlapping regions, centred on density depths of the tracer density field, embedding a fixed density contrast $\delta_{\rm v}^{\rm NL}$ (see Sect. 4.1). Our choice of modelling the underdensity regions as spheres is aimed at comparing void statistics directly to theoretical models based on the spherical evolution (see Sect. 2.2.1). We stress the fact that we do not need to reconstruct accurately the real shape of individual voids. Although real voids are not spherical objects, the mean void ellipticity is small in standard cosmological frameworks (see e.g. Verza et al., 2019). We can thus reasonably assume that the voids' geometry is spherical on average (Lavaux & Wandelt, 2012).

As a consequence of the cleaning procedure, the void number counts result lower with respect to the original output of `VIDE`. Moreover, as it can be seen from Table 6.1, (*i*) the total number of void counts tends to decrease for tracer catalogues with higher mass selections due to the lowering of the resolution, and (*ii*) the void radii are shifted towards higher values because of the consequent reduction of the mean mass density.

Another important step in the data preparation is the removal of the spatial scales affected by the low resolution of the tracer catalogue. Tracer sparsity leads to a drop of counts for small voids in the measured void size function (Sutter et al., 2014a; Jennings, Li & Hu, 2013; Ronconi et al., 2019; Verza et al., 2019). In particular, the incompleteness depends on the mean separation of the tracers used to identify the voids, therefore on the spatial resolution of the catalogue, as we saw in Figs. 4.4 and 5.5. This scale selection

[1] The algorithm makes use of a linking length $\ell = 0.2\,\overline{d}$, gathering the DM particles as primary tracers of the local mass density, and then attaching baryonic particles to the FoF group of their nearest neighbour.

[2] Other methods to measure halo masses were applicable in this case, e.g. using spherical overdensity masses (see Sect. 2.3.1). Anyway, the mass-cut criterion, as well as the redshift selection, are not relevant in our work and do not influence the outcomes of this chapter.

Table 6.1: Void counts in 5 logarithmic bins of void effective radii, $\overline{R}_{\rm eff}$, in the range [18–60] h^{-1} Mpc, for DM halo catalogues with different mass and redshift selections, after the cleaning procedure has been applied.

$z = 0.00$						
		$\overline{R}_{\rm eff}$ $[h^{-1}$ Mpc$]$				
		20.5	26.0	33.1	42.1	53.6
$M_{\rm min}$ $[h^{-1}\ M_\odot]$	$N_{\rm tot}$	$N(\overline{R}_{\rm eff})$				
2×10^{12}	1063	719	288	53	3	0
5×10^{12}	1007	544	333	115	15	0
10^{13}	803	291	309	160	39	4
$z = 0.55$						
		$\overline{R}_{\rm eff}$ $[h^{-1}$ Mpc$]$				
		20.5	26.0	33.1	42.1	53.6
$M_{\rm min}$ $[h^{-1}\ M_\odot]$	$N_{\rm tot}$	$N(\overline{R}_{\rm eff})$				
2×10^{12}	1053	690	301	56	6	0
5×10^{12}	943	444	356	120	22	1
10^{13}	693	196	256	176	49	7
$z = 1.00$						
		$\overline{R}_{\rm eff}$ $[h^{-1}$ Mpc$]$				
		20.5	26.0	33.1	42.1	53.6
$M_{\rm min}$ $[h^{-1}\ M_\odot]$	$N_{\rm tot}$	$N(\overline{R}_{\rm eff})$				
2×10^{12}	1090	698	314	72	6	0
5×10^{12}	850	370	301	146	33	0
10^{13}	557	140	170	156	77	14

therefore is a fundamental requirement when exploiting the void size function for deriving cosmological constraints: it is crucial to avoid contamination from poorly sampled spatial scales to obtain unbiased results but, at the same time, it is important to preserve the void number counts to avoid loss of signal and maximise the constraining power of this statistics. Nevertheless, modelling the drop of counts for small voids is not trivial. To avoid falling in this regime, we conservatively exclude from the analysis voids with radii falling in the range of scales affected by incompleteness.

In this chapter we adopt the conservative choice to reject voids with $R_{\rm eff} < 2.5$ times the mean separation between the tracers of the corresponding tracer catalogue. We will call this quantity the mean particle separation (MPS), meaning with "particle" whatever time of mass tracers. The factor 2.5 is chosen empirically based on the drop of void counts and on the steep departure from the theoretical model. In future works, different approaches will be explored to improve the void selection also at small radii: among these, the application of machine learning techniques (Cousinou et al., 2019) is promising to carefully remove only spurious voids and consequently enhance the performance of the void size function as a cosmological tool.

6.3 A new extension of the Vdn model

Dealing with mass tracers, the effect of the tracer bias has to be taken into account to extract accurate cosmological constraints from the void number counts (see e.g. Pollina et al., 2017, 2019). Let us assume a cosmic void whose profile can be traced by both DM particles and biased mass tracers. Looking at the density contrast inside a void-centred sphere we have, at least in the internal parts of the void, a deeper density profile measured with biased tracers with respect to the one measured in the DM particle field. This is illustrated in Fig. 6.1, which shows the spherically-averaged void density profiles[3] as traced by either DM or DM haloes with different biases, at three different redshifts. We can also notice that, rescaling the sample of voids identified in different biased tracer field to the same density contrast, the corresponding mean effective radius increases with the minimum mass of the sample (i.e. with the tracer bias).

After these observations, a possible solution to predict the abundance of voids in biased tracer fields seems to be a bias-dependent underdensity threshold: we can find the internal density contrast $\delta^{\rm NL}_{\rm v,tr}$ at which the void radii have to be rescaled to match the threshold $\delta^{\rm NL}_{\rm v,DM}$, converted in linear theory, imposed in the void size function model. Given that the DM density field within voids is linearly related to the density field traced by biased tracers (Pollina et al., 2019), we find:

$$\delta^{\rm NL}_{\rm v,tr} = b\,\delta^{\rm NL}_{\rm v,DM}\ . \tag{6.1}$$

However, it is evident that for $b > 1$ the density contrast may assume values too low to be reached, unless we rescale the radii to the very central parts (usually excluded because of the minimum spatial resolution required to not be dominated by Poisson noise), as we can see in Fig. 6.1. For large values of the tracer bias and deep underdensity thresholds,

[3]All the void profiles with effective radii, $R_{\rm eff}$, larger than 2 MPS are stacked in these plots. As a result of the cleaning procedure, which rescales every void radii at the same level of density contrast, the profiles do not show a clear dependence on the void effective radius and they are therefore averaged together.

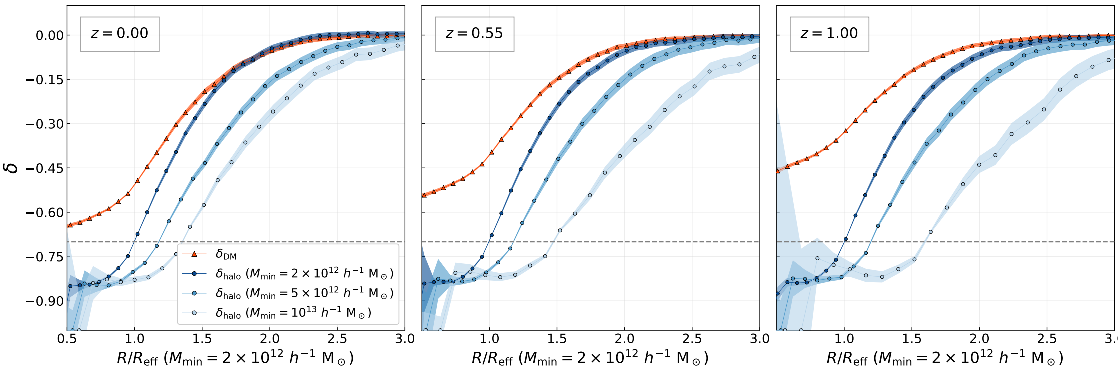

Figure 6.1: Spherically-averaged density profiles measured from the centres of voids identified in the tracer distribution at redshifts $z = 0$ (*left*), $z = 0.55$ (*centre*), $z = 1$ (*right*). The red lines represent the median of the profiles computed in the DM particle distribution, while the blue ones indicate the profiles in the DM halo catalogues with different mass-cuts. The horizontal dashed line indicates the value of the density contrast threshold ($\delta^{\rm NL}_{\rm v,tr} = -0.7$) selected in the cleaning procedure. All the profile radii are rescaled to the mean effective radius of the catalogue with $M_{\rm min} = 2 \times 10^{12}\ h^{-1}\ M_\odot$, in order to show the effect of the rescaling procedure of the cleaning algorithm. The shaded areas represent 2σ confidence regions, that is 2 times the standard deviation of the distribution of the mean values.

the rescaling may even imply a nonlinear void internal density < -1, which is physically unreachable.

We conclude that is not possible to perform this technique to rescale the void radii in the case of biased tracers. For this reason, we adopt the opposite approach to select a value of density contrast in the rescaling procedure, fixing the threshold in the tracer distribution, and derive from it the correspondent threshold in the DM field to be used in the theoretical model. We describe below the guidelines of our procedure.

First, we rescale all the voids found in the tracer catalogues to an effective radius such that the spherically-averaged density contrast they contain is equal to a fixed value $\delta^{\rm NL}_{\rm v,tr}$. It is important to notice that the choice to rescale the void radii to this specific density contrast is not universal. Every negative density threshold $-1 < \delta^{\rm NL}_{\rm v} < 0$ is allowed in principle, provided that the same value, converted to linear theory, is used in the theoretical size function. The selection of the void threshold is based on the following reasoning: on the one hand the more negative the threshold, the more the identified underdensities are free of contamination by Poisson noise (see also Neyrinck, 2008; Cousinou et al., 2019, for a discussion on spurious voids and possible treatments) and the stronger the impact of the cosmology on the void size function; on the other hand, an excessively negative threshold entails both a low statistic and a higher uncertainty in the rescaled void radius, caused by the sparsity of galaxies tracing such extreme underdense regions. For the analysis described in this chapter, we selected the threshold $\delta^{\rm NL}_{\rm v,tr} = -0.7$, which ensures a good compromise on the aforementioned effects.

Second, we assume that voids identified in the DM particle and in the biased tracer field are equal in number (neglecting those scales affected by different spatial resolutions), and that their centre positions are approximately the same[4]. Since the Vdn model can

[4]We tested this hypothesis using a catalogue of voids identified in the DM density field and cleaning

predict the number of voids with a certain radius, the simplest procedure to apply is to rescale the theoretical size function dividing the chosen threshold by the bias value:

$$\delta_{\mathrm{v,DM}}^{\mathrm{NL}} = \frac{\delta_{v,\,\mathrm{tr}}^{\mathrm{NL}}}{b} \text{ , with } \delta_{\mathrm{v,tr}}^{\mathrm{NL}} = -0.7 \,. \tag{6.2}$$

To use the rescaled threshold in the Vdn model, we convert $\delta_{\mathrm{v,DM}}^{\mathrm{NL}}$ to its linear counterpart with the fitting formula provided by Bernardeau (1994):

$$\delta_{\mathrm{v,DM}}^{\mathrm{L}} = \mathcal{C}\left[1 - (1 + \delta_{\mathrm{v,DM}}^{\mathrm{NL}})^{-1/\mathcal{C}}\right] , \tag{6.3}$$

with $\mathcal{C} = 1.594$. This equation is exact for models with null cosmological constant Λ, and is a good fit for any values of Λ, especially for the underdense regions. The quantity obtained, $\delta_{\mathrm{v,DM}}^{\mathrm{L}}$, has to be entered in Eqs. (4.4) and (4.5). We will analyse in details in the next sections the characteristics of the quantity b reported in Eq. (6.2), representing the value of the tracer bias measured inside voids.

This procedure is basically equivalent to expand the radii of voids identified in the DM field (embedding the same density contrast -0.7), predicted by the Vdn model, up to the same radius of the ones identified in the tracer field. In this way, we are able to compute a theoretical void size function model that takes into account the effect of the bias[5], which in practise causes a shift in the number count predictions toward higher void radii.

6.4 Bias of tracers in overdensity and underdensity regions

As seen in Sect. 2.1.4, the bias of cosmic tracers is a nonlinear stochastic function described by the conditional probability of tracer density contrast, δ_{tr}, given the mass density contrast δ_{DM} (see e.g. Desjacques, Jeong & Schmidt, 2018, for an extensive review). This is shown in Figs. 6.2 and 6.3, where the density contrast of a halo catalogue analysed in this chapter ($M_{\mathrm{min}} = 2 \times 10^{12}\ h^{-1}\ M_\odot$ at $z = 0$) is plotted against the corresponding DM density contrast, smoothing the density field at 1000 random positions with top-hat spherical filters with different radii. In Fig. 6.2, we show that the data are well fitted by a second-order polynomial. However, looking at Fig. 6.3 we can see that a linear model is accurate enough to describe separately the points in the overdensity and in the underdensity regions. Indeed, fitting all the points with a second-order polynomial the reduced chi square is $\tilde{\chi}^2 = 1.977$, while fitting $\delta_{\mathrm{DM}} > 0$ and $\delta_{\mathrm{DM}} < 0$ separately with a linear relation we obtain $\tilde{\chi}^2 = 1.758$ and $\tilde{\chi}^2 = 2.780$, respectively. The slope of the former, $b\,[\delta_{\mathrm{DM}} > 0]$, represents the linear bias that can be approximately inferred e.g. from the

it using the corresponding distribution of DM haloes as tracer. The results obtained are in agreement with the ones found with the voids identified in the biased tracer distribution. Therefore this assumption can be considered statistically valid, even if the correspondence between void centres identified by `VIDE` in different mass density fields is not always exact because of the uncertainties related to a sparser tracer distribution.

[5] A new algorithm to rescale the void size function model as a function of the tracer bias has been implemented in the `CosmoBolognaLib`. The code requires in input the values of the radii at which the model is computed, the redshift of the sample, the size function model to use (e.g. SvdW, Vdn) and the effective bias of the catalogue, b_{eff}. The latter can be automatically converted to $\mathcal{F}(b_{\mathrm{eff}})$ using the relation that will be calibrated in this chapter (see Sect. 6.5). Moreover, a python notebook is provided to explain, step by step, how to clean a void catalogue, and how to measure and model the void size function, according to the method described in this chapter.

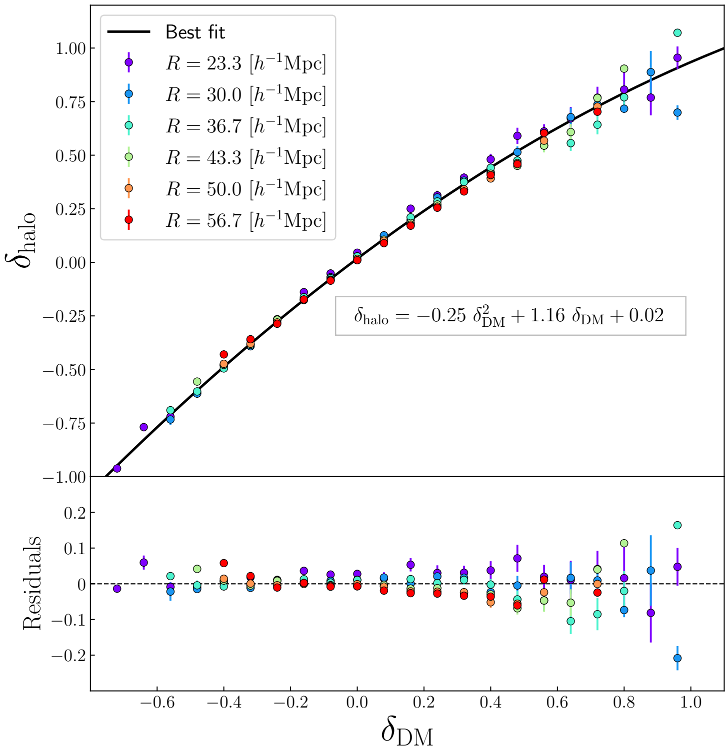

Figure 6.2: Relation between the density contrast computed in the DM distribution ($\delta_{\rm DM}$) and in the tracer distribution ($\delta_{\rm halo}$). The data points are computed as the spherically-averaged density contrast for 1000 random positions in the halo catalogue with $M_{\rm min} = 2 \times 10^{12}\ h^{-1}\ M_\odot$ at $z = 0$, for 6 radius bins. The different colours refer to the different radius sizes of the spheres used to compute the density contrast. In the *upper panel* the data are computed as the median of the values of $\delta_{\rm halo}$ in different bins of $\delta_{\rm DM}$, with error bars computed as the ratio between the standard deviation and the square root of the number counts in each bin. The points are fitted with a second-order polynomial, whose equation is reported in the insert and represents the nonlinear bias function. In the *lower panel* are reported the residuals from the quadratic fit.

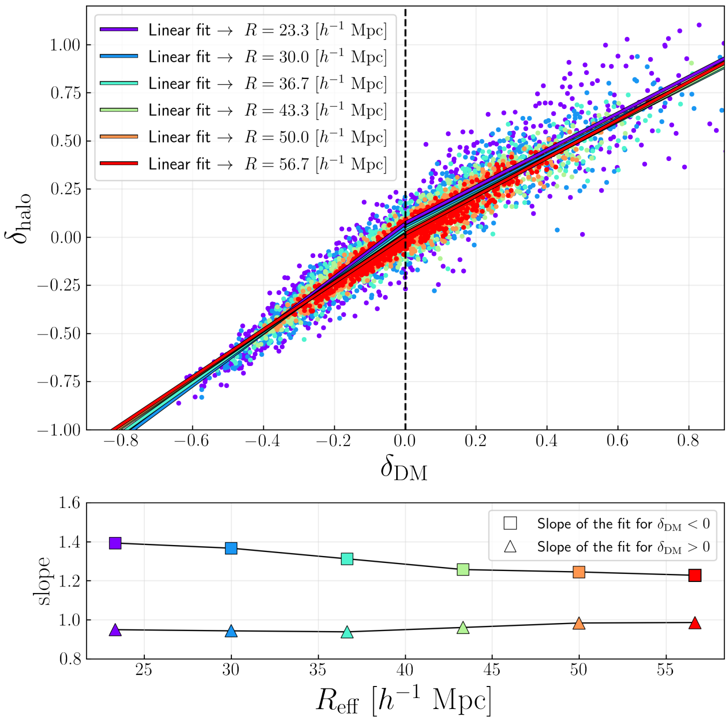

Figure 6.3: Same data as the Fig. 6.2, but without binning the quantity $\delta_{\rm DM}$. In the *upper panel* the points with $\delta_{\rm DM} > 0$ and $\delta_{\rm DM} < 0$ of each radius bin are fitted separately with a linear relation. In the *lower panel* is shown the variation of the slope of each fit as a function of the radius of the sphere used to compute the averaged density contrast.

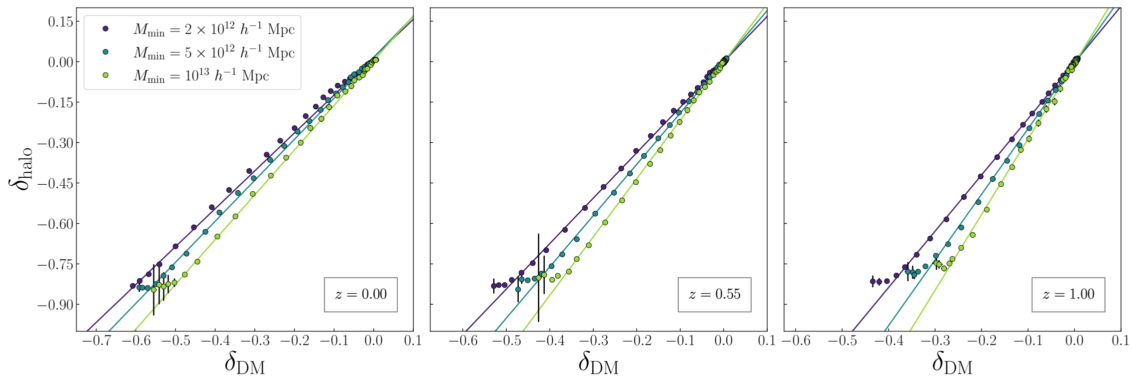

Figure 6.4: The ratio of the stacked density profiles shown in Fig. 6.1, i.e. $\delta^{\rm NL}_{\rm v,DM}$ as a function $\delta^{\rm NL}_{\rm v,tr}$, at redshifts $z = 0$ (*left*), $z = 0.55$ (*centre*), $z = 1$ (*right*). Different colours correspond to the halo catalogues with $M_{\rm min} = 2 \times 10^{12}\ h^{-1}\ M_\odot$ (in violet), $M_{\rm min} = 5 \times 10^{12}\ h^{-1}\ M_\odot$ (in blue) and $M_{\rm min} = 10^{13}\ h^{-1}\ M_\odot$ (in green). The black error bars represent the 1σ uncertaintiy. As expected, the slope of the fit becomes steeper (i.e. the value of bias inside voids increases) with the redshift and with higher mass-cuts.

tracer large-scale 2PCF (see Sect. 2.1.2). The slope of the latter, $b\ [\delta_{\rm DM} < 0]$, represents approximately the bias of the tracers inside cosmic voids, which is the value we actually need in order to properly rescale the void size function, as we will explain in the next section. As shown in Fig. 6.3, $b\ [\delta_{\rm DM} < 0] > b\ [\delta_{\rm DM} > 0]$.

Moreover, the behaviour of $b\ [\delta_{\rm DM} < 0]$ computed in void-centred spheres is shown in Figure 6.4, where different tracer bias values (i.e. different $M_{\rm min}$ values of the halo sample) and redshifts are analysed. In particular, we can further notice that $b\ [\delta_{\rm DM} < 0]$ is well-represented by a linear relation, especially at an intermediate distance from the void centre, i.e. excluding the innermost and the outermost parts of the void density profile. Then, it emerges how the value of $b\ [\delta_{\rm DM} < 0]$ increases with the tracer large-scale bias and the redshift of the void sample. These results are consistent with those of Pollina et al. (2017), who first performed this kind of analysis.

Since $b\ [\delta_{\rm DM} < 0]$ is generally not directly measurable, we shall calibrate a relation between $b\ [\delta_{\rm DM} > 0]$ and $b\ [\delta_{\rm DM} < 0]$ to be able to model the size function of voids detected from real tracer catalogues. Specifically, we search for a relation between the effective linear bias of the tracers used to detect cosmic voids, $b_{\rm eff} \sim b\ [\delta_{\rm DM} > 0]$ (that we measure from the tracer 2PCF at large scales, as described in Appendix A), and the linear bias of tracers *inside* the detected voids. A convenient estimate of the latter can be assessed through the ratio between $\delta^{\rm NL}_{\rm v,halo}$ and $\delta^{\rm NL}_{\rm v,DM}$ at a distance of $R_{\rm eff}$ from void centres:

$$b_{\rm punct} \equiv \left\langle \frac{\delta^{\rm NL}_{\rm v,tr}(R = R_{\rm eff})}{\delta^{\rm NL}_{\rm v,DM}(R = R_{\rm eff})} \right\rangle . \tag{6.4}$$

The *punctual bias* given by Eq. (6.4) characterises the relation between the density contrast measured in the tracer field and in the DM field *punctually*, i.e. at $R = R_{\rm eff}$. Since in our analysis the value of $\delta_{\rm halo}(R_{\rm eff})$ is fixed at -0.7, then $\delta_{\rm DM}(R_{\rm eff})$ is exactly the value we need to rescale the void size function model (see Sect. 6.3).

6.5 Results: calibration on the data

Figure 6.5 shows the ratio between the density contrast of haloes and DM, $\delta_{\rm halo}/\delta_{\rm DM}$, measured at $R = R_{\rm eff}$ and averaged over voids of similar effective radii, together with their weighted average values (Eq. 6.4), $b_{\rm punct}$, for all the considered simulated catalogues. In other words, in this figure the points are obtained by computing the ratio $\delta^{\rm NL}_{\rm v,tr}(R = R_{\rm eff})/\delta^{\rm NL}_{\rm v,DM}(R = R_{\rm eff})$ for each void of the catalogues (with $R_{\rm eff}$ being the effective radius of that specific void) and binning the result as a function of $R_{\rm eff}$. Then, to compute the value of $b_{\rm punct}$, we perform a weighted fit of these data with a constant. For comparison, we show also the effective tracer bias, $b_{\rm eff}$, estimated from the 2PCF at large scales, as explained in Appendix A. As shown in Fig. 6.5, the $\delta_{\rm halo}/\delta_{\rm DM}$ ratio tends to $b_{\rm eff}$ at large radii, in agreement with the results obtained by Pollina et al. (2017, 2019). Despite some dependencies on the effective void radius, especially at small scales (where the effects of the spatial resolution start to play a role), we find that an average constant value of $b_{\rm punct}$ is sufficient to properly rescale the void size function, as we will show in Sect. 6.6.

To apply this methodology to real data catalogue we have to consider that, in most of the cases, it is not possible to infer the underlying DM distribution inside voids. So it is worth to search for a relation between $b_{\rm punct}$ and $b_{\rm eff}$, since the latter can be accurately estimated e.g. from clustering measurements. This relation is displayed in Fig. 6.6. As it can be seen, the data can be well fitted by a simple linear model.

However, the $b_{\rm punct}$ values estimated for the halo catalogues with the higher minimum mass tend to systematically depart from the fit, especially at high redshifts. The reason of this slight deviation is, at least partially, related to the method used to find the void centres. In fact, if the detected voids are traced by too few tracers, the `VIDE` method might not be sufficiently accurate to localise their centres. This issue becomes more relevant at high redshift, where the void are shallower and their density minima are more difficult to identify. Computing the spherically-averaged density contrast starting from a point that is not a local minimum of the density field causes systematic errors in the bias measurements. This is a natural consequence of the cleaning procedure: when rescaling the void radii, the selected threshold might be reached at smaller radii if overdense regions are included in the measurement, due to a bad centring. This is an issue especially for catalogues with a high mass selection.

As a possible strategy to alleviate the problem, is to repeat our bias measurements using in all cases the centre positions of the voids detected in the catalogues with the lowest mass-cut. We will refer to this method as our *best-centring* technique, and we will call $b_{\rm punct}$ (bc) the corresponding bias. As shown in Fig. 6.6, these bias values (shown as coloured circles) are in better agreement with a linear model. Therefore we use them to calibrate the relation between the bias and the one computed inside cosmic voids, expressed in the following form:

$$b_{\rm punct}\ ({\rm bc}) = B_{\rm slope} \cdot b_{\rm eff} + B_{\rm offset}\,, \tag{6.5}$$

for which we found the values $B_{\rm slope} = 0.854 \pm 0.007$ and $B_{\rm offset} = 0.420 \pm 0.010$, representing the slope and the offset of the linear fit reported in Fig. 6.6, respectively. This relation can be used to estimate the bias of the tracers inside voids from the effective bias of the whole tracer population. Hereafter, the bias obtained using Eq. (6.5) will be called

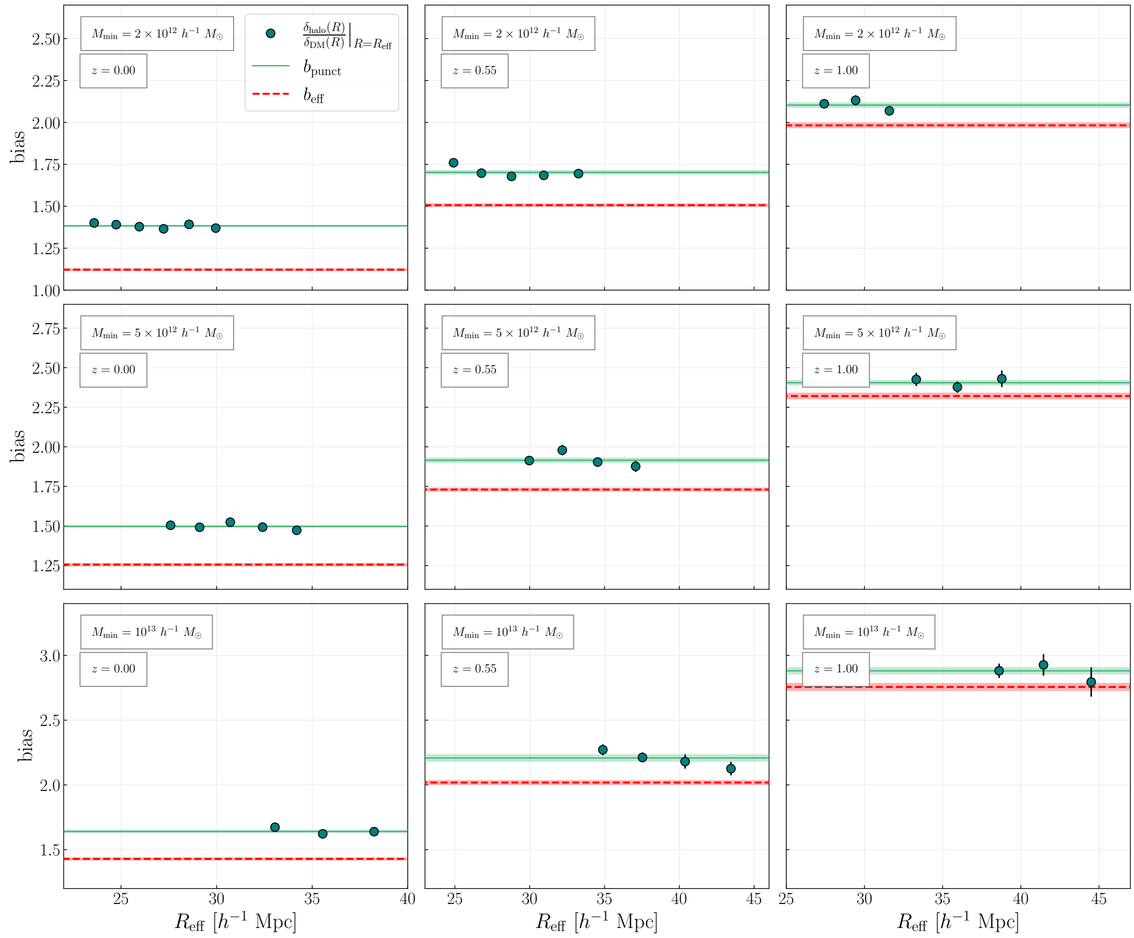

Figure 6.5: Measure of the tracer bias estimated as the ratio between the density contrast computed in the halo ($\delta_{\rm halo}$) and in the DM ($\delta_{\rm DM}$) density fields, at a distance of 1 $R_{\rm eff}$ from the void centres. The different panels show the results obtained from the halo catalogues with $M_{\rm min} = 2 \times 10^{12}\ h^{-1}\ {\rm M}_\odot$, $5 \times 10^{12}\ h^{-1}\ {\rm M}_\odot$ and $10^{13}\ h^{-1}\ {\rm M}_\odot$ (columns from *left* to *right*), at redshifts $z = 0$, $z = 0.55$, $z = 1$ (rows from *top* to *bottom*). The dark green points indicate the median of the ratio for different radius bins, with error bars representing the 1σ uncertainty. The green lines are the weighted fit of the data, $b_{\rm punct}$, while the red dashed lines show the effective bias, $b_{\rm eff}$. The shaded regions show the 1σ errors on the bias values.

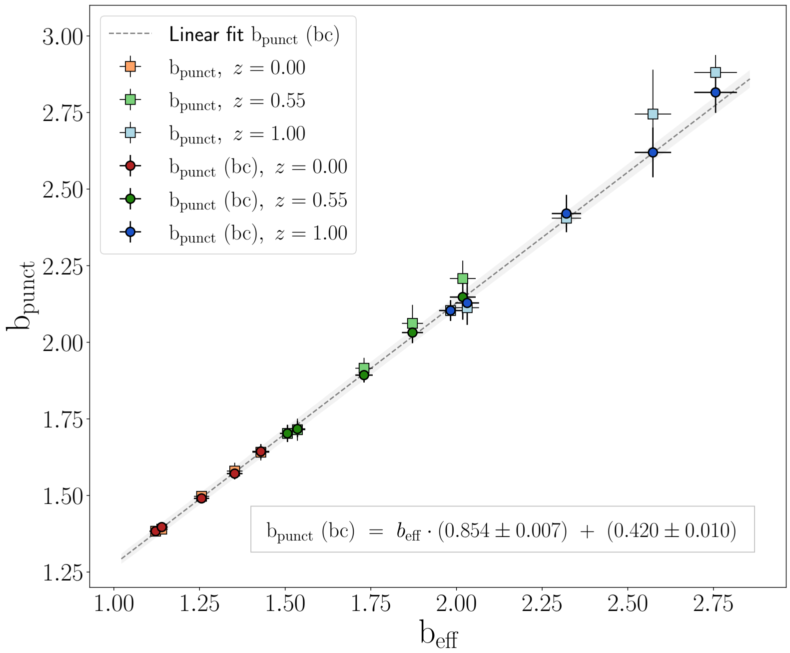

Figure 6.6: Relation between the effective bias, b_{eff}, and the bias measured inside voids, b_{punct}, at different redshifts. The points correspond to the data reported in Table 6.2, with 1σ errors. The squares are the values of b_{punct}, obtained with the method presented in Fig. 6.5, while the circles are estimated with the *best-centring* technique and correspond to $b_{\text{punct}}(\text{bc})$. The black line is the linear fit of the $b_{\text{punct}}(\text{bc})$ values. The best-fit parameters are reported in the label in the lower right corner.

Table 6.2: The values of the bias with 1σ uncertainties measured in the overdensity, $b_{\rm eff}$, and in the underdensity regions, $b_{\rm punct}$ and $b_{\rm punct}$ (bc), for all halo mass selections and redshifts analysed in this chapter.

$M_{\rm min}$ [h^{-1} $M_\odot$]	$z = 0.00$		
	$b_{\rm eff}$	$b_{\rm punct}$	$b_{\rm punct}$ (bc)
2×10^{12}	1.122 ± 0.006	1.383 ± 0.006	1.383 ± 0.006
2.5×10^{12}	1.140 ± 0.009	1.390 ± 0.005	1.397 ± 0.004
5×10^{12}	1.256 ± 0.011	1.497 ± 0.008	1.491 ± 0.007
7.5×10^{12}	1.353 ± 0.011	1.580 ± 0.014	1.571 ± 0.009
10^{13}	1.429 ± 0.012	1.641 ± 0.013	1.644 ± 0.012
$M_{\rm min}$ [h^{-1} $M_\odot$]	$z = 0.55$		
	$b_{\rm eff}$	$b_{\rm punct}$	$b_{\rm punct}$ (bc)
2×10^{12}	1.507 ± 0.011	1.702 ± 0.014	1.702 ± 0.014
2.5×10^{12}	1.536 ± 0.011	1.715 ± 0.018	1.717 ± 0.013
5×10^{12}	1.730 ± 0.013	1.915 ± 0.017	1.893 ± 0.012
7.5×10^{12}	1.872 ± 0.015	2.06 ± 0.03	2.032 ± 0.017
10^{13}	2.018 ± 0.019	2.21 ± 0.03	2.15 ± 0.04
$M_{\rm min}$ [h^{-1} $M_\odot$]	$z = 1.00$		
	$b_{\rm eff}$	$b_{\rm punct}$	$b_{\rm punct}$ (bc)
2×10^{12}	1.983 ± 0.017	2.104 ± 0.017	2.104 ± 0.017
2.5×10^{12}	2.301 ± 0.017	2.113 ± 0.017	2.13 ± 0.04
5×10^{12}	2.32 ± 0.02	2.41 ± 0.02	2.42 ± 0.03
7.5×10^{12}	2.57 ± 0.03	2.75 ± 0.07	2.62 ± 0.04
10^{13}	2.76 ± 0.03	2.88 ± 0.03	2.82 ± 0.03

$\mathcal{F}(b_{\text{eff}})$. The different bias values we computed in this chapter analysis are reported in Table 6.2.

It is important to notice that the best-centring technique is not employable with real mocks, since in that case it is not possible to use more numerous tracers to improve the centre of a void. Nevertheless, in this chapter we choose to rely on this technique to obtain a better calibration of the relation between b_{punct} and b_{eff}. Indeed, it is convenient to calibrate the latter with $b_{\text{punct}}(\text{bc})$ to minimise the deviation of the data associated to the catalogues with higher mass selections from the linear fit. Using the best-centring technique to alleviate the problem of the sparsity of the tracers, we are able to extend our pipeline also to catalogues with lower spatial resolution. We will show further analysis on the dependence of the $\mathcal{F}(b_{\text{eff}})$ on the tracer characteristics on Chapter 7.

6.6 Results: size function of voids in biased tracers

Now we have all the required tools to measure the void size function of our cleaned catalogues and compare it with the theoretical predictions given by the *extended* (or *re-parametrised*) Vdn model. To this end, we reject the voids that are too close to the boundaries of the simulation box, as their radii cannot be accurately rescaled by our cleaning algorithm, and we correct consequently the effective volume of the box. Then, the theoretical size function is modelled taking into account the effect of the bias of DM haloes inside voids, as described in Sect. 6.3.

Figure 6.7 displays our results. The new re-parametrised void size function model accurately describes all our measurements, in the full range of redshift and mass (thus bias) selections. We show both the size function models obtained by rescaling with b_{punct} and $\mathcal{F}(b_{\text{eff}})$, that appear fully consistent, especially at low redshift and bias values. The uncertainty in the identification of void centres in low density tracer catalogues causes the slight discrepancies that can be seen at high redshifts and biases, which in any case appear not statistically significant. For comparison, we also show the model obtained by rescaling the Vdn model with the effective bias of the full DM halo population, b_{eff}. As it is clearly evident in the figure, this case under-predicts systematically the measured size function at all redshifts and biases.

The final goal of this analysis is to investigate the cosmological constraints that can be derived from the void size function at different redshifts. To mimic real data analyses, we suppose to have access only to the tracer density field. With no information about the underlying total matter distribution, we have to rely on the relation found in Sect. 6.5. We first estimate the effective bias of the sample, b_{eff}, and we consider the coefficients shown in Eq. (6.5), B_{slope} and B_{offset}. These coefficients are necessary to convert b_{eff} into $\mathcal{F}(b_{\text{eff}})$, which in turn is required to re-parametrise the underdensity threshold of Vdn model, as shown in Fig. 6.7. Then, we perform a Bayesian statistical Markov chain Monte Carlo (MCMC) analysis of the measured void size function by sampling the posterior distribution of the parameters σ_8 and Ω_{m}. We assume a Gaussian likelihood and uniform prior distributions for σ_8 and Ω_{m}. We leave as free parameters also b_{eff}, B_{slope} and B_{offset}, assuming in this case Gaussian prior distributions centred at the corresponding estimated values of these parameters, with standard deviations equal to their relative 1σ uncertainties. We will show in Chapter 8 the effect of considering the covariance between the parameters B_{slope} and B_{offset} and the impact of the calibration on the resulting cosmological constraints.

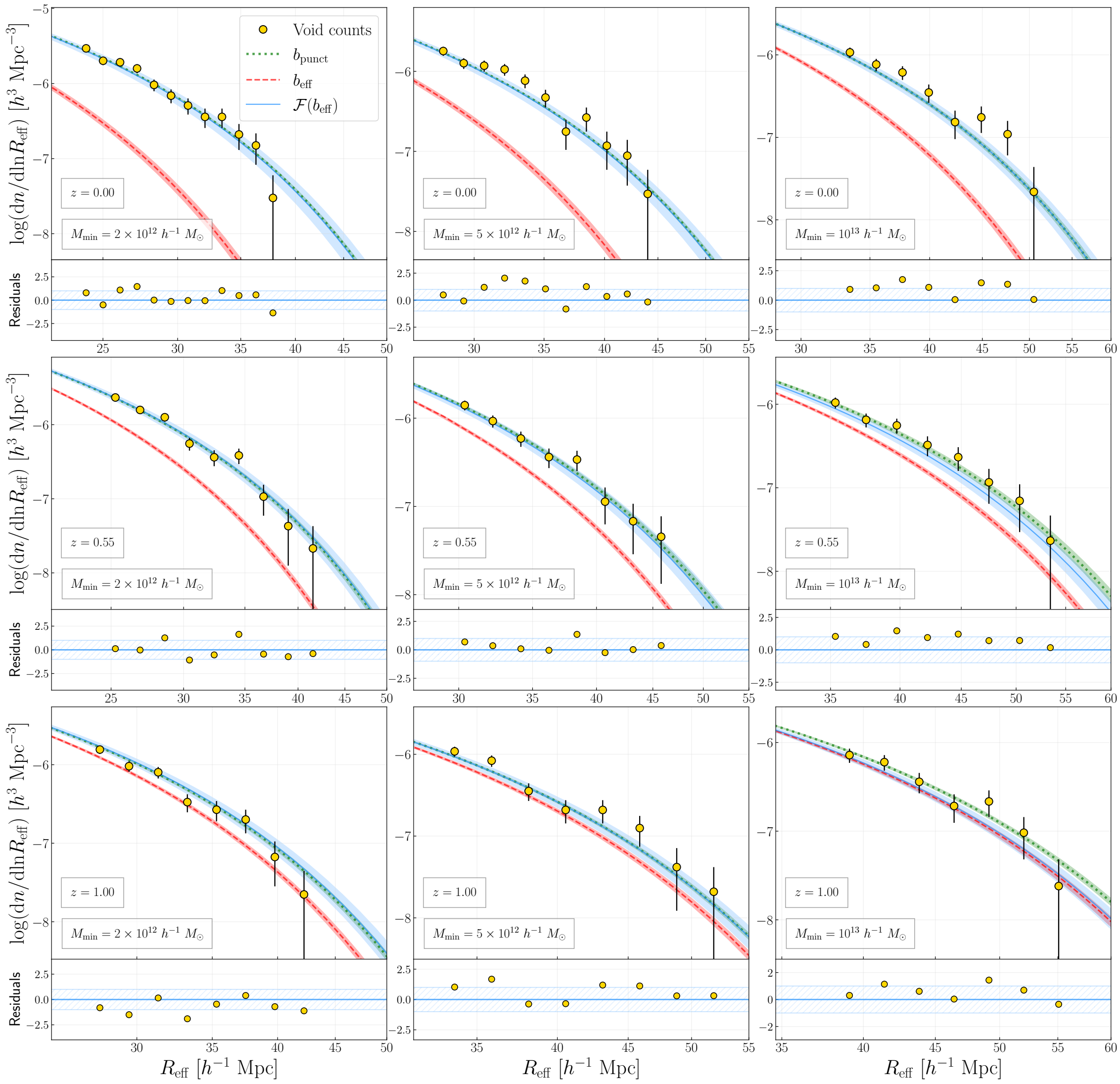

Figure 6.7: The measured size function of the voids (yellow dots) identified in the DM halo catalogues with $M_{\rm min} = 2 \times 10^{12}\ h^{-1}\ {\rm M}_\odot$, $5 \times 10^{12}\ h^{-1}\ {\rm M}_\odot$ and $10^{13}\ h^{-1}\ {\rm M}_\odot$ (rows from *top* to *bottom*), at redshifts $z = 0$, $z = 0.55$, $z = 1$ (columns from *left* to *right*). Voids with $R_{\rm eff} < 2.5\,{\rm MPS}$ are rejected from the analysis. *Upper sub-panels*: the blue dashed lines represent the void size function obtained by rescaling the Vdn model with $\mathcal{F}(b_{\rm eff})$, that is the value of the bias computed from the relation shown in Fig. 6.6. The green solid lines show the model rescaled with the value of $b_{\rm punct}$. The red dashed lines represent the model rescaled with the effective bias, $b_{\rm eff}$. In all cases, the shaded areas indicate the variation of the model obtained applying 1σ errors on the value of the tracer bias. *Lower sub-panels*: the residuals of the void counts, computed as the ratio between the difference *data − model* and the *data errors*, where the data are the measured void size function and the model is given by the re-parametrisation of the Vdn model with $\mathcal{F}(b_{\rm eff})$. The blue hatched areas indicate the regions in which the discrepancy between the data and the model is within the data errors.

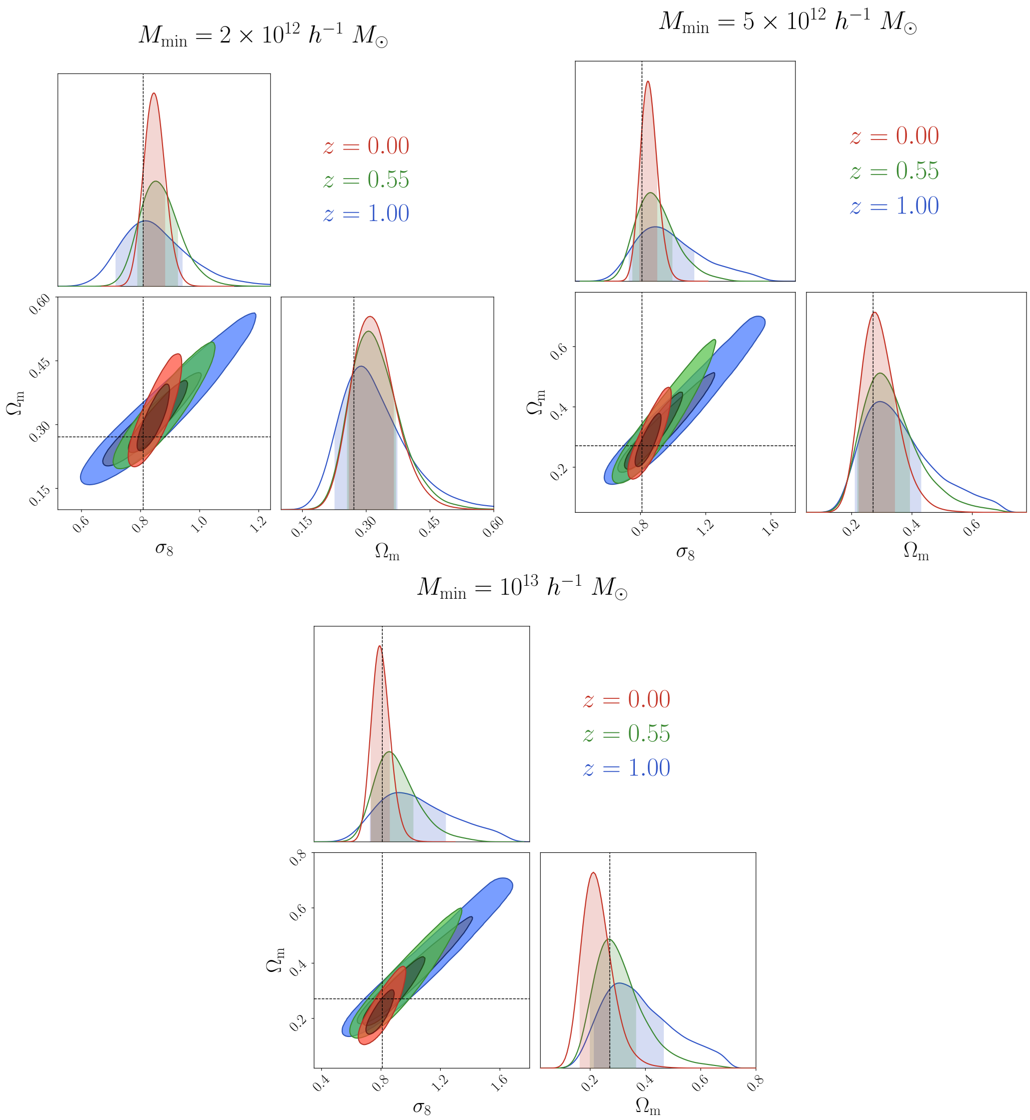

Figure 6.8: 1σ (68%) and 2σ (95%) confidence levels in the σ_8–$\Omega_{\rm m}$ plane, for the halo catalogues with $M_{\rm min} = 2 \times 10^{12}\ h^{-1}\ {\rm M}_\odot$ (*top left*), $5 \times 10^{12}\ h^{-1}\ {\rm M}_\odot$ (*top right*), and $10^{13}\ h^{-1}\ {\rm M}_\odot$ (*bottom*). The colour of ellipses corresponds to different redshifts: red for $z = 0$, green for $z = 0.55$ and blue for $z = 1$. The prior distributions are uniform for σ_8 and $\Omega_{\rm m}$, and Gaussian for $b_{\rm eff}$, $B_{\rm slope}$ and $B_{\rm slope}$. The projected 1D posterior distributions of σ_8 and $\Omega_{\rm m}$ are shown in the *top* and *bottom-right* panels of each plot, respectively. The black lines represent the true WMAP7 values ($\sigma_8 = 0.809$ and $\Omega_{\rm m} = 0.2711$).

Table 6.3: Mean and standard deviation of the posterior distributions for the parameters σ_8 and Ω_m. The latter are computed from the Bayesian statistical analysis of the measured void size functions for the DM halo catalogues with $M_\mathrm{min} = 2 \times 10^{12}\ h^{-1}\ M_\odot$, $5 \times 10^{12}\ h^{-1}\ M_\odot$ and $10^{13}\ h^{-1}\ M_\odot$ at $z = 0$, $z = 0.55$ and $z = 1$. The last line of each table reports the results obtained by combining the 1D posterior distributions at the three different redshifts.

$M_\mathrm{min} = 2 \times 10^{12}\ h^{-1}\ M_\odot$				
	σ_8		Ω_m	
	Mean	St. dev.	Mean	St. dev.
$z = 0.00$	0.85	0.04	0.321	0.05
$z = 0.55$	0.87	0.07	0.33	0.06
$z = 1.00$	0.86	0.12	0.32	0.08
combined	0.85	0.03	0.31	0.03

$M_\mathrm{min} = 5 \times 10^{12}\ h^{-1}\ M_\odot$				
	σ_8		Ω_m	
	Mean	St. dev.	Mean	St. dev.
$z = 0.00$	0.85	0.05	0.30	0.06
$z = 0.55$	0.90	0.12	0.33	0.09
$z = 1.00$	1.00	0.2	0.36	0.12
combined	0.86	0.05	0.29	0.04

$M_\mathrm{min} = 10^{13}\ h^{-1}\ M_\odot$				
	σ_8		Ω_m	
	Mean	St. dev.	Mean	St. dev.
$z = 0.00$	0.80	0.06	0.23	0.05
$z = 0.55$	0.91	0.15	0.31	0.09
$z = 1.00$	1.1	0.3	0.38	0.13
combined	0.82	0.05	0.26	0.04

The results for our simulated catalogues with three different mass-cuts and redshifts are reported in Fig. 6.8. The corresponding mean values and the related uncertainties are reported in Table 6.3. We can notice that the true values of the cosmological parameters are within the 68% level in all cases and that the constraining power is higher for the low redshifts and minimum halo mass, which are indeed associated to a larger number of voids.

We perform now a preliminary exploration of the constraining power given by the combination of the parameter 1D (i.e. projected) posterior distributions derived for different redshifts. We consider the results achieved for halo catalogues with fixed minimum mass and different redshifts, exploiting the redshift dependence of the degeneracy directions to infer tighter constraints on σ_8 and Ω_m. Despite our samples cannot be considered completely independent, we multiply the 1D posterior probabilities of both σ_8 and Ω_m[6] at

[6] For simplicity we do not take into account the covarance between the parameters in this chapter, a

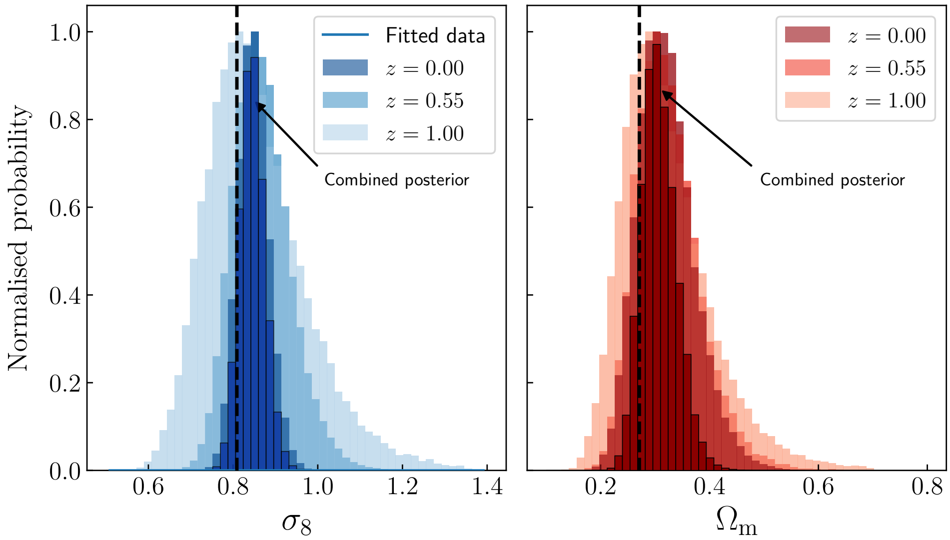

Figure 6.9: Normalised 1D posterior probabilities of σ_8 (*left*) and Ω_m (*right*) computed for the halo catalogue with $M_\mathrm{min} = 2 \times 10^{12}\ h^{-1}\ M_\odot$ at redshift $z = 0$, $z = 0.55$ and $z = 1$. The histograms with black outlines represent the combined distributions achieved by multiplying all the posterior probabilities relative to different redshifts. The black dashed lines indicate the true WMAP7 values ($\sigma_8 = 0.809$ and $\Omega_\mathrm{m} = 0.2711$).

different redshifts as if they were achieved from independent data, in order to reproduce the results that would be obtained from separate redshift shells in real surveys. We show in Fig. 6.9 the results for the halo catalogue with $M_\mathrm{min} = 2 \times 10^{12}\ h^{-1}\ M_\odot$, obtained by multiplying the parameter posterior distributions at $z = 0$, $z = 0.55$ and $z = 1$. Table 6.3 reports the mean values and the standard deviations of the posterior distributions of σ_8 and Ω_m at these redshifts also for the catalogues with $M_\mathrm{min} = 5 \times 10^{12}\ h^{-1}\ M_\odot$ and $10^{13}\ h^{-1}\ M_\odot$, together with the analogous quantities obtained for the combined posterior probability. As expected, by joining the information at different redshifts, we can achieve more precise constraints on the cosmological parameters, as shown by the decreasing of the width of the combined posterior distributions.

We refer the reader to Appendix B for further investigations on the cosmological constraints derived within this chapter. These concern in particular the impact of the assumption of a relation $\mathcal{F}(b_\mathrm{eff})$ that is or wrong (i.e. $\mathcal{F}(b_\mathrm{eff}) = b_\mathrm{eff}$) or affected by systematic errors.

more accurate and realistic statistical treatment of the degeneracies between the cosmological parameters will be performed in Chapter 8.

Chapter 7

Voids in modified gravity scenarios with massive neutrinos

MG models (introduced in Sect. 3.1.2) suppose the standard GR to be inadequate on certain cosmological scales, implying the introduction of new physical degrees of freedom in the gravitational theory (see e.g. Dolgov & Kawasaki, 2003; Nojiri & Odintsov, 2006; Clifton et al., 2012; Joyce et al., 2015; Ishak, 2019). In particular, MG models tend to closely mimic the effect of the cosmological constant on the expansion history of the Universe. To satisfy the solar system tests and the local high-precision measurements (Le Verrier, 1859; Bertotti, Iess & Tortora, 2003; Will, 2005), these models have to introduce a *screening mechanism*, that basically recovers the predictions of standard GR on small scales (Khoury & Weltman, 2004c; Hinterbichler & Khoury, 2010; Brax & Valageas, 2013, 2014). Most viable MG models are quite degenerate at the background level and can produce discernible features only through their effects on structure formation at linear and nonlinear scales.

Additionally, it has been recently highlighted the presence of strong observational degeneracies between the effects of some of these models and those including massive neutrinos (He, 2013; Motohashi, Starobinsky & Yokoyama, 2013; Baldi et al., 2014; Wright, Winther & Koyama, 2017; Giocoli, Baldi & Moscardini, 2018). Neutrinos (presented in Sect. 3.1.3) are indeed another elusive component of the ΛCDM cosmology and although the Standard Model of particle physics assumes they are massless, the evidence of solar neutrino oscillations proved they in fact possess a mass (Becker-Szendy et al., 1992; Fukuda et al., 1998; Ahmed et al., 2004). Of particular interest are degeneracies emerging from a proper combination of the parameters of the $f(R)$ class of MG models and of the total neutrino mass $\sum M_\nu$. Indeed, the typical range of the fifth force for $f(R)$ models, determined by the Compton wavelength μ^{-1}, is comparable with the free-streaming scale of neutrinos (see Sects. 3.1.2 and 3.1.3). The latter can have therefore a counteractive effect on the enhanced growth of the cosmic structures, causing a compensation on the cosmological statistical variations given by MG theories. This poses a notable challenge for cosmology, since robust methods and different cosmological probes are required to achieve tight constraints on both massive neutrinos and MG, and especially to disentangle their combined effects. In particular, Baldi et al. (2014) have demonstrated that many standard cosmological statistics, as the nonlinear matter power spectrum, the halo abundance and the halo bias, show a limited discriminating power for some specific combinations of $f(R)$

gravity parameters and neutrino mass values, which lead to results statistically consistent with the ΛCDM predictions.

In this chapter we focus on the possible disentanglement of these degenerate cosmological scenarios by using cosmic voids. As we saw in Sect. 4.7, thanks to their unique features, voids constitute indeed excellent laboratories for investigating the implications of MG theories and the presence of massive neutrinos. Here we report the work presented in Contarini et al. (2021), which proposes an accurate analysis of void radial profiles and abundances with the aim of showcasing where the deviations of the $f(R)$ and massive neutrino models from the standard Λ scenario are more pronounced.

7.1 DUSTGRAIN-*pathfinder* simulations

In this chapter we use a subset of the cosmological N-body simulations suite called DUSTGRAIN-*pathfinder* (Dark Universe Simulations to Test GRAvity In the presence of Neutrinos). These simulations have been specifically designed with the aim of investigating the degeneracies between $f(R)$ gravity models and massive neutrinos, and have been recently exploited in different papers finalised to the study of possible methods to disentangle these cosmic degeneracies, that is exploiting weak-lensing (Giocoli, Baldi & Moscardini, 2018; Peel et al., 2018) and clustering statistics (García-Farieta et al., 2019), investigating the abundance of massive haloes (Hagstotz et al., 2019), the large-scale velocity field (Hagstotz et al., 2019), and exploring machine learning techniques (Peel et al., 2019; Merten et al., 2019). The DUSTGRAIN-*pathfinder* simulations have been carried out using `MG-GADGET`, a code based on an updated version of `GADGET2` (Springel, 2005) developed by Puchwein, Baldi & Springel (2013) to include $f(R)$ gravity models. This code has then been combined with the particle-based implementation described in Viel, Haehnelt & Springel (2010) to include the effects of massive neutrinos.

The DUSTGRAIN-*pathfinder* simulations follow the evolution of an ensemble of $(2\cdot)768^3$ particles of DM (and massive neutrinos) within a periodic cosmological box of $750\ h^{-1}$ Mpc per side. In the reference ΛCDM simulation (i.e. the one characterised by GR and $M_\nu = 0$ eV) the CDM particle mass is equal to $M^{\rm p}_{\rm cdm} = 8.1 \times 10^{10}\ h^{-1}\ M_\odot$ and the gravitational softening is set to $\varepsilon_g = 25\ h^{-1}$ kpc, corresponding to about 1/40 of the MPS. The cosmological parameters assumed in these simulations are consistent with the Planck 2015 constraints (see Planck Collaboration et al., 2016a) $\Omega_{\rm m} = \Omega_{\rm cdm} + \Omega_{\rm b} + \Omega_\nu = 0.31345$, $\Omega_\Lambda = 0.68655$, $h = 0.6731$, $A_s = 2.199 \times 10^{-9}$, $n_s = 0.9658$, which give for the ΛCDM case $\sigma_8 = 0.842$. The remaining set of simulations is created to sample the joint $f(R)$–M_ν parameter space. The $|f_{R0}|$ parameter assumes the values in the range $[10^{-6}$–$10^{-4}]$, while M_ν belongs to the range [0–0.3] eV. All the parameters characterising the simulations considered in this chapter are reported in Table 7.1. Note that the total $\Omega_{\rm m}$ (including neutrinos) is kept fixed to compare the density power spectrum between cosmologies with and without neutrinos. This results in equal positions of the peak of the power spectrum and ensures that the spectra are identical in the long-wavelength limit. For a more detailed description of the DUSTGRAIN-*pathfinder* simulations see Giocoli, Baldi & Moscardini (2018) and Hagstotz et al. (2019).

Among all the comoving snapshots available for this project, we select the ones at the redshifts $z = 0, 0.5, 1, 2$, considering only CDM particles also in the case of simulations containing massive neutrinos, though this assumption does not have a major impact on the

Table 7.1: Summary of the main numerical and cosmological parameters of the subset of the DUSTGRAIN-*pathfinder* simulations considered in this chapter. These simulations are carried out in a volume of $(750\ h^{-1}\ \mathrm{Mpc})^3$ and are composed of 768^3 CDM particles for the ΛCDM, fR4, fR5 and fR6 models, with the addition of as many massive neutrino particles for the non-ΛCDM cases. The third column provides the value of the MG parameter f_{R0}, while the fourth column the neutrino mass M_ν. The other columns provide $\Omega_{\rm cdm}$ and Ω_ν, that are the CDM and neutrino density parameters respectively, and the CDM and neutrino particle masses $M^{\rm p}_{\rm cdm}$ and $M^{\rm p}_\nu$. The value in the last column is the σ_8 parameter, which corresponds to the linear power normalisation computed at $z = 0$.

Simulation name	Gravity model	f_{R0}	M_ν [eV]	$\Omega_{\rm cdm}$	Ω_ν	$M^{\rm p}_{\rm cdm}$ $[h^{-1}M_\odot]$	$M^{\rm p}_\nu$ $[h^{-1}M_\odot]$	σ_8
ΛCDM	GR	–	0	0.31345	0	8.1×10^{10}	0	0.842
fR4	$f(R)$	-1×10^{-4}	0	0.31345	0	8.1×10^{10}	0	0.963
fR4_0.3eV	$f(R)$	-1×10^{-4}	0.3	0.30630	0.00715	7.92×10^{10}	1.85×10^{9}	0.887
fR5	$f(R)$	-1×10^{-5}	0	0.31345	0	8.1×10^{10}	0	0.898
fR5_0.1eV	$f(R)$	-1×10^{-5}	0.1	0.31107	0.00238	8.04×10^{10}	6.16×10^{8}	0.872
fR5_0.15eV	$f(R)$	-1×10^{-5}	0.15	0.30987	0.00358	8.01×10^{10}	9.25×10^{8}	0.859
fR6	$f(R)$	-1×10^{-6}	0	0.31345	0	8.1×10^{10}	0	0.856
fR6_0.06eV	$f(R)$	-1×10^{-6}	0.06	0.31202	0.00143	8.07×10^{10}	3.7×10^{8}	0.842
fR6_0.1eV	$f(R)$	-1×10^{-6}	0.1	0.31107	0.00238	8.04×10^{10}	6.16×10^{8}	0.831

resulting halo catalogues (see e.g. Villaescusa-Navarro et al., 2013, 2014; Castorina et al., 2014; Lazeyras, Villaescusa-Navarro & Viel, 2020). In the following analyses concerning voids in the DM density fields, we apply a subsampling factor to DM particles to reduce the computational time, keeping the 25% of the original particle sample.

Then, the collapsed DM structures have been identified for each snapshot following the approach of Despali et al. (2016). In particular, the halo catalogues have been obtained by applying the `Denhf` algorithm (Tormen, Moscardini & Yoshida, 2004; Giocoli, Tormen & van den Bosch, 2008, and see Sect. 2.3.1 for the details) to the DM particle sample, finding DM haloes as gravitationally bound structures, without including sub-haloes. The halo mass is therefore assigned according to Eq. (2.72), in which Δ_c is fixed to 200 or 500. In the analysis presented in this chapter we employ 200c halo catalogues only, thus those derived imposing $\Delta_\mathrm{c} = 200$, except for the comparison test that we will show in Fig. 7.9. The 500c haloes, identified with $\Delta_\mathrm{c} = 500$, are indeed rarer objects and their sparsity does not allow to identify a sufficiently large sample of cosmic voids.

Moreover, we reject the haloes with a number of embedded DM particles less than 30, in order to keep only statistically relevant objects and to avoid contamination by spurious density fluctuations. This mass cut corresponds to $M_\mathrm{min} = 2.43\ h^{-1}\ M_\odot$ for the ΛCDM case, and has been chosen to select a complete and, at the same time, dense enough sample of DM haloes, which is fundamental for identifying a statistically significant number of cosmic voids. The effect of this assumption has been investigated by repeating the analysis with different low mass selections, with the requirement of having a good agreement between the measured effective bias of DM haloes (see Appendix A) and the theoretical predictions, which we compute using the Tinker et al. (2010) model convolved with the halo mass function of the simulations (see Eq. A.4).

Two of the most important characteristics of the employed DM halo catalogues are the volume and the spatial resolution (see Sect. 2.3). The sample volume settles indeed the statistical relevance of the measured void abundance and affects the probability of finding large voids, while the spatial resolution determines the smallest scales at which the void number counts are not affected by numerical incompleteness. Before introducing our analysis, is therefore fundamental to compare these quantities with those of the upcoming wide field surveys like *Euclid* (Laureijs et al., 2011; Amendola et al., 2018), NGRST (Green et al., 2012) and LSST (LSST Dark Energy Science Collaboration, 2012), in order to put our results into the context of a future application with real data catalogues.

At first, with a volume of about 0.42 $(h^{-1}\ \mathrm{Gpc})^3$, the DUSTGRAIN-*pathfinder* simulations allow the identification of a relatively small sample of voids. This volume can be easily compared to the one of WFIRST, *Euclid* and LSST, that will cover about 17 $(h^{-1}\ \mathrm{Gpc})^3$, 44 $(h^{-1}\ \mathrm{Gpc})^3$ and 154 $(h^{-1}\ \mathrm{Gpc})^3$, respectively. Considering these volumes (two of which that are more than 100 times larger than the simulation volume considered our analysis), we expect that the uncertainties related to the void statistics presented in this chapter will decrease dramatically considering void samples extracted from future real galaxy catalogues. In particular, the Poissonian errors associated to both the stacked density profiles and void size functions will be reduced of a factor proportional to the square root of the increasing of the volume size, hence allowing to achieve a precision more than 10 times better.

Finally, the DM halo catalogues extracted from the DUSTGRAIN-*pathfinder* ΛCDM simulations are characterised by a MPS between 8.7 and 12.4 h^{-1} Mpc, for $z = 0$ and

$z = 2$ respectively. These values are indeed of the same order of the expected MPS for the *Euclid* spectroscopic survey that, with a sky area of ~ 15000 deg^2, will sample over 50 million of Hα galaxies, reaching a spatial resolution of $\sim 10\ h^{-1}$ Mpc. The predictions for the spatial resolution of the WFIRST survey are even more encouraging, thanks to the 20 million Hα galaxies that are expected to be detected in the redshift range $1.05 < z < 2$, sampled over a sky area of ~ 2400 deg^2. Considering instead the LSST photometric galaxy surveys, the MPS of the samples would drop to $\sim 3\ h^{-1}$ Mpc, though with a dramatic decreasing of the redshift accuracy. On the basis of these data, we can expect that the methodology presented in this chapter will gain statistical relevance when applied to the data of the upcoming surveys.

7.2 Data preparation for the unbiased and biased cases

We run `VIDE` on both the DM particle and DM halo distributions, building a void catalogue for each of the cosmological simulations and redshift considered in this chapter. Following the same procedure of Sect. 6.2, we clean the catalogues of voids identified in the DM halo distribution fixing in the cleaning algorithm (Sect. 5.3) the threshold $\delta^{\rm NL}_{\rm v,tr}$ at the value -0.7. On the contrary, dealing with voids in the DM particle distribution, the value $\delta^{\rm NL}_{\rm v,DM} = -0.7$ is less appropriate to identify cosmic underdensities. Indeed, only few and very deep voids could be rescaled to enclose such a low density contrast at high redshifts. Since the choice of the threshold does not affect the validity of the predictions of the Vdn model, we decided to use higher density contrasts to clean voids at earlier epochs, in order to enlarge the sample of voids and reduce the shot noise. For this reason, we adopt different thresholds depending on the redshift of the DM catalogues, using the growth factor $D(z)$ to rescale the nonlinear density contrast required in the cleaning algorithm:

$$\delta_{\rm v,DM}(z) = -0.8 \left[\frac{D(z)}{D(z=0)} \right]^2 . \tag{7.1}$$

Fixing the cosmological parameters to those of the ΛCDM simulations, we obtain the following values: $\delta_{\rm v,DM}(z=0) = -0.80$, $\delta_{\rm v,DM}(z=0.5) = -0.70$, $\delta_{\rm v,DM}(z=1) = -0.62$ and $\delta_{\rm v,DM}(z=2) = -0.52$. We verified that the values chosen for the underdensity threshold are effective to maximise the signal and reduce the noise associated to the measured void abundances. However, we tested different threshold choices, finding equivalent outcomes. Indeed, it is important to highlight, once again, that the matching between the measured void abundance and the predictions of the Vdn model is not affected by the specific choice of the underdensity threshold. As far as the same value is used to reshape voids and is also inserted, after the conversion to its linear counterpart, in Eqs. (4.4) and (4.5) of the Vdn model, the results will be in agreement with the model predictions. Therefore the reader should not be misled by the fact that the cleaning procedure is cosmology dependent. The usage of the growth factor is just a convenient prescription to select an effective threshold, depending on the redshift of the sample, and does not introduce any cosmology-driven bias.

Figure 7.1 shows the voids identified in the distribution of DM particles at $z = 0$, obtained following the methodology described in this section. For each cosmological model, we report the central regions of the simulation box, indicating the spherical underdensities selected in this analysis with circles traced within a slice of $20\ h^{-1}$ Mpc along the Z-axis.

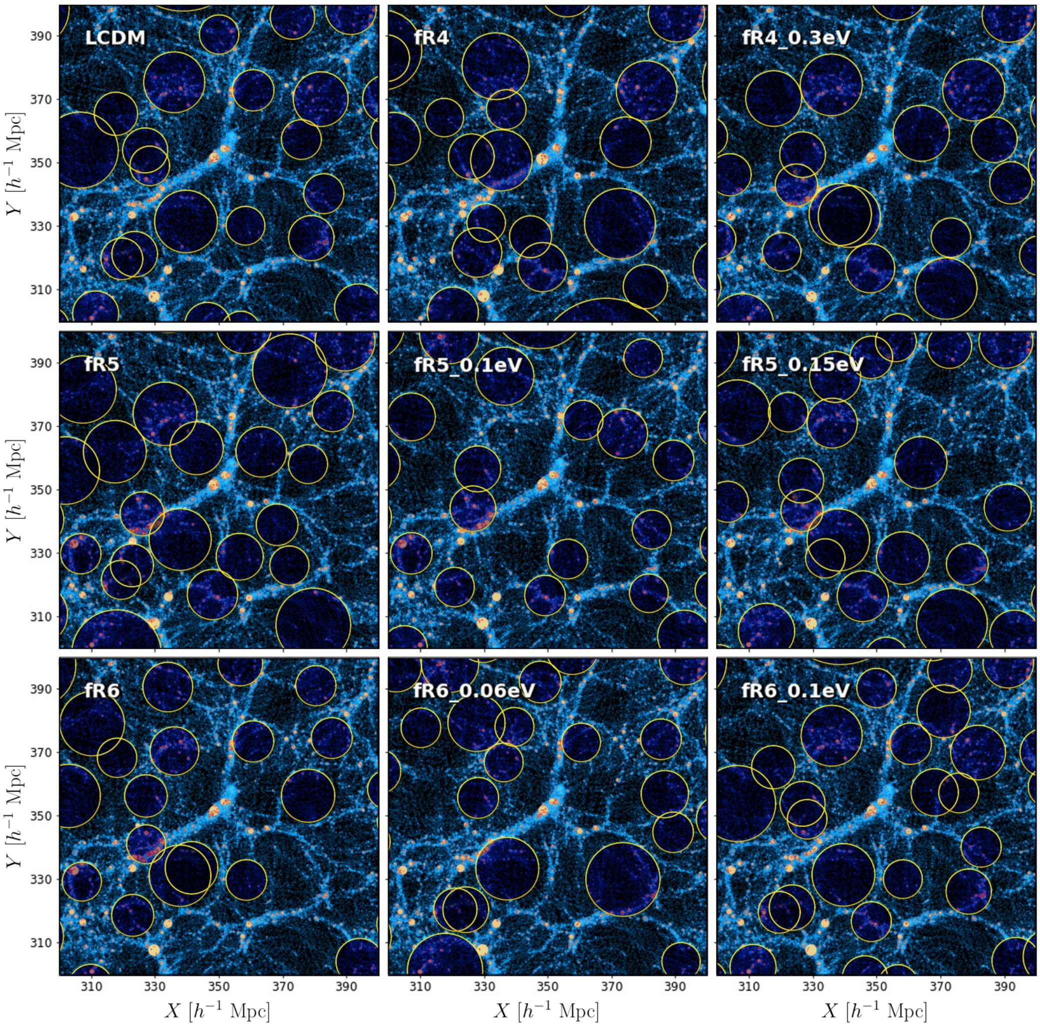

Figure 7.1: Visual representation of the voids identified in the DM distribution of the DUSTGRAIN-*pathfinder* simulations. We show a slice of 20 h^{-1} Mpc of the central part of the simulation box at $z = 0$, for each of the cosmological scenarios analysed in this chapter. The DM particles are displayed in light blue, while the DM haloes have colours from orange to yellow, the latter indicating the more massive ones. The yellow circles with a darker interior represent the voids obtained after the application of the cleaner procedure to the void catalogues previously built by applying the `VIDE` algorithm.

Any apparent overlapping between voids is a visual effect caused by the projection on the plane. As expected, the denser zones made up by filaments were not selected during void identification. On the contrary, some empty regions result not identified as voids, due to the superimposition with other underdensities not displayed in the figure because their centre is not included in the simulation slice. It is also interesting to note that the selected sample of voids is different depending on the cosmological scenario, even if the underlying distribution of matter looks remarkably similar.

7.3 Results: void profiles

We compute the stacked void density profiles by measuring the density contrast in shells around void centres. In particular, we calculate the mean of the density profiles computed between 0.3 and 3 times the effective radius R_{eff}, rescaling then each profile by its correspondent void effective radius. For this specific analysis we make use of the void catalogues obtained directly with `VIDE`, without applying the cleaning algorithm. This is due to the fact that the cleaning procedure is aimed at shaping voids according to the theoretical model of the void size function, and it is not particularly suitable for the study of the stacked void profiles. Indeed, using our cleaning prescriptions, the sample of voids is considerably reduced in number because of the removal of the voids-in-voids and voids-in-cloud (see Sect. 4.2), as well as of the overlapping cases. Moreover, with the cleaning algorithm we rescale the void radii to match a specific density contrast, whereas in the study of the stacked density profiles we aim at modelling voids to enhance the self-similarity between their shapes. Indeed, the `VIDE` void catalogues are composed of a hierarchy of voids separated by high density walls, and the effective radius assigned to each void is, by construction, in proximity to the compensation wall (see Sect. 4.4). These voids are therefore characterised by the same shape and their stacking allows to sharpen their peculiar features (see e.g. Hamaus, Sutter & Wandelt, 2014).

We start analysing the profiles computed in the DM particle distribution, considering only voids with radii included in the range [5–7]$\cdot$MPS, which corresponds to 1.55 h^{-1} Mpc, for all the sub-sampled catalogues. This range covers the central parts of the interval on which we perform the analysis of the abundance of voids in the DM density field that we will present in Sect. 7.4: the lower limit is given by the spatial resolution of the sample, while the upper limit is chosen to include a sufficient number of voids with large radii. Since the shape of the density profiles depends on the mean radius of the void sample (Hamaus, Sutter & Wandelt, 2014), we avoid to select a wider range of sizes to prevent an excessive mixing of different density profiles during the operation of average.

In Fig. 7.2 we report the results obtained with the ΛCDM simulations, compared to those with MG models characterised by $f_{R0} = -10^{-4}$, with and without massive neutrinos having $M_\nu = 0.3$ eV (namely, fR4 and fR4_0.3eV). The density profiles in different cosmologies appear very similar, at all redshifts. We note that the central zones become deeper with cosmic time, while the compensation wall grows and turns denser, as already verified in different works (see e.g. Hamaus, Sutter & Wandelt, 2014; Massara et al., 2015; Pollina et al., 2016). Differences among the cosmological models can be better appreciated by looking at the residuals, displayed in the lower sub-panels. Here we compute the difference between the mean density contrast measured in the fR4 or fR4_0.3eV simulations and the one measured in the ΛCDM simulations, divided by the errors associated to the

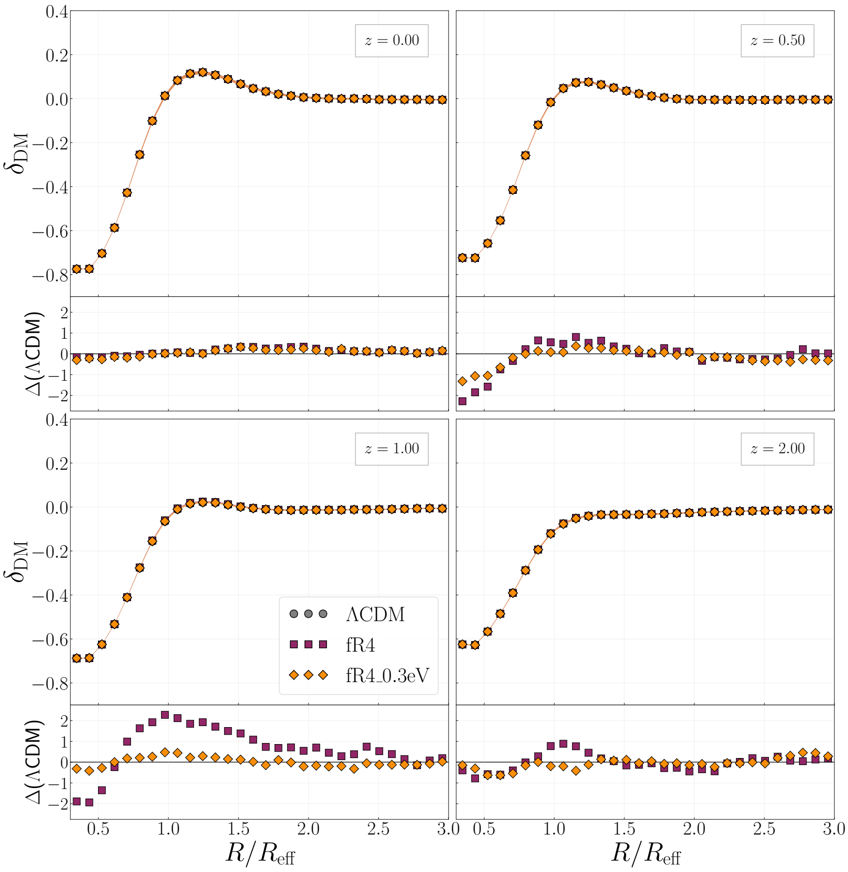

Figure 7.2: Density contrast profiles computed in shells around the centres of cosmic voids, identified with `VIDE` in the distribution of DM particles. The results are displayed for each cosmological model at redshifts $z = 0, 0.5, 1, 2$. We report the profiles measured considering the ΛCDM, fR4 and fR4_0.3eV simulations. These profiles are so similar that the markers with which they are represented result superimposed. However, the differences between them are highlighted in the residuals reported in each sub-panel, computed with respect to the ΛCDM case, in units of the errors associated to the profiles computed in the non-standard cosmologies. The latter are represented as a shaded region in the plots. In this case, given the high number of profiles, this uncertainty is so small to be represented with a simple line between the data points.

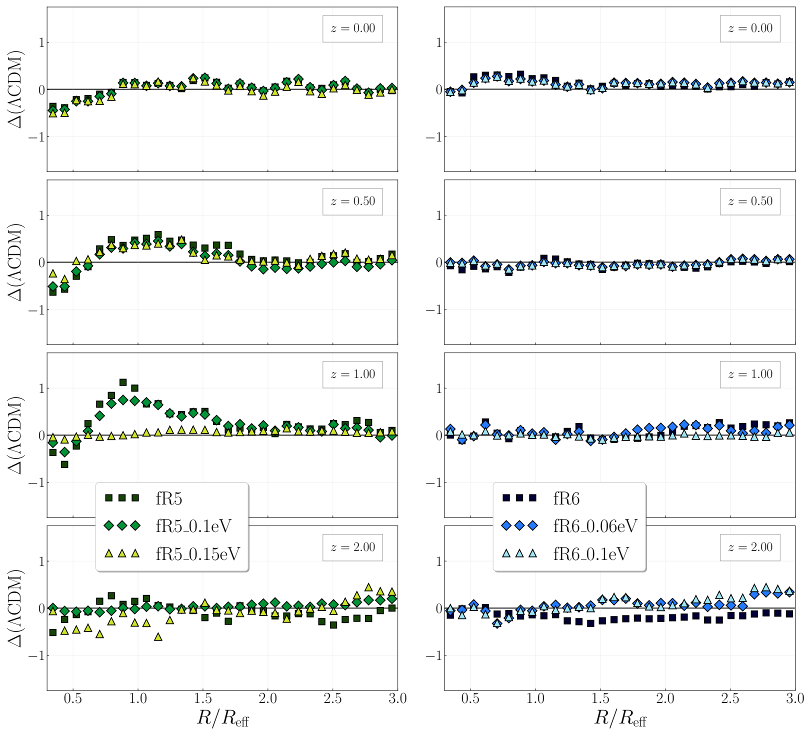

Figure 7.3: The same as Fig. 7.2 but for fR5 and fR6 MG models, with and without massive neutrinos. In this case, to highlight the deviations from the ΛCDM void profiles, we show only the residuals from the standard cosmological model.

former. The errors are evaluated as the standard deviation of all the profiles considered for each simulation, divided by the square root of their number. The most significant variation arises around $z = 1$, where the fR4 model shows an increase of the mean density in close proximity to the compensation wall and a lowering near the void centres. This is in agreement with the expected effect of enhancing the growth of structures in MG, which accelerates the process of void formation and evolution. The presence of emptier voids and steeper voids profiles has indeed already been observed and predicted by different authors who studied the behaviour of the fifth force in voids in Chameleon models (see e.g. Martino & Sheth, 2009; Clampitt, Cai & Li, 2013b; Perico et al., 2019). Nevertheless, these differences are almost completely cancelled by the effect of the neutrino thermal free-streaming, nullifying the possibility of disentangling the degeneracy between these models.

In Fig. 7.3 we present the normalised residuals obtained by comparing the density profiles measured using the remaining cosmological models to the ones of the ΛCDM simulation. Note that the y-range is shrunk compared to the previous plot for the sake of clarity. Also in the case of fR5 models, the most evident deviations from the ΛCDM profiles appear around $z = 1$, and they also tend to vanish in the presence of massive neutrinos. The effect is even milder in fR6 models, and statistically indistinguishable, at least with the current simulations.

In order to investigate possible trends related to the void mean size, we repeat the same analysis dividing the stacked void profiles into different bins of effective radii. We do not report the results of this analysis since we did not find any clear different behaviour in the profiles computed with the ΛCDM cosmology compared to the other models, at the same mean radii. Minor differences appear only for voids with large radii at $z = 2$, where an early formation of the compensation wall is revealed in the profiles measured in MG simulations without massive neutrinos. Larger voids manifest also a slightly deeper profiles at $z = 0$ in the very central regions of the voids, which is reduced by the presence of massive neutrinos. These results are not surprising given that larger voids are subject to a faster evolution compared to the smaller ones. Nevertheless, these deviations do not show a significance higher than 2σ, for all the redshifts and distances from the void centres considered.

Now we present the same analysis performed on void density profiles measured in the distribution of DM haloes with $\Delta_{\mathrm{c}} = 200$. In this case we consider voids with radii in the range $[2\text{–}5] \cdot \mathrm{MPS}$ of the ΛCDM simulation tracers, with $\mathrm{MPS} = 8.67\ h^{-1}$ Mpc. The choice of this interval of radii is motivated by the same reasons behind the previous analysis of DM void profiles. We report the results of this analysis in Figs. 7.4 and 7.5.

In the Fig. 7.4 we present the density profiles for the ΛCDM, fR4 and fR4_0.3eV models, while in Fig. 7.5 we show the residuals computed for the set of 6 simulations of the fR5 and fR6 models, with and without massive neutrinos. The residuals are computed as the difference between the profiles measured in non-standard cosmological models and the ones measured in the ΛCDM cosmology, divided by the uncertainty associated to the former. Compared to the stacked density profiles traced by DM particles, the profiles obtained using DM haloes result steeper and the compensation wall is clearly well developed also at early epochs, reaching more positive values of density contrast (in agreement with the results obtained by Massara et al., 2015). However, in this case the data are noisier because of the decreasing of void statistics, and it is hard to distinguish any significant

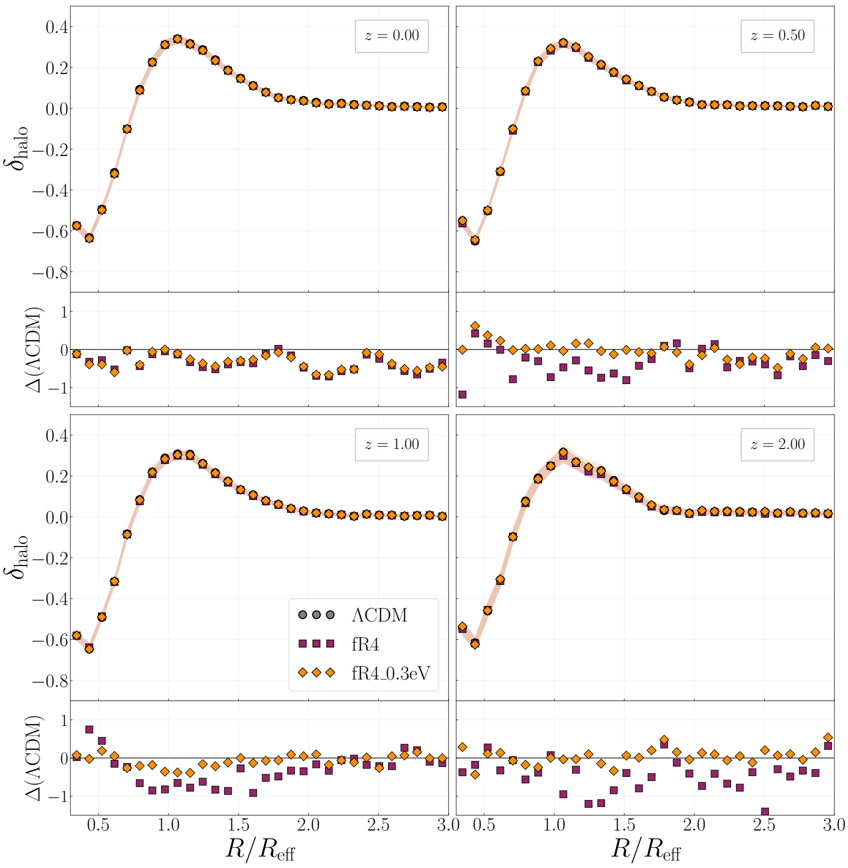

Figure 7.4: The same as Fig. 7.2, but for the cosmic voids identified with `VIDE` in the distribution of DM haloes with $\Delta_{\rm c} = 200$.

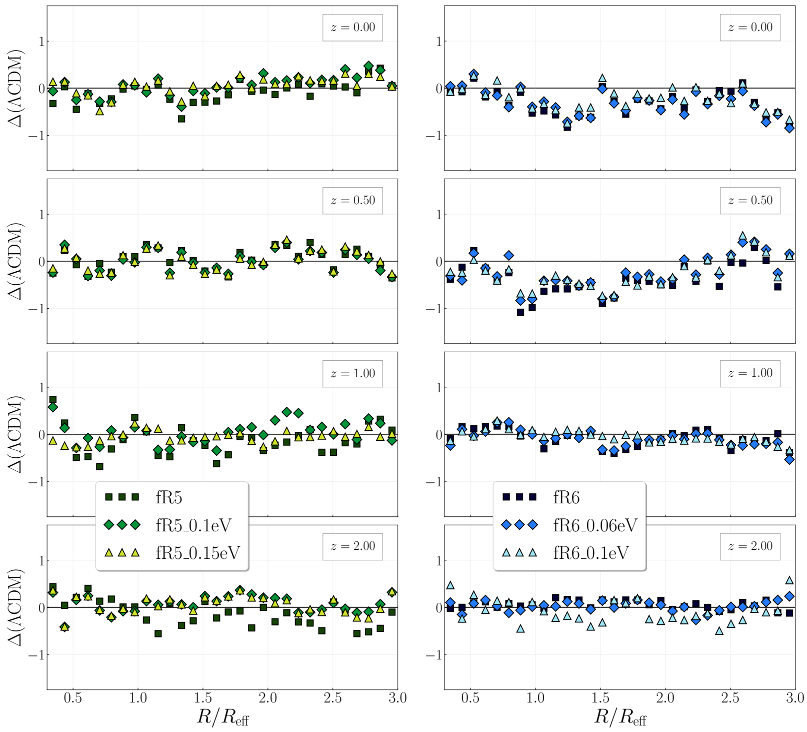

Figure 7.5: The same as Fig. 7.3, but for the cosmic voids identified with `VIDE` in the distribution of DM haloes with $\Delta_c = 200$.

trend. Since we expect to find the strongest deviations in the most extreme MG models, we focus now on the analysis of the density profiles computed using the simulations with $f_{R0} = -10^{-4}$ and $M_\nu = 0.3$ eV.

Looking at the residuals shown Fig. 7.4 it is possible to note a slight trend of the fR4 profiles towards lower values of the density contrast, which is almost completely cancelled by the effect of massive neutrinos, especially at high redshifts. The origin of these deviations is the shift of the mean radii of voids identified in MG scenarios by biased tracers. Indeed, being these voids more evolved due to the effect of the enhanced gravity, their average radii result larger. In turn, as demonstrated by Hamaus, Sutter & Wandelt (2014), the density profiles computed with larger voids have shallower interiors and lower density contrast values in the outer parts. We also tested the subdivision of the sample in different bins of void radii, but the increase of the noise does not allow us to discern any characteristic behaviour associated with voids of different sizes. We can conclude that the degeneracies between the considered models cannot be disentangled by the analysis of the void stacked profiles carried on in this chapter, especially making use of DM haloes as tracers of the matter distribution. Nevertheless, we underline that larger simulations could lead to slightly different results, since they would provide better void statistics and smaller errors, possibly allowing us to disentangle the models.

7.4 Results: void size function in the DM field

We focus now on the study of the abundance of cosmic voids as a function of their effective radius. In this analysis we compare the measured void size function with the predictions of the Vdn model, making use of samples of voids identified in the DM particle distribution. We analyse the simulations with different f_{R0} parameters and neutrino masses to build the catalogues of voids, exploiting the same pipeline described Sect. 6.2. To minimise the effect due to the spatial resolution of simulations, we apply the conservative choice of rejecting voids with radii smaller than 5.5 h^{-1} Mpc, corresponding to about 3.5 MGS.

When dealing with voids traced by the DM distribution, no bias prescription is required to rescale void radii. To include in the theoretical model the variations caused by both MG and massive neutrinos on the void size function, we make use of `MGCAMB`[1] (Zhao et al., 2009; Hojjati, Pogosian & Zhao, 2011; Zucca et al., 2019), a modified version of the public Einstein-Boltzmann solver `CAMB`[2] (Lewis, Challinor & Lasenby, 2000), which computes the linear power spectrum for a number of alternative cosmological scenarios, including the Hu & Sawicki $f(R)$ model studied in this chapter.

In Fig. 7.6 we show the results for the ΛCDM, fR4 and fR4_0.3eV models at redshift $z = 0, 0.5, 1, 2$. First of all, we notice that the overall trend of the void size functions measured in the simulations is well reproduced by the models. We considered Poissonian errors, thus the uncertainty on the void counts might be slightly underestimated. In the bottom panels we report the residuals evaluated with respect to the Vdn model computed for ΛCDM case. In particular, the residuals are calculated as the difference between the measured void abundance and the corresponding predicted one for a given model and the theoretical value of the ΛCDM void size function at the same radius, divided by the latter. Then, as expected, at low redshifts the fR4 model predicts a larger number of voids with larger sizes. The modification of gravity induces indeed a faster formation and evolution of cosmic structures, including cosmic voids.

Figures 7.7 and 7.8 show the results of the analysis performed for the remaining cosmological models, given by the set of simulations with $f_{R0} = -10^{-5}$ and $f_{R0} = -10^{-6}$. Also in these cases, the predictions of the Vdn model computed with `MGCAMB` are fully consistent with the measured void abundance. The deviations from the ΛCDM model are weaker in these cases, given the lower values of the f_{R0} parameter. As expected, the departure from the ΛCDM model are the more severe the stronger is the intensity of the fifth force, resulting more evident for large voids, in agreement to what found by Clampitt, Cai & Li (2013b) and Voivodic et al. (2017).

It is interesting to note that, despite at low redshifts the effect of massive neutrinos is effective in bringing the void size function towards the one computed in ΛCDM, this trend starts to revert at higher redshifts. In particular, it is evident that at $z = 2$ the presence of massive neutrinos makes the fR4_0.3eV void size function to depart from the ΛCDM one, causing a weakening of the growth of structures, more evident for voids with larger radii. This is a clear hint of the possibility of disentangling the degeneracies between the standard ΛCDM cosmology and MG with massive neutrino models. However, to achieve this task, it is required to explore the void abundance at high redshifts and in wide areas, in order to collect a sufficiently high number of large voids.

[1] https://github.com/sfu-cosmo/MGCAMB
[2] https://github.com/cmbant/CAMB

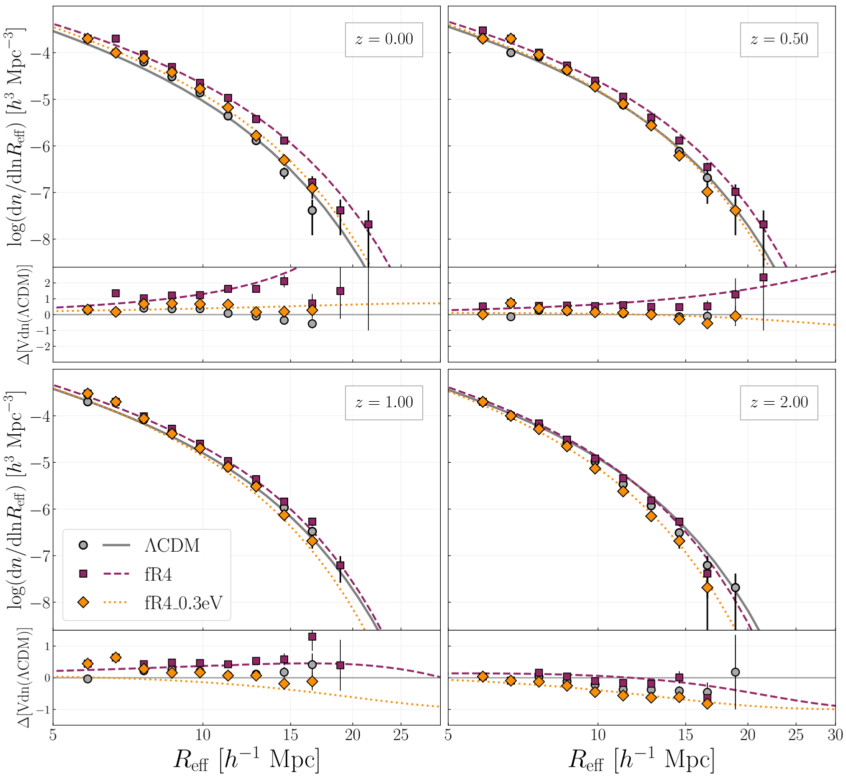

Figure 7.6: Measured and theoretical void size function computed for the ΛCDM, fR4 and fR4_0.3eV models, at redshifts $z = 0, 0.5, 1, 2$. The measured void abundances for each cosmological model are represented by different markers and colours, as described in the label. The errorbars are Poissonian uncertainties on the void counts. The predictions are instead displayed as lines with different colours and styles, according to the model to which they refer. The bottom sub-panel of each of the 4 plots reports the residuals calculated as the difference from the ΛCDM Vdn model divided by the value of the latter, for both the measured and the predicted void abundance.

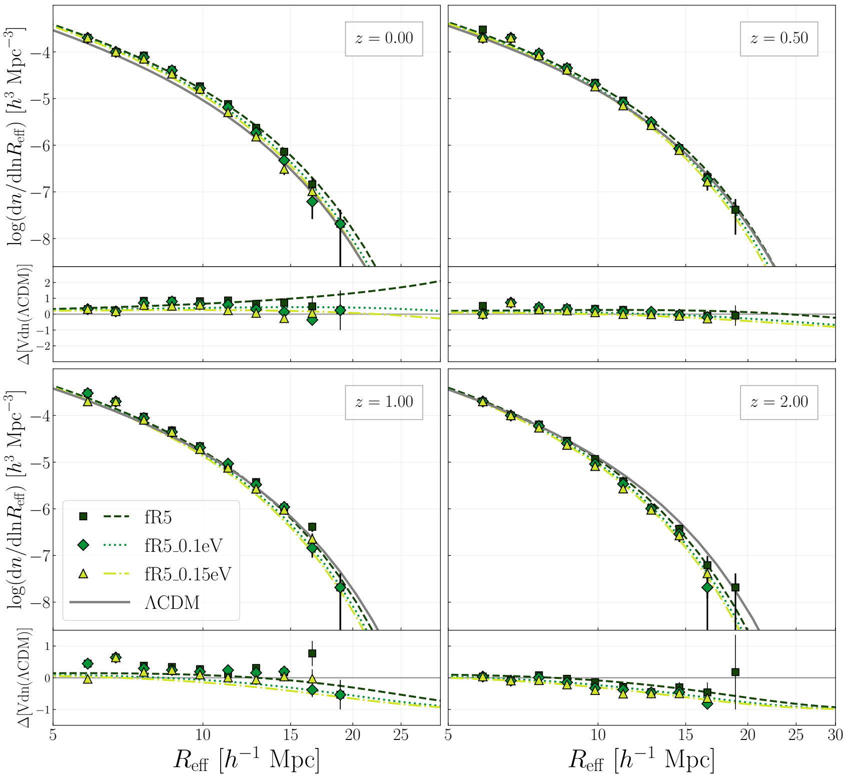

Figure 7.7: Measured and theoretical void size function computed at redshifts $z = 0, 0.5, 1, 2$ for the models fR5, fR5_0.1eV, fR5_0.15eV. The symbols of these plots is analogous to the one reported in the caption of Fig. 7.6.

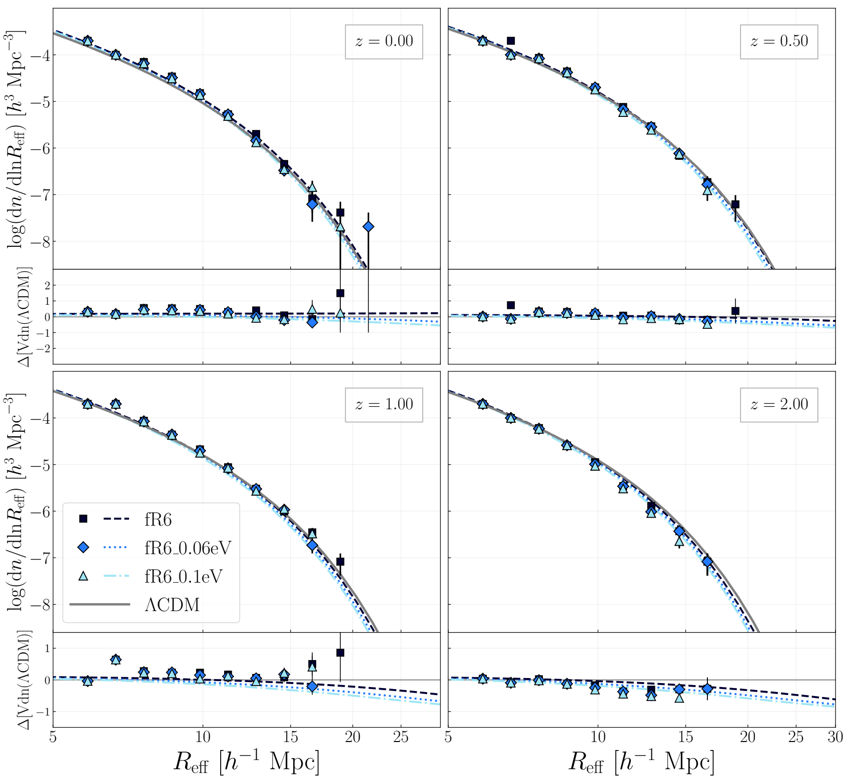

Figure 7.8: Measured and theoretical void size function computed at redshifts $z = 0, 0.5, 1, 2$ for the models fR6, fR6_0.06eV, fR6_0.1eV. The symbols of these plots is analogous to the one reported in the caption of Fig. 7.6.

7.5 Results: void size function in the biased tracer field

As shown in Chapter 6, we need to properly convert the underdensity threshold of the Vdn model to take into account the effect of the tracer bias on the predicted void abundances. We report here the re-parametrisation of the nonlinear threshold we already introduced:

$$\delta_{\mathrm{v,DM}}^{\mathrm{NL}} = \frac{\delta_{\mathrm{v,tr}}^{\mathrm{NL}}}{\mathcal{F}(b_{\mathrm{eff}})} \,, \tag{7.2}$$

with

$$\mathcal{F}(b_{\mathrm{eff}}) = B_{\mathrm{slope}} \cdot b_{\mathrm{eff}} + B_{\mathrm{offset}} \,, \tag{7.3}$$

The computation of the large-scale linear bias b_{eff} from the tracer 2PCF will be not discussed in this chapter, since it is estimated with a methodology analogous to the one described in details in Appendix A.

In Sect. 6.5 we calibrated the linear function $\mathcal{F}(b_{\mathrm{eff}})$ by fitting the values of b_{eff} and b_{punct} computed at different redshifts, using FoF halo catalogues extracted from the CoDECS simulations. We apply now the same procedure using the catalogues described in Sect. 7.1, focusing on those characterised by the ΛCDM cosmology. We consider both the halo catalogues obtained by applying the `Denhf` algorithm with $\Delta_{\mathrm{c}} = 200$ (200c hereafter) and $\Delta_{\mathrm{c}} = 500$ (500c hereafter) to make a comparison between the relations calibrated with halo samples identified by means of different methods.

Figure 7.9 shows the results of this analysis. We report here the linear relations for the 200c and 500c haloes, obtained by fitting the value of b_{punct} (see Eq. 6.4) as a function of b_{eff} at $z = 0, 0.5, 1, 2$. The fit obtained in Sect. 6.5 is also displayed as reference. We note that going from FoF to 200c and 500c haloes, the objects we are considering become more compact and denser. This results in a departure from the bisector of the plane b_{eff}–b_{punct}, representing the relation for matter tracers with an identical behaviour of the bias factor on all the regions of the density field. We find the following results from the fitting of the data at different redshifts:

$$\mathcal{F}(b_{\mathrm{eff}}) = (0.87 \pm 0.02)\ b_{\mathrm{eff}} + (0.36 \pm 0.03) \,, \text{ for 200c} \tag{7.4}$$

and

$$\mathcal{F}(b_{\mathrm{eff}}) = (0.82 \pm 0.02)\ b_{\mathrm{eff}} + (0.37 \pm 0.02) \,, \text{ for 500c} \,. \tag{7.5}$$

The linear function $\mathcal{F}(b_{\mathrm{eff}})$ shows a lowering of the slope related to the increase of the central density selection. We can conclude that the relation required to convert the large-scale effective bias has a slight dependence on the selection criteria applied to define the mass tracers, and that it has therefore to be calibrated according to the type of objects used to identify the voids.

We test also the possible dependence of the function $\mathcal{F}(b_{\mathrm{eff}})$ on the cosmological model. In Fig. 7.10 we report the linear relations found using the 200c haloes to compute both the values of b_{eff} and b_{punct} of the ΛCDM, fR4, fR5 and fR6 models. In this case, considering tracers with the same mass selection, the relation $\mathcal{F}(b_{\mathrm{eff}})$ obtained for the ΛCDM case results statistically indistinguishable from the ones computed for non-standard cosmological scenarios.

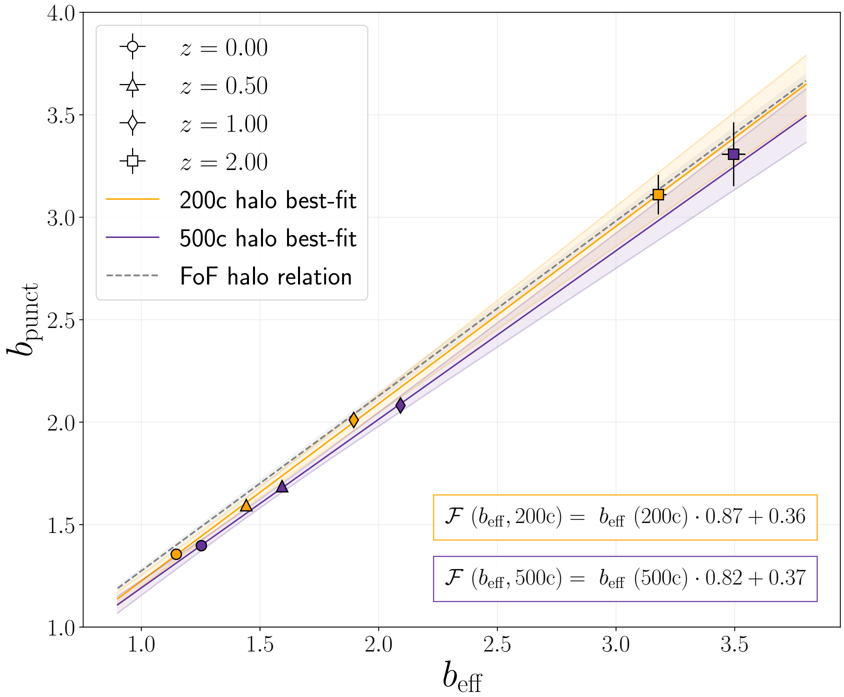

Figure 7.9: Linear relations between $b_{\rm eff}$ and $b_{\rm punct}$, calibrated using different halo catalogues for the standard ΛCDM scenario. The different markers show the data obtained in this section using 200c (in orange) and 500c (in violet) haloes at $z = 0, 0.5, 1, 2$. The fitted relations are shown by solid lines and the corresponding relations are represented in orange and violet for 200c and 500c, respectively. The dashed grey line represents the linear function calibrated in Sect. 6.5, using FoF haloes, extracted from the CoDECS simulations. The uncertainties related to the best-fit models are reported as shaded regions around each linear relation.

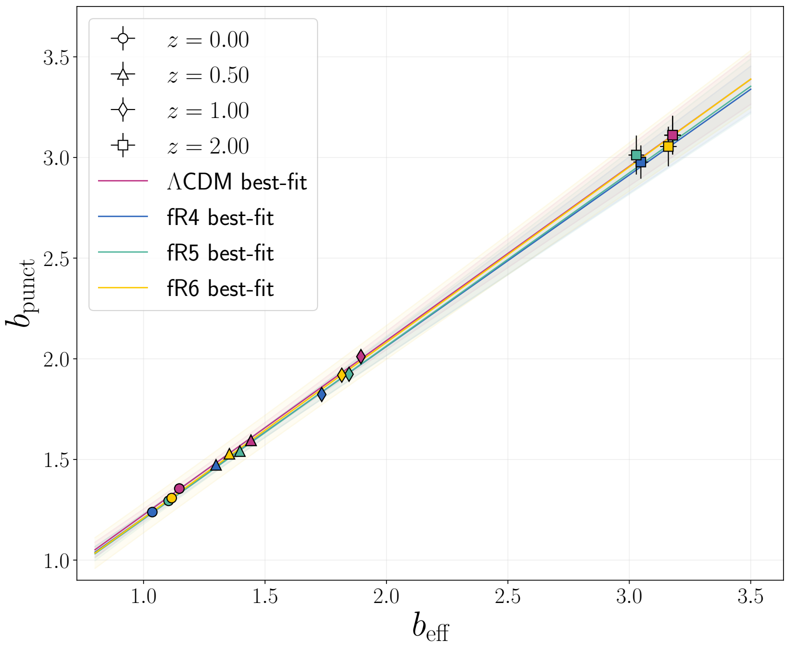

Figure 7.10: Linear relations between b_{eff} and b_{punct}, calibrated by means of 200c halo catalogues in different cosmological models. The different markers show the data obtained using the values computed for the ΛCDM (in magenta), fR4 (in blue), fR5 (in green) and fR6 (in yellow) models at $z = 0, 0.5, 1, 2$. The best-fit linear models are represented by solid lines with the same colours of the correspondent markers, while their uncertainties are reported as shaded areas around these lines.

We finally test the universality of the $\mathcal{F}(b_{\rm eff})$ relation analysing also the models with massive neutrinos, comparing the values of $b_{\rm eff}$ and $b_{\rm punct}$ measured for these scenarios using 200c haloes with those previously shown. As displayed in Fig. 7.11, the linear relation calibrated with the ΛCDM model is fully consistent with the data obtained for all analysed cosmological scenarios. For this reason, in the following analysis we will apply the calibration obtained for the ΛCDM standard scenario to obtain the theoretical void size function for every cosmological model, that is assuming that the $\mathcal{F}(b_{\rm eff})$ relation is universal, for a specific type of tracers.

In the last part of this section we make use of the 200c halo catalogues only, since the higher number of tracers and the lower bias factor ease the identification of voids. However, we tested the validity of the following methods considering also the 500c haloes as tracers, finding consistent, though less precise, results. After obtaining the linear function $\mathcal{F}(b_{\rm eff})$ from the analysis of both the DM particle and 200c halo density distribution, we can now use the coefficients shown in Eq. (7.4) to properly convert the threshold $\delta_{\rm v,tr}^{\rm NL} = -0.7$. This density contrast is used during the cleaning procedure of voids identified in the DM halo field and has to be properly converted to take into account the effect of the bias factor on the theoretical void size function. To this purpose, as explained in Sect. 6.3, we first apply Eq. (7.2) to obtain the nonlinear density contrast in the DM distribution. Then we evaluate its corresponding value in linear theory by means of Eq. (6.3), inserting this quantity in the theoretical expression of the Vdn model.

We repeat this pipeline to compute the theoretical void size function for each cosmological scenario, using `MGCAMB` to obtain the matter power spectrum, required to evaluate both the tracer effective bias, $b_{\rm eff}$, and the square root of the mass variance, $\sigma(z)$. To minimise numerical incompletenesses in the void sample, we discard the regions with $R_{\rm eff}$ less than $[2.75, 2.5, 2.5, 2.25] \cdot$ MPS of the ΛCDM halo catalogues for the redshifts $[0, 0.5, 1, 2]$, respectively (see also Sect. 6.2). In this case we did not apply a fixed cut at small radii to reject the voids affected by sparsity of the tracers. Indeed, contrary to what happens with the DM particles, the MPS of the DM haloes depends on the redshift and the interplay between the spatial resolution of the tracers and the incompleteness of the void number counts is not trivial. Therefore we prefer to apply these conservative selections relying on the drop observed at small radii in the measured void size function at different redshifts. We tested different minimum radius cuts and we verified that lower values would lead to a discrepancy between the measured and the predicted void counts, while higher values would cause a dramatic reduction of the void statistics.

Before starting the analysis of the size function of voids in biased tracers, we want to stress the fact that not only the void size function, but also $b_{\rm eff}$ depends on the presence of the fifth force and massive neutrinos. They are indeed both strongly correlated to the growth of cosmic structures, which is in turn influenced by modification of gravity and neutrino thermal free-streaming. Therefore the rescaling of the underdensity threshold $\delta_{\rm v,tr}^{\rm NL}$ by means of the large-scale effective bias can lead to degenerate effects on the resulting void abundance. A rigorous study of the interplay between these effects on the size function of voids identified using different types of matter tracers is left to future works.

In Fig. 7.12 we report the comparison between the measured void abundance for the ΛCDM, fR4 and fR4_0.3eV models, showing also the corresponding predictions of the extended Vdn model computed for each cosmological scenario. The shaded region around each curve represents the uncertainty derived from the propagation of the error associated

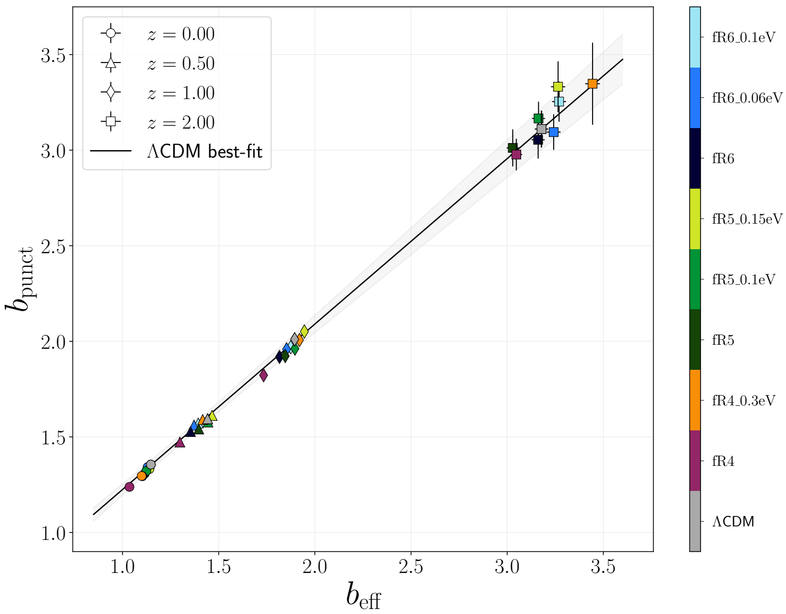

Figure 7.11: Values of $b_{\rm eff}$ and $b_{\rm punct}$ measured using 200c haloes at $z = 0, 0.5, 1, 2$, for all the cosmological models analysed. The colorbar on the right reports the colours associated to each cosmological model. The black line indicates the linear relation obtained by fitting the ΛCDM data only, while the shaded grey region shows its associated uncertainty.

to the value of $b_{\rm eff}$ computed for each case, converted by means of Eq. (7.4), and used to compute the theoretical models. The residuals reported in the bottom sub-panels are computed as the difference from the theoretical void size function of the ΛCDM model, in units of the latter, for both the measured and the predicted abundances. We find a good agreement between the predictions of the extended Vdn model and the measured void size functions. Nevertheless, the cosmic voids found in the DM halo simulations are so rare that the Poissonian noise does not allow us to distinguish a specific trend for the abundances measured in MG and massive neutrinos scenarios. This was previously verified also in other works analysing voids identified in biased tracers using cosmological simulations in MG gravity scenarios or with massive neutrinos (Voivodic et al., 2017; Kreisch et al., 2019b).

In Figs. 7.13 and 7.14 we show the results for the remaining cosmological models. Even more in these cases, the void abundances derived in different cosmologies are hardly discernable from the ΛCDM ones. The signal is stronger at higher redshifts due to the fact that the underdensity threshold used to rescale the voids moves towards values closer to 0 for higher values of $b_{\rm eff}$ (see Eq. 7.2). This causes the growth of the population of large voids and can lead to an overall increase of the number of voids with radii belonging to the range considered in this analysis. However, since this method implies the selection of shallower voids, it will be important to verify the purity of the void sample when it derives from real galaxy surveys, and thus to take into account the possible contamination by Poissonian noise. The accuracy of the measured void counts at high redshifts can be in fact compromised by systematic uncertainties still not parameterised in the model. Nevertheless, in our case the prescriptions adopted to prepare the void samples are proven

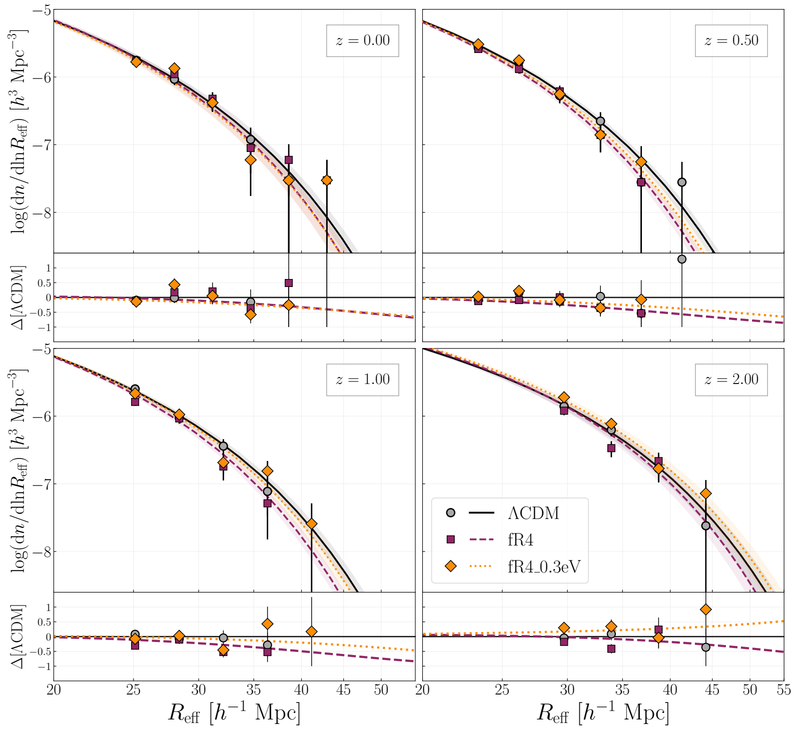

Figure 7.12: Measured and predicted abundances of cosmic voids identified in the distribution of the 200c haloes, extracted from the ΛCDM, fR4 and fR4_0.3eV simulations, at redshifts $z = 0, 0.5, 1, 2$. We represent with different colours and markers the abundances computed for each cosmological scenario, with Poissonian errorbars. The theoretical predictions computed for the considered models are reported with lines of the corresponding colours. The shaded region around each curve represents the uncertainty given by the propagation of the errors during the rescaling of the Vdn underdensity threshold by means of the function $\mathcal{F}(b_{\rm eff})$. The bottom sub-panels report the residuals computed as the difference from the ΛCDM theoretical predictions, divided by the value of the latter, for both the measured and the predicted void abundances.

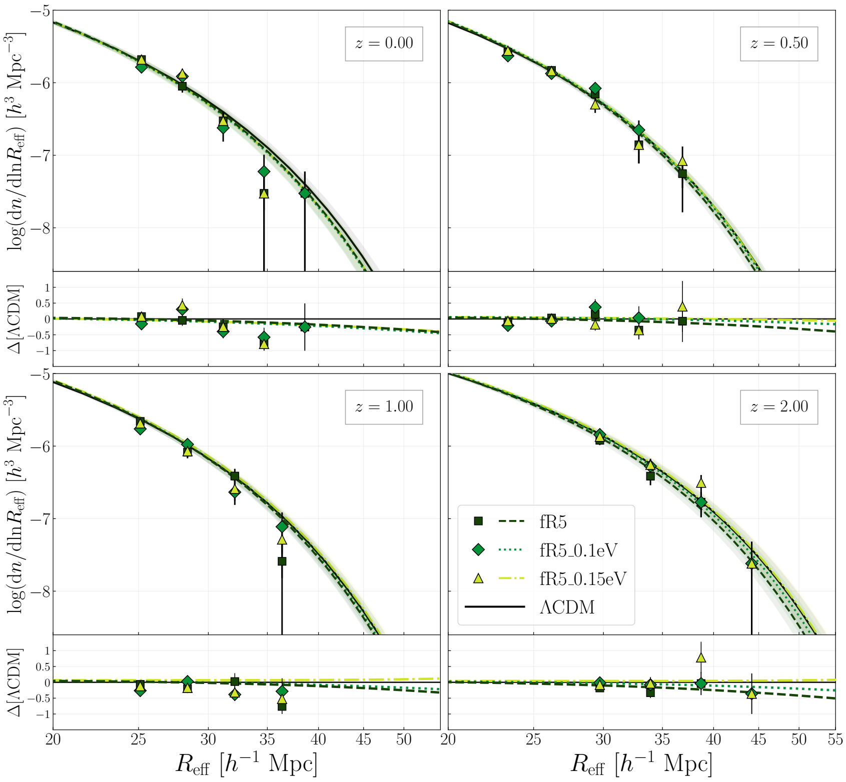

Figure 7.13: Measured and predicted abundances of cosmic voids identified in the distribution of 200c haloes, extracted from the fR5, fR5_0.1eV and fR5_0.15eV simulations, compared to the theoretical void size function for the ΛCDM model. In the bottom sub-panels we report the residuals with respect to the latter. The symbols and the styles are analogous those reported in Fig. 7.12.

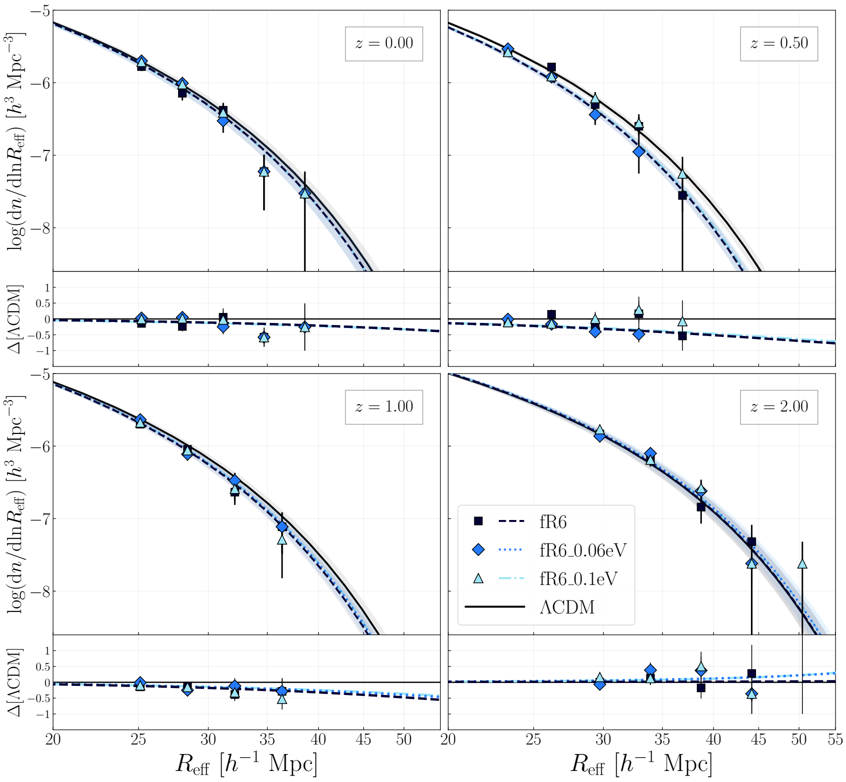

Figure 7.14: Measured and predicted abundances of cosmic voids identified in the distribution of 200c haloes, extracted from the fR6, fR6_0.06eV and fR6_0.1eV simulations, compared to the theoretical void size function for the ΛCDM model. In the bottom sub-panels we report the residuals with respect to the latter. The symbols and the styles are analogous those reported in Fig. 7.12.

to be compliant with the theoretical predictions and do not require further procedures of removal of spurious voids.

We also point out that, although from these plots the void counts could appear reduced in MG cosmologies, this is true in fact only for the large sizes. Looking at the Figs. 7.12 to 7.14, we note that the void size functions in the different cosmological models considered are significantly different only for large radii, an effect that is stronger for higher values of the f_{R0} parameter. While at $z = 0$ the predictions of the Vdn model for MG cosmologies with and without massive neutrinos are statistically indistinguishable, at intermediate redshifts the presence of massive neutrinos causes a shift of the void size function towards the one obtained for the standard ΛCDM model. This trend results even more relevant at $z = 2$, where the effect of the neutrino thermal free-streaming brings the theoretical curve above the one of the ΛCDM case. This outcome might seem counterintuitive, since the presence of massive neutrinos leads effectively to a slow down of the evolution cosmic voids. Nevertheless, this trend has been identified also in Kreisch et al. (2019b) using a methodology similar to the one reported in this Thesis work to select and characterise the void sample. This phenomenon is in fact due to the effect of the adopted bias-dependent threshold, that causes a rescaling of the detected underdensities toward greater radii and appears more evident for larger voids.

This is an obvious indicator of the possibility to use cosmic void abundances to disentangle the degeneracies between MG and massive neutrinos models. However, we recall that the effect of the tracer bias on the void size function may be partially compensated by the one of massive neutrinos and MG models, therefore the trends found in this analysis may be different using other simulations or different tracers (see also Kreisch et al., 2019b).

To facilitate the comparison of these results and maximise the signal obtained from the measured void abundance, we compare now the total void number counts with the abundance computed by integrating the theoretical void size function over the same range of radii. Even if the total void counts is not commonly used to derive cosmological constraints, it can constitute in this case a useful quantity to analyse. Indeed, it allows to perform a simple validation of the predictions of the void size function models, collapsing the information on void number counts related to different spatial scales and sharping the signal achieved from the measured abundances.

We present in Table 7.2 the comparison between the integrated values of the void number counts inferred from the theoretical void size function models and our measurements, for each of the cosmological models and redshifts explored in this analysis. We report also the value of the tracer effective bias, used to re-parametrise the characteristic threshold of the Vdn model. We also show, for completeness, the measured abundance derived from the `VIDE` void catalogues before performing the cleaning procedure[3]. The abundances extracted from the raw `VIDE` void catalogues are significantly larger than those obtained after the cleaning procedure, but they are clearly not in agreement with the Vdn model predictions. This outcome is not surprising since these voids are not defined according to the theory described in Sect. 4.3.

[3]Since the `VIDE` void radii are systematically larger than the ones rescaled by means of the cleaning algorithm (see Sect. 5.3), we applied a more severe cut to discard the voids affected by the sparsity of the tracers. In particular, to minimise the numerical incompleteness for small radii, we increase the minimum radius of the accepted voids by a factor of 1.5 with respect to the selection adopted for the cleaned catalogues.

Table 7.2: The most relevant quantities related to the voids identified in the distribution of 200c haloes. The table is structured in 4 parts, which separate the values computed for different redshifts. Each line shows the set of data relative to each of the cosmological models analysed in this chapter. The values of the tracer effective bias used to re-parametrise the threshold of the Vdn model are reported in the column named $b_{\rm eff}$. The following column provides the void abundances predicted by the theory, obtained by integrating the extended Vdn model over the range of void radii described in this section. Then we report the number of voids extracted from the void catalogues built with `VIDE`, for completeness. The last columns represent the void counts derived from the catalogues of voids, which have been modelled with the cleaning algorithm and counted on the same range of void radii used to compute the theoretical abundances.

Model	$b_{\rm eff}$	Vdn model	`VIDE` voids	Cleaned voids	$b_{\rm eff}$	Vdn model	`VIDE` voids	Cleaned voids
			$z = 0$				$z = 0.5$	
ΛCDM	1.147 ± 0.009	119 ± 16	703 ± 27	109 ± 10	1.44 ± 0.01	193 ± 17	949 ± 31	185 ± 14
fR4	1.036 ± 0.008	111 ± 19	682 ± 26	117 ± 11	1.30 ± 0.01	163 ± 18	912 ± 30	168 ± 13
fR4_0.3eV	1.099 ± 0.009	104 ± 16	703 ± 27	119 ± 11	1.42 ± 0.01	173 ± 17	941 ± 31	199 ± 14
fR5	1.103 ± 0.009	116 ± 17	690 ± 26	112 ± 11	1.40 ± 0.01	192 ± 17	919 ± 30	179 ± 13
fR5_0.1eV	1.124 ± 0.009	112 ± 16	679 ± 26	107 ± 10	1.44 ± 0.01	199 ± 17	930 ± 30	170 ± 13
fR5_0.15eV	1.140 ± 0.009	113 ± 16	683 ± 26	126 ± 11	1.47 ± 0.01	201 ± 17	922 ± 30	177 ± 13
fR6	1.116 ± 0.008	108 ± 16	702 ± 26	96 ± 8	1.35 ± 0.01	149 ± 15	907 ± 30	180 ± 13
fR6_0.06eV	1.131 ± 0.009	107 ± 15	715 ± 27	113 ± 11	1.37 ± 0.01	148 ± 15	900 ± 30	165 ± 13
fR6_0.1eV	1.140 ± 0.009	106 ± 15	723 ± 27	113 ± 11	1.39 ± 0.01	153 ± 15	929 ± 30	173 ± 13
			$z = 1$				$z = 2$	
ΛCDM	1.90 ± 0.01	154 ± 17	734 ± 27	152 ± 12	3.18 ± 0.03	97 ± 17	470 ± 22	92 ± 10
fR4	1.73 ± 0.01	129 ± 13	727 ± 27	108 ± 10	3.05 ± 0.03	92 ± 15	435 ± 21	73 ± 9
fR4_0.3eV	1.92 ± 0.02	147 ± 15	731 ± 27	140 ± 12	3.44 ± 0.04	114 ± 18	469 ± 22	121 ± 11
fR5	1.85 ± 0.01	154 ± 16	750 ± 27	133 ± 12	3.03 ± 0.03	85 ± 14	460 ± 21	73 ± 9
fR5_0.1eV	1.90 ± 0.01	155 ± 16	743 ± 27	120 ± 11	3.16 ± 0.03	93 ± 16	477 ± 22	90 ± 9
fR5_0.15eV	1.95 ± 0.02	164 ± 17	742 ± 27	125 ± 11	3.26 ± 0.04	101 ± 17	479 ± 22	93 ± 10
fR6	1.82 ± 0.01	132 ± 15	744 ± 27	125 ± 11	3.16 ± 0.03	98 ± 17	456 ± 21	96 ± 10
fR6_0.06eV	1.85 ± 0.01	136 ± 16	737 ± 27	136 ± 12	3.24 ± 0.04	103 ± 17	484 ± 22	101 ± 10
fR6_0.1eV	1.87 ± 0.01	136 ± 16	742 ± 27	128 ± 11	3.27 ± 0.04	103 ± 17	468 ± 22	111 ± 11

Now we focus on the comparison of the total counts of cleaned voids with the predictions achieved with the extended Vdn model. The errors associated with the latter are evaluated by propagating the uncertainties related to $b_{\rm eff}$ and $b_{\rm punct}$ during the calibration of the function $\mathcal{F}(b_{\rm eff})$, while those associated with the measured void abundances are assumed to be Poissonian. We can see that the theoretical void abundances are overall consistent with the observed ones, considering the uncertainties on both the values. As expected from the results shown in Figs. 7.12 to 7.14, a significant differentiation between the analysed cosmological models is reached at $z = 2$, despite the scarcity of void counts makes their distinction challenging. Nevertheless, despite the simulations considered in this analysis do not allow us to have enough statistics for large voids at high redshifts, we can conclude that this approach will lead to a relevant contribution in discerning between degenerate cosmological scenarios in wide-field surveys.

Chapter 8

Void size function forecasts for the *Euclid* mission

As already introduced in Chapter 1, the Universe is in a phase of accelerated expansion that we explain mathematically by introducing new component, dominant in terms of energy density, called DE for its unknown nature. The full understanding the origin of Universe's expansion is one of the most compelling challenges of the next decades. The *Euclid* mission is exactly designed to this purpose. *Euclid*'s main goal is the (indirect) study of the nature of DE through the analysis of the observable structures of the Universe. In particular, it aims at determining the DE equation of state (see Sect. 3.1.1) by constraining its constant and time varying terms to a 1σ precision of 0.02 and 0.1 respectively. Moreover, *Euclid* will test the validity of GR by measuring the rate of cosmic structure growth to a 1σ precision of 0.02, sufficient to distinguish GR from a wide range of MG theories (see Sect. 3.1.2). Additionally, *Euclid* will map the DM distribution with unprecedented accuracy, allowing us to reveal also the feeble features produced by the presence of massive neutrinos, whose total mass is expected to be constrained with a 1σ upper limit of 0.03 eV (see Euclid Collaboration: Blanchard et al. (2020) for further details and updated data).

Whether the acceleration is produced by a new scalar field or by modified laws of gravity, its effect will have a different impact on the LSS, leaving imprints that can be effectively discerned by using several orthogonal methods. The *Euclid* mission is indeed optimised for two independent primary cosmological probes: weak gravitational lensing and galaxy clustering. However, given the necessity of breaking the degeneracies between the parameters of the assumed cosmological model, *Euclid* will rely on a large set of secondary and additionally probes. Among these, we have cosmic voids, which has been demonstrated not only to be especially suited for constraining DE and MG theories, as well as the neutrino mass (see Sect. 4.7), but also to show great complementary with the *Euclid* standard probes (see e.g. Biswas, Alizadeh & Wandelt, 2010; Kreisch et al., 2021, and also Sect. 9.2).

In this chapter we introduce the work that will be presented in Contarini et al. (2022, in preparation), which has been carried on within the *Euclid* "Working Package 8: Voids". The main goal of this work is to provide forecasts on the cosmological constraining power of the void size function from the *Euclid* survey. In this analysis we identify voids in the largest *Euclid*-like light-cone, the *Flagship* simulation (Potter, Stadel & Teyssier, 2017).

The latter mimics, although for reduced sky area, the spectroscopic[1] galaxy distribution expected for *Euclid*. We aim at measuring and theoretically modelling the void size function from the Flagship simulation, providing a state-of-the-art forecast for void number counts to be expected from the *Euclid* survey.

8.1 Flagship simulation

In this analysis we employ the version 1.8.4 of the *Euclid* Flagship mock galaxy catalogue. This catalogue is created by running a simulation of two trillion DM particles in a periodic box of $L = 3780\ h^{-1}$ Mpc per side, with a flat ΛCDM cosmology characterised by the parameters $\Omega_\mathrm{m} = 0.319$, $\Omega_\mathrm{b} = 0.049$, $\Omega_\Lambda = 0.681$, $\sigma_8 = 0.83$, $n_s = 0.96$ and $h = 0.67$, as obtained by *Planck* in 2015 (Planck Collaboration et al., 2016a). The simulation box has been converted into a light-cone and the dark matter haloes have been identified using the `Rockstar` halo finder (Behroozi, Wechsler & Wu, 2013, see Sect. 2.3.1 for the details). These haloes have been populated with central and satellite galaxies using a combination of the HOD and HAM methods (see Sect. 2.3.2) to reproduce all the observables relevant for *Euclid*'s main cosmological probes. Specifically, the HOD algorithm has been calibrated exploiting several local observational constraints, using for instance the local luminosity function for the faintest galaxies (Blanton et al., 2003; Blanton et al., 2005) and the galaxy clustering as a function of luminosity and colour (Zehavi et al., 2011). This galaxy sample is composed of more than two billion objects and presents a cut at magnitude $H < 26$ or equivalently on the Hα flux $f_{\mathrm{H}\alpha} > 2 \times 10^{-16}$ ergs s^{-1} cm^{-2}, which mimics the observation range expected for *Euclid*. To match the completeness and the spectroscopic performance expected for the *Euclid* survey, we uniformly downsample the galaxy catalogue to consider only 60% of the galaxies originally included in it. Furthermore we associate a Gaussian error of $\sigma_z = 0.001$ to the redshift of each galaxy (Euclid Collaboration: Blanchard et al., 2020). The full catalogue spans a large redshift range, up to $z = 2.3$, and covers one octant of the sky (close to 5157 deg^2).

The *Euclid* satellite will observe $\sim 15\,000$ deg^2 of the sky with patches that extend up to ~ 6000 deg^2. The total area covered by the satellite will be significantly larger than the available Flagship area. By rescaling it, we can approximately compute the full predicting power from *Euclid*. The larger *Euclid* survey coverage will allow us to increase statistics, reducing the size of the error bars in particular for the high radius end of the void size function, and to better account for super-sample covariance. On the other hand, the *Euclid* survey is expected to have a less regular pattern than the Flagship box, which might affect the void statistics. Conversely to galaxies, voids are strongly sensitive to survey area specifics because of their extended nature: while contiguous regions are a great advantage for void search, as they provide larger voids, void statistics can be reduced in the case of patchy survey coverage, because voids touching survey edges must be excluded from the analysis. However, we expect these effects, not included in our analysis, to not impact significantly the precision of our cosmological forecasts.

We focus our analysis on the expected sub-sample corresponding to *Euclid* spectroscopic data, selecting galaxies from redshift 0.9 to 1.8. We obtain a resulting mock cat-

[1]Despite the spectroscopic galaxy sample is characterised by lower number of objects and redshift coverage with respect to the photometric one, it allows us to achieve a particularly accurate and reliable identification of cosmic voids thanks to its small galaxy redshift errors.

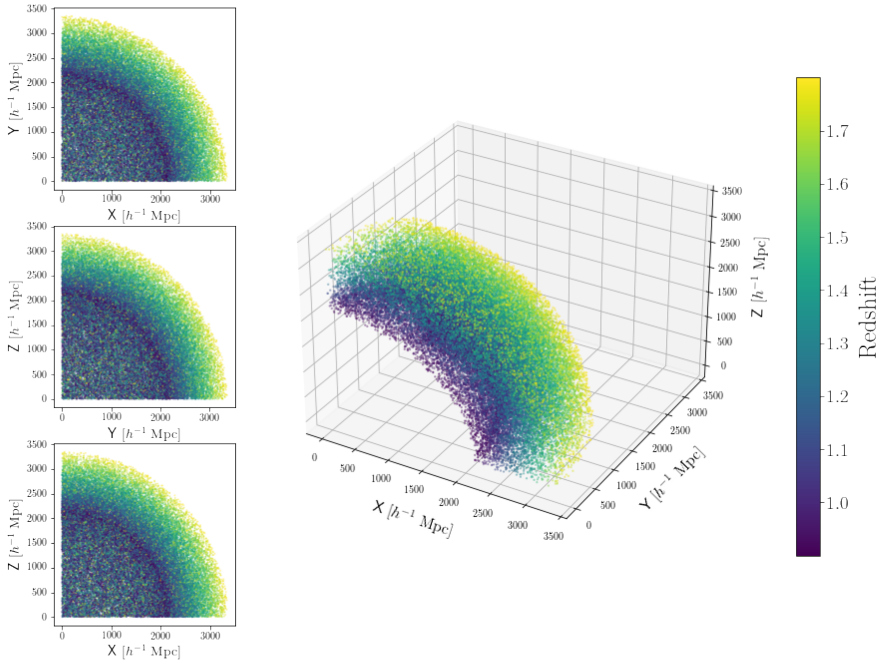

Figure 8.1: Galaxy distribution in the Flagship simulation octant projected on the three coordinate axes (*left*) and represented in 3D (*right*). In different colors the galaxies from $z = 0.9$ to $z = 1.8$.

alogue composed of about 6.5×10^6 galaxies, having the spatial distribution of a shell of sphere octant. We report in Fig. 8.1 the distribution of the objects belonging to the selected sample.

8.2 Void catalogues

We build void catalogues using `VIDE` from the galaxy sample both with real and redshift-space coordinates, given by true and observed redshifts respectively. Note that the redshift-space catalogue is identical to the one used by Hamaus et al. (2022) (see also Sect. 9.1.1). As we saw in Sect. 4.6.2, in the true redshift catalogue, the galaxy redshift corresponds to the cosmological one only, while in the observed redshift catalogue it corresponds to the cosmological plus Doppler shift due to the peculiar velocity. `VIDE` takes into account the presence of a survey mask, and prevents voids from including volumes outside the survey extent. We apply the mask following the simulated $\sim 5000\ \mathrm{deg}^2$ octant. While the actual *Euclid* data will be more complex (due to e.g. more elaborate survey mask and survey-related systematic effects), this methodology partially accounts for mask effects in our pipeline, preparing the analysis of future *Euclid* data.

We further process the void catalogues following the same pipeline reported in Sect. 6.2. In this case, the cleaning algorithm is applied to a light-cone so the entire procedure is performed by taking into account the variation of the tracer density with redshift. In Fig. 8.2 we report some properties of the galaxy and void catalogues considered. We show

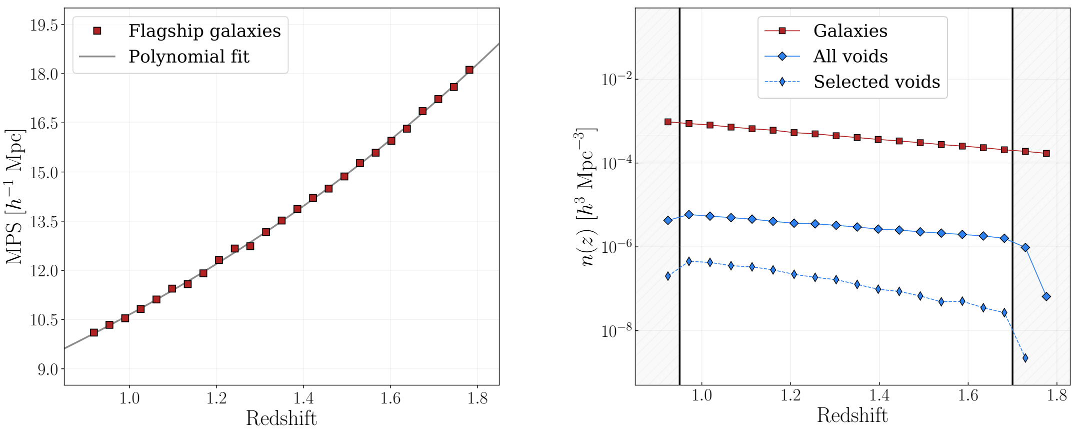

Figure 8.2: Properties of the *Euclid*-like galaxies of the Flagship simulation and of the void samples built. *Left*: MPS as a function of the redshift computed for the sample of galaxies extracted with the same specifics expected for the *Euclid* mission. We represent with a grey line the 3rd-order polynomial used to reproduce the trend of this quantity. *Right*: number density of galaxies (in red) and voids (in blue) of the Flagship sample. We show the values relative to the void catalogue built with `VIDE` and after the cleaning procedure, both with a minimum void radius $R > 2\,\mathrm{MPS}$, with a solid and a dashed line respectively. The two bands on the sides represent the ranges of redshift excluded from the analysis due to the uncertainty of voids identified near the survey edges.

the variation of the galaxy catalogue MPS[2], in the left and we use a 3rd-order polynomial to reproduce this trend: the coefficients of this fit can be used in the cleaning algorithm to prepare the sample of voids identified in the same distribution of galaxies. The public version of the cleaning algorithm we developed (see Sect. 5.3) incorporates also this tool. In right plot of Fig. 8.2 we report the number density of the galaxy and the void catalogue, the latter considered both before and after the cleaning procedure. Here, we can notice the strong impact of the preparation of the void sample to make it suitable for the exploitation of the number counts.

Aiming to a very conservative void selection at the edges of the survey's footprint, we apply an additional cut to ensure the mask is not affecting the cleaning procedure: we remove all voids whose centre is closer than 30 h^{-1} Mpc to the edge and correct the model accordingly for the selected volume. We then prune voids at low and high redshifts to further avoid selection effects given by redshift boundaries of the light-cone, and we divide the sample in 6 redshift bins. This number is found as the optimal compromise between maximising the number of redshift shells and keeping void numbers in bins high enough to avoid falling in the shot-noise dominated regime. In order to have shells with roughly the same number of cleaned voids identified in redshift space and to avoid border effects at the light-cone redshift boundaries, we selected the following redshift bin edges: $z_i = [0.950, 1.035, 1.126, 1.208, 1.318, 1.455, 1.700]$. Each shell contains at least 340 voids, within the range of effective radii considered in the analysis of the measured void size function described below.

[2]We computed the value of the mean inter-galaxy separation as $\mathrm{MPS} = (V_{\mathrm{shell}}/N_{\mathrm{gal}})^{1/3}$, where V_{shell} is the volume of the redshift shell analysed and N_{gal} is the number of galaxies present in it.

Table 8.1: Void counts measured in the redshift-space mock galaxy catalogue considering the redshift bins and selections used for this analysis. The first column represents the minimum and the maximum redshift values for each bin, while the second and the third columns provide the volume in units of $(h^{-1}\ \mathrm{Gpc})^3$ corresponding to each shell of the sky octant, and the MPS, respectively. The fourth column reports the factor, $\mathrm{f}(z)$, used to select voids unaffected by the incompleteness of counts. The last two columns show the number counts of voids identified by the `VIDE` void finder with $R > \mathrm{f}(z)\,\mathrm{MPS}$ and of voids obtained after the cleaning procedure with $R_{\mathrm{eff}} > \mathrm{f}(z)\,\mathrm{MPS}$, respectively. In the last row we show the total volume of all redshift shells, the mean MPS and $\mathrm{f}(z)$ values and the total void counts corresponding to the entire range of redshifts.

z range	shell volume $[(h^{-1}\ \mathrm{Gpc})^3]$	MPS $[h^{-1}\ \mathrm{Mpc}]$	$\mathrm{f}(z)$	all voids	voids after cleaning
0.950 – 1.035	1.157	10.28	2.30	4989	343
1.035 – 1.126	1.329	11.02	2.24	4935	343
1.126 – 1.208	1.269	11.74	2.18	4232	342
1.208 – 1.318	1.796	12.63	2.12	5302	341
1.318 – 1.455	2.363	13.51	2.06	5935	342
1.455 – 1.700	4.490	14.45	2.00	8435	343
0.950 – 1.700	12.40	13.69	2.15	33828	2054

To exclude the spatial scales affected by void number count incompleteness (see Sect. 6.2) we remove voids with radii smaller than MGS $\cdot$ f(z), where f(z) is a factor dependent of the redshift of the sample. The factor f(z) is chosen empirically based on the departure of void number counts from the trend given by the theoretical model. We find that values spanning from 2.3 (lowest redshift bin) to 2 (highest redshift bin) for f(z) ensure the exclusion of spatially unresolved voids in redshift space. Since we expect the resulting void size function in redshift space to be shifted towards greater effective radii due to the effects of RSD (Pisani, Sutter & Wandelt, 2015; Zhao et al., 2016; Nadathur, 2016; Correa et al., 2020), we extend the minimum radius for the real-space case, adding an extra bin at small radii while keeping the same binning of the redshift-space case for higher bins. We verified that these choices allow us to be outside of the number count incompleteness regime, for both the void size function in real and redshift space.

In Table 8.1 we show the number counts of voids selected from the redshift-space mock galaxy catalogue. For each of the redshift bins with edges z_i we report the volume occupied by the shell and the MGS of the tracers, together with the factor f(z) used to compute the minimum void radius considered in this analysis. For completeness, we show the void number counts both before and after the cleaning procedure. The sharp decrease of the void number is an expected outcome of the cleaning procedure, which selects the largest and deepest underdensities identified by `VIDE` and rescales their sizes towards smaller values, causing a more severe rejection of voids during the removal of the spatial scales affected by the incompleteness of counts. Although this conservative approach leads to a loss of the void size function constraining power, it ensures the selection of an high-purity void sample and a robust treatment of void number counts.

8.3 Calibration methodology

To extract cosmological constraints from void number counts we follow a procedure analogous to the pipeline described in Sect. 6.5. We aim therefore at calibrating the parameters of the Vdn model (see Sect. 4.3) extended by means of a linear function of the large-scale effective bias, $\mathcal{F}(b_{\mathrm{eff}})$ (see Eq. 7.2). However, in this case the coefficients of this relation, B_{slope} and B_{offset}, cannot be calibrated exploiting the ratio of void profiles measured in the DM particle and in the mass tracer field as in Chapters 6 and 7. Indeed, the simulations we employed do not provide information on the total matter density field, but only on observable objects (galaxies in our case). The alternative approach we follow is to calibrate B_{slope} and B_{offset} by fitting the void number counts measured with Flagship simulation, both in real and in redshift space. This methodology allow us to calibrate the size function model directly from cosmic void data expected for *Euclid*.

Aside from the measured number counts, the other ingredient we need to calibrate the void size function model the large-scale effective bias, b_{eff}. We compute this quantity in the redshift shells presented in Sect. 8.2 applying the technique described in Appendix A. We underline that the relative error associated to b_{eff} is expected to be smaller than the real one because of the strategy used to compute it, i.e. relying on the galaxy catalogue in real space and assuming the true cosmological parameters of the simulation. A more complete and realistic treatment will be performed in the future, including in the analysis the modelling of the multipoles of the 2PCF, which will allow us to take into account the effects of redshift-space and geometrical distortions (see e.g. Scoccimarro, 2004; Taruya, Nishimichi & Saito, 2010; Beutler et al., 2017; Pezzotta et al., 2017). Additionally, an alternative methodology to extract the Flagship galaxy bias is to follow e.g. Tutusaus et al. (2020), who parametrised the Flagship galaxy bias as a function of z, albeit for the photometric redshift selection.

At this point, we can extract the value of $B_{\rm slope}$ and $B_{\rm offset}$ by leaving them as free parameters with uniform priors of the extended Vdn model: we fit simultaneously all the measured void number counts at different redshifts, considering also a Gaussian prior for $b_{\rm eff}$ at each redshift. We notice that, since the error on the effective bias only corresponds to a few percent of its value, the variation allowed for this parameter during the fit is small. All the remaining cosmological parameters are kept fixed to the Flagship simulation values during this calibration.

8.4 Bayesian statistical analysis

In this chapter we use a reliable method to forecast the sensitivity of the void size function in constraining the cosmological model, based on a parameter extraction from Bayesian likelihood analysis with MCMC (Perotto et al., 2006; Wang et al., 2009; Lahav et al., 2010; Martinelli et al., 2011; de Bernardis et al., 2011; Wolz et al., 2012; Hamann, Hannestad & Wong, 2012; Khedekar & Majumdar, 2013; Audren et al., 2013).

In order to forecast the sensitivity of the void counts in *Euclid*, we have first to consider that the Flagship simulation covers about 1/3 of the *Euclid* survey. So w obtain the *Euclid* predicted void number counts relying on the theoretical void size function model validated on the Flagship simulation. In particular, we consider a fiducial ΛCDM cosmology having the cosmological parameters of the Flagship (see Sect. 8.1) and the calibration of the extended Vdn model with redshift-space void abundances (which results will be presented in Sect. 8.6). Then we assume the same binning of void radii employed in our Flagship analysis but we extend the void number count prediction to a survey area matching the one expected for *Euclid* (roughly 3 times the Flagship area), by rescaling the Poissonian errors of the void number counts consistently by a factor $\sqrt{3}$.

This allows us to use an MCMC analysis to explore the posterior distribution in the parameter space without any assumption on the Gaussianity of parameter distributions and local approximations around the fiducial values, as in Fisher forecasts (Fisher, 1935). Moreover, according to the Cramér-Rao inequality, the Fisher matrix gives a lower bound on the parameter errors (Kendall, Stuart & Ord, 1987), while the MCMC is proven to be more realistic, in particular in the presence of degeneracies (Perotto et al., 2006; Wolz et al., 2012; Audren et al., 2013; Sellentin, Quartin & Amendola, 2014). Finally, this kind of approach allows us to compute unbiased constraints, with confidence contours centred on the Flagship simulation cosmological parameters and on the calibrated nuisance parameters $B_{\rm slope}$ and $B_{\rm offset}$.

According to Bayes's theorem, given a set of data $\mathcal{D}$, the distribution of a set of parameters Θ in the cosmological model considered is given by the posterior probability:

$$\mathcal{P}(\Theta|\mathcal{D}) \propto \mathcal{L}(\mathcal{D}|\Theta)\, p(\Theta)\,, \tag{8.1}$$

where $\mathcal{L}(\mathcal{D}|\Theta)$ is the likelihood and $p(\Theta)$ the prior distribution. Since in this chapter we consider the number counts of cosmic voids, the likelihood can be assumed to follow

Poisson statistics (Sahlén, Zubeldía & Silk, 2016):

$$\mathcal{L}(\mathcal{D}|\Theta) = \prod_{i,j} \frac{N(r_i, z_j|\Theta)^{N(r_i,z_j|\mathcal{D})} \exp\{[-N(r_i, z_j|\Theta)]\}}{N(r_i, z_j|\mathcal{D})!}\,, \tag{8.2}$$

where the product is over the radius and redshift bins, labeled as i and j respectively. The $N(r_i, z_j|\mathcal{D})$ quantity corresponds to the number of voids in the i-th radius bin and j-th redshift bin, while $N(r_i, z_j|\Theta)$ corresponds to the expected value in the cosmological model considered, given a set of parameters Θ. In our case, the former is obtained from the Flagship analysis (with the void size function model validated on the Flagship simulation, but considering that the *Euclid* area will be 3 times larger), while the latter is given by the predictions of the void size function model varying the considered cosmological parameters Θ.

In performing the MCMC analysis, the mapping between redshift and comoving distance changes with the cosmological parameters assumed at each step of the chain. As we saw in Sect. 4.6.1, this introduces geometrical distortions for all the considered sets of cosmological parameters (different from the true one). We used a fiducial cosmology to build up the void catalogue, and, in computing the likelihood, we theoretically account for the distortion effects on the quantities we measured. In particular, geometrical distortions can be modelled with two effects: they vary the inferred survey comoving volume and introduce the AP effect (see Sect. 4.6.1). The effect on the survey volume impacts the number of voids expected in the survey. Therefore, to obtain the total number of voids, the theoretical number density of voids given by the Vdn model has to be multiplied by the volume, which is impacted by the cosmology. On the other hand, the AP distortion affects the size of voids and introduces an anisotropy between the orthogonal and the parallel direction with respect to the line-of-sight. As we saw in Sect. 4.6.1, these quantities can be expressed through Eq. (4.19) and consequently the true effective void radius can be derived as reported in Eq. (4.22). In this case the true cosmology is assumed in each MCMC step and is used to computed the expected void size function, which is shifted as a function of the fiducial cosmology via the AP correction. We checked the validity of the method varying the cosmology used to get the comoving distances from redshifts and consequently correcting the radius $R_{\rm eff}$ at which voids reach the underdensity threshold $\delta_{\rm v,tr}^{\rm NL}$.

With this approach we are implicitly assuming the void centres to remain at the same locations at different cosmologies. Indeed, while void shapes can suffer from symmetric geometrical distortions, this marginally affects the identification of void centres, and the effect is even smaller since the void size function is an averaged quantity. Furthermore, the variation caused by the change of the cosmological parameters on void radii is taken into account by the modelling of the AP effect, therefore the cleaning procedure is applied only once to the void sample, considering a fiducial ΛCDM cosmology. We finally note that the combination of the two effects – volume effect acting on the expected number density, and the AP effect acting on the void sizes – enhances the constraining power of the void size function.

8.5 Cosmological forecast models

In this chapter we aim at investigating the constraining power of the void number count statistic on cosmological parameters, focusing in particular on the DE equation-of-state parameters. We consider two cosmological models, extending the standard ΛCDM with different DE equation of states. The first model, wCDM, implements a constant DE equation of state w; the second one, $w_0 w_a$CDM, parametrises dynamical DE models with the popular CPL equation of state (Chevallier & Polarski, 2001; Linder, 2003) (see Sect. 3.1.1). Both cosmological models consider a flat universe. The MCMC analysis of each cosmological model is performed focusing on different sets of free cosmological parameters: together with the DE equation of state parameters (i.e. w or w_0 and w_a, depending on the cosmological model) the density parameter $\Omega_{\rm m}$ or the sum of neutrino masses M_ν are allowed to vary. Moreover, both the cases are analysed with two different approaches:

(i) fixing the parameters of the extended Vdn model, $B_{\rm slope}$ and $B_{\rm offset}$, to the median values obtained from the calibration performed with Flagship data (label: "fixed calibration");

(ii) allowing $B_{\rm slope}$ and $B_{\rm offset}$ to vary in the parameter space described by a 2D Gaussian distribution centred on their median values and given by the calibration with the Flagship mock catalogue (label: "relaxed calibration").

The two adopted approaches are meant to demonstrate the impact of the calibration that will be performed in Sect. 8.6 on the cosmological forecasts. In this Thesis work the constraints on the parameters $B_{\rm slope}$ and $B_{\rm offset}$ are indeed limited to the statistical relevance of the number counts of voids identified by means of the Flagship galaxies. The case in which the cosmological forecasts are computed fixing $B_{\rm slope}$ and $B_{\rm offset}$ to their exact calibrated values represents therefore an optimistic evaluation of the results that we may obtain in the future thanks to the usage of larger mock catalogues, or by means of a fully theoretical modelling of the tracer bias inside cosmic voids (see Sect. 6.4).

The cosmological model considered for the analysis is characterised by a primordial comoving curvature power spectrum amplitude fixed to the Flagship simulation value, $A_s = 2.11 \times 10^{-9}$. We follow the strategy to fix this parameter in order to mimic the future application to real data, which will be supported by the impressive constraints obtained from the study of CMB anisotropies by Planck Collaboration et al. (2020a). Thanks to this approach, for each MCMC step we can derive σ_8, i.e. the root mean square mass fluctuation in spheres with radius 8 h^{-1} Mpc. We rely on `CAMB` to compute this quantity as a derived parameter, which depends on all the cosmological parameters involved in the evolution of the matter power spectrum $P_{\rm m}(k)$.

The density parameter $\Omega_{\rm m}$ is computed as the sum of CDM, baryon and neutrino energy densities, $\Omega_{\rm m} = \Omega_{\rm cdm} + \Omega_{\rm b} + \Omega_\nu$, and its variation in the Bayesian statistical analysis is balanced by the changing of the DE density parameter, $\Omega_{\rm de}$, to keep flat the universe's geometry, $\Omega_{\rm de} = 1 - \Omega_{\rm m}$.

The implementation of massive neutrinos in the MCMC analysis is performed considering the sum of the mass of neutrinos as a free parameter in the cosmological model. Neutrinos are modelled with one massive eigenstate and two massless ones, assuming an effective number of neutrino species $N_{\rm eff} = 3.04$ (Froustey, Pitrou & Volpe, 2020; Bennett et al., 2020) and relating the neutrino mass to the neutrino density parameter as

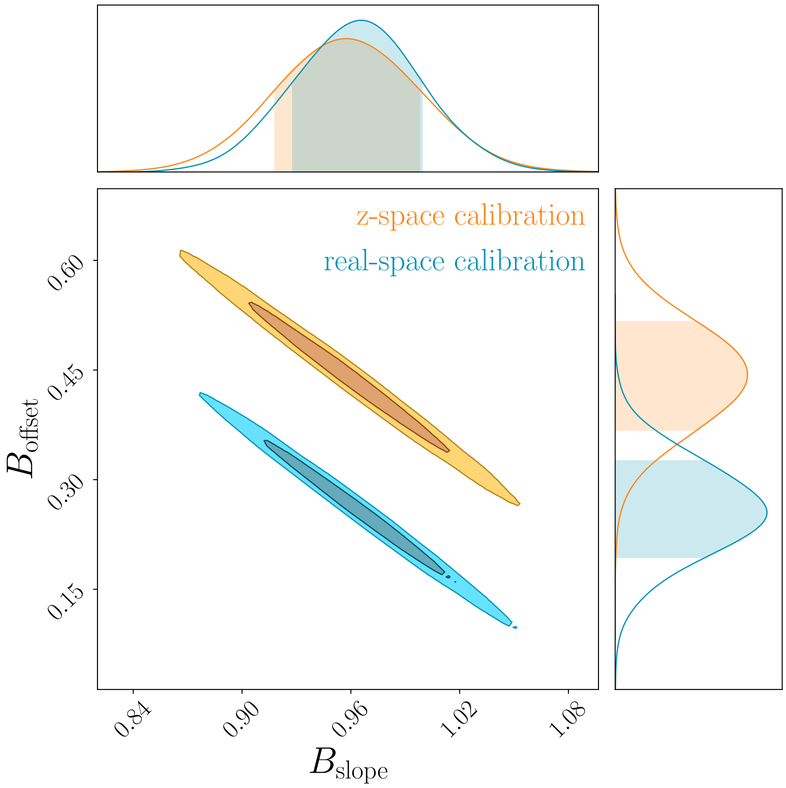

Figure 8.3: Posterior distribution of the parameters of the extended Vdn model, calibrated with Flagship simulation. 1σ (68%) and 2σ (95%) confidence levels in the $B_{\rm slope}$–$B_{\rm offset}$ plane for the void catalogues built both in real (blue) and in redshift space (orange).

Eq. (3.23), in analogy to what we did in Chapter 7. We include the variation of the neutrino density parameter, Ω_ν, in the MCMC analysis, by keeping the value of the total matter density $\Omega_{\rm m}$ fixed (see Sect. 8.1), thus rescaling consistently the CDM parameter $\Omega_{\rm cdm}$. We rely on `CAMB` for the computation of the total matter power spectrum used to predict the theoretical model of the void size function.

8.6 Results: calibration and comparison with mock data

In this section we use the Flagship mock catalogues to perform the calibration of the free parameters of the extended Vdn model and consequently we compare our theoretical predictions with measured void number counts. With the prescriptions described in Sect. 8.3 we obtain the confidence levels reported in Fig. 8.3, for the void size function measured in both real and redshift space. The resulting coefficients for the calibrated relations are:

$$\mathcal{F}(b_{\rm eff}) = (0.96 \pm 0.04)\; b_{\rm eff} + (0.44 \pm 0.07)\;, \tag{8.3}$$

$$\mathcal{F}(b_{\rm eff}) = (0.96 \pm 0.03)\; b_{\rm eff} + (0.26 \pm 0.06)\;\;, \tag{8.4}$$

for the redshift-space and the real-space void abundance, respectively.

We show in Fig. 8.4 the corresponding linear relations obtained with these calibrations, with a shaded area representing an uncertainty of 2σ. As a comparison, we present in the

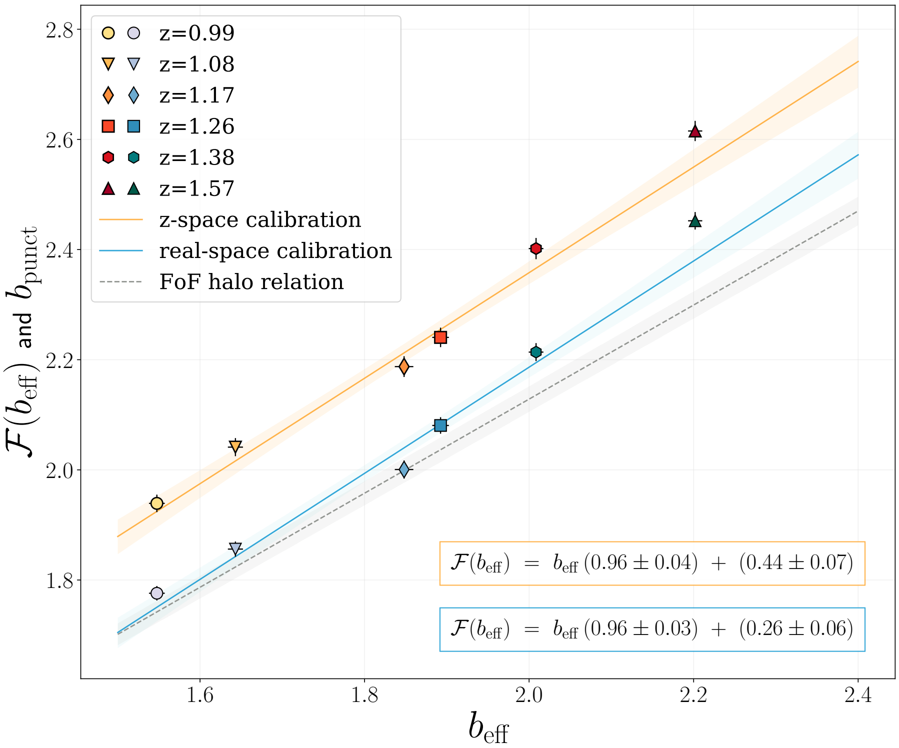

Figure 8.4: Calibration of the relation $\mathcal{F}(b_{\rm eff})$, required for the conversion of the threshold $\delta_{\rm v,tr}$ in Eq. (7.2). The solid lines represent the resulting linear relations $\mathcal{F}(b_{\rm eff})$ obtained with the calibrated coefficients $B_{\rm slope}$ and $B_{\rm offset}$ for real (blue) and redshift space (orange), while the shaded regions indicate an uncertainty of 2σ on the relationships. The markers represent the calibration obtained for each bin of redshift, leaving $b_{\rm punct}$ as the only free parameter of the void size function model when fitting the measured void number counts. This alternative calibration provides a value of $b_{\rm punct}$ for each redshift of the sample and is associated with the value of the effective bias $b_{\rm eff}$ of the Flagship galaxies at that specific redshift. As a comparison we also show the linear function we calibrated Sect. 6.5 using FoF DM haloes in real space, displayed with a dashed grey line.

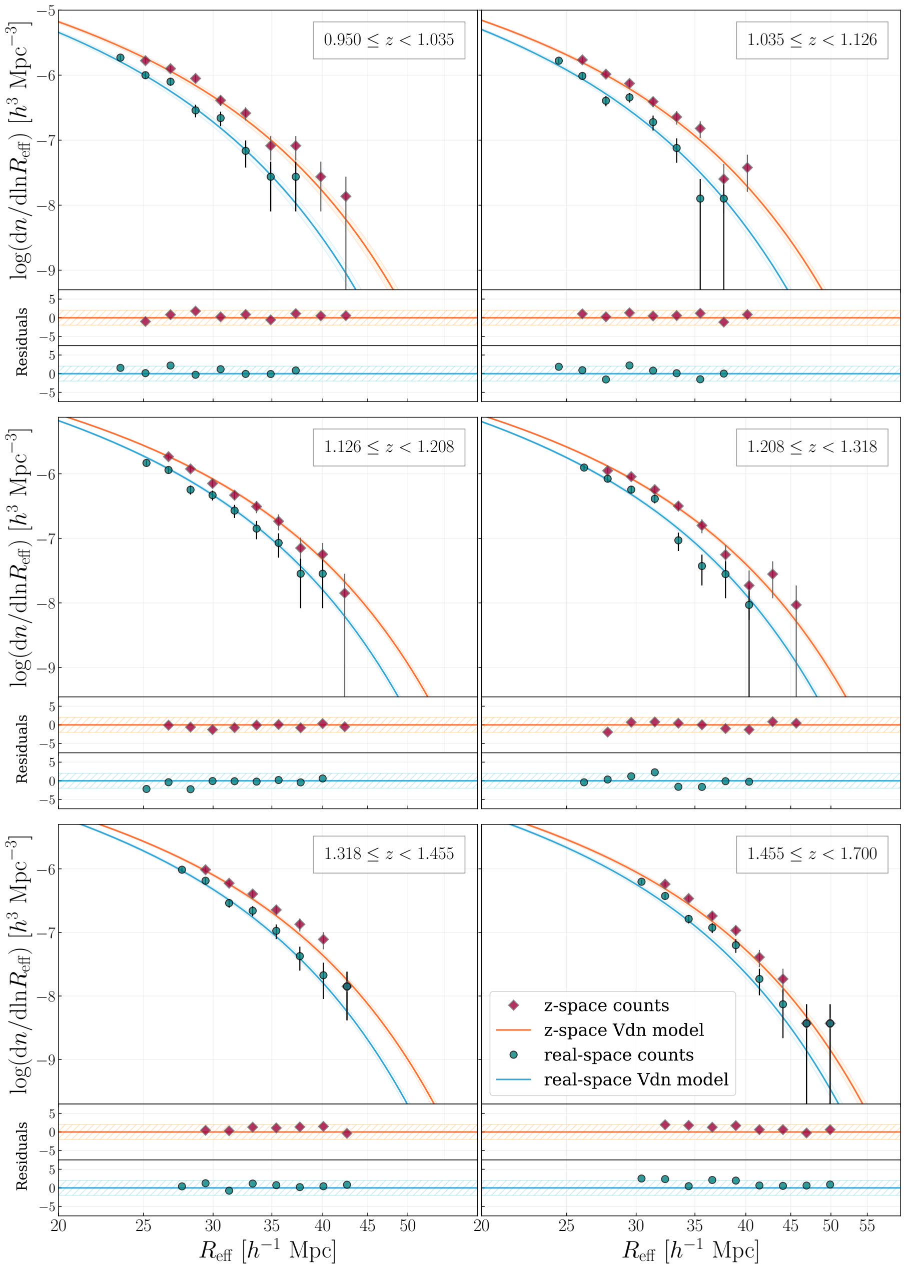

Figure 8.5: Comparison between the measured void number counts as a function of R_{eff} and the theoretical predictions given by the extended Vdn model, in 6 different redshift bins. The dark green circles and the dark red diamonds represent the measured void size functions in real and redshift space, respectively, while the corresponding model predictions are depicted in light blue and orange. The shaded regions indicate the uncertainty of 2σ assigned to the model through the calibration of the extended Vdn parameters. Bottom panels report the residuals computed as the difference of data points from the relative theoretical model, divided by the Poissonian error associated with each data point. The hatched regions represent a band with amplitude 2 useful to check if the data points, considered with a 2σ error, are compatible with the main theoretical curve.

same plot the 6 values computed for $b_{\rm punct}$, leaving it as the only free parameter of the model and fitting separately the measures at different redshifts. In other words, we fit the measured void number counts for each redshift bin using the Vdn model and rescaling its underdensity threshold (expressed in nonlinear theory) as:

$$\delta^{\rm NL}_{\rm v,DM} = \frac{\delta^{\rm NL}_{\rm v,tr}}{b_{\rm punct}}\,, \tag{8.5}$$

making $b_{\rm punct}$ free to vary in the MCMC model. This analysis is aimed at testing the precision of the calibrated relations for each redshift: in Fig. 8.4 the markers with the best match with the linear relations correspond in Fig. 8.5 to the redshift bins for which the calibrated model more accurately reproduces the measured void number counts, while points that depart from the linear relationship in Fig. 8.4 will lead to a slightly worse agreement between theory and model in Fig. 8.5.

Finally, in the plot (Fig. 8.4) we report also the calibration obtained in Sect. 6.5, represented in grey in Fig. 8.4. At lower redshifts the calibration we measured in this chapter is in good agreement with the calibration from the CoDECS simulation, characterised by a WMAP7 cosmology (Komatsu et al., 2011), but it slightly deviates from the latter at higher redshift values. The reason for this minor deviation is twofold. Firstly it is linked to the kind of cosmic tracers (i.e. DM haloes or galaxies) and the selection criteria (i.e. minimum mass or magnitude) used to identify the voids (see Sect. 7.5). Secondly it is related to the fact that in Sect. 6.5 the calibration was performed for redshift from 0 to 1, while here we are testing this relationship beyond this range. The physics underlying the function $\mathcal{F}(b_{\rm eff})$ and its relation with the cosmological objects used to trace the voids will be investigated in future works.

More importantly, since the void size function will be measured on real data from the *Euclid* survey, we have to deal with voids detected in redshift space. As we saw in Sect. 4.6.2, the overall effect of RSD on voids, relevant for the void size function, is an apparent enlargement of the volume of voids, due to the elongation along the line of sight. This is reflected in a mean shift of the measured void size function towards greater radii. Even if this effect can in principle be theoretically modelled[3] (Pisani, Sutter & Wandelt, 2015; Correa et al., 2020), we decide to parametrise it empirically as described below.

We found that the parametrisation of $\mathcal{F}(b_{\rm eff})$ can be exploited to encapsulate also the modifications on the void sizes caused by the enlargement of cosmic voids in redshift space. This approach has the advantage of being both simple to model and robust, allowing us to take into account, with the same parameter, both the impact of tracer bias in voids and of the RSD. Moreover, this approach is fully agnostic and does not require any assumption about the void density profile, nor any other modelling, making it particularly suited to survey analyses.

It is worth noting that the relation obtained for voids in redshift space shows a greater offset but almost the same slope with respect to its analog in real space. This difference reflects the increase of void sizes in redshift space. It also opens the way to test theoretical implementations in future works, indicating that a simple modelling of those effects should suffice to extract robust constraints.

[3] This theoretical approach would require the knowledge of the void matter density profile for the entire void population, which can be characterised by using simulations but may introduce some model dependencies.

Equipped with these calibrated relations, we now have all the elements necessary to compare the measured void size function with the theoretical predictions given by the extended Vdn model, in which the underdensity threshold is converted as described in Sect. 8.3. Figure 8.5 provides the main results of our Flagship analysis. We show the comparison between the measured void number counts and the corresponding theoretical void size functions, both in real and redshift space, for the 6 equi-populated bins in redshift. The Poissonian errors related to the data are represented by the error bars, while the uncertainty related to the theoretical model is shown as a shaded region. The latter is computed associating an error to $\mathcal{F}(b_{\rm eff})$ given by the interval delimited by the colored bands in Fig. 8.4. The residuals are reported at the bottom of each sub-plot and are calculated as the difference from the theoretical model, in units of the data errors. Looking at the residuals we can appreciate the excellent agreement between simulated data and theoretical models, both for real and redshift space. The measured void number counts are indeed within an uncertainty of 2σ, shown by the hatched colored bands in the bottom panels, represented in units of the data errors. To test the goodness of the fits shown in Fig. 8.5 we compute the reduced χ^2 using the weighted sum of squared deviations of the two data sets from their corresponding models and dividing the results by the degrees of freedom, ν, of the two systems. The results are $\chi^2_\nu = 1.60$ and $\chi^2_\nu = 1.02$ for real and redshift space, respectively.

8.7 Results: forecasts on the void size function constraining power

In this section we provide the cosmological forecasts obtained using the void size function in redshift space in the perspective of the *Euclid* mission. We apply the statistical analysis described in Sect. 8.4 to derive constraints on the parameters of the two cosmological models analysed, labelled as wCDM and w_0w_aCDM, following the two approaches decribed in Sect. 8.5. For the wCDM model we assume a flat prior for all the free cosmological parameters of the model; for the w_0w_aCDM model we assume a Gaussian prior distribution with standard deviation $\sigma = 5$ for w_0 and $\sigma = 15$ for w_a, both centred on the true values of the Flagship simulation cosmology ($w_0 = -1$, $w_a = 0$). We preferred to use very wide Gaussian priors instead of uniform ones to improve the numerical stability of the whole pipeline, but we tested that uniform priors yield consistent results. The remaining cosmological parameters analysed in this chapter ($\Omega_{\rm m}$ and M_ν) are included in the void size function modelling with uniform prior distributions.

In Figs. 8.6 and 8.7 we present the 1σ and 2σ confidence levels of the constraints on the model wCDM. In Fig. 8.6 we show the *Euclid* forecasts from a void size function model characterised by w and $\Omega_{\rm m}$ as free cosmological parameters. We represent with different colours and borders the results obtained with the two approaches described in Sect. 8.5: by fixing the extended Vdn parameters $B_{\rm slope}$ and $B_{\rm offset}$, and by relaxing the calibration constraints by means of a 2D Gaussian prior on $B_{\rm slope}$ and $B_{\rm offset}$, which distribution is represented in Fig. 8.3. In Fig. 8.7 we display the same forecasts but considering a void size function model with the neutrino total mass M_ν as free parameter instead of the matter density $\Omega_{\rm m}$. In all the presented cases σ_8 is computed as a derived parameter. As expected, the effect of relaxing the calibration constraints is to broaden the confidence contours.

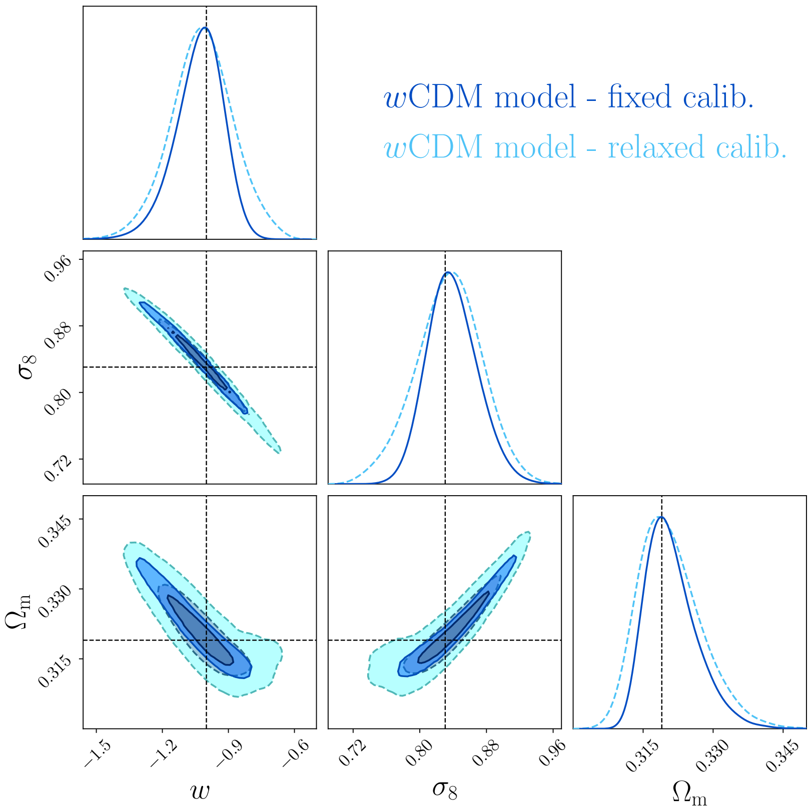

Figure 8.6: Cosmological forecasts for the *Euclid* mission from the void size function for the wCDM model, characterised by a DE component described by a constant w. The contours represent the 1σ (68%) and 2σ (95%) confidence levels obtained by means of the Bayesian statistical analysis described in Sect. 8.4. The forecasts are computed for a cosmological model with w and $\Omega_{\rm m}$ as free cosmological parameters. We report the constraints obtained by fixing the calibration parameters with blue contours marked by a solid line and the results obtained by relaxing the calibration constraints with light-blue contours marked by a dashed line (see Sect. 8.5). For each plot we show also the constraints on σ_8, computed as a derived parameter. The true values of the cosmological parameters are shown by a black dashed line.

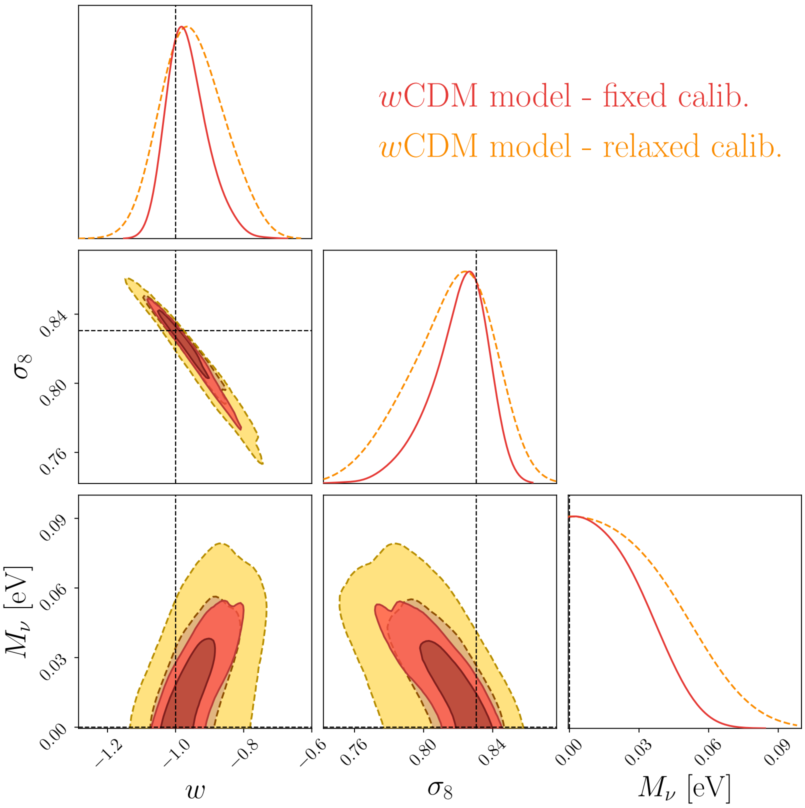

Figure 8.7: The same as Fig. 8.6 but for a cosmological model with w and M_ν as free cosmological parameters. We represent the results of the fixed calibration case as red confidence contours having solid borders and those of the relaxed calibration case as orange contours having dashed borders.

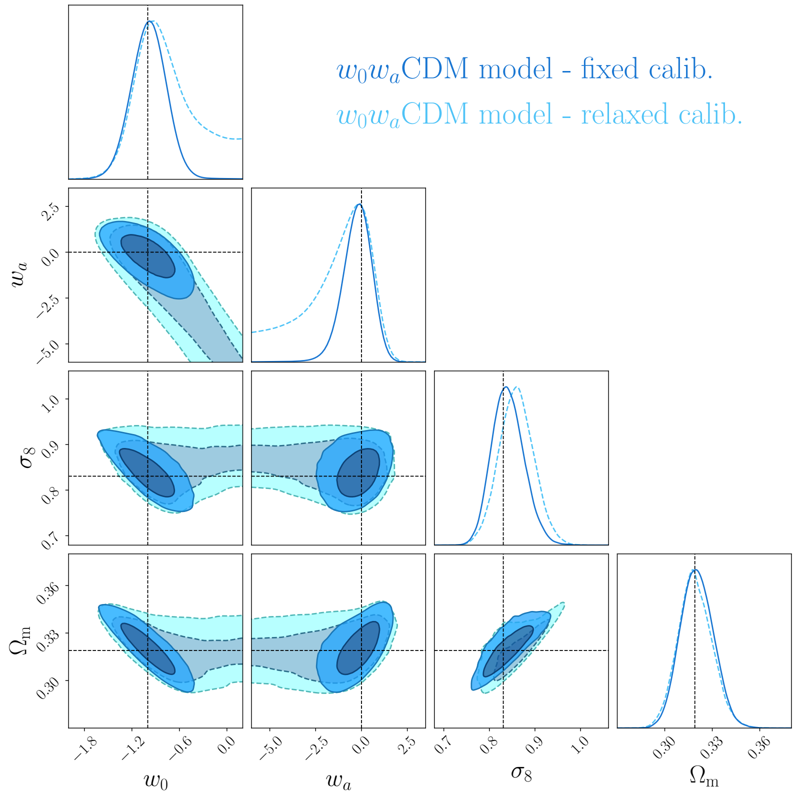

Figure 8.8: The same as Fig. 8.6 but for the cosmological model labelled as w_0w_aCDM, having a dynamical DE component described by the CPL parametrisation (see Sect. 8.5).

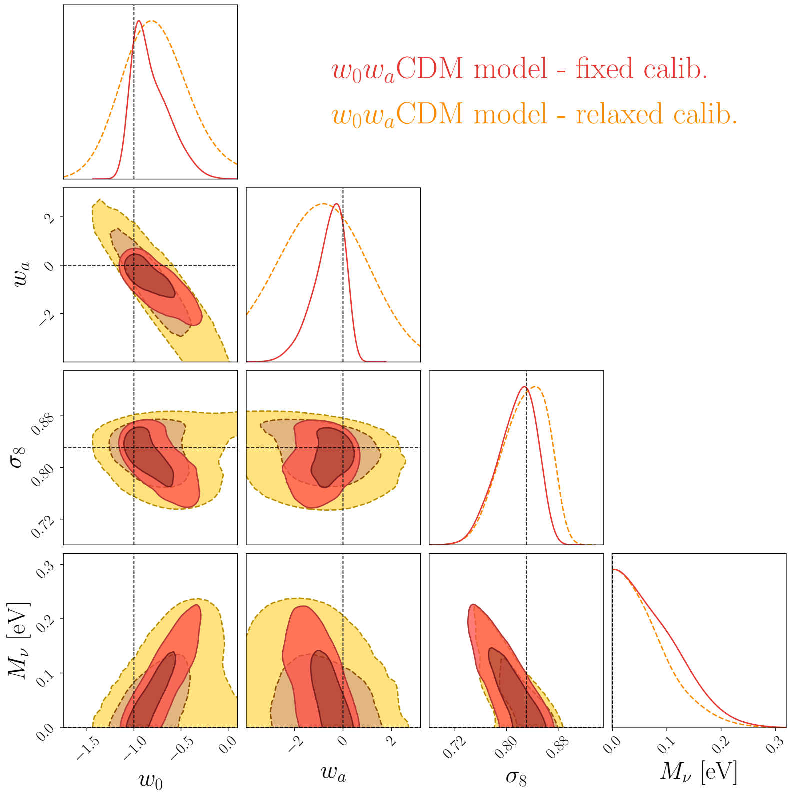

Figure 8.9: The same as Fig. 8.7 but for the cosmological model labelled as $w_0 w_a$CDM, having a dynamical DE component described by the CPL parametrisation (see Sect. 8.5).

In Figs. 8.8 and 8.9 we show the same contours represented in Figs. 8.6 and 8.7 but considering the w_0w_aCDM scenario. Here the free cosmological parameters of the void size function model are the coefficients of the DE equation of state, w_0 and w_a, together with $\Omega_{\rm m}$ (Fig. 8.8) or M_ν (Fig. 8.9). Also in this case, the relaxation of the constraining condition of the calibration parameters causes an enlargement of the confidence contours. In this scenario however, the strongest impact of the calibration constraints is on the w_0–w_a parameter plane, in particular along the diagonal where these parameters become degenerate. The effect of the calibration constraints on $\Omega_{\rm m}$ and M_ν has instead a lower impact.

In Tables 8.2 and 8.3 we report the values, with relative 1σ errors, of the cosmological constraints derived for the wCDM and w_0w_aCDM scenario, respectively. The constraints on the sum of neutrino masses M_ν are expressed as a 1σ upper limit. For each table we show the results for the two approaches followed in this analysis: fixing and relaxing the calibration constraints on the void size function model. The calibration parameters are reported in the columns $B_{\rm slope}$ and $B_{\rm offset}$ for completeness. Notice that each quantity reported without any uncertainty is considered fixed in the specific scenario presented in that table row.

For the w_0w_aCDM scenario, in order to evaluate the constraining power of the void size function on the DE equation of state, we derive the FoM for the coefficients of the CPL parametrisation w_0 and w_a. We compute this value by following the prescription of Wang (2008) (also in agreement with the Euclid Collaboration: Blanchard et al., 2020 adopted methodology):

$$\mathrm{FoM}_{w_0,w_a} = \frac{1}{\sqrt{\det\,\mathrm{Cov}(w_0,w_a)}}\,, \tag{8.6}$$

where $\mathrm{Cov}(w_0,w_a)$ represents the covariance matrix of the DE equation of state parameters. We report the FoM values in the last column of Table 8.3.

We can summarise our results as follows. In the wCDM scenario we forecast relative percentage errors on the constant DE component, w, below the 10% for each analysed case. In the w_0w_aCDM scenario, with the optimistic approach of fixing the model calibration parameters, we compute a FoM_{w_0,w_a} equal to 4.9 or 17, in the case of leaving $\Omega_{\rm m}$ or M_ν, respectively, as additional free cosmological parameters of the model. The marginalised constraints on the derived parameter σ_8 are lower than 5% in every analysed case, while the relative errors on $\Omega_{\rm m}$ are of the order of 2% in the wCDM scenario and of 3% in the w_0w_aCDM scenario. The 1σ upper limit on M_ν is instead of 0.03 eV in the most optimistic case of the wCDM scenario and of 0.08 eV in the w_0w_aCDM scenario. We recall that, in the cosmological models with free neutrino mass, the total matter energy density is fixed to the Flagship simulation true value, therefore the degeneracy of Ω_ν with $\Omega_{\rm m}$ is not explored in the results.

8.8 Results: study on the complementarity of the forecasted cosmological constraints

As a preliminary exploration of the cosmic void statistics combined power, we now compare the forecasts from the void size function provided in this chapter with those provided by other *Euclid* probes. We present as a first comparison the forecasts on the parameters

Table 8.2: Cosmological forecasts computed for the *Euclid* mission from the void size function for the cosmological wCDM model. In this table we report the results of the two analysis strategies adopted in this chapter: considering the parameters $B_{\rm slope}$ and $B_{\rm offset}$ fixed to the respective median calibrated values (label: fixed calib.) or with a multivariate Gaussian with the same median value but an amplitude given by the calibration procedure with Flagship (label: relaxed calib.). For each of the two cases we present, in the upper and lower lines, the forecasts obtained fixing M_ν or $\Omega_{\rm m}$ to the Flagship simulation true values, respectively. All the constraints are reported with errors of 1σ confidence level.

Model	w	σ_8	$\Omega_{\rm m}$	M_ν [eV]	$B_{\rm slope}$	$B_{\rm offset}$
fixed calib.	$-1.01^{+0.09}_{-0.11}$	0.83 ± 0.03	$0.319^{+0.005}_{-0.004}$	0	0.96	0.44
	$-0.99^{+0.06}_{-0.04}$	$0.83^{+0.1}_{-0.2}$	0.319	< 0.03	0.96	0.44
relaxed calib.	-1.0 ± 0.1	0.84 ± 0.04	$0.318^{+0.008}_{-0.005}$	0	0.96 ± 0.02	0.44 ± 0.04
	$-0.98^{+0.10}_{-0.07}$	$0.83^{+0.02}_{-0.03}$	0.319	< 0.06	0.95 ± 0.02	0.46 ± 0.04

Table 8.3: The same as Table 8.2 but for the $w_0 w_a$CDM scenario. In this case we present in the last column also the values computed with Eq. (8.6) to estimate the FoM for the DE equation of state.

Model	w_0	w_a	σ_8	Ω_m	M_ν [eV]	B_slope	B_offset	FoM_{w_0,w_a}
fixed calib.	-1.0 ± 0.2	$-0.1^{+0.7}_{-0.9}$	$0.84^{+0.04}_{-0.03}$	0.32 ± 0.01	0	0.96	0.44	4.9
	$-1.0^{+0.2}_{-0.6}$	$-0.1^{+0.3}_{-0.8}$	$0.83^{+0.02}_{-0.03}$	0.319	< 0.08	0.96	0.44	17
relaxed calib.	$-0.8^{+1.6}_{-0.6}$	$-0.9^{+3.6}_{-9.6}$	0.86 ± 0.04	0.32 ± 0.01	0	$1.01^{+0.03}_{-0.04}$	$0.35^{+0.08}_{-0.05}$	0.78
	$-0.9^{+0.3}_{-0.2}$	$-0.5^{+0.9}_{-1.3}$	$0.86^{+0.02}_{-0.05}$	0.319	< 0.08	$0.99^{+0.01}_{-0.04}$	$0.38^{+0.07}_{-0.01}$	2.3

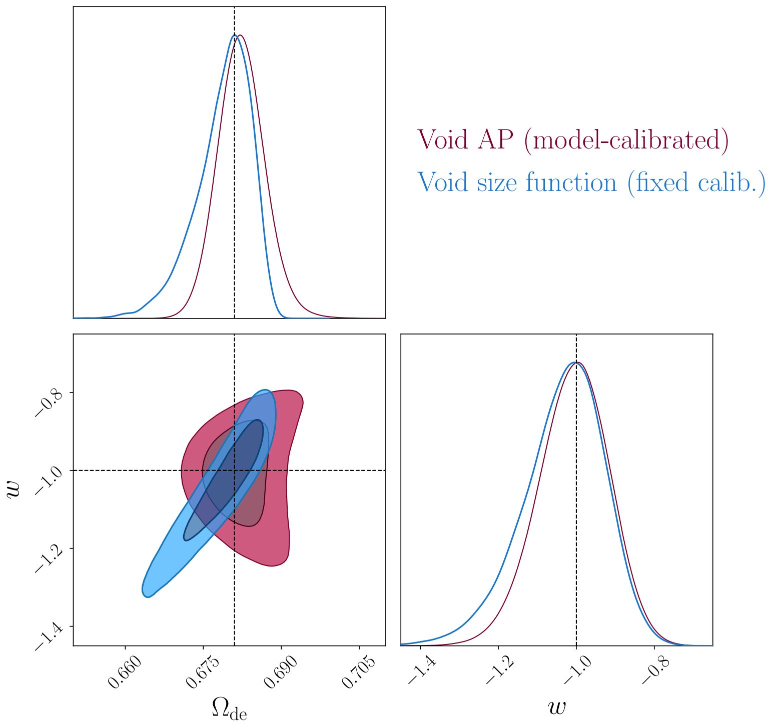

Figure 8.10: Comparison between the 1σ (68%) and 2σ (95%) confidence levels computed in this chapter with the void size function and the void-galaxy cross-correlation *Euclid* forecasts. Specifically, the cosmological constraints on the $\Omega_{\rm de}$–w plane provided by our analysis (in blue) considering a wCDM scenario with fixed calibration parameters and in Hamaus et al. (2022) (in magenta), modelling the void-galaxy cross-correlation function in redshift space, with a model-calibrated approach.

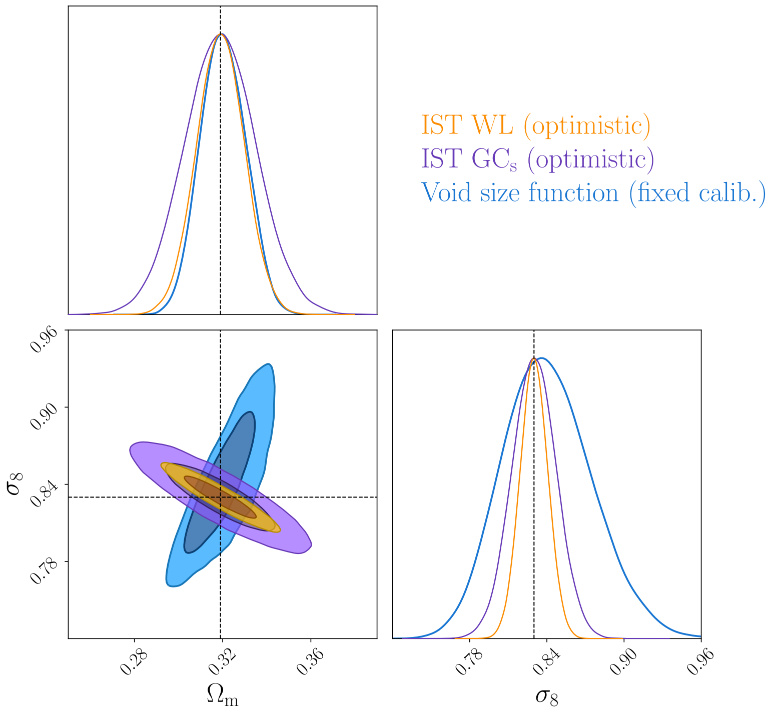

Figure 8.11: Comparison between the 1σ (68%) and 2σ (95%) confidence levels computed in this chapter with the void size function and IST forecasts. Specifically, the cosmological constraints on the Ω_m–σ_8 plane provided by our analysis considering a w_0w_aCDM scenario (in blue) with fixed calibration parameters and the marginalised IST Fisher forecasts computed in the optimistic setting with spectroscopic galaxy clustering (in purple) and weak lensing (in orange).

$\Omega_{\rm de}$ and w obtained in Hamaus et al. (2022) (and described also in Sect. 9.1.1). This analysis is performed by modelling, via RSD and the AP effects (Sect. 4.6), the observable distortions of average shapes, for voids to be measured in the *Euclid* spectroscopic galaxy distribution. To have an appropriate comparison, we consider our results for the wCDM scenario with fixed neutrino mass and we focus on the $\Omega_{\rm de}$–w parameter space. Given the assumption of flat spatial geometry, to compute the corresponding $\Omega_{\rm de}$ forecasts, we converted $\Omega_{\rm m}$ obtained in the MCMC analysis as $\Omega_{\rm de} = 1 - \Omega_{\rm m}$.

As a second comparison, we take the results of the Fisher analysis reported in the IST forecasts (Euclid Collaboration: Blanchard et al., 2020) obtained for the single probes weak lensing and galaxy clustering. We consider in this case the flat $w_0 w_a$CDM scenario with fixed neutrino mass and we focus on the $\Omega_{\rm m}$–σ_8 degeneracy. To compute the IST confidence contour we make use of the publicly available Fisher matrices[4] and we marginalise over the parameters not reported in the plot with the code `CosmicFish` (Raveri et al., 2016). We recall that the amplitude of density fluctuations at $z = 0$, σ_8, is computed as a derived parameter in our analysis and its variation is given by the modifications caused by the free cosmological parameters of the model to the total matter power spectrum. We also stress the fact that a larger set of cosmological parameters is used in IST forecasts. This includes in particular the baryon matter energy density, $\Omega_{\rm b}$, the dimensionless Hubble parameter, h and the spectral index of the primordial density power spectrum, $n_{\rm s}$. The impact on the forecasts when including these parameters in the model will be tested in future works.

In Figs. 8.10 and 8.11 we compare the forecasts computed in this analysis from the void size function model with fixed calibration parameters (see Sect. 8.5) with the results of aforementioned analyses. In particular, in Fig. 8.10 the comparison is with the forecasts obtained in Hamaus et al. (2022) with a model-calibrated approach, i.e. calibrating the nuisance parameters of the model with the Flagship data (we will provide further details in Sect. 9.1.1). In Fig. 8.11 we show instead the comparison with the confidence contour provided by the IST forecasts, considering the optimistic setting for weak lensing and galaxy clustering (see Euclid Collaboration: Blanchard et al., 2020, for the details).

Additionally, we show in Figs. 8.12 and 8.13 the same forecast comparison presented in Figs. 8.10 and 8.11 but using less optimistic settings for the analyses. The confidence contours we represent in these plots are those computed in our analysis by considering relaxed calibration parameters (see Sect. 8.5). In Fig. 8.12 we compare with the *Euclid* forecasts computed with the void-galaxy cross-correlation function with a model-independent approach. Finally, in Fig. 8.13, we present the comparison with the IST forecasts for the weak lensing and galaxy clustering probes, which are in this case computed with the pessimistic setting described in Euclid Collaboration: Blanchard et al. (2020).

In all the presented comparisons we can appreciate the comparable extension of the presented contours and notice, especially in the $\Omega_{\rm m}$–σ_8 plane, the strong complementarity of the void size function forecasts with those of the *Euclid* primary probes. While a more accurate analysis would require a proper accounting for the covariance between analysed cosmological constraints, Figs. 8.10 to 8.13 show how the presented probes explore the parameter space differently and motivates investigations on probe combination to be performed in future works.

[4]See `https://github.com/euclidist-forecasting/fisher_for_public`.

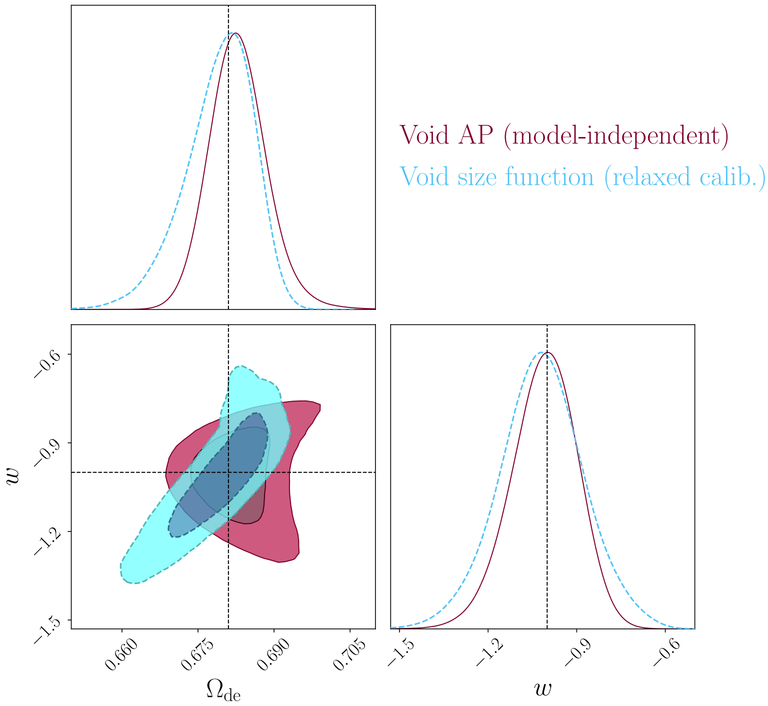

Figure 8.12: Same as Fig. 8.10 but for different forecast settings. In this case the confidence contours obtained in this chapter from the void size function model (light-blue contours with dashed lines) are derived relaxing the constraints given by calibration parameters, while the *Euclid* forecasts computed by Hamaus et al. (2022) with void cross-correlation are computed with a model-independent approach.

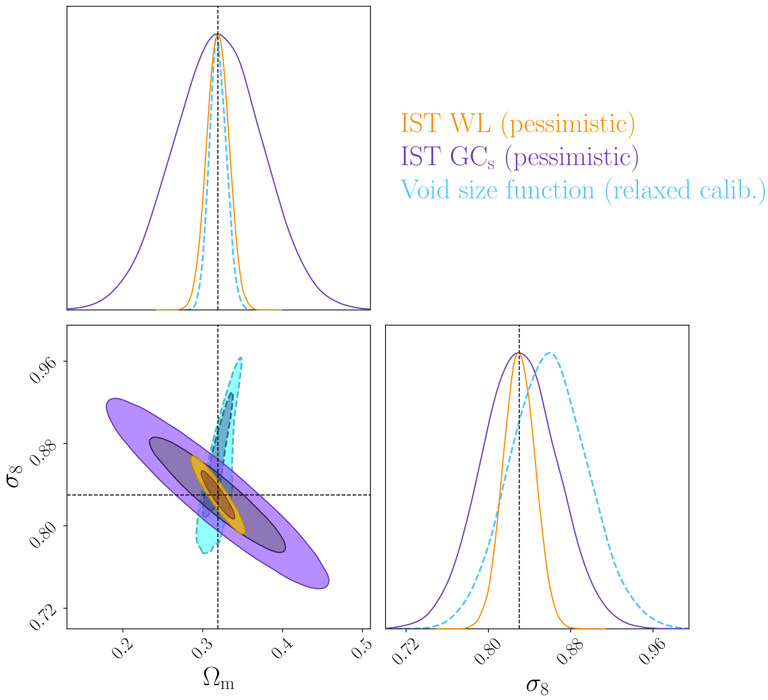

Figure 8.13: Same as Fig. 8.11 but for different forecast settings. The contours from the void size function are computed relaxing the constraints given by calibration parameters (light-blue contours with dashed lines), while IST forecasts are computed with the pessimistic setting described (Euclid Collaboration: Blanchard et al., 2020).

Chapter 9

Further studies with voids as cosmological probes

In this chapter we will present an overview on some of the researches carried on complementarily to the main PhD project, on which we want to bring the reader's attention. We will first explore the impressive *Euclid* forecasts computed exploiting the stacked void-galaxy cross-correlation function (Hamaus et al., 2022, Sect. 9.1.1) and the void-lensing cross-correlation (Bonici et al., 2022, in preparation, Sect. 9.1.2). Then we will introduce the work that will be presented in Pelliciari et al. (2022, in preparation), in which we will provide a first exploration of the possible synergy between the void size function and the mass function of galaxy clusters.

9.1 Further *Euclid* forecasts with voids

In the following subsections we will show the main results obtained in two other projects belonging to the *Euclid* "Working Package 8: Voids", which are complementary to the work presented in Chapter 8. Despite we will provide an accurate overview on the methodology adopted for both the analyses, together with the main results obtained, we highly recommend the reader to refer to the corresponding papers for more details.

The first work (Sect. 9.1.1) has been published in Hamaus et al. (2022). In this study, we investigate the imprints of geometric (Sect. 4.6.1) and dynamic (Sect. 4.6.2) distortions of average void shapes, and we make use of the same sample of galaxies and voids employed in Chapter 8: the Flagship mock galaxies prepared according to the *Euclid* spectroscopic survey specifics, and the void sample identified with `VIDE` in the distribution of these galaxies. The second work (Sect. 9.1.2) will be presented in Bonici et al. (2022, in preparation), where we predict the constraining power of the angular void clustering, galaxy weak lensing and their cross-correlation from the *Euclid* photometric survey[1].

[1] The *Euclid* photometric survey will provide a galaxy catalogue characterised by a surface density of $n_{\rm g} = 30$ arcmin^{-2} (Laureijs et al., 2011). The redshift of these galaxies will be measured in photometric mode, i.e. using the *Near Infrared Spectrometer Photometer* (NISP) instrument (Costille et al., 2018), complemented by ground-based observations. This survey will also provide the shapes of about one billion galaxies, observed in the visible range with the VIS instrument (Cropper et al., 2018).

9.1.1 Void-galaxy cross-correlation cosmology

In the work of Hamaus et al. (2022) we forecast the constraining power on cosmological parameters for a combined analysis of the AP and RSD effects on the void-galaxy cross-correlation function. We provided the theoretical background required for this analysis in Sects. 4.5 and 4.6. However, to get to the full void-galaxy cross-correlation function modelling used in this work we need to further develop the theory explained up to here. First of all, we need Eqs. (4.27) and (4.28) to determine the mapping between the real, $\mathbf{r}$, and redshift-space, $\mathbf{s}$, coordinates of galaxies inside voids:

$$\mathbf{s} = \mathbf{r} - \frac{f(z)}{3}\,\Delta(r)\,\mathbf{r}_{||}\ . \tag{9.1}$$

This allows us to express the void-galaxy cross-correlation function in redshift space as:

$$\xi^s(\mathbf{s}) \simeq \xi(r) + \frac{f}{3}\Delta(r) + f\mu^2[\delta(r) - \Delta(r)]\ , \tag{9.2}$$

where $\mu \equiv r_{||}/r$ is the cosine of the angle between $\mathbf{r}$ and the line-of-sight (see also Fig. 4.6) and the superscript s is used to indicate quantities computed in redshift space. In this relation the real-space quantities $\xi(r)$, $\delta(r)$ and its integral $\Delta(r)$ can be derived from observables with some basic assumptions. First, $\xi(r)$ can be obtained via deprojection of the projected void-galaxy cross-correlation function $\xi^s_{\rm p}(s_\perp)$ in redshift space that, by construction, is insensitive to RSD (Pisani et al., 2014; Hawken et al., 2017). Second, the matter density contrast inside voids can be related to $\xi(r)$ assuming the linear relation seen in Eq. (2.34). Using the same tracer bias used in Chapter 8, this yields to $\xi(r) = b\,\delta(r)$[2]. With these assumptions, Eq. (9.2) becomes:

$$\xi^s(\mathbf{s}) \simeq \xi(r) + \frac{1}{3}\frac{f}{b}\bar{\xi}(r) + \frac{f}{b}\mu^2[\xi(r) - \bar{\xi}(r)]\ , \tag{9.3}$$

where

$$\bar{\xi}(r) \equiv 3r^{-3}\int_0^r \xi(r')\,r'^2\,\mathrm{d}r'\ . \tag{9.4}$$

We underline that the model in Eq. (9.3) is accurate only at the linear order since the RSD are modelled with simplified assumptions (as in Kaiser, 1987) and the deprojection procedure is itself approximate.

Therefore, two additional nuisance parameters are necessary to account for systematic effects: one to correct for potential inaccuracies arising from the deprojection technique and from the contamination of the void sample (Cousinou et al., 2019), and the other to account for possible selection effects during the identification of voids in redshift space (Pisani, Sutter & Wandelt, 2015; Correa et al., 2020, 2021). These parameters are denoted as $\mathcal{M}$ and $\mathcal{Q}$, respectively, and lead to the model form:

$$\xi^s(s_\perp, s_{||}) = \mathcal{M}\left\{\xi(r) + \frac{f}{b}\bar{\xi}(r) + 2\mathcal{Q}\,\frac{f}{b}\mu^2\left[\xi(r) - \bar{\xi}(r)\right]\right\}\ . \tag{9.5}$$

[2] We highlight that here the value b is the bias measured on large scales, and not the one computed inside cosmic voids, so we expect this relation to be approximate.

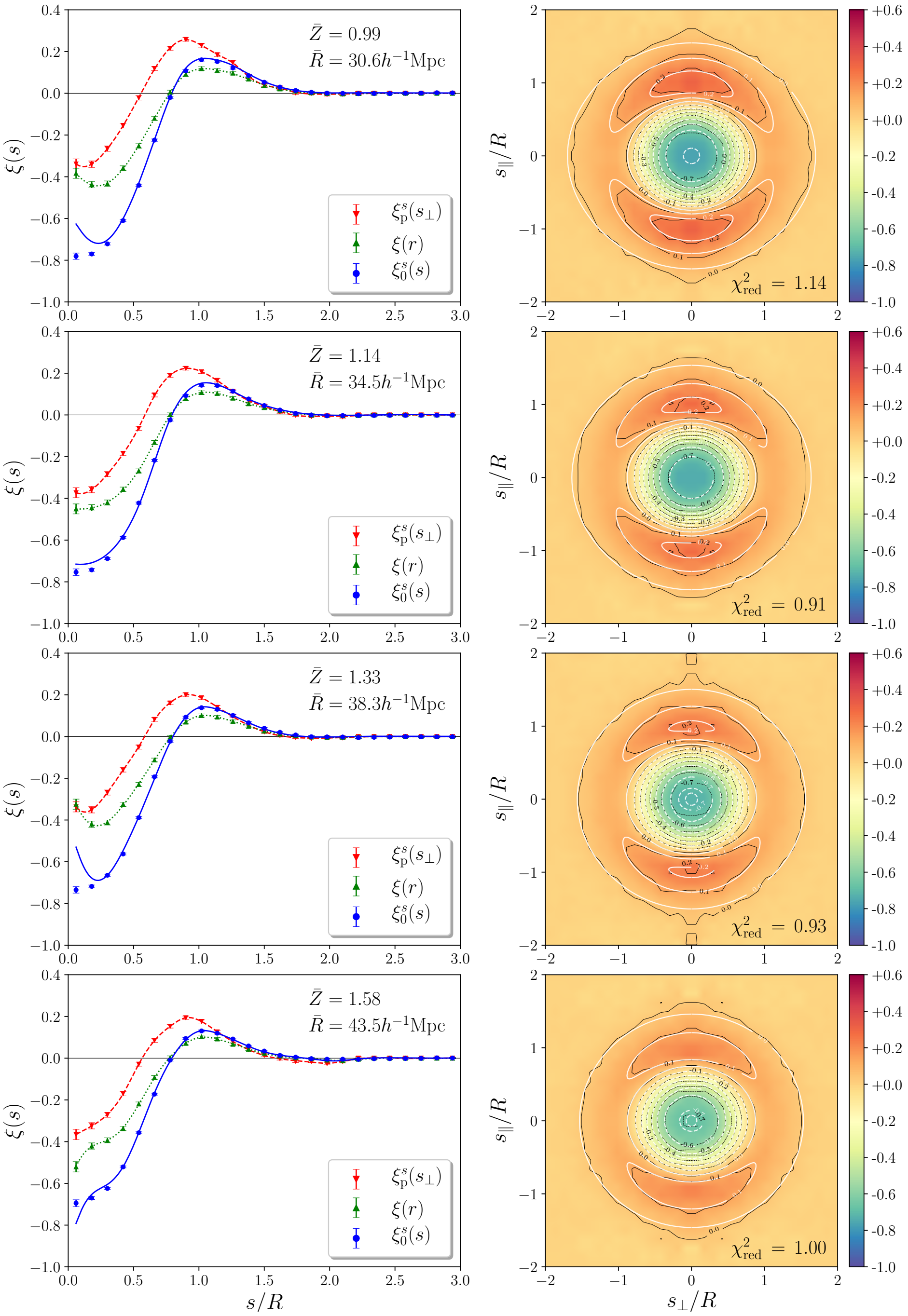

Figure 9.1: Stacked void-galaxy cross-correlation function in redshift space. *Left*: projected void-galaxy cross-correlation function, $\xi^s_{\rm p}(s_\perp)$, in redshift space (red wedges, interpolated with dashed line) and its real-space counterpart inferred from a 3D deprojection, $\xi(r)$ (green triangles interpolated with dotted line). The redshift-space monopole, $\xi^s_0(s)$ (blue dots) and its best-fit model based on Eqs. (9.5) and (9.6) (solid line) are shown as comparison. On the top-right corner of each panel we report the mean redshift, $\bar{Z}$, and the mean effective radius, $\bar{R}$, of the void sample analysed. *Right*: 2D representation of $\xi^s(s_\perp, s_\parallel)$ (color map with black contours) and its best-fit model from Eqs. (9.5) and (9.6) (white contours). The reduced χ^2 value computed for the 4 redshift bins is reported in the bottom-right corner of the corresponding panel.

The mapping from the observed separations $s_\perp$ and $s_{||}$ to r and μ is obtained by using Eq. (9.1) together with Eq. (4.19) for the AP effect. This yields to the following relations between real and redshift-space coordinates:

$$r_\perp = q_\perp s_\perp \, , \qquad r_\| = q_\| s_\| \left[1 - \frac{1}{3} \frac{f}{b} \mathcal{M} \, \bar{\xi}(r) \right]^{-1} \, . \tag{9.6}$$

These coordinate transformations can be solved via iteration to determine $r = \left(r_\perp^2 + r_{||}^2\right)^{1/2}$ and $\mu = r_{||}/r$, starting assigning $r = s$ as initial value (Hamaus et al., 2020). Now, expressing all the void-centric distances in units of the effective void radius in redshift space by using Eq. (4.22), only the ratio of $q_\perp$ and $q_{||}$ appears in Eq. (9.6). Therefore the quantities $r_\perp$ and $r_{||}$ result dependent on the parameter $\varepsilon \equiv q_\perp / q_{||}$ (Eq. 4.21). The latter, together with f/b and the nuisance parameters $\mathcal{M}$ and $\mathcal{Q}$, will be constrained by modelling the stacked void-galaxy cross-correlation function with Eq. (9.5).

The measurement of $\xi^s(s_\perp, s_{||})$ is done in 4 bins of redshifts equi-populated in voids by exploiting the Landy & Szalay (1993) estimator (see Sect. 2.1.5), and calculating the associated uncertainty as the diagonal elements of the covariance matrix estimated with Jackknife (see Hamaus et al., 2022, for the details). A comparison between the measured stacked void-galaxy cross-correlation function and its modelling, for the 4 bins of redshift analysed, is reported in left-column plots of Fig. 9.1. For the sake of completeness, in these plots we also report the monopole of the redshift-space correlation function, $\xi_0^s(s)$, which nicely follows the shape of the deprojected $\xi(r)$ (see Hamaus et al., 2020, 2022, for further details). Moreover, we can notice how the model from Eqs. (9.5) and (9.6) provides a very accurate fit to this monopole everywhere apart from its innermost bins, implying that any residual errors in the model are negligible in that regime. In the right-column plots of Fig. 9.1 we show instead the stacked void-galaxy cross-correlation projected along the directions $s_\perp$ and $s_{||}$. For each redshift bin, the agreement between the model and the data is quantified by the reduced χ^2 that, being extremely close to unity, proves the great accuracy of the theoretical modelling reported in Eqs. (9.5) and (9.6) in reproducing the observed data.

A MCMC analysis is then performed to sample the posterior probability distribution of all model parameters. For each redshift, the obtained precision on f/b ranges from 7.3% and 8.0%, while the one on ε is between 0.87% and 0.91%. These results are computed with the Flagship mock data so we can expect the achieved precision to increase by a factor $\sqrt{3}$ when extrapolated to the volume of the *Euclid* survey. The attainable precision can also be improved by relying on the calibration of the nuisance parameters $\mathcal{M}$ and $\mathcal{Q}$. Nevertheless, we underline this technique introduces a priori dependence on the cosmological parameters assumed in the mocks, so it underestimates the final uncertainty and may lead to biased results. With this approach, the computed constraints for the *Euclid* survey are roughly of 1% on f/b and 0.4% on ε per each redshift bin. From now on, we will refer to the analysis performed by fixing the $\mathcal{M}$ and $\mathcal{Q}$ nuisance parameters to their Flagship best-fit values as "model-calibrated" analysis, while to the one with free $\mathcal{M}$ and $\mathcal{Q}$ as "model-independent" analysis.

From the posterior distributions on f/b and ε we compute constraints on $f\sigma_8$ and $D_\mathrm{M}H$. The first is derived by assuming $\xi(r) \propto b\sigma_8$ and hence multiplying f/b by $b\sigma_8$, considering this factor fixed to the value computed with the Flagship mock, assuming the

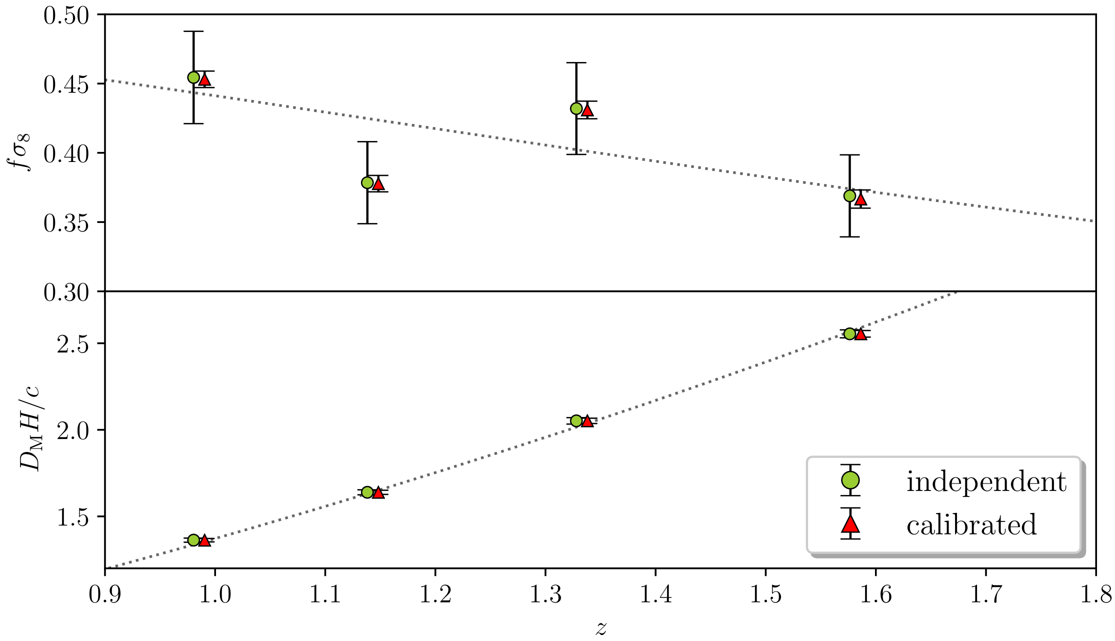

Figure 9.2: Measured values of $f\sigma_8$ and $D_{\rm M}H$ from `VIDE` voids in the Flagship catalogue as a function of redshift z. The green circles indicates the results for the model-independent analysis and the red triangles for the model-calibrated one. The markers are slightly shifted horizontally for visibility. The dotted lines represent the predictions for the Flagship input cosmology. These results are computed for the Flagship octant, so the expected precision for the 3 times larger *Euclid* sky area is a factor of about $\sqrt{3}$ higher.

simulation true cosmology[3]. The second is derived from ε multiplying by the value of $D_{\rm M}H$ computed for the assumed cosmological model parameters (see Eq. 4.21). The results for $f\sigma_8$ and $D_{\rm M}H$ achieved for both the independent- and calibrated-model analyses are shown in Fig. 9.2. Comparing the results of the independent- and calibrated-model techniques, we can notice here the larger errors associated to the former that, however, appear to be more in agreement with the predictions computed with the true underlying Flagship cosmology, when considering all the redshift bins. This outcome is evident especially for $f\sigma_8$ and is a direct consequence of the model-calibration technique, which improves the precision but may introduce biased results.

We now exploit the achieved constraints for $f\sigma_8$ and $D_{\rm M}H$ to further test the cosmological model. Assuming a flat ΛCDM scenario, the quantity $D_{\rm M}H$ results dependent only on $\Omega_\Lambda = 1 - \Omega_{\rm m}$ (see Eqs. 1.55 and 4.24). So, from the measured values of $D_{\rm M}H$, we derive the joint posterior distribution of all redshift bins combined. In order to compute forecasts for the *Euclid* mission, we also consider these measures with errors rescaled by a factor $1/\sqrt{3}$ and we centre their mean values to the input cosmology of Flagship. The resulting sampled posterior yields $\Omega_\Lambda = 0.6809 \pm 0.0048$, for the independent analysis, and $\Omega_\Lambda = 0.6810 \pm 0.0039$, for the calibrated one. In the left plot of Fig. 9.3 we show a

[3]This procedure is meant to provide a comparison with other results in the literature. We underline that the operation of multiplying by b and σ_8 is performed assuming the true cosmological model and both the quantities without errors.

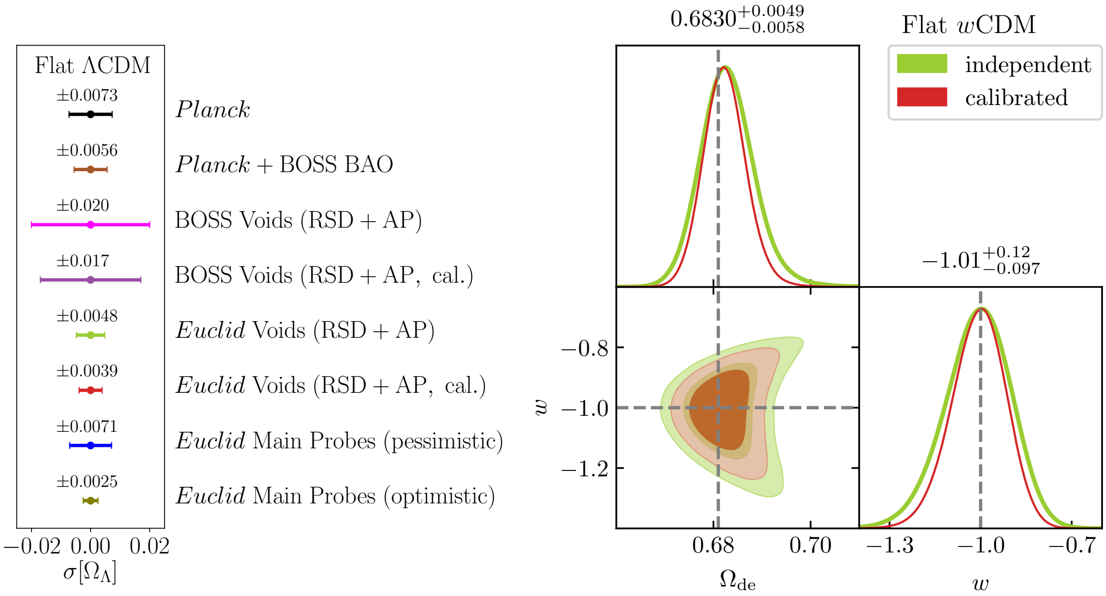

Figure 9.3: Forecasts on the DE constraints from the void-galaxy cross-correlation function for the *Euclid* survey. *Left*: comparison of the constraining power on Ω_Λ in a flat ΛCDM cosmology from different probes and surveys. We show the constraints computed by Planck Collaboration et al. (2020a) with CMB lensing alone and when combined with BOSS BAO data (Alam et al., 2017). Below, the constraints achieved with BOSS voids via RSD and AP (Hamaus et al., 2020), as expected from *Euclid* voids (this analysis), and as expected from the combination of *Euclid*'s main cosmological probes (Euclid Collaboration: Blanchard et al., 2020), for both the pessimistic and optimistic settings. The constraints from the model-calibrated analysis presented here are indicated by the abbreviation "cal." *Right*: 1σ (68%) and 2σ (95%) confidence contours from *Euclid* voids on $\Omega_{\rm de}$ and the equation-of-state parameter w in a flat wCDM cosmology. We show both the model-independent (green) and the model-calibrated results (red), indicating with grey dashed lines the values of the Flagship input cosmology. The marginalised posterior distributions, together with the corresponding mean parameter values and their 1σ errors, are reported in the upper and right sub-plots.

comparison of our results with those obtained by Planck in 2018 (Planck Collaboration et al., 2020a) with CMB lensing only and with the combination with BOSS BAO data (Alam et al., 2017). In the same plot we report also the constraints forecasted for the *Euclid* main probes, for both a pessimistic and optimistic scenario (see Euclid Collaboration: Blanchard et al., 2020), and the results previously obtained in Hamaus et al. (2020) by applying the same methodology presented here but to the BOSS survey voids.

Then, to explore cosmological models beyond the standard ΛCDM, we repeat the analysis just presented but considering a flat wCDM scenario (see Sect. 3.1.1). Now the cosmological dependence of the quantity $D_{\rm M}H$ is on the parameter pair $(\Omega_{\rm de}, w)$. The inferred posterior distribution is reported in the right plot of Fig. 9.3 for both the independent- and the calibrated-model analysis; the obtained constraints on the DE equation of state parameters are $w = -1.01^{+0.12}_{-0.10}$ (i.e. 9% precision) $w = -1.01^{+0.10}_{-0.08}$ (i.e. 11% precision), respectively. These results are extremely competitive with those of Planck Collaboration et al. (2020a) and remarkably in agreement with those Fisher forecasts early provided by Lavaux & Wandelt (2012) by exploiting the AP test with voids.

As we saw in Sect. 8.8, the already impressive constraining power forecasted from void RSD and AP for the *Euclid* survey will be considerably improved thanks to the combination with other void statistics and other cosmological probes. This will allow the exploration of a larger scope of parameters and so the testing of different cosmological models, leading towards a full cosmological exploitation of the cosmic void potential.

9.1.2 Void-lensing cross-correlation cosmology

As anticipated, the forecasts that will be provided with this analysis, contrary to those found in Chapter 8 and Section 9.1.1, are computed for the *Euclid* photometric survey. Therefore in this case the Flagship catalogue has been prepared to have galaxy redshifts spanning from 0.001 to 2.5, with associated Gaussian photometric errors of $\Delta z = 0.05(1+z)$. Moreover, cosmic voids have been identified in this catalogue by applying the 2D void finder of Sánchez et al. (2017b) and Vielzeuf et al. (2019) (see also Sect. 5.2). The resulting void radii span from a minim of $r_{\rm v,min} \sim 25\ h^{-1}$ Mpc to a maximum of $r_{\rm v,max} \sim 300\ h^{-1}$ Mpc. We show in the left panel of Fig. 9.4 the void projected number density for 10 equi-spaced redshift bins, computed as the ratio between the void number in each bin and the bin width.

The forecasts presented in this work are based on the exploitation of the angular power spectrum, $C(\ell)$, which is defined as the spherical harmonic transform of the 2PCF (see Eq. 2.18) and is a function of the multipole ℓ. In particular, in this analysis we focus on three kinds of statistics: the void-void auto-correlation $C^{\rm vv}(\ell)$, the lensing-lensing auto-correlation $C^{\gamma\gamma}(\ell)$ and the void-lensing cross-correlation $C^{\rm v\gamma}(\ell)$. We estimate these quantities with a *tomographic* approach (Hu, 1999), by computing their value, $C^{\rm AB}(\ell)$[4], over two bins $(i-j)$. For example, $C^{\rm v\gamma}_{i,j}(\ell)$ is the spherical harmonic transform of the correlation function between the void and the lensing signal in the i-th and j-th redshift bins. In particular, we express the tomographic $C(\ell)$ by using the Limber approximation (Limber, 1953). This leads the power spectrum $P_{\rm AB}(k,z)$ to enter into the integral form:

$$C^{\rm AB}_{i,j}(\ell) \simeq \frac{c}{H_0}\int_{z_{\rm min}}^{z_{\rm max}} \frac{W^{\rm A}_i(z)W^{\rm B}_j(z)}{E(z)r^2(z)} P_{\rm AB}\left[\frac{\ell+1/2}{r(z)}, z\right]{\rm d}z\ , \tag{9.7}$$

where $E(z)$ is the function introduced in Eq. (1.55), $r(z)$ is the comoving distance (we notice that here the notation is different with respect to Eq. 1.19 and $W^{\rm A/B}_i(z)$ are suitable weight functions for the probes A and B, which will be introduced in the following.

The void weight function is defined as:

$$W^{\rm v}_i(z) = \frac{H(z)}{c} n^i_{\rm v}(z)\, b^i_{\rm v,eff}\ , \tag{9.8}$$

where $n^{\rm v}_i(z)$ is the projected void density distribution represented (in its normalised version) in the left panel of Fig. 9.4, and $b^i_{\rm v,eff}$ is the void effective bias defined in Eq. (4.17), both evaluated at the centre of the i-th tomographic bin. Following Euclid Collaboration: Blanchard et al. (2020), we express the lensing weight function as:

$$W^{\gamma}_i(z) = \frac{3}{2}\left(\frac{H_0}{c}\right)^2 \Omega_{\rm m}\,(1+z)\,r(z)\,\tilde{W}^{\gamma}_i(z)\ , \tag{9.9}$$

[4]We use the subscripts/superscripts A and B to refer to both voids and lensing and are left generic to indicate all the three possible combinations of these probes.

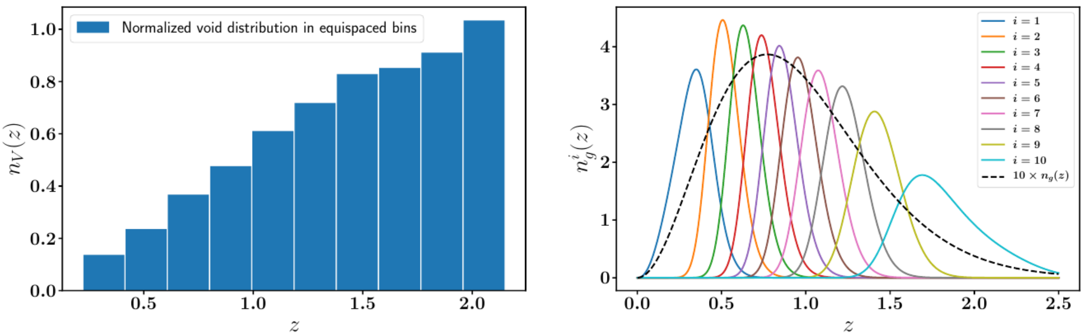

Figure 9.4: *Left*: dimensionless normalised projected void density distribution, $n_{\mathrm{v}}(z)$, in 10 equispaced bins of redshift. *Right*: dimensionless normalised projected galaxy distribution, $n_{\mathrm{g}}^i(z)$, over 10 bins labelled with the index $i = [1, 10]$ equi-populated in galaxies. The black dashed line represents a rescaling of the galaxy distribution function, $n_{\mathrm{g}}(z)$.

where $\tilde{W}_i^{\gamma}(z)$ is the lensing efficiency, defined as:

$$\tilde{W}_i^{\gamma}(z) = \int_z^{z_{\max}} n_{\mathrm{g}}^i(z') \left[1 - \frac{r(z)}{r(z')}\right] \mathrm{d}z' \ . \tag{9.10}$$

Here $n_{\mathrm{g}}^i(z)$ is the observed galaxy distribution in the i-th tomographic bin; it is computed as the convolution of the galaxy distribution, $n_{\mathrm{g}}(z)$, and the photometric instrument response. A detailed description of these functions is provided in Bonici et al. (2022, in preparation). The results of this convolution for the different redshift bins are reported in the right plot of Fig. 9.4, together with a rescaled version of the function $n_{\mathrm{g}}(z)$.

Now, in order to evaluate the angular power spectra of Eq. (9.7) we need to compute the void auto-power spectrum, $P_{\mathrm{vv}}(k, z)$, the void-matter cross-spectrum $P_{\mathrm{vm}}(k, z)$ and the matter auto-power spectrum $P_{\mathrm{mm}}(k, z)$. The latter is estimated, once again, with the Boltzmann solver `CAMB` (Lewis, Challinor & Lasenby, 2000). $P_{\mathrm{vv}}(k, z)$ is instead estimated adopting the following relation:

$$P_{\mathrm{vv}}(k, z) = b_{\mathrm{v}}^2(z)\, \hat{P}_{\mathrm{mm}}(k, z) + 1/\bar{n}_{\mathrm{v}}(z) \ , \tag{9.11}$$

where $b_{\mathrm{v}}(z)$ is the void bias introduced in Eq. (4.16), $\bar{n}_{\mathrm{v}}(z)$ is the void number density, and $\hat{P}_{\mathrm{mm}}(k, z) \equiv [1 - S_{\mathrm{N}}(k)] P_{\mathrm{mm}}(k, z)$ is the nonlinear matter power spectrum filtered at small scales with the function $S_{\mathrm{N}}(k)$. The low-k pass filter, $S_{\mathrm{N}}(k)$, is necessary to suppress the inaccuracies arising from the 1-void (or shot noise) term (Hamaus et al., 2014), which makes $P_{\mathrm{vv}}(k, z)$ deviate at small scales from the linear modelling reported in Eq. (9.11) (see Bonici et al., 2022, in preparation, for further details). Analogously, the void-matter cross-spectrum can be expressed as:

$$P_{\mathrm{vm}}(k, z) = b_{\mathrm{v}}(z)\, \hat{P}_{\mathrm{mm}}(k, z) + 1/\bar{n}_{\mathrm{v}}(z) \ . \tag{9.12}$$

The power spectra $P_{\mathrm{mm}}(k)$, $P_{\mathrm{vv}}(k)$ and $P_{\mathrm{vm}}(k)$ are reported in Fig. 9.5, together with the angular power spectra $C_{i,j}^{\gamma\gamma}(\ell)$, $C_{i,j}^{\mathrm{vv}}(\ell)$ and $C_{i,j}^{\mathrm{v}\gamma}(\ell)$ with $i = j = [1, 10]$. Here we can appreciate the effect of the filter $S_{\mathrm{N}}(k)$, which cuts the large values of the wavenumber

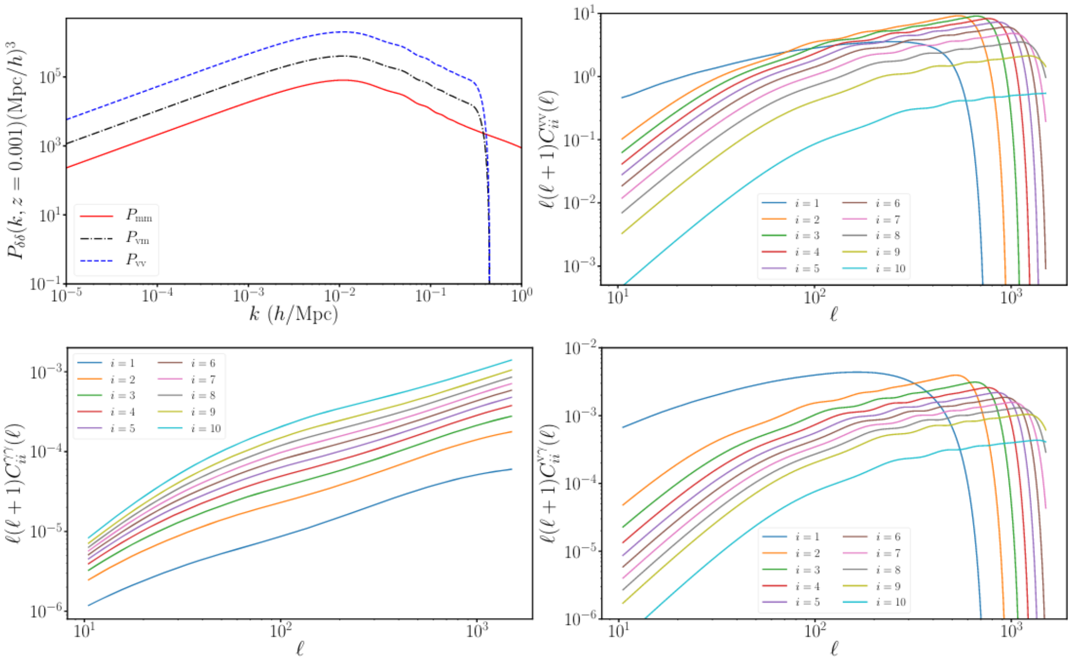

Figure 9.5: Nonlinear power spectra and angular power spectra computed at redshift $z = 0.001$ with the Flagship input cosmology. In the *top-left* panel we report the nonlinear matter auto-power spectrum $P_{\rm mm}$ (red solid line), the void auto-power spectrum $P_{\rm vv}$ (blue dashed line) computed assuming $b_{\rm v,eff} \approx -11.9$, and the absolute value of the void-matter cross-power spectrum $P_{\rm vm}$ (black dot-dashed line). We show the void angular auto-power spectra, $C^{\rm vv}_{i,j}(\ell)$, the lensing auto-power spectra, $C^{\gamma\gamma}_{i,j}(\ell)$, and the void-lensing angular cross-spectra $C^{\gamma\gamma}_{i,j}(\ell)$ computed for the diagonal ($i = j$) of the 10 tomographic bins (equi-populated in the photometric galaxy catalogue), in the *top-right*, *bottom-left*, *bottom-right* panels, respectively.

Table 9.1: Marginalised 1σ errors computed for two different cosmological scenarios and three probes: galaxy weak lensing (WL), angular void clustering (V) and their combination including the cross-correlation (WL+V+XC).

Probe	h	$\Omega_{\rm m}$	$\Omega_{\rm b}$	σ_8	$n_{\rm s}$	M_ν [eV]	w_0	w_a	FoM_{w_0,w_a}
					w_0w_aCDM				
WL	0.14	0.0095	0.024	0.010	0.030	-	0.12	0.43	54
V	0.064	0.093	0.018	0.11	0.17	-	0.39	1.6	5.1
WL+V+XC	0.011	0.0065	0.0035	0.0065	0.0043	-	0.079	0.25	106
					νw_0w_aCDM				
WL	0.14	0.0095	0.025	0.012	0.031	0.23	0.12	0.43	54
V	0.068	0.099	0.018	0.12	0.17	0.66	0.41	1.7	4.6
WL+V+XC	0.011	0.0065	0.0051	0.0093	0.0046	0.18	0.079	0.25	105

k and so the large multipoles ℓ, in the void power spectra and angular power spectra respectively.

To obtain the cosmological forecasts for *Euclid* we adopt in this analysis the Fisher matrix formalism (Fisher, 1935): we compute the matter auto-correlation spectrum $P_{\rm mm}(k,z)$ for a set of input cosmological parameters, which are varied with respect to the fiducial cosmology, given by the Flagship build-in parameters (see Sect. 8.1). This variation affects the computation of the $C(\ell)$ derivatives, the growth factor $D(z)$[5], the Hubble parameter $H(z)$ and the comoving distance $r(z)$. We provide further details on the Fisher forecast computation in Appendix C.

Now we report the main results of this analysis. We will show the forecasts computed for the two most extreme scenarios considered in Bonici et al. (2022, in preparation): the flat w_0w_aCDM and νw_0w_aCDM cosmologies, i.e. implementing a CPL parametrisation of the DE equation of state (w_0 and w_a parameters), with the addition of a free neutrino mass (M_ν parameter) in the latter case. Moreover, we will present only the results for the optimistic scenario: the void size function and the void bias are both supposed to be cosmology-dependent, with a dependency on the cosmology given by the growth factor entering in the redshift evolution of the mass variance σ (see Sect. 4.3). Also, in this scenario the angular power spectra are evaluated with $\ell \in [10, 5000]$. We refer the interested reader to Bonici et al. (2022, in preparation) for the additional forecasts on the ΛCDM and $\nu\Lambda$CDM cosmologies and for the corresponding results computed with the pessimistic settings[6].

In Figs. 9.6 and 9.7 we report the results for the w_0w_aCDM and the νw_0w_aCDM cosmologies, respectively. We also report a summary of the corresponding cosmological parameter constraints in Table 9.1. The first thing to notice is that the galaxy weak

[5]The growth factor $D(z)$ enters in the effective void bias definition, and in particular in the void size function used to weight the void bias (see Eq. 4.17).

[6]In this scenario the redshift evolution of the bias is supposed to be known from the linear theory, but not its absolute normalisation. In particular, we suppose the void bias to have a today fiducial value of $b_{\rm v,eff}(z=0) = -11.9$ and we evolve it with the growth factor of the fiducial cosmology, marginalising over it as a nuisance parameter. Moreover in this case the angular power spectra are computed for a tighter monopole range, i.e. $\ell \in [10, 1500]$.

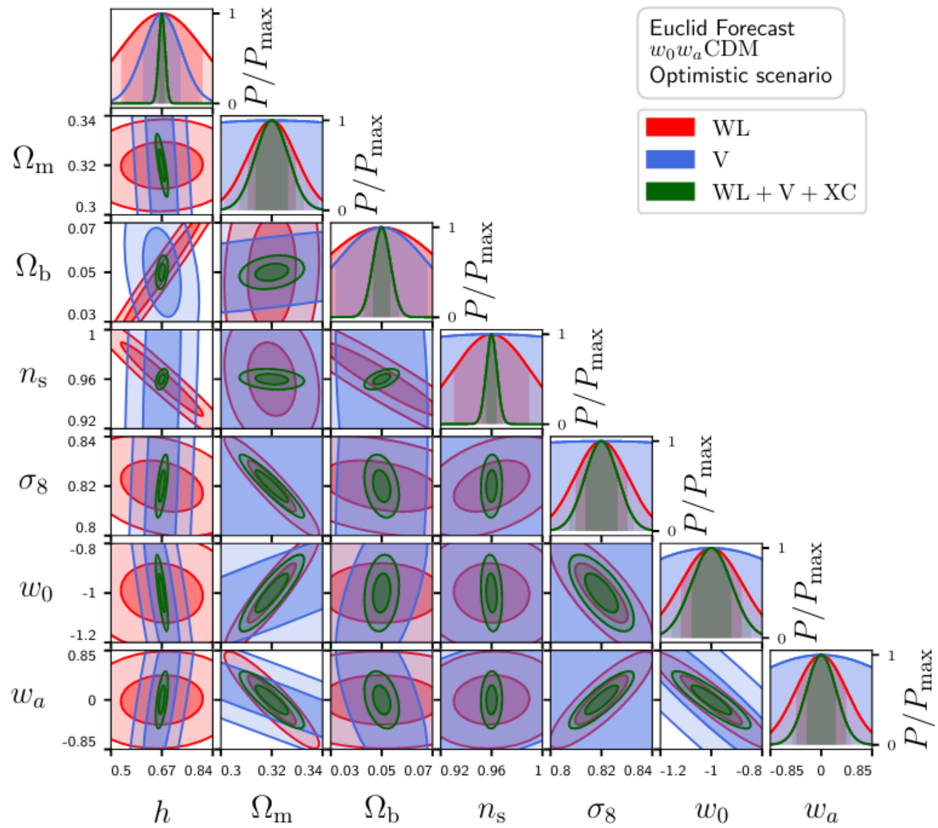

Figure 9.6: Fisher matrix contours for the flat w_0w_aCDM cosmological model for the galaxy weak lensing (WL, in red), the angular void clustering (V, in blue) and their combination including the cross-correlation (WL+V+XC, in green)

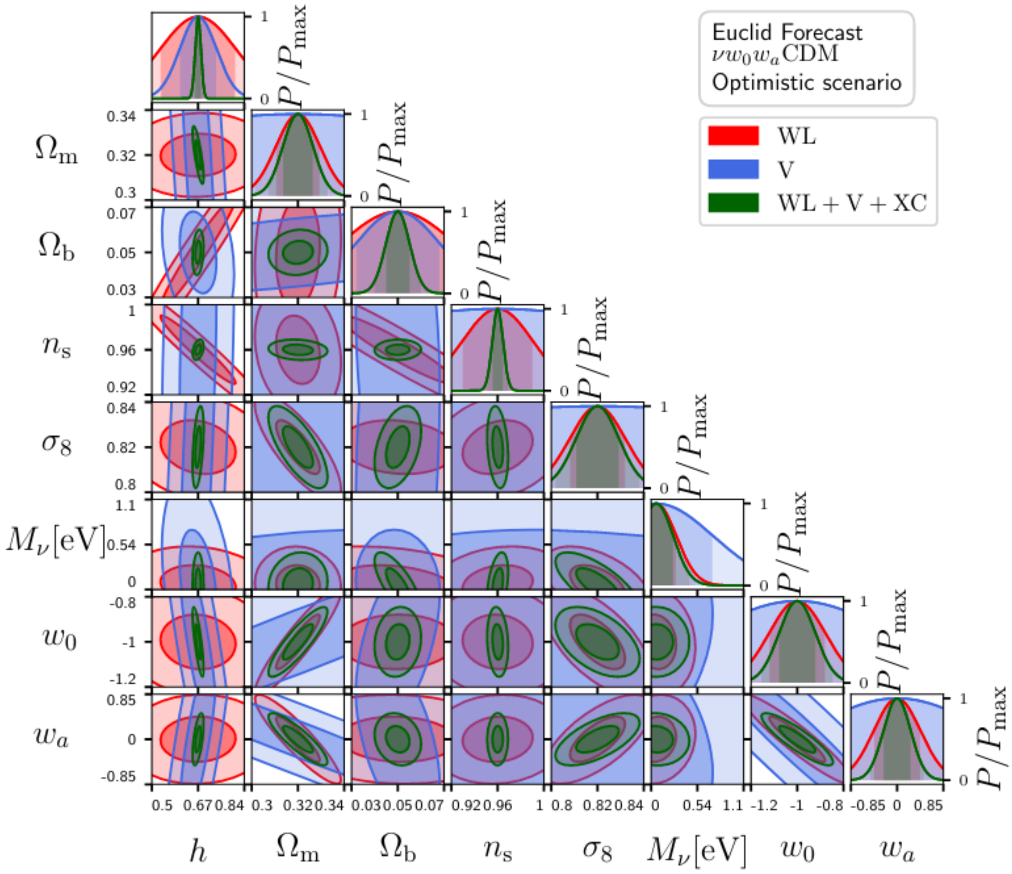

Figure 9.7: The same as Fig. 9.6 but for the $\nu w_0 w_a$CDM scenario.

lensing has a larger constraining power than the photometrc void clustering, except for h and Ω_b. This is due to the form of the weak lensing kernel and the integration along the line-of-sight, and to the presence of the BAO in the $C^{\mathrm{vv}}(\ell)$ and $C^{\gamma\mathrm{v}}(\ell)$, which are instead completely washed out in the $C^{\gamma\gamma}(\ell)$ (see Fig. 9.5). We also underline that the major improvements due to the void clustering and galaxy lensing combination with cross-terms are not only on the h and Ω_b parameters but also on n_s, thanks to the orthogonality of the n_s–Ω_b contours. Then, we can see that the addition of M_ν as free parameter mainly impacts the constraints on σ_8 and Ω_b. This, however, allows the void clustering to impact positively on the neutrino mass constraints: when cross-combining with the void statistic the error on M_ν decreases of $\sim 20\%$ with respect to the galaxy lensing case alone. Then, for both the analysed cosmologies, the FoM_{w_0,w_a} (see Eq. 8.6) reaches a value of ~ 105 when cross-combining the two probes. This represents an enhancement in the constraining power of $\sim 49\%$ with respect to galaxy lensing case alone.

Additional analyses are presented in Bonici et al. (2022, in preparation) to (i) evaluate the impact of void-lensing cross-signal, by assuming the two probes to be independent and (ii) further combine the cross-correlated void-lensing contours with the spectroscopic galaxy clustering. Once again, we refer the interested reader to the aforementioned paper for a full description of these analyses.

As a final consideration, we point out how these results are very competitive with other kinds of probe combination (e.g. galaxy lensing, photometric galaxy clustering, and their cross-correlation Tutusaus et al., 2020) and extremely promising in the perspective of the *Euclid* mission. Indeed, the inclusion of the void clustering and the void-lensing cross-correlation in the galaxy weak lensing analysis will lead to a considerable improvement of the *Euclid* performances, gaining important constraints on the neutrino mass and the DE equation of state parameters.

9.2 Probe combination: void and cluster number counts

In this section we describe the methodology and the preliminary results of the work that we will present in Pelliciari et al. (2022, in preparation). In this work we investigate the synergy between the number counts of galaxy clusters and cosmic voids, which is expected to be particularly effective for these probes. Clusters and voids map indeed complementary aspects of the matter density field, i.e. its peaks and depths, so their joint study is expected to provide orthogonal constraints on the growth of cosmic structures.

For this analysis we use the *Magneticum* cosmological simulations (Dolag et al., in preparation), one of the largest set of hydrodynamical simulations (Sect. 2.3.2) performed to date. These simulations follow a wide range of physical processes (see Hirschmann et al., 2014; Teklu et al., 2015, for details), which are important for the study of the formation of galaxies, galaxy clusters and AGN. They are built assuming ΛCDM cosmology, with parameters fixed to the WMAP7 data (Komatsu et al., 2011), i.e. $\Omega_\mathrm{m} = 0.272$, $h = 0.704$, $\Omega_\Lambda = 0.728$, $n_s = 0.963$ and $\sigma_8 = 0.809$. Among the Magneticum suite boxes available we selected the one denoted "Box1a", with side 896 h^{-1} Mpc and 1512^3 particles of gas and DM (see also e.g. Marulli et al., 2017). In particular, we employ four snapshots with redshifts $z = 0.2, 0.52, 1, 2$, exploiting the information on the galaxy stellar mass, M_*, and the galaxy cluster mass $M_{500\mathrm{c}}$. The latter has been assigned by identifying clusters in the distribution of DM particles with the `SUBFIND` algorithm (see Sect. 2.3.1) and imposing a threshold $\Delta_{\rm c} = 500$. To mimic the range of masses sampled by real surveys and avoid those objects affected by number count incompleteness, we selected galaxies and galaxy cluster with a minimum mass value: $M_* \geq 10^{10}\ h^{-1}\ M_\odot$ and $M_{500c} \geq 10^{14}\ h^{-1}\ M_\odot$, for galaxy and galaxy clusters respectively. This selection precludes the usage of the galaxy cluster catalogue at $z = 2$ due to the small number of massive objects already formed at that epoch. Cosmic voids are then identified running `VIDE` (see Sect. 5.2) on the distribution of galaxies, for each of the four redshifts. The obtained void sample is then cleaned following the same procedure described in Sect. 6.2, rescaling all the underdensities to an internal density threshold of $\delta^{\rm NL}_{\rm v,gal} = -0.7$ and selecting voids with $R_{\rm eff} > 3\,{\rm MPS}$, being here MPS the mean separation of the selected galaxies.

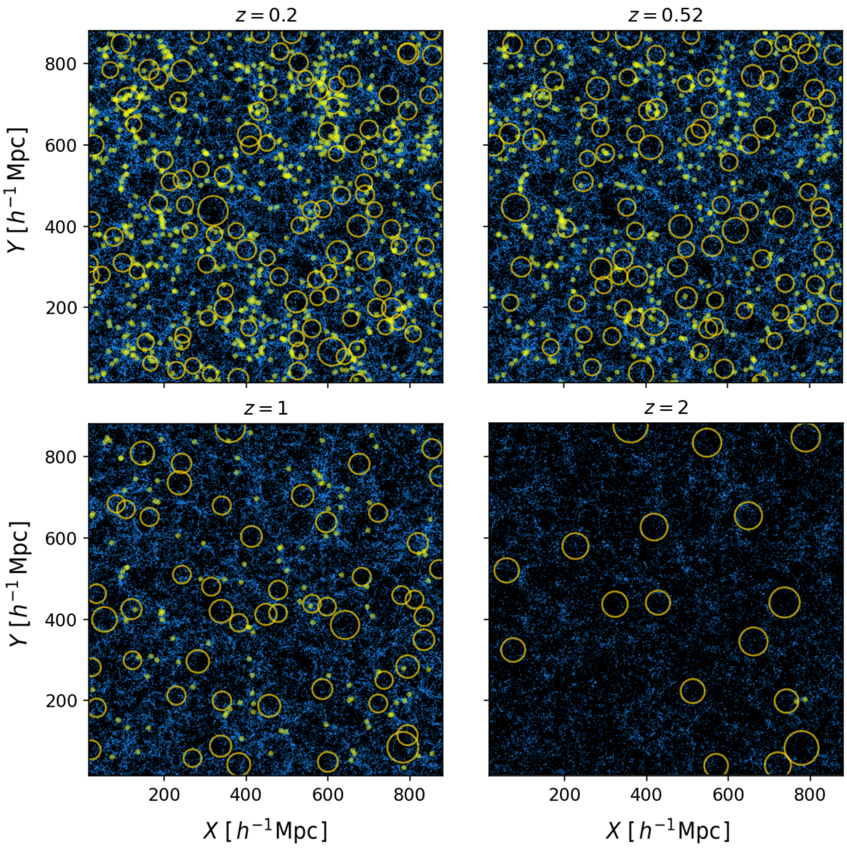

Figure 9.8: Evolution of the LSS in the Magneticum simulations (Box1a) in a 50 h^{-1} Mpc wide slice of the Z-axis, from redshift $z = 0.2$ to $z = 2$. The yellow dots represent galaxy clusters with mass $M_{500c} \geq 10^{14}\ M_\odot\ h^{-1}$, while the blue dots galaxies with stellar mass $M_* \geq 10^{10}\ h^{-1}\ M_\odot$. The latter trace the distribution of matter used to identify cosmic voids, which have been prepared by means of the cleaning procedure (see Sect. 5.3) and further selected by imposing $R_{\rm eff} > 3\,{\rm MPS}$, with MPS the mean galaxy separation. Voids are represented here by yellow circles having sizes corresponding to the effective radius.

A visual representation of the three selected samples (galaxy clusters, galaxies and voids) is reported in Fig. 9.8. We represent the central regions of each snapshot, extracting a slice of 50 h^{-1} Mpc along the Z-axis of the simulation box. As expected, the number of the selected objects (galaxy, galaxy clusters and voids) dramatically decreases with the redshift. As we stated for Fig. 7.1, any apparent overlapping between voids is a visual effect caused by the projection on the X-Y plane. Some mostly empty regions may result not marked as voids due to the superimposition with other underdensities not displayed in the figure, or because composed of voids rejected from our analysis.

The first statistics we want to explore is the halo mass function, i.e. the comoving number density of haloes as a function of their mass. We assume here our clusters to be modelled with accuracy by the same theory used for the DM haloes (see Castro et al., 2021, for a targeted study on the impact of baryons on the halo mass function). In this analysis we rely on the theoretical model provided by Despali et al. (2016), in which the halo mass function is parametrised by means of the variable ν (firstly proposed by Sheth & Tormen, 1999):

$$\nu = \frac{\delta_{\rm c}^{\rm L}(z)^2}{\sigma_M^2(M)} \ , \tag{9.13}$$

where $\delta_{\rm c}^{\rm L}(z)$ is the critical overdensity threshold computed in the linear theory, rescaled at different redshift using the growth factor $D(z)$. With this parametrisation the halo mass function can be written as:

$$\nu f(\nu) = \frac{M^2}{\bar{\rho}} \frac{{\rm d}n}{{\rm d}M} \frac{{\rm d}\ln M}{{\rm d}\ln \nu} \ , \tag{9.14}$$

where:

$$\nu f(\nu) = A\left(1 + \frac{1}{\nu'^p}\right)\left(\frac{\nu'}{2\pi}\right)^{1/2} e^{-\nu'/2} \ , \tag{9.15}$$

with $\nu' = a\nu$. This form is determined by the parameters (a, p, A), which define the mass function cut-off at high masses, its form in the low-mass range and its normalisation, respectively. Their values have been calibrated as a function of the overdensity $\Delta(z)$ used to define DM haloes, making use of simulations with different cosmologies, volumes and resolutions. In particular, Despali et al. (2016) performed a fit of the measured halo number counts by expressing the parameters (a, p, A) as a function of the quantity x, defined as:

$$x \equiv \log[\Delta(z)/\Delta_{\rm vir}(z)] \ , \tag{9.16}$$

where $\Delta_{\rm vir}(z)$ is the virial overdensity[7], obtaining the following relations:

$$\begin{aligned} a &= 0.4332x^2 + 0.2263x + 0.7665 \\ p &= -0.1151x^2 + 0.2554x + 0.2488 \\ A &= -0.1362x + 0.3292 \ . \end{aligned} \tag{9.17}$$

Since the Magneticum simulation clusters have been identified following a different mass definition with respect to the DM haloes analysed by Despali et al. (2016) (we recall also that our clusters are partially affected by the effects of baryonic physics), we perform a new calibration of the coefficients reported in Eq. (9.17). In this procedure, we fixed the

[7]This value derives from the solution to the collapse of a spherical top-hat perturbation under the assumption that the cluster has just virialised (Peebles, 1980, see also Sect. 2.2.1). It depends on the redshift and the cosmological model and can be approximated following e.g. the prescriptions of Bryan & Norman (1998) and Eke et al. (1998).

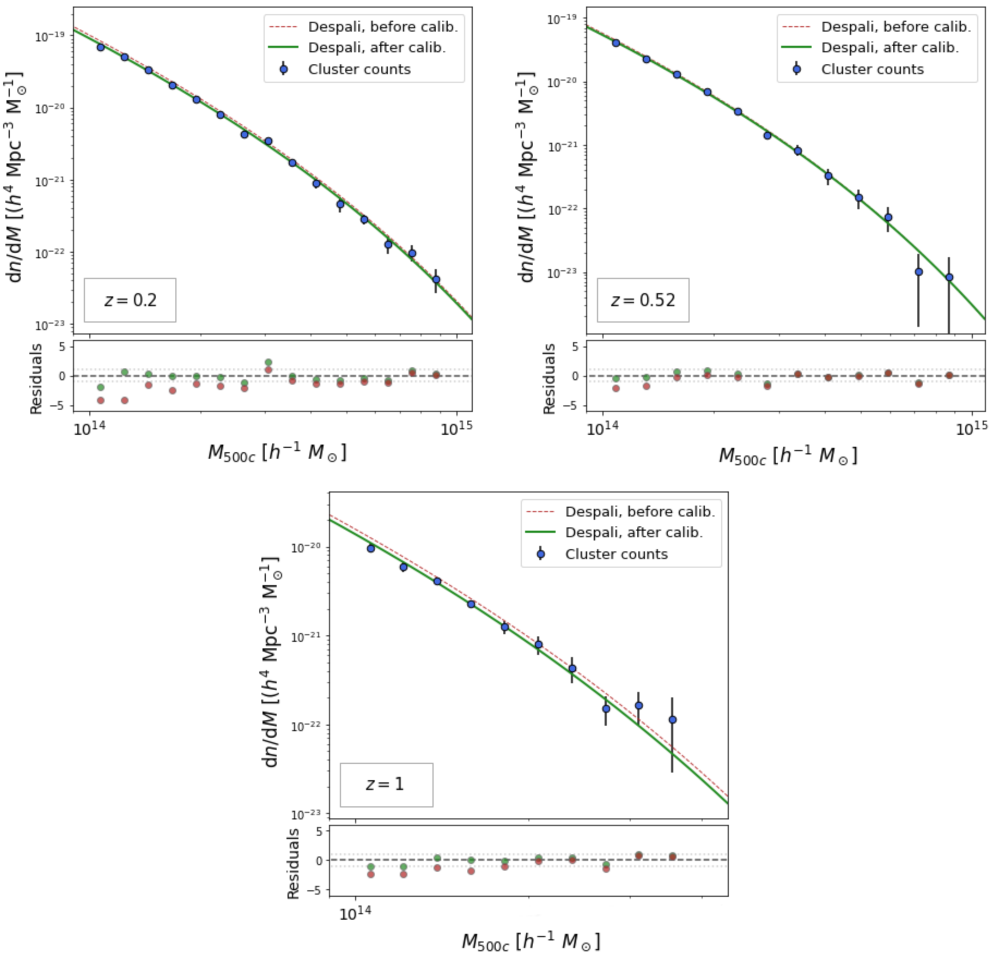

Figure 9.9: Measured mass function of galaxy clusters (blue dots) identified in the Magneticum simulations, having $M_{500c} \geq 10^{14}\ h^{-1}\ M_\odot$, at redshifts $z = 0.2, 0.52, 1$. *Upper sub-panels*: the red dashed line represents the theoretical halo mass function computed with the parameters provided by Despali et al. (2016), while the green solid line shows the predictions of the same model after the re-calibration performed in this analysis. *Lower sub-panels*: residuals of the measured cluster number counts from the models, expressed in units of the Poissonian error associated to the measures. The different colours indicate the residuals with respect to the two models considered in the upper sub-panels. The grey dotted lines delimit a region of 1σ, useful to evaluate the agreement of the data with the two represented models.

parameter p to its best-fit value, provided in Despali et al. (2016), since its variation affects only the low-mass range of the halo mass function and not relevant for our analysis. For the remaining coefficients, we leave them as free parameters of the halo mass function model, computed with Magneticum simulations true cosmology, and we sample their posterior distribution by performing a Bayesian MCMC analysis. The resulting 5D Gaussian distribution provides a new calibration for the halo mass function given in Eq. (9.14); we report in the following the new derived expressions for the parameters in Eq. (9.17):

$$\begin{aligned} a &= (7 \pm 4)\ x^2 - (7 \pm 4)\ x + (3 \pm 1) \\ A &= (-0.2 \pm 0.4)\ x + (0.3 \pm 0.2) \\ p &= 0.2536\ . \end{aligned} \tag{9.18}$$

These coefficients show a high degenerate behaviour and, also because of their large inferred uncertainties, they result consistent within 2σ with the values calibrated by Despali et al. (2016). This re-calibrated model, based on the Magneticum cluster abundance, is shown in Fig. 9.9, where we also report the comparison with the halo mass function model computed with the coefficient reported in Eq. (9.17). As it clearly appears in this figure, the re-calibrated halo mass function model fits accurately the measured cluster number counts at all redshift and, as expected, is slightly more in agreement with these data with respect to the model as originally calibrated by Despali et al. (2016).

For what concerns the analysis of the void size function, we chose to follow the same procedure reported in Sect. 8.3: we use the measured abundance of cosmic voids to calibrate the parameters $B_{\rm slope}$ and $B_{\rm offset}$ of the extended Vdn model presented in Sect. 6.3. So, we measure the effective bias of the galaxies used as mass tracers, $b_{\rm eff}$, at different redshifts, following the methodology reported in Appendix A, then we use these values in Eq. (7.3), used to re-parametrise the underdensity threshold of the Vdn model given by Eq. (4.10). We perform a Bayesian MCMC analysis to fit the void number counts with the extended Vdn model computed with the Magneticum simulation true cosmology, leaving $B_{\rm slope}$ and $B_{\rm offset}$ as free parameters and marginalising over $b_{\rm eff}$. The resulting calibration yields:

$$\mathcal{F}(b_{\rm eff}) = (0.77 \pm 0.02)\, b_{\rm eff} + (0.36 \pm 0.04)\ . \tag{9.19}$$

We show the re-calibrated void size function model in Fig. 9.10, where we also report the comparison with the model calibrated in Chapter 6 by means of FoF DM haloes. As studied in Chapters 6 to 8, the number counts of voids identified in the distribution of cosmic tracers with different mass selections are expected to be reproduced by different coefficients of the function $\mathcal{F}(b_{\rm eff})$ (Eq. 7.3). So we are not surprised to see significantly different predictions between the two models represented in Fig. 9.10: only the one calibrated with voids identified in the Magneticum galaxies accurately fits the number counts of the analysed data sample.

We are now ready to extract cosmological constraints from the number counts of both galaxy clusters and cosmic voids. We chose to focus on the parameters $\Omega_{\rm m}$ and σ_8, which are highly degenerate and so very important to constrain. Moreover, both the halo mass function and the void size function are expected to be particularly sensitive to the variations of these parameters.

We run once again the MCMC on the measured number counts, using this time uniform priors for $\Omega_{\rm m}$ and σ_8, and multivariate Gaussian priors for the calibration parameters

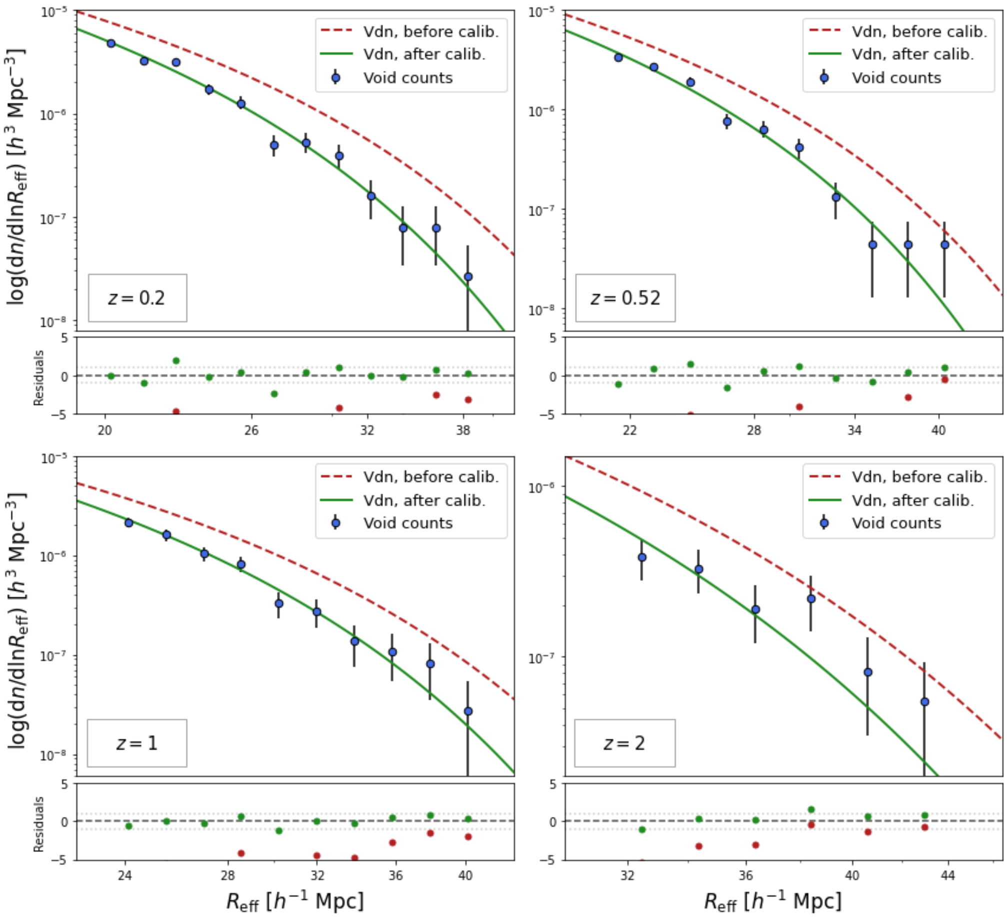

Figure 9.10: The measured size function of voids (blue dots) identified in the distribution of the Magneticum simulations galaxies with $M_* \geq 10^{10}\ h^{-1}\ M_\odot$, at redshifts $z = 0.2, 0.52, 1, 2$. The selected sample is composed of voids with $R_{\rm eff} > 3\,\mathrm{MPS}$, with MPS the mean separation of the selected galaxies. *Upper sub-panels*: the red dashed line represents the theoretical void size function computed with the parametrisation of the Vdn model proposed in Chapter 6, while the green solid line shows the predictions of the same model after the re-calibration performed in this analysis. *Lower sub-panels*: the description is analogous to the one provided for Fig. 9.9 but for the void number counts.

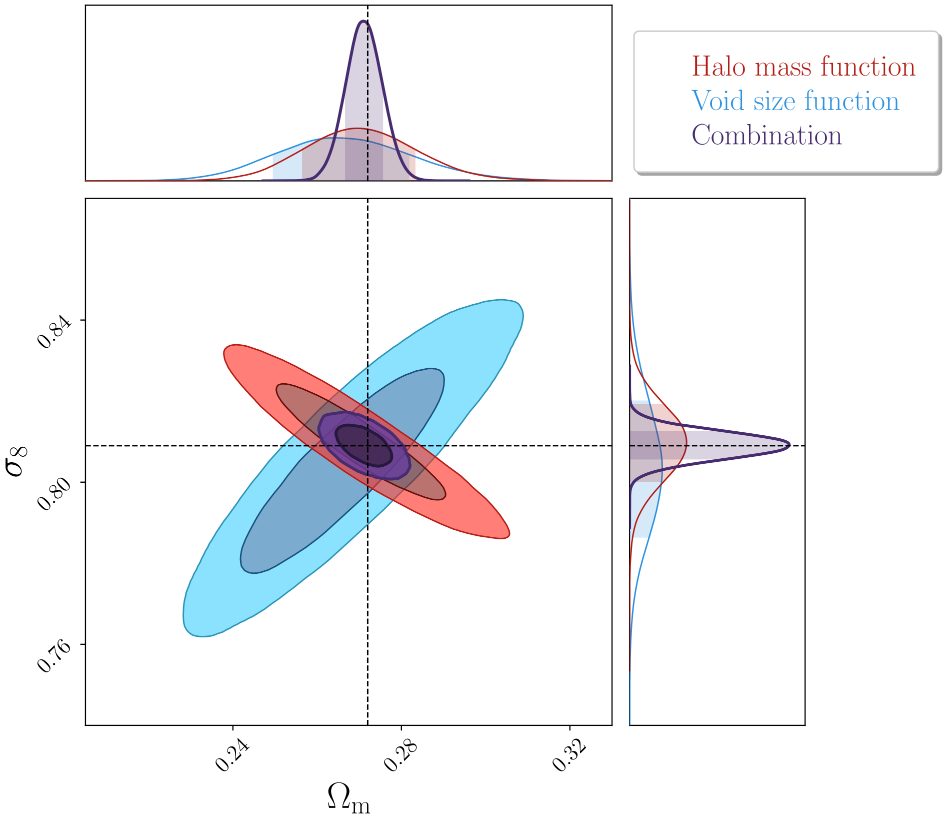

Figure 9.11: 1σ (68%) and 2σ (95%) confidence contours from the halo mass function (in red), the void size function (in blue) and their combination as independent probes (in purple). The values of the underlying cosmological parameters of the Magneticum simulations, i.e. $\Omega_{\rm m} = 0.272$ and $\sigma_8 = 0.809$, are reported with black dashed lines.

of the presented theoretical models. In particular, we use as prior the 5D Gaussian distribution derived for the coefficients in Eq. (9.18) for the halo mass function model, and the 2D Gaussian distribution derived for the parameters $B_{\rm slope}$ and $B_{\rm slope}$ for the void size function model. Then, to combine the two probes, we compute the product of the their posteriors assuming cluster and void number count to be independent. This hypothesis has been tested by estimating the cross-covariance matrix of the data sets analysed, verifying the negligibility of the off-diagonal blocks[8]. The code we use for this analysis has been implemented in the `CosmoBolognaLib` (see Sect. 5.1), together with others that exploit different combination techniques and that we verified providing fully consistent results.

Figure 9.11 shows the cosmological constraints derived in our analysis. We firstly point out the strong orthogonality of the confidence contours presented for the halo mass function and the void size function. Thanks to their nearly perpendicular intersection, their combination results indeed extremely effective: the precision on the constraints increases roughly by a factor of 2 and 3 with respect to those derived using the halo mass function alone, for $\Omega_{\rm m}$ and σ_8 respectively. The median values and the 1σ errors inferred for the

[8] We refer the reader to the Pelliciari et al. (2022, in preparation) for details on this analysis.

Table 9.2: Median and the 1σ errors of the constraints derived for the parameters Ω_m and σ_8 exploiting as cosmological probes the halo mass function, the void size function and their joint analysis.

Probe	Ω_m	σ_8
Halo mass function	0.27 ± 0.01	$0.810^{+0.009}_{-0.010}$
Void size function	$0.26^{+0.02}_{-0.01}$	0.80 ± 0.02
Combination	$0.271^{+0.005}_{-0.004}$	$0.809^{+0.003}_{-0.004}$

marginalised posterior distributions are reported in Table 9.2.

The analysis presented in this section further supports the promising results found in Sects. 8.8 and 9.1.2. It clearly emerges that the study of cosmic voids allows the exploration of methods orthogonal to those of the standard probes and is key in the prospective of future wide-field surveys, because of its fundamental contribution in breaking the degeneracies between the cosmological parameters.

Chapter 10

Conclusions and future perspectives

With this chapter our journey comes to an end. We have gone through the main aspects of the standard cosmological scenario and its possible extensions, exploring different aspects of the observed Universe and venturing then into its largest and darkest regions: cosmic voids. We have studied in particular the constraining power achievable with the study of their abundance, with a keen eye on its future exploitation in Cosmology. Finally, we are ready to sum up the results gathered in this Thesis work.

We first provided the reader a wide overview on the currently accepted standard cosmological model, describing its mathematical fundamentals and predictions, as well as its theoretical and observational issues and possible modifications. Then, we brought our attention on void statistics, i.e. abundance, density profiles and correlation functions.

We focused on the theory to model the number counts of cosmic voids as a function of their radius, i.e. the void size function (Sect. 4.3). We presented the so-called Vdn model, proposed by Jennings, Li & Hu (2013) and initially developed by Sheth & van de Weygaert (2004), and we tested it with voids identified in cosmological simulations of DM particles. We verified the accuracy of this model in predicting the size function of voids specifically prepared for this study, i.e. rescaled and selected by means of a cleaning procedure (see Sect. 5.3). Then we extended the study to voids identified in the distribution of biased tracers, namely DM haloes. This step is obviously a fundamental requirement in the perspective of exploiting the void abundance with real data.

To this end, we introduced in Chapter 6 a new parametrisation of the Vdn model to take into account the effect of the tracer bias on cosmic voids. In particular, we rescaled the characteristic underdensity threshold used in this model by means of a function of the large-scale tracer bias, $\mathcal{F}(b_{\mathrm{eff}})$, which we calibrated using simulated catalogues at different redshifts and biases. We also performed a first exploration of the constraining power of the void size function on the parameters Ω_{m} and σ_8, finding quite promising results especially when combining the statistics at different redshifts.

Afterwards, in Chapter 7 we tested our model on simulations built with alternative cosmological models. In particular, we analysed the degeneracies arising from a proper combination of MG, in the form of $f(R)$ gravity (Hu & Sawicki, 2007), and massive neutrinos. We first tested the disentangling power of the stacked density profiles of voids identified in both the distribution of DM particles and DM haloes. This analysis revealed the presence of deviations of the MG model profiles from those computed in a ΛCDM cosmology, more evident for the most extreme scenarios. These differences are particularly strong at $z = 1$, when the growth of cosmic structures shows an enhancement given by the effect of the fifth force. Nevertheless, we showed that the neutrino thermal free-streaming almost completely erases any peculiar trend of the density profiles, making void profiles predicted by these models almost indistinguishable from the ΛCDM ones.

Secondly, we studied the number counts of voids identified in the same cosmological simulations. Using voids traced by the DM particles we found an excellent agreement between the measured abundances and the theoretical predictions obtained with the Vdn model for the different cosmological scenarios analysed. We also noticed a significant reduction in the void abundance at high redshifts for the models characterised by both MG and massive neutrinos, with respect to the ΛCDM scenario. This trend is caused by the different redshift dependence of MG and massive neutrinos imprints on structure formation: the effect of massive neutrinos to damp the evolution of voids is already in place at early epochs when MG effects are still negligible.

Aiming at analysing the number counts of voids identified in the DM halo distribution, we firstly re-calibrated the coefficients of the linear function $\mathcal{F}(b_{\mathrm{eff}})$ to match the selection criteria used to build the samples of DM haloes. By calibrating this relation with DM haloes characterised by different compactness, we found a slight dependence of $\mathcal{F}(b_{\mathrm{eff}})$ on the type of objects used to identify the voids. We have also tested the universality of this relation by comparing the calibration obtained for the ΛCDM model with those computed using non-standard cosmologies, finding statistically consistent results.

Equipped with the parametrisation of Vdn model we obtained for our halo samples we finally compared the measured and predicted abundances of voids identified in the DM halo catalogues, finding a good agreement in the full range of void radii probed by our simulations. However, all the cosmological models considered in our analysis predict statistically indistinguishable void abundances. We therefore concluded that larger simulations are required to increase the statistical relevance of our measures, especially at large scales, where the differences in the void size function are expected to be stronger, thus allowing to break the cosmic degeneracies.

Then, in Chapter 8 we extended our analysis to the forecasts from the void size function to be expected from the ESA medium-class mission *Euclid* (Laureijs et al., 2011; Amendola et al., 2018). We measured the void number counts from the *Euclid* mock galaxy spectroscopic light-cone in redshift bins, with which we calibrated the relation $\mathcal{F}(b_{\mathrm{eff}})$, used in our extension of the Vdn model. We exploited this new parametrisation also to account for the modifications on the void sizes caused by the volume change of cosmic voids in redshift space. We obtained a remarkable agreement between the measured and predicted void size functions, both in real and redshift space, for all the redshift bins and the spatial scales considered in our analysis.

We performed a MCMC analysis, estimating the constraints expected for the *Euclid* spectroscopic survey from void number counts on two main cosmological models: assuming in one case a scenario characterised by a constant equation-of-state parameter, wCDM, and in the other a scenario with a dynamical DE component described by the CPL parametrisation (Chevallier & Polarski, 2001; Linder, 2003), w_0w_aCDM. In the wCDM scenario we forecasted a 10% precision on w, while in the w_0w_aCDM scenario we computed a FoM_{w_0,w_a} equal to 17 for the most optimistic scenario considered. For each case analysed, the achieved precision on σ_8 (as derived parameter) and Ω_m is instead of about 5% and 3%, respectively. An optimistic estimate of the upper limit on the neutrino mass M_ν is instead of 0.03 eV and 0.08 eV, for the wCDM and the w_0w_aCDM scenario respectively.

Finally, we presented a first exploration of the combination of our results with other cosmological probes, i.e. galaxy clustering and weak lensing (Euclid Collaboration: Blanchard et al., 2020), on the Ω_m–σ_8 parameter space, and void-galaxy cross-correlation function (Hamaus et al., 2022), on the Ω_de–w one. We showed that our results are competitive and highly orthogonal to those provided by these probes, proving the strong constraining power that will derive from their combination.

Additionally, in Chapter 9 we reported the results achieved in projects complementary to the main PhD one. We presented the analysis performed in Hamaus et al. (2022), where we forecasted the constraining power from the void-galaxy cross-correlation function for the *Euclid* spectroscopic survey. The methodology we applied is based on the observable distortions of average void shapes caused by RSDs and the AP effect (introduced in Sect. 4.6): we modelled the (anisotropic) void-galaxy cross-correlation function in redshift space by exploiting a deprojection technique and assuming linear mass conservation. We predicted the constraining power for *Euclid* assuming two flat cosmological models – ΛCDM and wCDM – finding results extremely competitive with that achieved with main probes as the CMB lensing and BAO data. In particular, we predicted a precision of 0.6%-0.7% on Ω_Λ and 9%-11% on w, depending on the possible calibration of the model.

Furthermore, we reported the analysis that will be presented in Bonici et al. (2022, in preparation), where we provide forecasts for the *Euclid* photometric survey from the combination of galaxy lensing, void angular two-point correlation and their cross-correlation. We used the *Euclid* photometric mock galaxy catalogue to evaluate the abundance and the void radius range expected for the mission, together with the void and galaxy mean densities, $n_\mathrm{v}(z)$ and $n_\mathrm{g}(z)$. With this information we computed the angular power spectra tomographically (Hu, 1999) in a set of redshift bins. Then we used a Fisher matrix approach to compute the expected constraints on different cosmological scenarios. The results we found are extremely encouraging as they allow the improvement of the constraints on several cosmological parameters, in particular the neutrino mass and the DE equation of state.

Finally we introduced the work that we will present in Pelliciari et al. (2022, in preparation), where we explored the synergy of cluster mass function and void size function using hydrodynamical simulations. We measured the abundance of galaxy clusters and of voids identified in the distribution of galaxies, and then we performed a re-calibration of both the mass function model (Despali et al., 2016) and of the extended Vdn model on these data. We performed a MCMC analysis to evaluate the respective constraints on the parameters Ω_m and σ_8, proving once again the complementarity of voids with the standard probes. To conclude, we tested the cosmological combination of cluster and voids number counts, assuming these probes as independent. Thanks to the orthogonality of the two derived confidence contours, we found their combination to provide an improvement up to a factor of 3 in the constraining power with respect to the mass function alone.

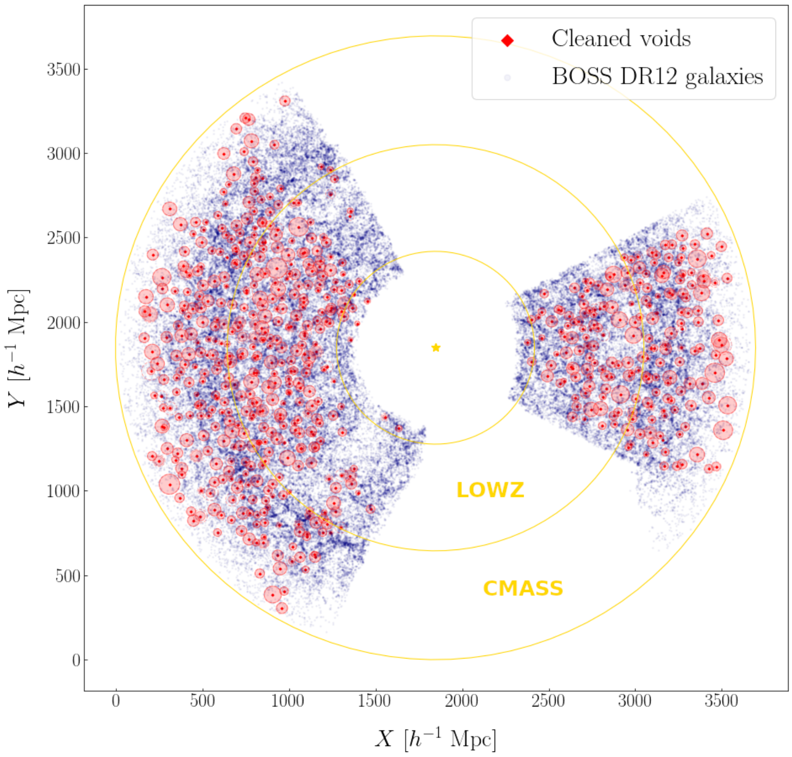

Figure 10.1: Visual representation of the BOSS survey galaxies, composed of the target selections LOWZ ($0.2 < z < 0.4$) and CMASS ($0.4 < z < 0.75$). We show a slice of 50 h^{-1} Mpc of the Z-axis and the voids identified and selected in this sample of galaxies.

The natural extension of this journey implies the application of our pipeline to real galaxy surveys. The first step in this direction has been already taken with a first exploration of the final SDSS-III Baryon Oscillation Spectroscopic Survey (BOSS) Data Release 12 (Dawson et al., 2013). An example of this work is shown in Fig. 10.1, where we represent the sample of voids identified in the BOSS survey galaxy, and cleaned to match the void definition used in the void size function model. To this end, we will also test our void size function modelling pipeline with a number of analyses that will include e.g.: the usage of different void finding algorithms, the inclusion in the model of more cosmological parameters, the extension to different cosmological scenarios, and finally the assessment of the contribution of realistic observational uncertainties, such as more complex errors on the tracer redshifts and survey mask effects. These analyses will allow us to build a robust and strictly validated methodology to be applied in the near future to study the voids that will be identified by the upcoming wide field surveys like *Euclid*, NGRST (Green et al., 2012) and LSST (LSST Dark Energy Science Collaboration, 2012).

We expect the results we presented in this Thesis to pave the way towards a full cosmological exploitation of cosmic voids and to encourage the future exploitation of this novel and promising cosmological probe.

Appendices

Appendix A

Measuring the linear bias

In this appendix, we describe the methods employed in this work to estimate the large-scale effective linear bias of the tracers used to identify the voids. We followed the same prescriptions as in Marulli et al. (2013, 2018), exploiting the 2PCF of the DM haloes of our simulated catalogues, and performing a Bayesian statistical analysis to infer the effective bias, $b_{\rm eff}$.

The angle-averaged 2PCF is computed using the Landy & Szalay (1993) estimator (see Sect. 2.1.5). Then, we computed the covariance matrix $C_{i,j}$, which measures the variance and correlation between the different bins of the 2PCF, with the Bootstrap method, dividing the original catalogues in 125 sub-catalogues, and constructing 100 realisations by resampling from the sub-catalogues, with replacement. We constructed the random catalogue by extracting the object coordinates randomly, preserving the same 3D coverage and the same geometry of the initial catalogue. In particular, we build the random catalogue to be 4 times larger than the DM halo sample, since this proportion allows to have sufficiently small Poissonian errors in the DR counts, compared to the errors in DD. We also performed tests with different sizes of the random catalogue, finding consistent results.

The covariance matrix is defined as follows:

$$C_{i,j} = \mathcal{F} \sum_{k=1}^{N_R} (\xi_i^k - \overline{\xi}_i)(\xi_j^k - \overline{\xi}_j) \ , \tag{A.1}$$

where the subscripts i and j run over the 2PCF bins, while k refers to the 2PCF of the k-th of N_R catalogue realisations, and $\overline{\xi}$ is the mean 2PCF of the N_R samples. $\mathcal{F}$ is the normalisation factor, which takes into account the fact that the $N_{\rm R}$ realisations might not be independent (Norberg et al., 2009), and is $\mathcal{F} = 1/(N_{\rm R} - 1)$ in the case of the Bootstrap method.

Finally, we performed a full MCMC analysis of the 2PCF, using a Gaussian likelihood function $\mathcal{L}$, defined as:

$$-2\ln\mathcal{L} = \sum_{i=1}^{N} \sum_{j=1}^{N} (\xi_i^d - \xi_i^{\rm m}) C_{i,j}^{-1} (\xi_j^{\rm d} - \xi_j^{\rm m}) \ , \tag{A.2}$$

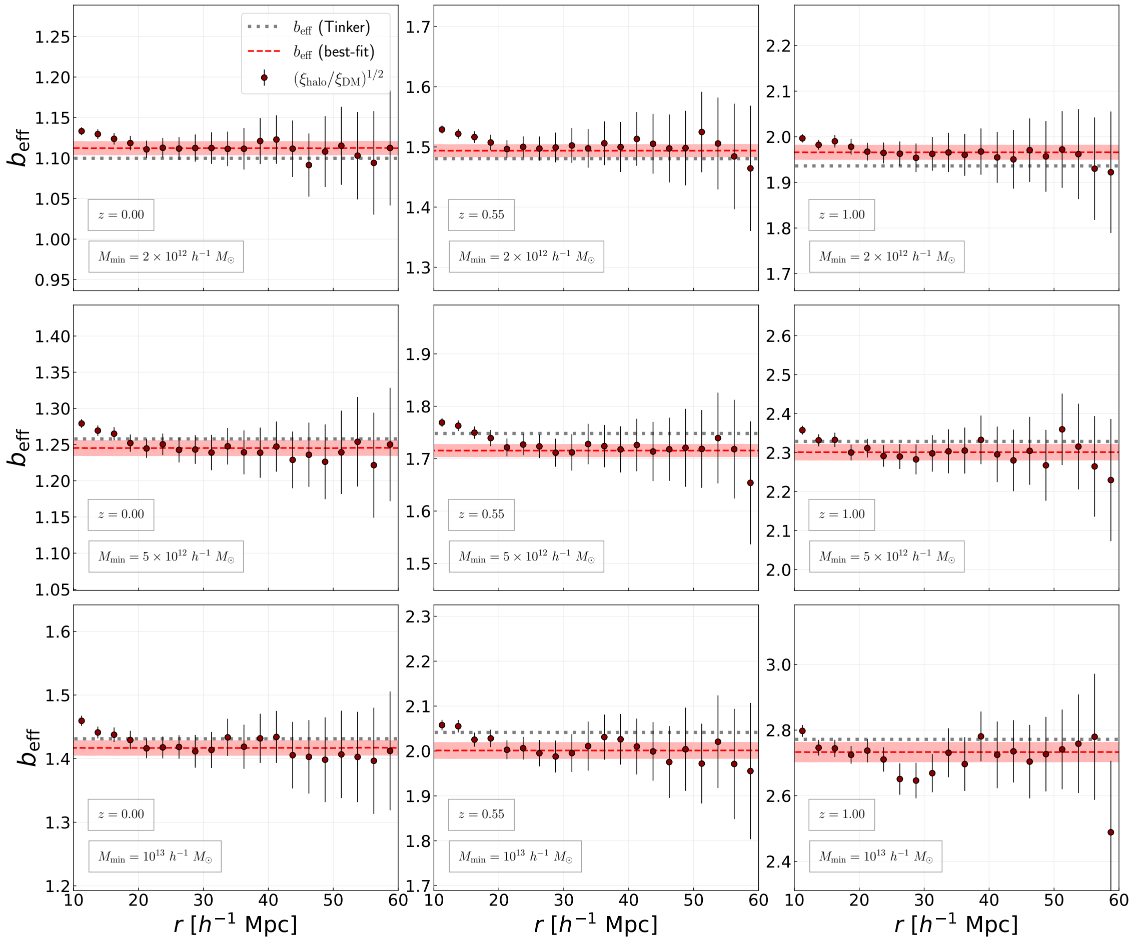

Figure A.1: The halo bias for the catalogues with $M_{\rm min} = 2{\times}10^{12}\ h^{-1}\ M_\odot$, $5{\times}10^{12}\ h^{-1}\ M_\odot$ and $10^{13}\ h^{-1}\ M_\odot$ (rows from *top* to *bottom*), at redshifts $z = 0$, $z = 0.55$, $z = 1$ (columns from *left* to *right*). The black points represent the square root of the ratio between the auto-correlation function of the haloes and the DM particles (see Eq. 2.36). The error bars are the diagonal elements of the covariance matrix estimated with Bootstrap. The red shaded areas show the 1σ uncertainties on the best-fit bias values estimated with the MCMC modelling, fitting in the range of radii of [20–40] h^{-1} Mpc. The dashed grey lines show the theoretical predictions given by the Tinker et al. (2010) model.

where $C_{i,j}^{-1}$ is the inverse of the covariance matrix, N is the number of comoving separation bins at which the 2PCF is estimated, and the superscripts d and m stand for data and model, respectively. The 2PCF model, $\xi_{\rm m}(r)$, is computed as follows:

$$\xi_m(r) = b_{\rm eff}^2 \, \xi_{\rm DM}(r) \ , \tag{A.3}$$

where $\xi_{\rm DM}(r)$ is the DM 2PCF, which is estimated by Fourier transforming the power spectrum, $P_{\rm DM}(k)$, computed with the `CAMB`. An accurate estimate of the effective bias parameter, $b_{\rm eff}$, and its uncertainty are assessed by sampling its posterior distribution.

Figure A.1 shows the results of this analysis. The data points are the square root of ratio between the tracer and matter 2PCFs (see Eq. 2.36), while the dashed red lines show the best-fit values and uncertainties of $b_{\rm eff}$, estimated from the median and quartiles of the posterior distribution sampled with the MCMC analysis.

We compared these values to the theoretical effective bias of DM haloes, computed as follows:

$$b_{\rm eff}(z) = \frac{\displaystyle\int_{M_{\rm min}}^{M_{\rm max}} {\rm d}M \, b(M,z)\Phi(M,z)}{\displaystyle\int_{M_{\rm min}}^{M_{\rm max}} {\rm d}M \, \Phi(M,z)} \ , \tag{A.4}$$

where $\Phi(M,z)$ is the halo mass function of the catalogue, and $M_{\rm min}$ and $M_{\rm max}$ are the lowest and largest masses in the sample, respectively. To compute the linear bias $b(M,z)$, we relied on the theoretical model developed by Tinker et al. (2010).

Appendix B

Testing systematic uncertainties deriving from the calibrated bias relation

In this appendix we first test the effect of using the value of b_{eff} instead of $\mathcal{F}(b_{\mathrm{eff}})$ to recover the cosmological parameters. In particular, we repeat the MCMC analysis of the measured size functions performed in Sect. 6.6 employing a wrong theoretical model, i.e. a Vdn model re-scaled with the linear bias inferred from the tracer large-scale 2PCF, which is equivalent to setting the parameters $B_{\mathrm{slope}} = 1$ and $B_{\mathrm{offset}} = 0$. As demonstrated in Fig. 6.7, the model obtained using the tracer bias b_{eff} cannot fit properly the measured void abundances, unless it is previously converted in its corresponding value computed inside voids by means of the linear relation $\mathcal{F}(b_{\mathrm{eff}})$. As shown in Fig. B.1, the contour levels achieved with the effective bias are on average smaller with respect to the ones presented in Fig. 6.8. In fact, the uncertainties associated to the theoretical model re-parametrised directly with b_{eff} are smaller, since the errors of A_{rel} and B_{rel} are not included in the model. As expected, the contour levels obtained using the wrong bias value tend to shift from the real values of σ_8 and Ω_{m}, especially for low redshifts and mass-cuts. Indeed, in these cases the values of b_{eff} and b_{rel} are significantly different from each other, whereas at higher redshifts and mass-cuts they tend to be more similar, as showed in Fig. 6.5.

We secondly assess the systematic errors on the cosmological constraints caused by uncertainties in the estimation of the coefficients of the conversion relation, calibrated in Sect. 6.5. This is particularly useful in the perspective of a future application on real surveys. To propagate a possible systematic error on the Eq. (6.5) to the final cosmological constraints, we repeated the MCMC analysis described in Sect. 6.6 assuming different values for the coefficient B_{slope} and B_{offset}. In particular, to test the cases with the major discrepancy from the calibrated relation, we increased or decreased both the parameters by 1σ, where 1σ is the uncertainty derived by the weighted fit of the data in Fig. 6.6. Specifically, we set $B'_{\mathrm{slope}} = 0.854 + 0.007$ and $B'_{\mathrm{offset}} = 0.420 + 0.010$ in the first case, whereas $B''_{\mathrm{slope}} = 0.854 - 0.007$ and $B''_{\mathrm{offset}} = 0.420 - 0.010$ in the second case. In Fig. B.2 we report the results for the catalogue with $M_{\mathrm{min}} = 2 \times 10^{12}\ h^{-1}\ M_{\odot}$ at $z = 0$. As shown in this figure, the real values of σ_8 and Ω_{m} are within the 68% confidence levels obtained in both cases. Moreover, the posterior distribution of Ω_{m} is almost unchanged, while σ_8 results shifted towards greater values using a conversion relation with B''_{slope} and

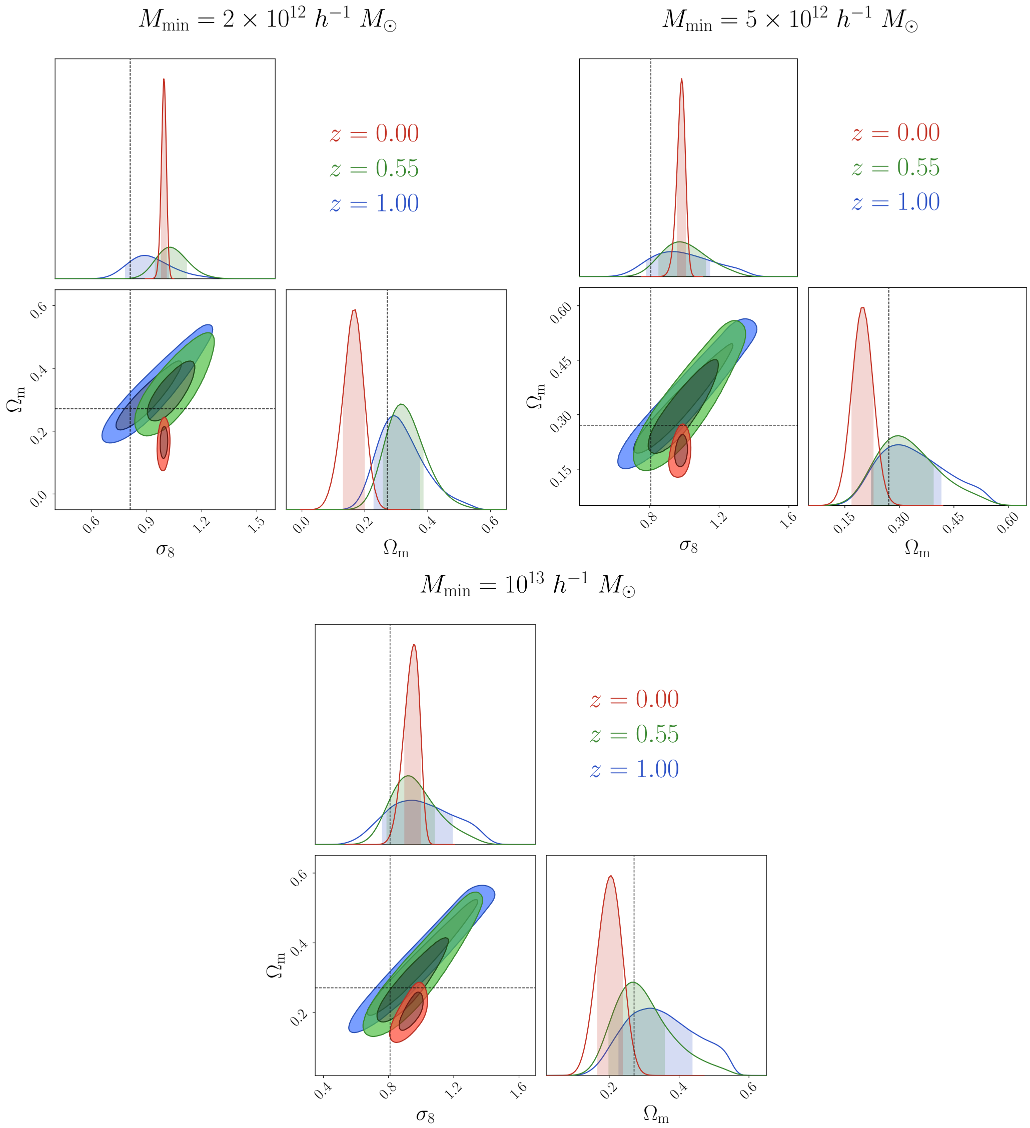

Figure B.1: 1σ (68%) and 2σ (95%) confidence levelsin the σ_8–$\Omega_{\rm m}$ plane, for the halo catalogues with $M_{\rm min} = 2 \times 10^{12}\ h^{-1}\ M_\odot$ (*top left*), $5 \times 10^{12}\ h^{-1}\ M_\odot$ (*top right*), and $10^{13}\ h^{-1}\ M_\odot$ (*bottom*), obtained by re-parametrising the Vdn model directly with $b_{\rm eff}$, thus without converting this value by means of the Eq. (6.5). The colour of ellipses corresponds to different redshifts: red for $z = 0$, green for $z = 0.55$ and blue for $z = 1$. The prior distributions are uniform for σ_8 and $\Omega_{\rm m}$, and Gaussian for $b_{\rm eff}$. The 1D distributions (top and bottom right subpanels) show the marginalised posterior probability of σ_8 and $\Omega_{\rm m}$, respectively. The black lines represent the true WMAP7 values ($\sigma_8 = 0.809$ and $\Omega_{\rm m} = 0.2711$).

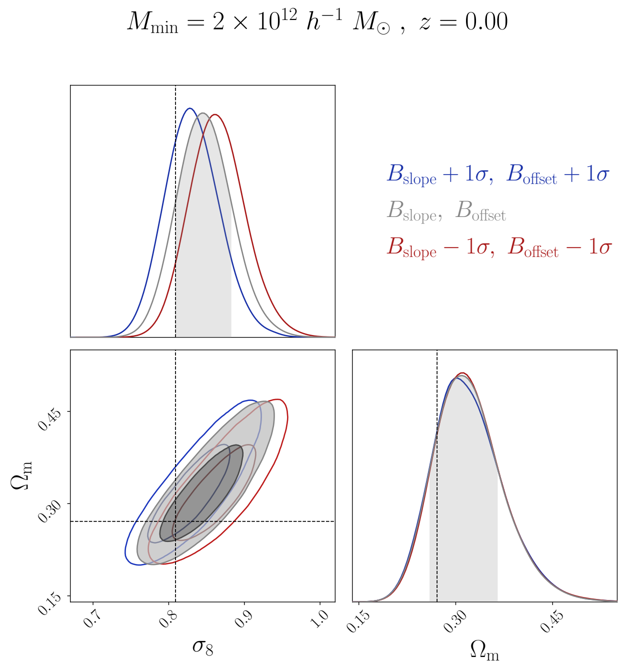

Figure B.2: 1σ (68%) and 2σ (95%) confidence levels in the σ_8–$\Omega_{\rm m}$ plane, for the halo catalogue with $M_{\rm min} = 2{\times}10^{12}\ h^{-1}\ M_{\odot}$ at $z = 0$. 1D curves (top and bottom right panels) show the posterior distributions of σ_8 and $\Omega_{\rm m}$, respectively. The grey filled contours represent the confidence levels obtained using Eq. (6.5), while the blue and red contours indicate the results obtained by converting the value of $b_{\rm eff}$ shifting both the values of $B_{\rm slope}$ and $B_{\rm offset}$ by $+1\sigma$ and -1σ, respectively. The black lines represent the true WMAP7 values ($\sigma_8 = 0.809$ and $\Omega_{\rm m} = 0.2711$).

$B''_{\rm offset}$ and towards lower values for the case with $B'_{\rm slope}$ and $B'_{\rm offset}$. We obtained the same results also for the catalogue with higher redshift and mass selections. The larger is the tracer bias, the larger is the discrepancy of the modified relation from the one calibrated in Eq. (6.5). Indeed, shifting both the values of $B_{\rm slope}$ and $B_{\rm offset}$ by $+1\sigma$ and -1σ, the resulting linear equations tend to move even further away from the calibrated relation with $b_{\rm eff}$. This causes a systematic error that has more impact on the theoretical size functions associated to the catalogues with higher $b_{\rm eff}$. Nevertheless, we verified that even in these cases the constraints are still consistent with the real values of σ_8 and $\Omega_{\rm m}$. We can conclude that, even with a systematic error of $\pm 1\sigma$ on the values of the coefficients in the calibrated relation, the void size function still provides reliable cosmological constraints.

Appendix C

The void-lensing Fisher matrix

In this appendix we summarise the Fisher matrix formalism (Fisher, 1935) and we provide details on its application to predict the constraining power of void clustering, galaxy weak lensing and their combination (including their cross-correlation) on the cosmological parameters (see Sect. 9.1.2).

The Fisher matrix is computed as the expectation value of the second derivatives of the logarithm of the likelihood $\mathcal{L}$:

$$F_{\alpha\beta} = \left\langle \frac{\partial^2 \ln \mathcal{L}}{\partial\alpha\partial\beta} \right\rangle , \tag{C.1}$$

where α and β are the considered model parameters. The expected *error covariance matrix* is defined as the inverse of the Fisher matrix F:

$$\mathcal{C}_{\alpha\beta} = (F^{-1})_{\alpha\beta} . \tag{C.2}$$

The diagonal elements of $\mathcal{C}_{\alpha\beta}$ are then given by square root of the marginalised 1σ errors on the parameters:

$$\sigma_\alpha = \sqrt{\mathcal{C}_{\alpha\alpha}} . \tag{C.3}$$

Let us now introduce the matrix for the angular power spectra, $\Sigma^{\rm AB}_{i,j}$, which is associated to a given $C^{\rm AB}_{i,j}(\ell)$ (see Eq. 9.7) as:

$$\Sigma^{\rm AB}_{i,j}(\ell) = \sqrt{\frac{2}{(2\ell+1)\Delta\ell f_{\rm sky}}}\left[C^{\rm AB}_{i,j}(\ell) + N^{\rm AB}_{i,j}(\ell)\right] , \tag{C.4}$$

where $\Delta\ell$ is the multipole bin width, $f_{\rm sky}$ the sky fraction covered by the survey, and $N^{\rm AB}_{i,j}(\ell)$ the shot noise matrix. The latter depends on the particular probe we want to use. For the void clustering, galaxy lensing, and void-lensing angular power spectrum we have:

$$N^{\rm vv}_{i,j} = \frac{1}{\overline{n}^i_{\rm v}}\delta_{i,j} , \qquad N^{\gamma\gamma}_{i,j} = \frac{\sigma^2_\epsilon}{\overline{n}^i_{\rm g}}\delta_{i,j} , \qquad N^{\gamma{\rm v}}_{i,j} = N^{{\rm v}\gamma}_{i,j} = 0 , \tag{C.5}$$

where $\delta_{i,j}$ is the Kronecker delta, σ_ϵ^2 is the galaxy shape noise, and $\overline{n}_{\rm g}^i$ and $\overline{n}_{\rm v}^i$ are the unnormalised average galaxy and void surface densities in the i-th tomographic bin computed with the fiducial cosmology, respectively. We refer the reader to Bonici et al. (2022, in preparation) for the survey specifications used to compute the covariances.

When considering a single probe, i.e. $(A = B)$, the $C(\ell)$ covariance matrix is simply given by Eq. (C.4). Instead, to combine two or more probes we need to construct the full covariance matrix, $\mathbf{\Sigma}^{\rm XC}$, composed of the matrix blocks defined in Eq. (C.4). For the void clustering and the galaxy weak lensing we have in particular:

$$\mathbf{\Sigma}^{\rm XC}(\ell) = \begin{pmatrix} \mathbf{\Sigma}^{\gamma\gamma}(\ell) & \mathbf{\Sigma}^{\gamma{\rm v}}(\ell) \\ \mathbf{\Sigma}^{{\rm v}\gamma}(\ell) & \mathbf{\Sigma}^{\rm vv}(\ell) \end{pmatrix} , \tag{C.6}$$

which yields to the associated error covariance matrix:

$$\mathcal{C}^{\rm XC}(\ell) = \begin{pmatrix} \mathcal{C}^{\gamma\gamma}(\ell) & \mathcal{C}^{\gamma{\rm v}}(\ell) \\ \mathcal{C}^{{\rm v}\gamma}(\ell) & \mathcal{C}^{\rm vv}(\ell) \end{pmatrix} . \tag{C.7}$$

Assuming the coefficients of the spherical harmonic 2D decomposition to follow a multivariate Gaussian distribution, we get the following analytical expression for the Fisher matrix elements:

$$F_{\alpha\beta} = \sum_{\ell=\ell_{\rm min}}^{\ell_{\rm max}} {\rm Tr}\left\{ [\mathbf{\Sigma}]^{-1} \frac{\delta\partial\mathcal{C}(\ell)}{\partial\alpha} [\mathbf{\Sigma}]^{-1} \frac{\delta\partial\mathcal{C}(\ell)}{\partial\beta} \right\} , \tag{C.8}$$

where Tr indicates the matrix trace. This formula applies both to the single- and two-probe correlation cases, provided that the $C(\ell)$ and the covariance matrices are chosen accordingly.

Bibliography

Aarseth S. J., 1963, Mon. Not. R. Astron. Soc., 126, 223

Abbott T. M. C. et al., 2018a, Phys. Rev. D, 98, 043526

Abbott T. M. C. et al., 2018b, Phys. Rev. D, 98, 043526

Achitouv I., 2016, Phys. Rev. D, 94, 103524

Achitouv I., Blake C., Carter P., Koda J., Beutler F., 2017, Phys. Rev. D, 95, 083502

Agarwal S., Feldman H. A., 2011, Mon. Not. R. Astron. Soc., 410, 1647

Ahmed S. N. et al., 2004, Phys. Rev. Lett., 92, 181301

Alam S. et al., 2017, Mon. Not. R. Astron. Soc., 470, 2617

Alcock C., Paczynski B., 1979, Nature, 281, 358

Amendola L. et al., 2018, Living Reviews in Relativity, 21, 2

Amendola L. et al., 2013, Living Reviews in Relativity, 16, 6

Anderson L. et al., 2014, Mon. Not. R. Astron. Soc., 441, 24

Audren B., Lesgourgues J., Bird S., Haehnelt M. G., Viel M., 2013, J. Cosm. Astro-Particle Phys., 2013, 026

Bagla J. S., Padmanabhan T., 1997, Pramana, 49, 161

Baker T., Clampitt J., Jain B., Trodden M., 2018, Phys. Rev. D, 98, 023511

Baldi M., 2012, Mon. Not. R. Astron. Soc., 422, 1028

Baldi M., Pettorino V., Robbers G., Springel V., 2010, Mon. Not. R. Astron. Soc., 403, 1684

Baldi M., Villaescusa-Navarro F., 2016, arXiv e-prints, arXiv:1608.08057

Baldi M., Villaescusa-Navarro F., Viel M., Puchwein E., Springel V., Moscardini L., 2014, Mon. Not. R. Astron. Soc., 440, 75

Ballinger W. E., Peacock J. A., Heavens A. F., 1996, Mon. Not. R. Astron. Soc., 282, 877

Banerjee A., Dalal N., 2016, J. Cosm. Astro-Particle Phys., 2016, 015

Barnes J., Hut P., 1986, Nature, 324, 446

Barreira A., Cautun M., Li B., Baugh C. M., Pascoli S., 2015, J. Cosm. Astro-Particle Phys., 2015, 028

Barrow J. D., Cotsakis S., 1988, Physics Letters B, 214, 515

Bartelmann M., Schneider P., 2001, Phys. Rept., 340, 291

Becker-Szendy R. et al., 1992, Phys. Rev. D, 46, 3720

Behroozi P. S., Wechsler R. H., Wu H.-Y., 2013, Astrophys. J., 762, 109

Bennett C. L. et al., 2013, Astrophys. J. Suppl., 208, 20

Bennett J. J., Buldgen G., de Salas P. F., Drewes M., Gariazzo S., Pastor S., Wong Y. Y. Y., 2020, arXiv e-prints, arXiv:2012.02726

Bernal J. L., Verde L., Riess A. G., 2016, J. Cosm. Astro-Particle Phys., 2016, 019

Bernardeau F., 1994, Astrophys. J., 427, 51

Bernardeau F., Colombi S., Gaztañaga E., Scoccimarro R., 2002, Phys. Rept., 367, 1

Bertotti B., Iess L., Tortora P., 2003, Nature, 425, 374

Beutler F. et al., 2011, Mon. Not. R. Astron. Soc., 416, 3017

Beutler F. et al., 2017, Mon. Not. R. Astron. Soc., 466, 2242

Bianchi E., Rovelli C., 2010, arXiv e-prints, arXiv:1002.3966

Biswas R., Alizadeh E., Wandelt B. D., 2010, Phys. Rev. D, 82, 023002

Blanton M. R. et al., 2003, The Astrophysical Journal, 592, 819–838

Blanton M. R., Lupton R. H., Schlegel D. J., Strauss M. A., Brinkmann J., Fukugita M., Loveday J., 2005, Astrophys. J., 631, 208

Bond H. E., Nelan E. P., VandenBerg D. A., Schaefer G. H., Harmer D., 2013, Astrophys. J. Lett., 765, L12

Bond J. R., Cole S., Efstathiou G., Kaiser N., 1991, Astrophys. J., 379, 440

Bonici M., Carbone C., Davini S., et al., 2022, in preparation, *Euclid* : Forecasts from the void-lensing cross-correlation, currently on internal ECEB review

Bos E. G. P., van de Weygaert R., Dolag K., Pettorino V., 2012, Mon. Not. R. Astron. Soc., 426, 440

Brandbyge J., Hannestad S., 2009, J. Cosm. Astro-Particle Phys., 2009, 002

Brandbyge J., Hannestad S., 2010, J. Cosm. Astro-Particle Phys., 2010, 021

Brandbyge J., Hannestad S., Haugbølle T., Thomsen B., 2008, J. Cosm. Astro-Particle Phys., 2008, 020

Brandbyge J., Hannestad S., Haugbølle T., Wong Y. Y. Y., 2010, J. Cosm. Astro-Particle Phys., 2010, 014

Brans C., Dicke R. H., 1961, Physical Review, 124, 925

Brax P., Valageas P., 2013, Phys. Rev. D, 88, 023527

Brax P., Valageas P., 2014, Phys. Rev. D, 90, 023507

Bryan G. L., Norman M. L., 1998, Astrophys. J., 495, 80

Bull P. et al., 2016, Physics of the Dark Universe, 12, 56

Burgess C. P., 2013, arXiv e-prints, arXiv:1309.4133

Cabré A., Vikram V., Zhao G.-B., Jain B., Koyama K., 2012, J. Cosm. Astro-Particle Phys., 2012, 034

Cai Y.-C., Padilla N., Li B., 2015, Mon. Not. R. Astron. Soc., 451, 1036

Calabrese E., Slosar A., Melchiorri A., Smoot G. F., Zahn O., 2008, Phys. Rev. D, 77, 123531

Capozziello S., Carloni S., Troisi A., 2003, arXiv e-prints, astro

Capozziello S., Fang L. Z., 2002, International Journal of Modern Physics D, 11, 483

Carroll S. M., 2001, Living Reviews in Relativity, 4, 1

Carroll S. M., Duvvuri V., Trodden M., Turner M. S., 2004, Phys. Rev. D, 70, 043528

Castorina E., Carbone C., Bel J., Sefusatti E., Dolag K., 2015, J. Cosm. Astro-Particle Phys., 7, 043

Castorina E., Sefusatti E., Sheth R. K., Villaescusa-Navarro F., Viel M., 2014, J. Cosm. Astro-Particle Phys., 2014, 049

Castro T., Borgani S., Dolag K., Marra V., Quartin M., Saro A., Sefusatti E., 2021, Mon. Not. R. Astron. Soc., 500, 2316

Cataneo M. et al., 2015, Phys. Rev. D, 92, 044009

Cautun M., Paillas E., Cai Y.-C., Bose S., Armijo J., Li B., Padilla N., 2018, Mon. Not. R. Astron. Soc., 476, 3195

Ceccarelli L., Ruiz A. N., Lares M., Paz D. J., Maldonado V. E., Luparello H. E., Garcia Lambas D., 2016, Mon. Not. R. Astron. Soc., 461, 4013

Chan K. C., Hamaus N., Biagetti M., 2019, Phys. Rev. D, 99, 121304

Chevallier M., Polarski D., 2001, International Journal of Modern Physics D, 10, 213

Chiang C.-T., LoVerde M., Villaescusa-Navarro F., 2019, Phys. Rev. Lett., 122, 041302

Chiba T., 2003, Physics Letters B, 575, 1

Clampitt J., Cai Y.-C., Li B., 2013a, Mon. Not. R. Astron. Soc., 431, 749

Clampitt J., Cai Y.-C., Li B., 2013b, Mon. Not. R. Astron. Soc., 431, 749

Clampitt J., Jain B., 2015, Mon. Not. R. Astron. Soc., 454, 3357

Clifton T., Ferreira P. G., Padilla A., Skordis C., 2012, Phys. Rept., 513, 1

Colberg J. M. et al., 2008, Mon. Not. R. Astron. Soc., 387, 933

Cole S., 1991, Astrophys. J., 367, 45

Coles P., Lucchin F., 2002, Cosmology: The Origin and Evolution of Cosmic Structure, Second Edition. John Wiley & Sons Inc

Contarini S., Marulli F., Moscardini L., Veropalumbo A., Giocoli C., Baldi M., 2021, Mon. Not. R. Astron. Soc., 504, 5021

Contarini S., Ronconi T., Marulli F., Moscardini L., Veropalumbo A., Baldi M., 2019, Mon. Not. R. Astron. Soc., 488, 3526

Contarini S., Verza G., Pisani A., et al., 2022, in preparation, *Euclid* : Cosmological forecasts from the void size function, currently on internal ECEB review

Correa C. M., Paz D. J., Padilla N. D., Sánchez A. G., Ruiz A. N., Angulo R. E., 2021, arXiv e-prints, arXiv:2107.01314

Correa C. M., Paz D. J., Sánchez A. G., Ruiz A. N., Padilla N. D., Angulo R. E., 2020, arXiv e-prints, arXiv:2007.12064

Costanzi M., Sartoris B., Viel M., Borgani S., 2014, J. Cosm. Astro-Particle Phys., 2014, 081

Costille A. et al., 2018, in Society of Photo-Optical Instrumentation Engineers (SPIE) Conference Series, Vol. 10698, Space Telescopes and Instrumentation 2018: Optical, Infrared, and Millimeter Wave, Lystrup M., MacEwen H. A., Fazio G. G., Batalha N., Siegler N., Tong E. C., eds., p. 106982B

Cousinou M. C., Pisani A., Tilquin A., Hamaus N., Hawken A. J., Escoffier S., 2019, Astronomy and Computing, 27, 53

Crocce M., Scoccimarro R., 2008, Phys. Rev. D, 77, 023533

Cropper M. et al., 2018, in Society of Photo-Optical Instrumentation Engineers (SPIE) Conference Series, Vol. 10698, Space Telescopes and Instrumentation 2018: Optical, Infrared, and Millimeter Wave, Lystrup M., MacEwen H. A., Fazio G. G., Batalha N., Siegler N., Tong E. C., eds., p. 1069828

Cuesta A. J., Niro V., Verde L., 2016, Physics of the Dark Universe, 13, 77

Cyburt R. H., Fields B. D., Olive K. A., Yeh T.-H., 2016, Reviews of Modern Physics, 88, 015004

Davies C. T., Paillas E., Cautun M., Li B., 2021, Mon. Not. R. Astron. Soc., 500, 2417

Davis M., Efstathiou G., Frenk C. S., White S. D. M., 1985, Astrophys. J., 292, 371

Dawson K. S. et al., 2013, Astron. J., 145, 10

de Bernardis F., Martinelli M., Melchiorri A., Mena O., Cooray A., 2011, Phys. Rev. D, 84, 023504

de Lapparent V., Geller M. J., Huchra J. P., 1986, Astrophys. J. Lett., 302, L1

Desjacques V., Jeong D., Schmidt F., 2018, Phys. Rept., 733, 1

Despali G., Giocoli C., Angulo R. E., Tormen G., Sheth R. K., Baso G., Moscardini L., 2016, Mon. Not. R. Astron. Soc., 456, 2486

Di Valentino E. et al., 2021a, Astroparticle Physics, 131, 102605

Di Valentino E. et al., 2021b, Astroparticle Physics, 131, 102604

Di Valentino E. et al., 2021c, Astroparticle Physics, 131, 102607

Di Valentino E., Melchiorri A., Silk J., 2020, Nature Astronomy, 4, 196

Dolag K., Borgani S., Murante G., Springel V., 2009, Mon. Not. R. Astron. Soc., 399, 497

Dolag K., et al., in preparation, Unknown, unknown title and authors

Dolgov A. D., Kawasaki M., 2003, Physics Letters B, 573, 1

Dvali G., Turner M. S., 2003, arXiv e-prints, astro

Ebrahimi A. S., Monemzadeh M., Moshafi H., 2018, arXiv e-prints, arXiv:1802.05087

Efstathiou G., 1999, Mon. Not. R. Astron. Soc., 310, 842

Einstein A., 1915, Sitzungsberichte der Königlich Preußischen Akademie der Wissenschaften (Berlin), Seite 778-786.

Eisenstein D. J. et al., 2005a, Astrophys. J., 633, 560

Eisenstein D. J. et al., 2005b, Astrophys. J., 633, 560

Eke V. R., Cole S., Frenk C. S., Patrick Henry J., 1998, Mon. Not. R. Astron. Soc., 298, 1145

Elder B., Khoury J., Haslinger P., Jaffe M., Müller H., Hamilton P., 2016, Phys. Rev. D, 94, 044051

Elyiv A., Marulli F., Pollina G., Baldi M., Branchini E., Cimatti A., Moscardini L., 2015, Mon. Not. R. Astron. Soc., 448, 642

Elyiv A. A., Karachentsev I. D., Karachentseva V. E., Melnyk O. V., Makarov D. I., 2013, Astrophysical Bulletin, 68, 1

Erben T. et al., 2013, Mon. Not. R. Astron. Soc., 433, 2545

Erickcek A. L., Smith T. L., Kamionkowski M., 2006, Phys. Rev. D, 74, 121501

Etherington I. M. H., 1933, Philosophical Magazine, 15, 761

Euclid Collaboration: Blanchard A. et al., 2020, Astron. Astrophys., 642, A191

Falck B., Koyama K., Zhao G.-B., Cautun M., 2018, Mon. Not. R. Astron. Soc., 475, 3262

Finelli F., García-Bellido J., Kovács A., Paci F., Szapudi I., 2016, Mon. Not. R. Astron. Soc., 455, 1246

Fisher R. A., 1935, Journal of the Royal Statistical Society, 98, 39

Fixsen D. J., Cheng E. S., Gales J. M., Mather J. C., Shafer R. A., Wright E. L., 1996, Astrophys. J., 473, 576

Forero-Romero J. E., Hoffman Y., Gottlöber S., Klypin A., Yepes G., 2009, Mon. Not. R. Astron. Soc., 396, 1815

Freedman W. L. et al., 2001, Astrophys. J., 553, 47

Freedman W. L. et al., 2019, Astrophys. J., 882, 34

Friedmann A., 1922, Zeitschrift fur Physik, 10, 377

Frieman J. A., Turner M. S., Huterer D., 2008, Annu. Rev. Astron. Astrophys., 46, 385

Froustey J., Pitrou C., Volpe M. C., 2020, J. Cosm. Astro-Particle Phys., 2020, 015

Fukuda Y. et al., 1998, Phys. Rev. Lett., 81, 1562

García-Farieta J. E., Marulli F., Veropalumbo A., Moscardini L., Casas-Mirand a R. A., Giocoli C., Baldi M., 2019, Mon. Not. R. Astron. Soc., 488, 1987

Giocoli C., Baldi M., Moscardini L., 2018, Mon. Not. R. Astron. Soc., 481, 2813

Giocoli C. et al., 2016, Mon. Not. R. Astron. Soc., 461, 209

Giocoli C., Tormen G., van den Bosch F. C., 2008, Mon. Not. R. Astron. Soc., 386, 2135

Green J. et al., 2012, arXiv e-prints, arXiv:1208.4012

Gregory S. A., Thompson L. A., 1978, Astrophys. J., 222, 784

Gunn J. E., Gott, J. Richard I., 1972, Astrophys. J., 176, 1

Guth A. H., 1981, Phys. Rev. D, 23, 347

Guth A. H., Pi S.-Y., 1982, Physical Review Letters, 49, 1110

Hagstotz S., Costanzi M., Baldi M., Weller J., 2019, Mon. Not. R. Astron. Soc., 486, 3927

Hagstotz S., Gronke M., Mota D., Baldi M., 2019, Astron. Astrophys., 629, A46

Hamann J., Hannestad S., Wong Y. Y. Y., 2012, J. Cosm. Astro-Particle Phys., 2012, 052

Hamaus N. et al., 2022, Astron. Astrophys., 658, A20

Hamaus N., Pisani A., Choi J.-A., Lavaux G., Wandelt B. D., Weller J., 2020, arXiv e-prints, arXiv:2007.07895

Hamaus N., Pisani A., Sutter P. M., Lavaux G., Escoffier S., Wand elt B. D., Weller J., 2016, Phys. Rev. Lett., 117, 091302

Hamaus N., Sutter P. M., Lavaux G., Wand elt B. D., 2014, J. Cosm. Astro-Particle Phys., 2014, 013

Hamaus N., Sutter P. M., Lavaux G., Wand elt B. D., 2015, J. Cosm. Astro-Particle Phys., 2015, 036

Hamaus N., Sutter P. M., Wandelt B. D., 2014, Phys. Rev. Lett., 112, 251302

Handley W., 2021, Phys. Rev. D, 103, L041301

Hawken A. J. et al., 2017, Astron. Astrophys., 607, A54

He J.-h., 2013, Phys. Rev. D, 88, 103523

Heavens A., Fantaye Y., Sellentin E., Eggers H., Hosenie Z., Kroon S., Mootoovaloo A., 2017, Phys. Rev. Lett., 119, 101301

Heymans C. et al., 2012, Mon. Not. R. Astron. Soc., 427, 146

Hildebrandt H. et al., 2020, Astron. Astrophys., 633, A69

Hildebrandt H. et al., 2017, Mon. Not. R. Astron. Soc., 465, 1454

Hinterbichler K., Khoury J., 2010, Phys. Rev. Lett., 104, 231301

Hirschmann M., Dolag K., Saro A., Bachmann L., Borgani S., Burkert A., 2014, Mon. Not. R. Astron. Soc., 442, 2304

Hockney R. W., Eastwood J. W., 1981, Computer Simulation Using Particles. CRC press

Hojjati A., Pogosian L., Zhao G.-B., 2011, J. Cosm. Astro-Particle Phys., 2011, 005

Howlett C., Lewis A., Hall A., Challinor A., 2012, J. Cosm. Astro-Particle Phys., 2012, 027

Hu W., 1998, Astrophys. J., 506, 485

Hu W., 1999, Astrophys. J. Lett., 522, L21

Hu W., Kravtsov A. V., 2003, Astrophys. J., 584, 702

Hu W., Sawicki I., 2007, Phys. Rev. D, 76, 064004

Hui L., Nicolis A., Stubbs C. W., 2009, Phys. Rev. D, 80, 104002

Icke V., 1984a, Mon. Not. R. Astron. Soc., 206, 1P

Icke V., 1984b, Mon. Not. R. Astron. Soc., 206, 1P

Iocco F., Mangano G., Miele G., Pisanti O., Serpico P. D., 2009, Phys. Rept., 472, 1

Ishak M., 2019, Living Reviews in Relativity, 22, 1

Jain B., 2011, Philosophical Transactions of the Royal Society of London Series A, 369, 5081

Jain B., VanderPlas J., 2011, J. Cosm. Astro-Particle Phys., 2011, 032

Jassal H. K., Bagla J. S., Padmanabhan T., 2005, Phys. Rev. D, 72, 103503

Jenkins A., Frenk C. S., White S. D. M., Colberg J. M., Cole S., Evrard A. E., Couchman H. M. P., Yoshida N., 2001, Mon. Not. R. Astron. Soc., 321, 372

Jennings E., Li Y., Hu W., 2013, Mon. Not. R. Astron. Soc., 434, 2167

Jimenez R., Cimatti A., Verde L., Moresco M., Wandelt B., 2019, J. Cosm. Astro-Particle Phys., 2019, 043

Joudaki S. et al., 2017, Mon. Not. R. Astron. Soc., 465, 2033

Joudaki S. et al., 2018, Mon. Not. R. Astron. Soc., 474, 4894

Joyce A., Jain B., Khoury J., Trodden M., 2015, Phys. Rept., 568, 1

Joyce A., Lombriser L., Schmidt F., 2016, Annual Review of Nuclear and Particle Science, 66, 95

Kaiser N., 1984, Astrophys. J. Lett., 284, L9

Kaiser N., 1987, Mon. Not. R. Astron. Soc., 227, 1

Kamenshchik A., Moschella U., Pasquier V., 2001, Physics Letters B, 511, 265

Kendall M. G., Stuart A., Ord J. K., 1987, Kendall's Advanced Theory of Statistics. Oxford University Press, Inc., USA

Khedekar S., Majumdar S., 2013, J. Cosm. Astro-Particle Phys., 2013, 030

Khoury J., Weltman A., 2004a, Phys. Rev. D, 69, 044026

Khoury J., Weltman A., 2004b, Phys. Rev. Lett., 93, 171104

Khoury J., Weltman A., 2004c, Phys. Rev. Lett., 93, 171104

Kim Y., Park C.-G., Noh H., Hwang J.-c., 2021, arXiv e-prints, arXiv:2112.04134

Kitayama T., Suto Y., 1996, Astrophys. J., 469, 480

Knebe A. et al., 2011, Mon. Not. R. Astron. Soc., 415, 2293

Koivisto T., Mota D. F., 2006, Phys. Rev. D, 73, 083502

Komatsu E. et al., 2011, Astrophys. J. Suppl., 192, 18

Kreisch C. D., Pisani A., Carbone C., Liu J., Hawken A. J., Massara E., Spergel D. N., Wandelt B. D., 2019a, Mon. Not. R. Astron. Soc., 488, 4413

Kreisch C. D., Pisani A., Carbone C., Liu J., Hawken A. J., Massara E., Spergel D. N., Wandelt B. D., 2019b, Mon. Not. R. Astron. Soc., 488, 4413

Kreisch C. D., Pisani A., Villaescusa-Navarro F., Spergel D. N., Wandelt B. D., Hamaus N., Bayer A. E., 2021, arXiv e-prints, arXiv:2107.02304

Kumar S., Nunes R. C., 2016, Phys. Rev. D, 94, 123511

Lahav O., Kiakotou A., Abdalla F. B., Blake C., 2010, Mon. Not. R. Astron. Soc., 405, 168

Lambas D. G., Lares M., Ceccarelli L., Ruiz A. N., Paz D. J., Maldonado V. E., Luparello H. E., 2016, Mon. Not. R. Astron. Soc., 455, L99

Lambiase G., Mohanty S., Narang A., Parashari P., 2019, European Physical Journal C, 79, 141

Landy S. D., Szalay A. S., 1993, Astrophys. J., 412, 64

Laureijs R. et al., 2011, ArXiv e-prints

Lavaux G., Wandelt B. D., 2010, Mon. Not. R. Astron. Soc., 403, 1392

Lavaux G., Wandelt B. D., 2012, Astrophys. J., 754, 109

Lazeyras T., Villaescusa-Navarro F., Viel M., 2020, arXiv e-prints, arXiv:2008.12265

Le Verrier U. J., 1859, Annales de l'Observatoire de Paris, 5, 1

Lee J., Park D., 2009, Astrophys. J. Lett., 696, L10

Lesgourgues J., Mangano G., Miele G., Pastor S., 2013, Neutrino Cosmology. Cambridge University Press

Lesgourgues J., Pastor S., 2006, Phys. Rept., 429, 307

Lewis A., Challinor A., Lasenby A., 2000, Astrophys. J., 538, 473

Li B., Efstathiou G., 2012, Mon. Not. R. Astron. Soc., 421, 1431

Li Z., Wu P., Yu H., 2011, Astrophys. J. Lett., 729, L14

Limber D. N., 1953, Astrophys. J., 117, 134

Linder E. V., 2003, Phys. Rev. Lett., 90, 091301

Lorenz C. S., Calabrese E., Alonso D., 2017, Phys. Rev. D, 96, 043510

LSST Dark Energy Science Collaboration, 2012, arXiv e-prints, arXiv:1211.0310

Lu J., Liu M., Wu Y., Wang Y., Yang W., 2016, European Physical Journal C, 76, 679

Lu J.-S., Cao J., Li Y.-F., Zhou S., 2015, J. Cosm. Astro-Particle Phys., 2015, 044

Ma J.-Z., Zhang X., 2011, Physics Letters B, 699, 233

Mangano G., Miele G., Pastor S., Pinto T., Pisanti O., Serpico P. D., 2005, Nuclear Physics B, 729, 221

Martin J., 2012, Comptes Rendus Physique, 13, 566

Martinelli M., Calabrese E., de Bernardis F., Melchiorri A., Pagano L., Scaramella R., 2011, Phys. Rev. D, 83, 023012

Martino M. C., Sheth R. K., 2009, arXiv e-prints, arXiv:0911.1829

Marulli F. et al., 2013, Astron. Astrophys., 557, A17

Marulli F., Carbone C., Viel M., Moscardini L., Cimatti A., 2011, Mon. Not. R. Astron. Soc., 418, 346

Marulli F., Veropalumbo A., Moresco M., 2016, Astronomy and Computing, 14, 35

Marulli F., Veropalumbo A., Moscardini L., Cimatti A., Dolag K., 2017, Astron. Astrophys., 599, A106

Marulli F. et al., 2018, Astron. Astrophys., 620, A1

Massara E., Villaescusa-Navarro F., Viel M., Sutter P. M., 2015, J. Cosm. Astro-Particle Phys., 2015, 018

Melchior P., Sutter P. M., Sheldon E. S., Krause E., Wandelt B. D., 2014, Mon. Not. R. Astron. Soc., 440, 2922

Merten J., Giocoli C., Baldi M., Meneghetti M., Peel A., Lalande F., Starck J.-L., Pettorino V., 2019, Mon. Not. R. Astron. Soc., 487, 104

Micheletti D. et al., 2014, Astron. Astrophys., 570, A106

Mo H. J., White S. D. M., 1996a, Mon. Not. R. Astron. Soc., 282, 347

Mo H. J., White S. D. M., 1996b, Mon. Not. R. Astron. Soc., 282, 347

Monaco P., 1995, Astrophys. J., 447, 23

More S., Kravtsov A. V., Dalal N., Gottlöber S., 2011, Astrophys. J. Suppl., 195, 4

Moresco M., Marulli F., 2017, Mon. Not. R. Astron. Soc., 471, L82

Motohashi H., Starobinsky A. A., Yokoyama J., 2013, Phys. Rev. Lett., 110, 121302

Mukherjee S. et al., 2020, arXiv e-prints, arXiv:2009.14199

Mészáros P., 1974, Astron. Astrophys., 37, 225

Nadathur S., 2013, Mon. Not. R. Astron. Soc., 434, 398

Nadathur S., 2016, Mon. Not. R. Astron. Soc., 461, 358

Nadathur S., Hotchkiss S., 2015a, Mon. Not. R. Astron. Soc., 454, 2228

Nadathur S., Hotchkiss S., 2015b, Mon. Not. R. Astron. Soc., 454, 889

Nadathur S., Hotchkiss S., Diego J. M., Iliev I. T., Gottlöber S., Watson W. A., Yepes G., 2015, Mon. Not. R. Astron. Soc., 449, 3997

Nadathur S. et al., 2020, arXiv e-prints, arXiv:2008.06060

Neyrinck M. C., 2008, Mon. Not. R. Astron. Soc., 386, 2101

Nojiri S., Odintsov S. D., 2006, arXiv e-prints, hep

Norberg P., Baugh C. M., Gaztañaga E., Croton D. J., 2009, Mon. Not. R. Astron. Soc., 396, 19

Paillas E., Cai Y.-C., Padilla N., Sánchez A. G., 2021, Mon. Not. R. Astron. Soc., 505, 5731

Paillas E., Cautun M., Li B., Cai Y.-C., Padilla N., Armijo J., Bose S., 2019, Mon. Not. R. Astron. Soc., 484, 1149

Paz D., Lares M., Ceccarelli L., Padilla N., Lambas D. G., 2013, Mon. Not. R. Astron. Soc., 436, 3480

Peacock J. A., Heavens A. F., 1990, Mon. Not. R. Astron. Soc., 243, 133

Peebles P. J. E., 1970, Astron. J., 75, 13

Peebles P. J. E., 1980, The large-scale structure of the universe. Princeton University Press

Peebles P. J. E., 2001, Astrophys. J., 557, 495

Peebles P. J. E., Hauser M. G., 1974, Astrophys. J. Suppl., 28, 19

Peel A., Lalande F., Starck J.-L., Pettorino V., Merten J., Giocoli C., Meneghetti M., Baldi M., 2019, Phys. Rev. D, 100, 023508

Peel A., Pettorino V., Giocoli C., Starck J.-L., Baldi M., 2018, Astron. Astrophys., 619, A38

Pelliciari D., Contarini S., Marulli F., Moscardini L., Giocoli C., Dolag K., 2022, in preparation, Cosmology from probe combination: synergies between the number counts of galaxy clusters and cosmic voids, preliminary title and authors

Percival W. J. et al., 2010, Mon. Not. R. Astron. Soc., 401, 2148

Perico E. L. D., Voivodic R., Lima M., Mota D. F., 2019, arXiv e-prints, arXiv:1905.12450

Perlmutter S., et al., 1999, Astrophys. J., 517, 565

Perotto L., Lesgourgues J., Hannestad S., Tu H., Y Y Wong Y., 2006, J. Cosm. Astro-Particle Phys., 2006, 013

Pesce D. W. et al., 2020, Astrophys. J. Lett., 891, L1

Pezzotta A. et al., 2017, Astron. Astrophys., 604, A33

Pisani A., Lavaux G., Sutter P. M., Wandelt B. D., 2014, Mon. Not. R. Astron. Soc., 443, 3238

Pisani A., Sutter P. M., Hamaus N., Alizadeh E., Biswas R., Wandelt B. D., Hirata C. M., 2015, Phys. Rev. D, 92, 083531

Pisani A., Sutter P. M., Wandelt B. D., 2015, arXiv e-prints, arXiv:1506.07982

Planck Collaboration et al., 2016a, Astron. Astrophys., 594, A13

Planck Collaboration et al., 2016b, Astron. Astrophys., 594, A14

Planck Collaboration et al., 2020a, Astron. Astrophys., 641, A6

Planck Collaboration et al., 2020b, Astron. Astrophys., 641, A5

Platen E., van de Weygaert R., Jones B. J. T., 2007, Mon. Not. R. Astron. Soc., 380, 551

Pollina G., Baldi M., Marulli F., Moscardini L., 2016, Mon. Not. R. Astron. Soc., 455, 3075

Pollina G., Hamaus N., Dolag K., Weller J., Baldi M., Moscardini L., 2017, Mon. Not. R. Astron. Soc., 469, 787

Pollina G. et al., 2019, Mon. Not. R. Astron. Soc., 487, 2836

Potter D., Stadel J., Teyssier R., 2017, Computational Astrophysics and Cosmology, 4, 2

Poulin V., Boddy K. K., Bird S., Kamionkowski M., 2018, Phys. Rev. D, 97, 123504

Press W. H., Schechter P., 1974, Astrophys. J., 187, 425

Puchwein E., Baldi M., Springel V., 2013, Mon. Not. R. Astron. Soc., 436, 348

Ratra B., Peebles P. J. E., 1988, Phys. Rev. D, 37, 3406

Raveri M., Martinelli M., Zhao G., Wang Y., 2016, arXiv e-prints, arXiv:1606.06268

Reed D. S., Schneider A., Smith R. E., Potter D., Stadel J., Moore B., 2015, Mon. Not. R. Astron. Soc., 451, 4413

Riemer-Sørensen S., Parkinson D., Davis T. M., Blake C., 2013, Astrophys. J., 763, 89

Riess A. G., Casertano S., Yuan W., Macri L. M., Scolnic D., 2019, Astrophys. J., 876, 85

Riess A. G. et al., 2011, Astrophys. J., 730, 119

Riess A. G. et al., 2016, Astrophys. J., 826, 56

Riess A. G., et al., 1998, Astron. J., 116, 1009

Ronconi T., Contarini S., Marulli F., Baldi M., Moscardini L., 2019, Mon. Not. R. Astron. Soc., 488, 5075

Ronconi T., Lapi A., Viel M., Sartori A., 2020, Mon. Not. R. Astron. Soc., 498, 2095

Ronconi T., Marulli F., 2017, Astron. Astrophys., 607, A24

Ruiz A. N., Paz D. J., Lares M., Luparello H. E., Ceccarelli L., Lambas D. G., 2015, Mon. Not. R. Astron. Soc., 448, 1471

Ryden B., 2016, Introduction to Cosmology. Cambridge University Press

Sahlén M., 2019, Phys. Rev. D, 99, 063525

Sahlén M., Silk J., 2018, Phys. Rev. D, 97, 103504

Sahlén M., Zubeldía Í., Silk J., 2016, Astrophys. J. Lett., 820, L7

Saito S., Takada M., Taruya A., 2008, Phys. Rev. Lett., 100, 191301

Saito S., Takada M., Taruya A., 2009, Phys. Rev. D, 80, 083528

Sakstein J., Trodden M., 2020, Phys. Rev. Lett., 124, 161301

Sánchez A. G. et al., 2017a, Mon. Not. R. Astron. Soc., 464, 1640

Sánchez C. et al., 2017b, Mon. Not. R. Astron. Soc., 465, 746

Sandvik H. B., Tegmark M., Zaldarriaga M., Waga I., 2004, Phys. Rev. D, 69, 123524

Sartori S., Contarini S., Marulli F., Moscardini L., Baldi M., 2022, in preparation, BitVF: a back-in-time void finding algorithm, preliminary title and authors

Schlaufman K. C., Thompson I. B., Casey A. R., 2018, Astrophys. J., 867, 98

Schmidt B. P. et al., 1998, Astrophys. J., 507, 46

Schramm D. N., Turner M. S., 1998, Reviews of Modern Physics, 70, 303

Schuster N., Hamaus N., Pisani A., Carbone C., Kreisch C. D., Pollina G., Weller J., 2019, J. Cosm. Astro-Particle Phys., 2019, 055

Scoccimarro R., 2004, Phys. Rev. D, 70, 083007

Scrimgeour M. I. et al., 2012, Mon. Not. R. Astron. Soc., 425, 116

Seljak U., Slosar A., McDonald P., 2006, J. Cosm. Astro-Particle Phys., 2006, 014

Sellentin E., Quartin M., Amendola L., 2014, Mon. Not. R. Astron. Soc., 441, 1831

Shafieloo A., Clarkson C., 2010, Phys. Rev. D, 81, 083537

Shandarin S. F., Zeldovich Y. B., 1989, Rev. Mod. Phys., 61, 185

Sheth R. K., Tormen G., 1999, Mon. Not. R. Astron. Soc., 308, 119

Sheth R. K., Tormen G., 2002, Mon. Not. R. Astron. Soc., 329, 61

Sheth R. K., van de Weygaert R., 2004, Mon. Not. R. Astron. Soc., 350, 517

Shi K., Huang Y. F., Lu T., 2012, Mon. Not. R. Astron. Soc., 426, 2452

Solà J., 2013, in Journal of Physics Conference Series, Vol. 453, Journal of Physics Conference Series, p. 012015

Spolyar D., Sahlén M., Silk J., 2013a, Phys. Rev. Lett., 111, 241103

Spolyar D., Sahlén M., Silk J., 2013b, Phys. Rev. Lett., 111, 241103

Springel V., 2005, Mon. Not. R. Astron. Soc., 364, 1105

Springel V., White S. D. M., Tormen G., Kauffmann G., 2001, Mon. Not. R. Astron. Soc., 328, 726

Steigman G., 2007, Annual Review of Nuclear and Particle Science, 57, 463

Suto Y., Sato K., Sato H., 1984, Progress of Theoretical Physics, 71, 938

Sutter P. M. et al., 2015, Astronomy and Computing, 9, 1

Sutter P. M., Lavaux G., Hamaus N., Wand elt B. D., Weinberg D. H., Warren M. S., 2014a, Mon. Not. R. Astron. Soc., 442, 462

Sutter P. M., Lavaux G., Hamaus N., Wandelt B. D., Weinberg D. H., Warren M. S., 2014b, Mon. Not. R. Astron. Soc., 442, 462

Szapudi I. et al., 2015, Mon. Not. R. Astron. Soc., 450, 288

Tamayo D., Vázquez J. A., 2019, Mon. Not. R. Astron. Soc., 487, 729

Taruya A., Nishimichi T., Saito S., 2010, Phys. Rev. D, 82, 063522

Tegmark M. et al., 2004, Phys. Rev. D, 69, 103501

Teklu A. F., Remus R.-S., Dolag K., Beck A. M., Burkert A., Schmidt A. S., Schulze F., Steinborn L. K., 2015, Astrophys. J., 812, 29

Thompson L. A., Gregory S. A., 2011, arXiv e-prints, arXiv:1109.1268

Tikhonov A. V., Karachentsev I. D., 2006, Astrophys. J., 653, 969

Tinker J. L., Robertson B. E., Kravtsov A. V., Klypin A., Warren M. S., Yepes G., Gottlöber S., 2010, Astrophys. J., 724, 878

Tormen G., Moscardini L., Yoshida N., 2004, Mon. Not. R. Astron. Soc., 350, 1397

Troxel M. A. et al., 2018, Phys. Rev. D, 98, 043528

Tutusaus I. et al., 2020, arXiv e-prints, arXiv:2005.00055

Upadhye A., Biswas R., Pope A., Heitmann K., Habib S., Finkel H., Frontiere N., 2014, Phys. Rev. D, 89, 103515

Valcin D., Bernal J. L., Jimenez R., Verde L., Wandelt B. D., 2020, J. Cosm. Astro-Particle Phys., 2020, 002

van de Weygaert R., Platen E., 2011, in International Journal of Modern Physics Conference Series, Vol. 1, International Journal of Modern Physics Conference Series, pp. 41–66

van de Weygaert R., Schaap W., 2009, in Data Analysis in Cosmology, Martínez V. J., Saar E., Martínez-González E., Pons-Bordería M. J., eds., Vol. 665, Springer, pp. 291–413

Velten H. E. S., vom Marttens R. F., Zimdahl W., 2014, European Physical Journal C, 74, 3160

Verde L., Treu T., Riess A. G., 2019, Nature Astronomy, 3, 891

Verza G., Pisani A., Carbone C., Hamaus N., Guzzo L., 2019, J. Cosm. Astro-Particle Phys., 2019, 040

Viel M., Haehnelt M. G., Springel V., 2010, J. Cosm. Astro-Particle Phys., 2010, 015

Vielzeuf P. et al., 2019, arXiv e-prints, arXiv:1911.02951

Villaescusa-Navarro F., Bird S., Peña-Garay C., Viel M., 2013, J. Cosm. Astro-Particle Phys., 2013, 019

Villaescusa-Navarro F., Marulli F., Viel M., Branchini E., Castorina E., Sefusatti E., Saito S., 2014, J. Cosm. Astro-Particle Phys., 2014, 011

Voivodic R., Lima M., Llinares C., Mota D. F., 2017, Phys. Rev. D, 95, 024018

Wagner C., Verde L., Jimenez R., 2012, Astrophys. J. Lett., 752, L31

Wang X., Chen X., Zheng Z., Wu F., Zhang P., Zhao Y., 2009, Mon. Not. R. Astron. Soc., 394, 1775

Wang Y., 2008, Phys. Rev. D, 77, 123525

Wang Y., Xu L., Zhao G.-B., 2017, Astrophys. J., 849, 84

Weinberg S., 1972, Gravitation and Cosmology: Principles and Applications of the General Theory of Relativity. John Wiley & Sons, Inc

Weinberg S., 1989, Reviews of Modern Physics, 61, 1

Wen S., Wang S., Luo X., 2018, J. Cosm. Astro-Particle Phys., 2018, 011

Wetterich C., 1988, Nuclear Physics B, 302, 668

Will C. M., 2005, Phys. Rev. D, 71, 084027

Will C. M., 2014, Living Reviews in Relativity, 17, 4

Wojtak R., Powell D., Abel T., 2016, Mon. Not. R. Astron. Soc., 458, 4431

Wolz L., Kilbinger M., Weller J., Giannantonio T., 2012, J. Cosm. Astro-Particle Phys., 2012, 009

Wright B. S., Winther H. A., Koyama K., 2017, J. Cosm. Astro-Particle Phys., 2017, 054

Xu X., Cuesta A. J., Padmanabhan N., Eisenstein D. J., McBride C. K., 2013, Mon. Not. R. Astron. Soc., 431, 2834

Yadav J. K., Bagla J. S., Khandai N., 2010, Mon. Not. R. Astron. Soc., 405, 2009

Yang L. F., Neyrinck M. C., Aragón-Calvo M. A., Falck B., Silk J., 2015, Mon. Not. R. Astron. Soc., 451, 3606

Yèche C., Palanque-Delabrouille N., Baur J., du Mas des Bourboux H., 2017, J. Cosm. Astro-Particle Phys., 2017, 047

Yoo J., Watanabe Y., 2012, International Journal of Modern Physics D, 21, 1230002

Zehavi I. et al., 2011, Astrophys. J., 736, 59

Zeldovich I. B., Einasto J., Shandarin S. F., 1982, Nature, 300, 407

Zel'Dovich Y. B., 1970, Astron. Astrophys., 500, 13

Zeldovich Y. B., 1972, Mon. Not. R. Astron. Soc., 160, 1P

Zennaro M., Bel J., Dossett J., Carbone C., Guzzo L., 2018, Mon. Not. R. Astron. Soc., 477, 491

Zhao C., Tao C., Liang Y., Kitaura F.-S., Chuang C.-H., 2016, Mon. Not. R. Astron. Soc., 459, 2670

Zhao G.-B., Giannantonio T., Pogosian L., Silvestri A., Bacon D. J., Koyama K., Nichol R. C., Song Y.-S., 2010, Phys. Rev. D, 81, 103510

Zhao G.-B., Pogosian L., Silvestri A., Zylberberg J., 2009, Phys. Rev. D, 79, 083513

Zhao G.-B., Xia J.-Q., Li H., Tao C., Virey J.-M., Zhu Z.-H., Zhang X., 2007, Physics Letters B, 648, 8

Zivick P., Sutter P. M., Wandelt B. D., Li B., Lam T. Y., 2015, Mon. Not. R. Astron. Soc., 451, 4215

Zucca A., Pogosian L., Silvestri A., Zhao G. B., 2019, J. Cosm. Astro-Particle Phys., 2019, 001

Zwicky F., 1937, Astrophys. J., 86, 217